Energy Yield of Floating Offshore Wind Turbines

Influence of Floater Type and Mooring Stiffness for the IEA 15 MW Reference Turbine using OpenFAST

Ole Grootes

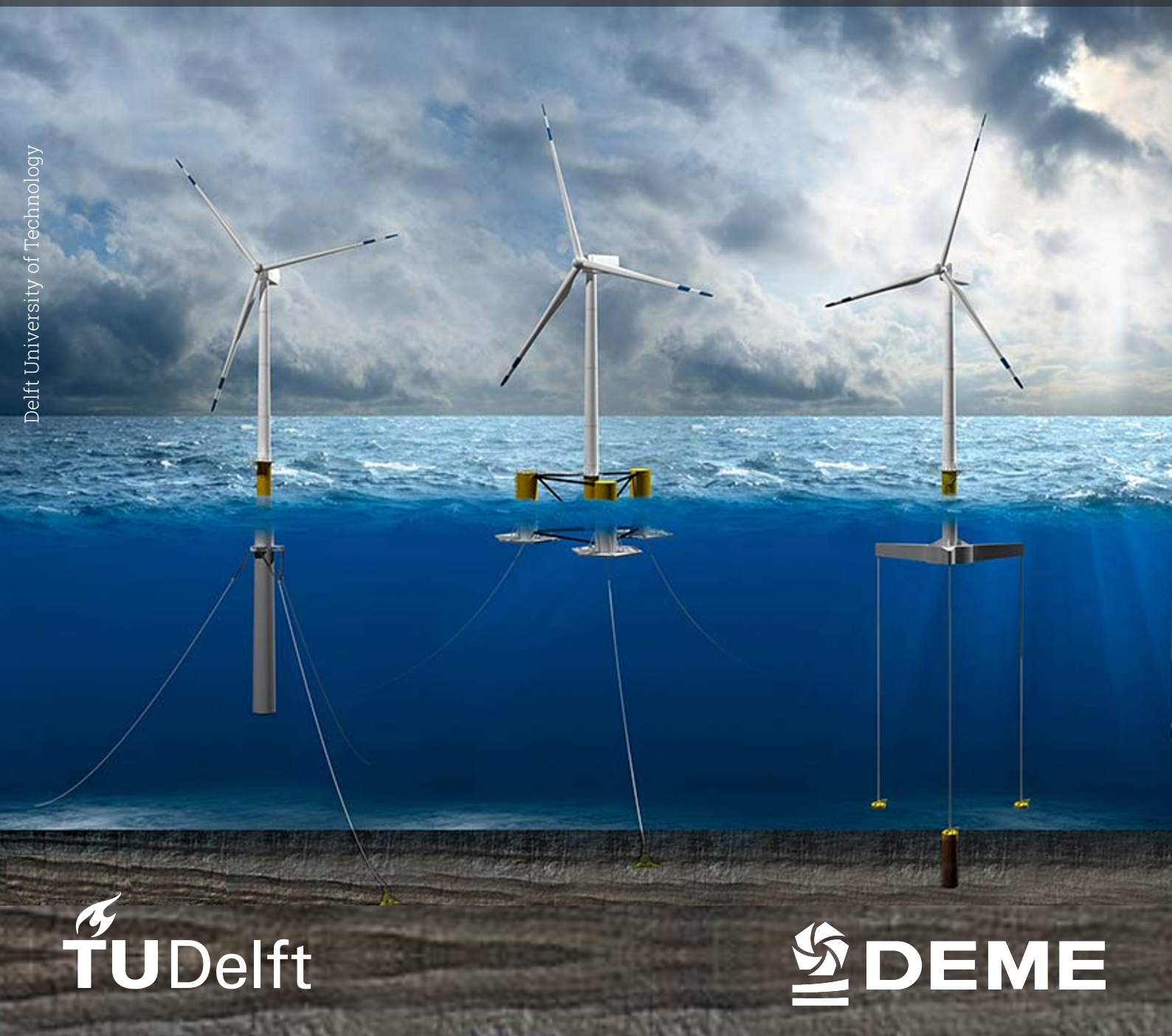

Delft University of Technology

TU Delft

DEME

Energy Yield of Floating Offshore Wind Turbines

Influence of Floater Type and Mooring Stiffness for the IEA 15 MW Reference Turbine using OpenFAST

by

Ole Grootes

to obtain the degree of Master of Science

at the Delft University of Technology,

to be defended publicly on Thursday 21 May 2026 at 10:00 AM.

Student number:	5070759	
Project duration:	1 September 2025 – 21 May 2026	
Faculty:	Faculty of Aerospace Engineering, TU Delft	
Thesis committee:	Prof.dr. D.A. von Terzi	TU Delft, Chair
	Dr.ing. S. Schreier	TU Delft, Examinor
	Prof.dr.ir. A. C. Viré	TU Delft, Supervisor
	Dr.ir. M. M. Mroczek	DEME, Supervisor
	Ir. J. de Haan	DEME, Supervisor

Cover image: Overview of the main floating wind platform concepts (from left to right): spar buoy, semi-submersible and tension-leg platform. Adapted from [1].

An electronic version of this thesis is available at `http://repository.tudelft.nl/`.

TU Delft DEME

Preface

With this master's thesis, I complete my studies in Aerospace Engineering at Delft University of Technology. After taking a gap year to work on the development of a foiling hydrogen-powered boat, I chose to further pursue my interest in wind energy and in particular floating wind turbines. This field brings together a long-standing fascination with wind energy, sparked by experiments during my high school years and my passion for sailing.

This thesis was carried out as part of my Master's programme at TU Delft in collaboration with DEME. The work focuses on the comparison of different floating wind turbine concepts. Conducting this research within an industry environment provided a valuable opportunity to engage with practical challenges and to better understand the engineering considerations behind real-world applications.

I would like to express my sincere gratitude to the people who contributed to this project. First, I thank my supervisors at DEME, Johan de Haan and Maciej Mroczek, for proposing an inspiring research topic and for their guidance, critical feedback and continuous support throughout the project. Their expertise and practical insights were invaluable in shaping both the direction and quality of this work. I am also very grateful to my TU Delft supervisor, Axelle Viré, for her academic guidance and constructive feedback, which helped me maintain a clear and structured approach throughout the thesis.

Furthermore, I had the pleasure of working with colleagues from the Design Department at DEME, based in both the Netherlands and Belgium. The team provided a welcoming and inspiring environment; everyone showed genuine interest in my work and gave valuable input from their own knowledge and experience. I particularly appreciated the informal moments, such as the occasional Spanish lessons, lunch walks or sport events we joined, which made it easy to feel part of the team. Attending the end-of-year event was a highlight that further strengthened this sense of belonging. All of this made the working environment both enjoyable and inspiring.

Finally, I would like to thank my friends, housemates and family for their continuous support throughout my studies. Their encouragement and times of relaxation along the way have been invaluable in maintaining balance during this journey. A special thanks goes to my girlfriend for her patience, unwavering support and constant encouragement. Her occasional reminders to actually put my thoughts down on paper have been more important than she might realise.

Ole Grootes
Delft, May 2026

Abstract

Floating offshore wind turbines enable the exploitation of deep-water regions with strong and consistent wind resources, where bottom-fixed foundations become economically unfeasible. However, the dynamic behaviour of floating support structures introduces additional complexity: platform motions and mooring characteristics influence turbine aerodynamics, control interactions and ultimately energy yield. A systematic understanding of how floater type and mooring stiffness affect power production and energy yield is therefore essential for the design of next-generation floating wind farms.

This thesis investigates the influence of the floater type and mooring stiffness on the energy yield of a floating offshore wind turbine using comparative time-domain simulations of the IEA 15 MW reference turbine. Four publicly available floating platform concepts are analysed: the WindCrete spar buoy, the ActiveFloat and VolturnUS-S semi-submersibles and a reference tension-leg platform (TLP). All configurations are modelled within the fully coupled aero-hydro-servo-elastic framework OpenFAST and evaluated under site-specific offshore conditions representative of the Buchan Deep site (Hywind Scotland). A fixed, rigidly mounted turbine is included as a baseline to isolate motion-induced influences.

Free-decay simulations first establish the natural periods and damping characteristics of each platform. Whereafter operational simulations across the full wind-speed range are used to assess platform motions and power variation and annual energy production (AEP) calculations based on Weibull-distributed wind conditions. Power variation is quantified using the coefficient of variation. In addition, sensitivity analyses investigate the robustness of the results with respect to wind-speed bin sizing, wave height and period, mooring stiffness variation and wind-wave misalignment.

The results show that floater type strongly influences platform dynamics: the TLP exhibits the smallest surge and pitch motions due to its stiff station-keeping system, while semi-submersible platforms display the largest horizontal excursions. Despite these differences, all floating platforms achieve AEP values within 2% of the fixed reference turbine. In contrast, power variation is significantly higher (4-14x) for floating configurations, particularly for platforms with larger surge and pitch responses. Increasing mooring stiffness primarily affects restoring-force-dominated degrees of freedom and increases heave damping for the spar and TLP, while its impact on mean power output remains limited. Sensitivity analyses demonstrate that wave conditions, wind-wave misalignment and wind-speed bin sizing have only a minor influence on AEP compared to wind-induced platform motion.

Overall, the findings indicate that floating support structures primarily affect power stability rather than long-term energy yield. While increased platform motions lead to higher short-term power variation, their impact on AEP remains modest for well-designed floating concepts. These results provide quantitative insight on trade-offs between floater dynamics, mooring design and energy performance, supporting informed decision-making during the early-stage design and selection of floating offshore wind turbine concepts for deep-water deployment.

Contents

List of Figures

List of Tables

List of Symbols

Abbreviations

AEP	Annual Energy Production
BEM	Blade element momentum
CFD	computational fluid dynamics
COB	Centre of buoyancy
COG	Centre of gravity
CoV	Coefficient of variation
DBEM	Dynamic BEM
DLC	Design load case
DLL	Dynamic link library
DNV	Det Norske Veritas
DOF	Degree of freedom
DTU	Technical University of Denmark
FOWT	Floating offshore wind turbine
GM	Metacentrich height
IEA	International Energy Agency
IEC	International Electrotechnical Commission
JONSWAP	Joint North Sea Wave Project
MARIN	Maritime Research Institute Netherlands
NREL	National Renewable Energy Laboratory
NRMSD	Normalised Root Mean Square Difference
OLAF	cOnvecting LAgrangian Filaments
OpenFAST	Open Fatigue, Aerodynamics, Structures & Turbulence
OWF	Offshore wind farm
PI	Proportional-integral
RAFT	Response Amplitudes of Floating Turbines
RAO	Response amplitude operator
RNA	Rotor nacelle assembly
ROSCO	Reference Open Source Controller
SWL	Still water level
TLB	Tension-leg buoy
TLP	Tension-leg platform
WAMIT	Wave Analysis Massachusetts Institute of Technology.

Subscripts

n	Normal direction
ref	Reference value
t	Tangential direction

Roman Symbols

$\dot{x}_{\text{surge}}$	Surge velocity platform	m/s
a	Axial induction factor	-
a'	Tangential induction factor	-
C_p	Coefficient of performance	-
D	Characteristic dimension for Morison strip theory	m
D	Drag force	N
F_b	Buoyancy force	N
F_g	Gravitational force	N
F_n	Normal force	N
F_t	Tangential force	N
F_t	Tendon force	N
g	Gravitational accelartion	m/s^2
H_s	Significant wave height	m
h_{hub}	Hub height	m
L	Lift force	N
M_R	Restoring moment	Nm
M_W	Wind and wave loading moment	Nm
P	Turbine power	W
R	Resultant aerodynamic force	N
r	Radial location airfoil	m
T	Aerodynamic thrust	N
T_p	Spectral peak period	s
T_z	Mean zero-upcrossing period	s
U	Freestream wind velocity	m/s
V_{app}	Apparent wind velocity	m/s
V_{rel}	Relative wind velocity	m/s
z	Height above mean sea level	m

Greek Symbols

α	Angle of attack	$^\circ$
α	Power law exponent	-
$\dot{\theta}_{\text{pitch}}$	Pitch velocity platform	rad/s
λ	Tip speed ratio	-
λ	Wave lenght	m
Ω	Angular velocity of the rotor	rad/s
ϕ	Inflow angle	$^\circ$
ρ	Air density	kg/m^3
σ	Standard deviation	-
θ	Section twist angle	$^\circ$

1 Introduction

A decade has passed since the historic signing of the Paris Agreement, which set the goal to limit global warming to 1.5 °C and avoid the most severe consequences of climate change [2]. To meet these goals, a rapid expansion of renewable energy production is essential to decarbonise the energy sector. Renewable technologies, such as solar, wind or hydro energy, can deliver large-scale, low-carbon electricity. According to the International Energy Agency's (IEA) Net Zero Roadmap, achieving these targets will demand a tripling of global renewable energy capacity between 2022 and 2030 [3]. Within this context, the European wind energy industry association, WindEurope, predicts that by 2030, 425 GW of wind energy will be required in the EU [4], while only 343 GW is expected to be installed [5]. This gap highlights a clear need to accelerate the growth of the wind energy sector.

A key challenge to meet these ambitious targets is that the current generation bottom-fixed turbines can access only 20% of Europe's windy regions [6], [7]. This limitation exists because the remaining 80% of these sites lie in water deeper than 60 metres and are therefore economically unviable for conventional bottom-fixed turbines. Although a few small-scale floating offshore wind farms have already been built, bottom-fixed turbines still account for the overwhelming majority of offshore installations [8]. Floating offshore wind turbines offer a promising solution, as they can be deployed in these deeper, high-wind areas that have remained inaccessible until now for large-scale offshore wind development. Exploiting these regions is critical for achieving Europe's offshore wind capacity targets and limiting global warming.

The remainder of this introduction outlines the key elements of the thesis research. Section 1.1 provides essential background information to situate the research within a broader context. The motivation for this research is presented in Section 1.2, followed by the research question in Section 1.3. The method used to adress the research question is summarised in Section 1.4. Lastly, the report layout is described in Section 1.5.

1.1. Background

Floating offshore wind turbines (FOWTs) employ a variety of floater types to enable deployment in deep waters. The three most common floater configurations, which are widely studied and deployed due to their proven performance, are the (A) spar buoy, (B) semi-submersible and (C) tension-leg platform (TLP), as illustrated in Figure 1.1, while other concepts include the barge concept with a moonpool and hybrid designs. Each of these systems differs in stability, motion response, mooring requirements, site conditions and its overall influence on the annual energy production of the turbine. In particular, the mooring lines, anchoring the platform to the seabed, play a critical role in constraining platform motion, influencing the natural frequencies and damping characteristics and overall stability of the floating turbine. Understanding and assessing these differences is key to the design of floating offshore wind turbines.

The early deployment of floating wind turbines illustrates how different floater concepts have been translated from prototypes into commercially significant offshore wind farms. The first of these prototypes, deployed by Blue H Technologies in 2007, was an 80 kW turbine mounted on a TLP and demonstrated the feasibility of floating concepts for energy generation [10]. Two years later, Equinor advanced the concept with the Hywind prototype, a 2.3 MW turbine installed on a steel spar buoy, marking the first large-scale floating wind demonstrator [11]. In 2011, Principle Power worked with a 2 MW turbine on a semi-submersible platform in the WindFloat project [12]. Since then, technological development has accelerated rapidly and multiple floating offshore wind farms have become operational. The most recent

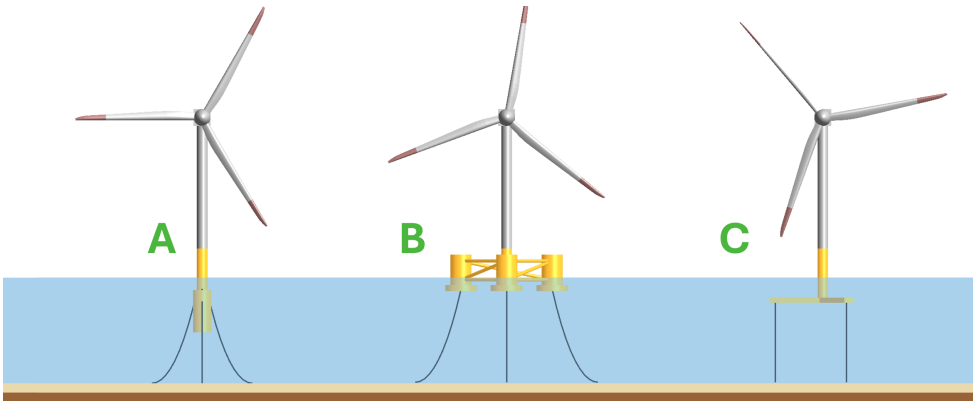

Figure 1.1: Overview of the main floating wind platform concepts:
(A) spar buoy, (B) semi-submersible and (C) tension-leg platform (TLP). Adapted from [9].

and currently the largest floating offshore wind farm, Hywind Tampen, consists of 11 turbines, each with an 8.4 MW rating, mounted on concrete spar buoys [13]. As of today, 245 MW of floating turbines are operational worldwide, while the global pipeline of planned or under-construction projects has reached 266 GW [14].

With multiple floating turbines now deployed worldwide and many more in the global pipeline, it is important to understand how each of the three main floater concepts' design features influences stability and performance. Firstly, the spar buoy (A) uses a long and heavy cylindrical hull, which extends deep below the water surface, to lower the centre of gravity like a fishing bobber. Secondly, the stability of the semi-submersible platform (B) is provided by the buoyancy of the wide and submerged base structure. This structure is made of several columns, often equipped with heave plates to reduce vertical motion in waves. Finally, the TLP (C) consists of a submerged structure connected to the seabed with tensioned mooring lines. These lines limit the movements of the platform in the pitch and vertical directions. More information about the different concepts can be found in Section 2.3.

1.2. Research Motivation

Recent developments in the offshore wind sector, especially the rapid increase in turbine size (see Figure 1.2) and efforts toward standardisation, highlight the importance of systematically evaluating floating support structures for future large-scale turbines. In 2025, offshore wind farms (OWFs) in Europe were equipped with turbines averaging 10.7 MW in capacity, while future orders have reached 14.6 MW [5]. These figures are expected to increase further, as GE's Haliade-X has recently been certified for 14.7 MW [15] and prototypes of even larger turbines, up to 26 MW, are being tested [16]. Next to the increase in turbine size, the industry is increasingly pursuing standardisation of wind turbines to reduce cost and improve reliability [17]. Initiatives such as the North Sea Standard, which aims to limit turbine height over the coming decade, could facilitate this process [18]. Therefore, the floating wind energy sector has significant steps to take to standardise and mature as an industry.

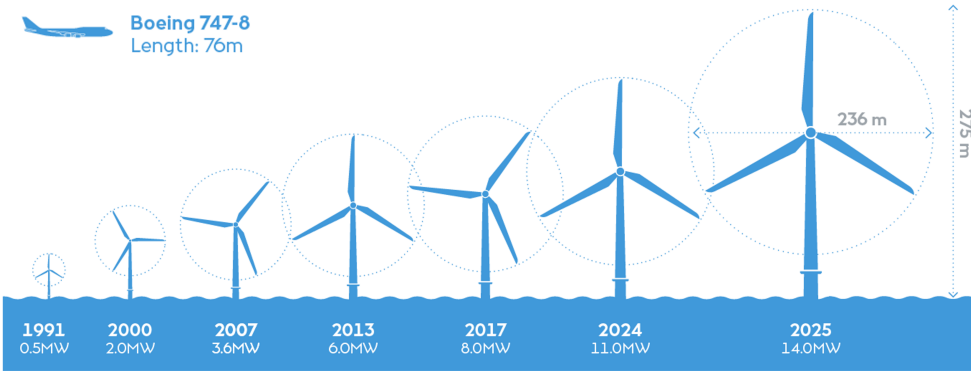

Figure 1.2: Evolution of the largest commercially installed wind turbines. Adapted from [19].

To support such comparative studies, various open-source reference turbines for offshore applications have been developed. Reference turbines are standardised models used to benchmark and compare wind turbine performance in simulations and experiments. The most widely known and used reference turbine is the NREL 5 MW turbine developed by the National Renewable Energy Laboratory (NREL) in 2009 [20]. The Technical University of Denmark (DTU) 10 MW reference turbine followed, which provided a reference for the increasing size of offshore turbines [21]. Subsequently, NREL and DTU collaborated to develop the IEA 10 MW [22], IEA 15 MW [23] and most recently, the IEA 22 MW [24] reference turbines. A detailed overview can be found in Subsection 2.2.1. Moreover, for these reference turbines (except 22 MW), several floater concepts exist, including spar buoy, semi-submersible and tension-leg platforms. Using the identical IEA 15 MW rotor across all different floaters concepts, they can be consistently compared across operating conditions, which is important to understand how turbine size and floating platform design interact.

Despite the significant developments in floating wind turbines outlined above, there is still no consensus about which floater type is most suitable for large-scale turbines, particularly as turbine sizes continue to grow. Early studies comparing multiple floaters have been limited to the NREL 5 MW reference turbine [25], [26], [27] or the DTU 10 MW reference turbine [28]. While these studies provided valuable insights, they are limited in scope and do not fully capture the behaviour of next-generation turbines under realistic operating conditions. In addition to these numerical comparisons, experimental campaigns have been conducted to validate the implementation of the reference turbines on different floaters in OpenFAST, a state-of-the-art, open-source simulation tool widely used in both academia and industry for coupled aero-hydro-elastic analysis of floating wind turbines. Moreover, experimental campaigns have been performed to verify and validate OpenFAST. For example, wave basin tests were performed at the Maritime Research Institute Netherlands (MARIN) for the NREL 5 MW [29]. For the DTU 10 MW reference turbine, wave basin tests [30], as well as wind tunnel tests [31] have been conducted.

Nevertheless, a systematic comparison of floater types and mooring configurations for larger turbines remains absent. In particular, the influence of floater type and mooring stiffness on energy yield has not yet been evaluated for the 15 MW reference turbine. Maximising annual energy production (AEP) is of particular importance in the floating wind sector, as floating installations carry significantly higher capital and operational costs than their bottom-fixed counterparts. Even small floater-induced losses in the AEP can have a substantial impact on the levelised cost of energy and the economic viability of a project. In addition, comparative studies between floating concepts and a bottom-fixed reference, such as a monopile configuration for the IEA 15 MW turbine, are currently absent. This limits the ability to benchmark floating designs against established technologies.In conclusion, these gaps underscore the need for systematic comparisons of floater types and mooring stiffness for the largest, next-generation turbines, which motivates the research presented in this thesis.

1.3. Research Question

To advance the floating offshore wind sector and address the research gap identified in Section 1.2, this research formulates the following research question:

> **Research question:** ”How do the floater type and the stiffness of the mooring system influence the energy yield of a floating offshore wind turbine, as investigated through comparative OpenFAST simulations of the IEA 15 MW reference turbine on different floating configurations?”

This research is addressed through the following subquestions, which break down the problem into manageable components:

1. How do the natural frequencies and damping characteristics vary among the floater types?
2. How does varying the mooring stiffness modify the motion amplitudes, restoring characteristics and stability of the floating system?
3. How do floater motions and control interactions affect instantaneous and mean power output of the wind turbine?
4. How does the annual energy production vary across floater types and mooring stiffness values?
5. How does the annual energy production compare to a bottom-fixed turbine?

1.4. Research Approach

The research approach is shaped by three considerations. First, the IEA 15 MW reference turbine is chosen as the baseline for this study. It is a publicly available next-generation offshore wind turbine representing current large-scale commercial projects and also has publicly available floater definitions across all three main floater families. Both enable a consistent and fair comparison. Second, OpenFAST is chosen as the simulation environment because it is the industry-standard open-source tool for coupled aero-hydro-servo-elastic analysis of floating wind turbines. Furthermore, existing validation campaigns for earlier and smaller-sized reference turbines provide confidence in OpenFAST's fidelity. Third, the Hywind Scotland wind farm site is used to derive realistic, statistically representative wind and wave conditions. This ensures that the AEP estimates reflect genuine offshore environments rather than idealised or arbitrary inputs.

Comparative OpenFAST simulations are conducted for the IEA 15 MW reference turbine mounted on four floater concepts: WindCrete spar [32], ActiveFloat [32] and VolturnUS-S semisubmersibles [33] and the Reference TLP [34]. A bottom-fixed configuration is used as a baseline to quantify floater-induced differences in energy yield to be directly quantified.

Platform performance is evaluated across the full operational wind speed range (cut-in to cut-out) using site-specific Weibull-distributed conditions and associated sea states from Hywind Scotland [35]. The analysis focuses on motion-induced variations in power production relative to a bottom-fixed baseline. Sensitivity analyses systematically isolate key parameters: (i) wave height and period influence (24 sea states at 9.5 m/s), (ii) wind speed bin sizing (1.0, 0.5 and 0.25 m/s bins), (iii) mooring stiffness (0.25-2.0× baseline stiffness) and (iv) wind-wave misalignment (0°-60°) to identify dominant hydrodynamic-aerodynamic coupling effects on annual energy production. The full simulation framework (floater and turbine models, ROSCO controller, design load cases and post-processing) is detailed in Chapter 3.

1.5. Report Layout

The introduction presents the topic by providing background information, identifying the research gap and stating the research question. Chapter 2 will offer a detailed review of the theoretical framework and existing literature. The methodology used to address the research question is described in Chapter 3. The results of the research will be presented in Chapter 4 and discussed in Chapter 5. Based on the results and discussion, the conclusion and recommendations for the industry and future research are provided in Chapter 6.

2

Theory & Literature

This chapter provides the theoretical background and reviews the current state of research on floating offshore wind turbines (FOWTs). Section 2.1 introduces the fundamental physical principles of FOWTs, followed by a discussion on the numerical modelling and simulation tools in Section 2.2. The chapter ends with a review of different floating platform concepts, their stability mechanisms and performance characteristics in Section 2.3 to establish the basis for the analyses presented in the subsequent chapters.

2.1. Fundamentals of Floating Offshore Wind Turbines

This section presents the core physical principles that govern the behaviour of floating offshore wind turbines (FOWTs). It starts with the analysis of the main components of FOWTs as shown in Figure 2.1:

- 2.1.1 Rotor Aerodynamics
- 2.1.2 Turbine Structural Elasticity
- 2.1.3 Floater Hydromechanics
- 2.1.4 Mooring System Principles
- 2.1.5 Turbine Control Systems
- 2.1.6 Platform Motions

Following this, the interactions between these components are examined in Subsection 2.1.7 and the influence of them on the power production is discussed in Subsection 2.1.8. Finally, Subsection 2.1.9 discusses experimental scaling laws used for experiments. Together, these fundamentals provide the foundation for understanding and accurately simulating the operation and performance of FOWTs.

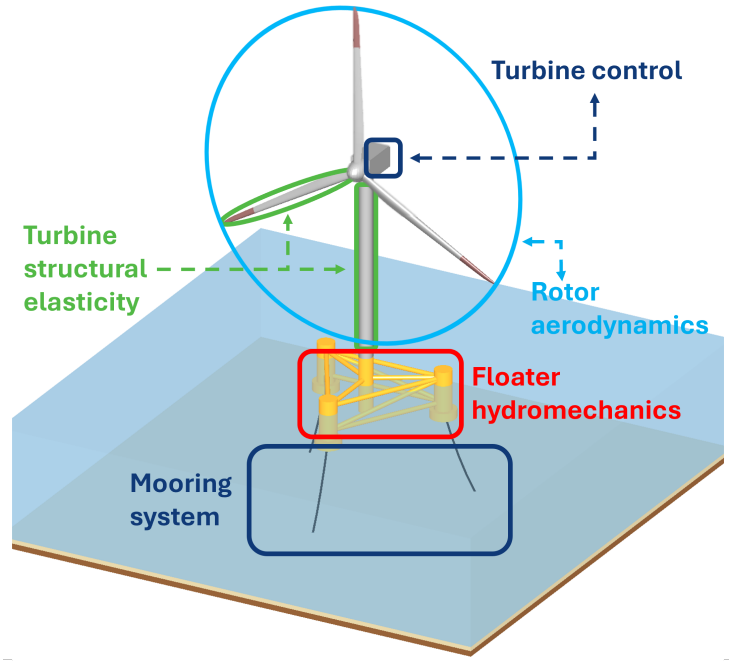

Figure 2.1: Main components of a floating offshore wind turbine. Adapted from [9].

2.1.1. Rotor Aerodynamics

Modern horizontal-axis wind turbines harness the kinetic energy of the wind by converting it into a rotational motion. This motion is used to drive a generator to produce electricity. However, not all the energy can be extracted from the wind to prevent a halt of the airflow at the rotor plane of the wind turbine. By applying the momentum theory, which assumes an idealised actuator disc placed in an undisturbed airstream, it is calculated that a maximum of 59.3% of the energy can be extracted; also known as the Betz limit [36], [37]. This is a theoretical limit, as in practice the available power is further reduced by aerodynamic and mechanical losses [38].

The rotational motion of a wind turbine is generated by the torque produced by the aerodynamic forces acting on the blades. These forces are a result of the interaction between the airfoil blade and the relative wind speed V_{rel}. This velocity combines the incoming wind speed U with the rotational component Ωr and the forces are usually assessed for individual blade elements, a short airfoil segment along the blade span. Figure 2.2 shows an airfoil, a cross-section of a wind turbine blade, with wind velocity components, necessary angles and the resulting force components. The force magnitude and direction depend on the angle of attack α and the magnitude of V_{rel}. The resultant force R can be decomposed into the lift L and drag force D, respectively perpendicular and parallel to V_{rel}. Another split can be made into the in-plane and out-of-plane force components, respectively the tangential F_t and normal force F_n. These components in the blade element theory are fundamental for predicting the aerodynamic performance of blade sections and therefore for the overall turbine power production [38], [39].

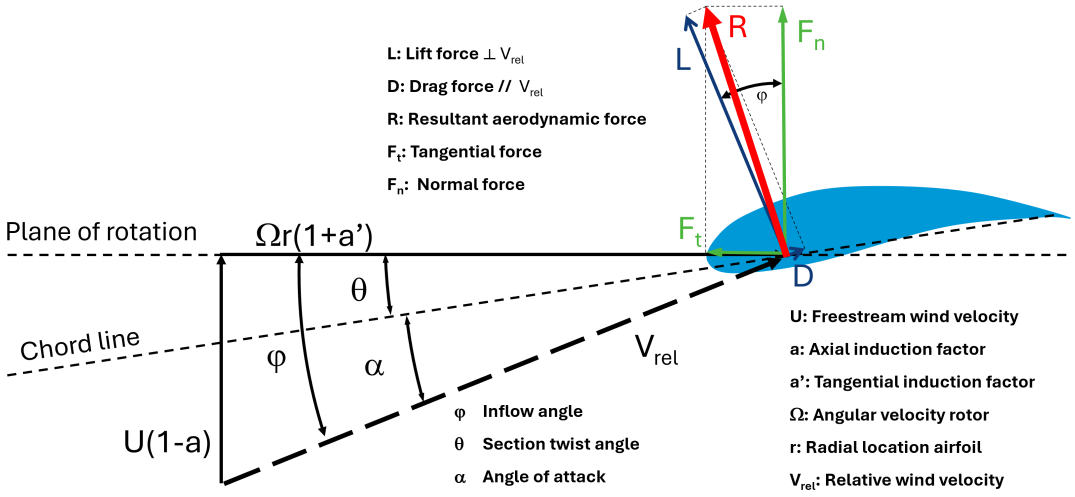

Figure 2.2: Cross-section of a wind turbine blade showing relative wind, angles of attack and inflow and the resulting lift, drag and force components. Adapted from [38].

While the previous section focused on the forces generated on individual blade elements, the overall behaviour of the rotor can also be examined using momentum theory, which models the rotor as a thin actuator disk in an undisturbed flow, an idealised rotor. The presence of the rotor already modifies the flow at the rotor plane itself and it slows down the air and generates the aerodynamic forces that produce torque. The fraction by which the wind speed is reduced at the rotor is characterised by the induction factor a. When the air flows further downstream, the extraction of kinetic energy produces a region of reduced wind speed and increased turbulence downstream, also known as the wake. To satisfy the conservation of mass, the streamtube through and beyond the rotor, as shown in Figure 2.3 [38], [40].

To predict rotor performance based on the aerodynamic forces discussed above, several aerodynamic modelling approaches exist. These models range from low-fidelity analytical models to high-fidelity computational fluid dynamic and vortex-based solvers. Among these, the blade element momentum (BEM) method remains the most widely used in wind turbine engineering because it offers a practical balance between accuracy and computational efficiency. While higher-fidelity methods capture complex three-dimensional and unsteady flow phenomena in greater detail, their computational cost makes them less suitable for iterative design studies or real-time analysis. For these reasons, this work focuses on BEM as a representative and widely adopted low-fidelity aerodynamic model.

The BEM theory combines the blade element theory and momentum theory to estimate the aerodynamic forces on the rotor. It calculates the rotor forces by iteratively solving for the axial and tangential induction factors a and a'. These factors link the local aerodynamic forces on the blades to the overall momentum

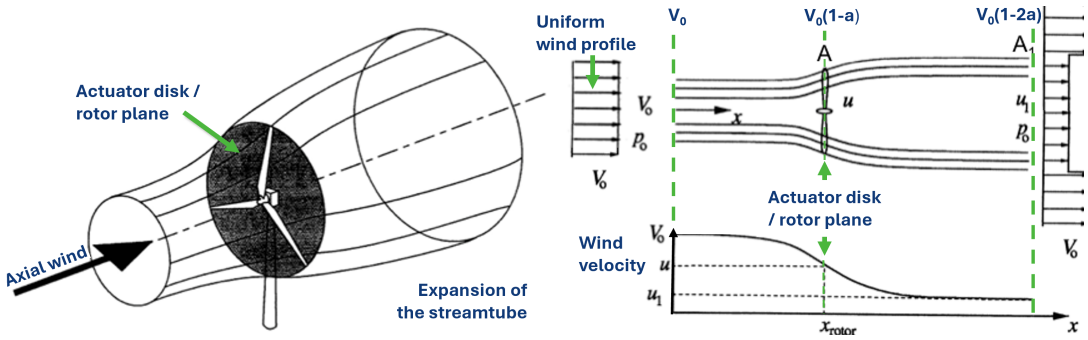

Figure 2.3: Simplified illustration of wind passing through the rotor area, showing reduced velocity at the actuator disk and the subsequent expansion of the streamtube. Adapted from [40].

change in the rotor's streamtube and thus ensure that the global forces on the actuator are equal to the sum of the local blade forces. Despite being computationally efficient, BEM's idealised assumptions need a number of empirical adjustments in order to represent real rotor behaviour. Standard corrections include Prandtl's tip and hub loss factors, which account for three-dimensional flow near the blade tip and hub and Glauert corrections for highly loaded regions [41]. Additional models may be included to account for unsteady aerodynamic effects such as dynamic inflow, dynamic stall and wake-related losses. Dynamic inflow models simulate the delayed response of the induced velocity to changing operating conditions for the whole rotor and dynamic stall models the flow of the local blade conditions at high angles of attack or rapidly changing inflow conditions. Empirical wake correction models are used to better approximate the complex flow (wake expansion and turbulence increase) behind the rotor. Although these simplifications and corrections reduce the model's accuracy, BEM remains a fast and robust low-fidelity aerodynamic model suitable for the early stages of wind turbine design or the analysis of floating wind turbines [38], [39].

In addition to BEM-specific corrections, general losses further reduce aerodynamic performance relative to ideal momentum theory. For example, yaw misalignment reduces the effective wind component normal to the rotor plane and profile and drag losses occur along the blade span due to viscous effects and a finite lift-to-drag ratio. Other losses arise from surface roughness, manufacturing imperfections or off-design conditions. An unavoidable energy loss is represented by the wake rotation as kinetic energy is carried away in the rotor's swirl. Accounting for all these combined effects is essential to generate realistic performance estimates and inform aerodynamic and structural design choices [38], [39].

2.1.2. Turbine Structural Elasticity

Wind turbine blades and towers are slender and therefore inherently flexible structures that deform under aerodynamic, gravitational and inertial loading. These elastic deformations modify the local angle of attack and the distribution of aerodynamic forces along the blade, which impacts the aerodynamic behaviour and overall turbine performance [42]. For FOWTs, this behaviour becomes even more significant as platform motions introduce additional variations in inflow direction and rotor loading. An accurate understanding of the turbine's elastic response is therefore essential for predicting dynamic behaviour, assessing fatigue life and evaluating the overall performance of floating wind systems [9].

Structural elasticity is modelled through the use of predefined mode-shape functions, classical beam theories or full finite-element formulations depending on the desired balance between accuracy and computational efficiency. In the early design phase of wind turbines, a combination of beam-theory formulations and predefined mode-shape functions is used. In this approach, each flexible component is idealised as a slender beam that deforms according to classical beam theory and used to compute a set of characteristic mode shapes: flapwise and edgewise bending of the blades and the fore-aft and side-side bending of the tower. The most dominant modes are used as a spatial basis function in a modal reduced-order model and combined through weighted sums to arrive at the total deformation. This approach offers a practical trade-off between fidelity and efficiency for predicting structural deformation and load distribution under varying operating conditions [42].

Each major component possesses its own natural frequencies and mode shapes. Environmental forces from wind and waves can excite these modes and cause amplification of the dynamic loads due to resonance. As illustrated in Figure 2.4, the first structural mode of a bottom-fixed turbine exhibits higher-frequency tower modes due to its rigid foundation, while a FOWT is typically dominated by low-frequency platform rigid-body motion. The second mode of the FOWT (tower bending mode) is more strongly associated with turbine-driven loading (e.g. rotor 3P frequency). To keep this mode at a higher frequency, the tower is often designed to be stiffer than that of a bottom-fixed turbine. The floater's design, with its corresponding platform modes, influences the coupling between structural and platform dynamics and thus the overall response of the floating system [9].

Elasticity also influences power capture. Blade and tower flexibility must be chosen to balance aerodynamic efficiency, structural robustness and cost. While extremely rigid constructions increase bulk and manufacturing costs, excessive flexibility may decrease power extraction by changing effective inflow conditions and increasing sensitivity to platform motion. Therefore, accurate structural elasticity modelling is essential for trustworthy aero-hydro-servo-elastic simulations to ensure appropriate separation of natural frequencies and predict fatigue and extreme loads. As a result, it will enable the design of stiffness distributions that optimise both power capture and structural performance of FOWTs.

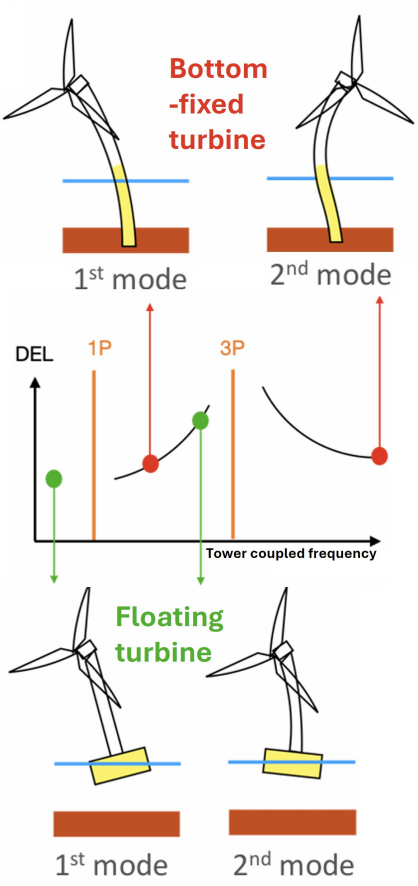

Figure 2.4: First and second structural modes of a bottom-fixed (top) and floating (bottom) offshore wind turbine [9].

2.1.3. Floater Hydromechanics

The hydrostatic and hydrodynamic principles govern the behaviour of floating structures. Properties such as stability, motion response and load transfer mechanisms of floaters are determined by a combination of buoyancy, restoring stiffness, wave-body interaction and viscous effects. The hydrostatics, hydrodynamics and stability mechanisms of floaters and the modelling approaches will be discussed in more detail to understand the key concepts.

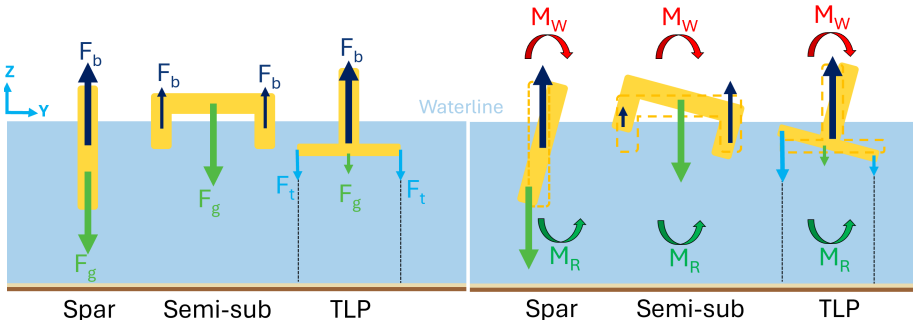

Figure 2.5: Floating principles and restoring mechanisms of spar buoy, semi-submersible and tension-leg platform floaters. Buoyancy (F_b), gravity (F_g) and tendon forces (F_t) determine static equilibrium. The wind and wave loading (M_W) induces platform motions and is counteracted by the restoring moment (M_R). Based on [43].

The hydrostatic forces ensures the equilibrium and initial stability of floating structures. The equilibrium position of each main floater type is shown at the left side of Figure 2.5. The buoyancy force F_b acts vertically upward through the centre of buoyancy (COB) and the gravitational force F_g acts downward through the centre of gravity (COG). A floater is in static equilibrium when these forces are equal in magnitude. When the floater is displaced by a small angle, the underwater geometry changes and the COB shifts horizontally. The intersection of the new buoyant force line with the original vertical axis defines the metacentre. The metacentric height GM, the distance between the COG and metacentre, expresses initial hydrostatic stability. A positive GM generates a restoring moment proportional to the displaced volume and rotation angle [44].

Building on these hydrostatic principles, Figure 2.5 also illustrates the main static stability mechanisms (right side). Spars obtain their restoring moment M_R mainly from the vertical separation between COG and COB: their deep draft and heavy keel ballast position the COG well below the COB. Thus even a small heel produces a significant righting lever arm as the COB shifts horizontally. In contrast, semi-submersibles rely on their large distributed waterplane area to generate restoring stiffness. When they tilt, the submerged and emergent columns generate differential buoyancy forces. The resulting righting moment scales with the waterplane area moment of inertia rather than with COG-COB offset. Tension-leg platforms behave differently from both concepts: their restoring capability is dominated by tendon force F_t from the high pretension in the vertical mooring tendons. If the platform pitches, the tension in some tendons will increase in some tendons and decrease in others. This produces strong restoring forces that exceed the hydrostatic contribution. As a result, TLPs act as stiff and vertically restrained systems with limited motion. In contrast, spars and semi-submersibles rely primarily on hydrostatic righting principles shaped by their geometry and mass distribution [25].

While hydrostatic stability maintains equilibrium under static conditions, hydrodynamic effects define a platform's response to time-varying environmental loads. Dynamic stability is therefore important to limit motion amplitudes and avoid resonance. Hydrodynamic forces arise from multiple sources: incident waves acting on the floater, the disturbance of those waves by the structure, fluid accelerations due to wave kinematics and the relative velocity between the fluid and the moving or stationary structure. The hydrodynamic forces can be divided into the following components [44], [45]:

- **Froude-Krylov force:** Integration of the incident (undisturbed) wave pressure over the wetted surface of the floater while assuming the waves are not disturbed by it.
- **Diffraction force:** Correction of the Froude-Krylov force to take the disturbances of the waves into account. Together with the Froude-Krylov component, it forms the first-order wave excitation force.
- **Radiation forces:** A moving floater accelerates the fluid around it, which is characterised by the added mass matrix. It increases the effective inertia of the platform and shifts the natural periods to higher values. Furthermore, the platform oscillations create wave radiation that depends on the excitation frequency, also called radiation damping. It suppresses resonance amplitudes but does not shift the natural frequency itself.
- **Viscous drag:** For slender elements (diameter-to-wavelength ratio satisfies $D/\lambda < 0.2$) and wave scattering is negligible, the Morison equation is used to compute hydrodynamic forces. It comprises three terms: an inertia term proportional to fluid acceleration, a quadratic drag term proportional to the square of the relative velocity between fluid and structure and a Froude-Krylov term accounting for the undisturbed wave pressure gradient. The relative importance of the drag and inertia terms is governed by the Keulegan-Carpenter number. At low KC, the inertia term dominates; at high KC, the quadratic drag term becomes increasingly significant. The Froude-Krylov force contributes across all flow regimes, as it depends solely on the undisturbed wave pressure gradient.
- **Current drag:** A steady current subjects the float to a hydrodynamic drag force caused by the relative velocity of the water.

The modelling of wave-induced forces depends on choosing an approach that fits both the floater's shape and the local wave conditions. Hydrodynamic coefficients are strongly frequency-dependent and this dependence is essential for predicting natural periods and overall dynamic stability. Large, bulky parts of a floater are typically modelled with potential-flow theory. This theory describes how waves move around the structure and how the structure radiates waves back into the sea. However, slender components are better represented using Morison-type approaches as viscous effects dominate and wave scattering is small. When the flow around a structure becomes strongly nonlinear or turbulent, more detailed computational fluid dynamics tools can be used to improve or verify the results. In practice, floating wind turbine models often combine these methods [9], [45].

2.1.4. Mooring System Principles

Mooring systems provide the station-keeping capability and hydromechanical restoring required for floating offshore wind turbines. The main components of a mooring system are anchors installed at the seabed and mooring lines connecting the floater to these anchors. Depending on the system configuration, several anchor concepts are available. The mooring lines can consist of steel chains, wire rope or synthetic fibre rope and several extra components, such as connectors, clump weights, buoyancy elements and in-line tensioners, are added to tune the force-displacement behaviour of the mooring system [46]. In this thesis, only the global mooring characteristics impacting the system-level behaviour are relevant and will be discussed in more detail.

The mooring lines restrict the horizontal and vertical movement of the floater by generating restoring forces through line geometry, axial elasticity or pre-tension. For small perturbations around an equilibrium position, the mooring restoring force is linearised. If the displacement of the floater becomes larger, the mooring lines will exhibit non-linear behaviour. In order to compute the mooring system forces, each line is divided into nodes connected by axial springs and dampers. For every node, static equilibrium between the internal forces (axial tension) and external forces (hydrodynamic, gravity, seabed contact loads) is solved for the given offset [47]. The dynamic high-voltage cable has little to no influence on the movement of the floater and is often neglected in simulations [48].

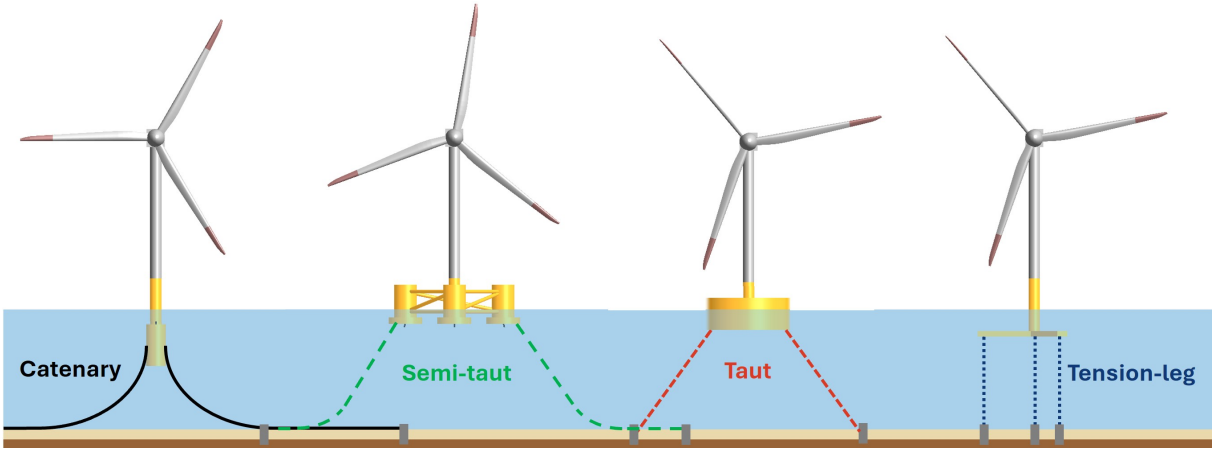

Figure 2.6: Examples of mooring system options (from left to right): catenary, semi-taut, taut, tension-leg. Based on [49].

Table 2.1: Main characteristics of standard floating wind mooring concepts [46], [47].

Property	Catenary	Semi-taut	Taut	Tension-leg
Surge & sway stiffness (horizontal)	Low	Moderate	High	Low/moderate
Heave stiffness (vertical)	Very low	Low	Low/moderate	Extremely high
Pitch & roll stiffness (rotational)	Very low	Low/moderate	Moderate	Extremely high
Yaw stiffness (rotational)	Very low	Low	Moderate	High
Line tension	Low	Moderate/high	High	Very high
Seabed contact	High	Moderate	Low	None
Seabed footprint	Very large	Large	Medium	Small
Design complexity	Low	Medium	Medium/high	High
Typical geometry	Bowed curve with chain on seabed	Partially tensioned, mixed chain/rope	Tensioned rope at angle to the seabed	Near-vertical pre-tensioned tendons
Restoring mechanism	Weight + geometry	Weight + axial stiffness	Axial stiffness	Pretension in tendons
Line type	Chain	Chain + synthetic/wire rope	Synthetic/wire rope	Synthetic/wire tendons
Advantages / Disadvantages	Mature technology and relatively simple installation procedure / High material demand	Suitable for deeper water and reduced material requirement / Less field-proven	Lightweight system and reduced motions / Challenging installation and high anchor loads	Limited motions / Challenging installation and high anchor loads; especially due to pretension
Common platforms	Spar & semi-submersible	Semi-submersible	Semi-submersible	TLP

Figure 2.6 illustrates the four main types of mooring system concepts used: catenary, taut, semi-taut and tension-leg configurations [46], [47]. Their characteristics affect power production primarily through their impact on platform motion and resulting aero-servo-hydrodynamic coupling, as discussed further in Subsection 2.1.7. The key features of each mooring type are summarised below and a detailed comparison can be found in Table 2.1:

- **Catenary moorings** rely on heavy chains lying partially on the seabed. This gives low initial horizontal stiffness and allows large horizontal motions. The pitch and roll motions are weakly constrained and mainly governed by the hydrodynamics of the floater. The vertical motion remains largely unaffected due to the near-horizontal line geometry. The catenary moorings offer low peak tensions, but platform motions and aero-hydro coupling increase.
- **Semi-taut moorings** combine seabed-contacting chain segments with inclined and tensioned upper sections. This combination increases horizontal stiffness and reduces surge/sway motions compared to catenaries and the inclined geometry moderately restrains pitch and roll. The semi-taut moorings offer a balanced compromise between motion control and mooring loads.
- **Taut moorings** are inclined and fully tensioned lines with no seabed contact. They provide high horizontal stiffness and significantly reduce surge and pitch, but leave heave relatively unconstrained. This stiffness increases the dynamic line and aero-hydro coupling.
- **Tension-leg moorings** use vertical and highly pretensioned tendons. These give extremely high vertical (heave) and rotational stiffness (pitch/roll), but horizontal movements (surge/sway) are weakly restrained. The improved stability comes at the cost of high tendon loads.

2.1.5. Turbine Control Systems

Modern wind turbines rely on closed-loop control systems to regulate aerodynamic power extraction and ensure structural safety across their full operating wind speed range. In general, these systems use feedback loops to track desired operating points and compensate for disturbances caused by wind variability, turbulence and inherent system dynamics. Several different controller designs are available: classical PI-based torque and pitch controllers to more advanced gain-scheduled or state-space approaches [50]. Figure 2.7 illustrates the three main control regimes of conventional bottom-fixed wind turbines in a torque-rotational-speed diagram with the maximum aerodynamic efficiency drawn as a dashed curve [38].

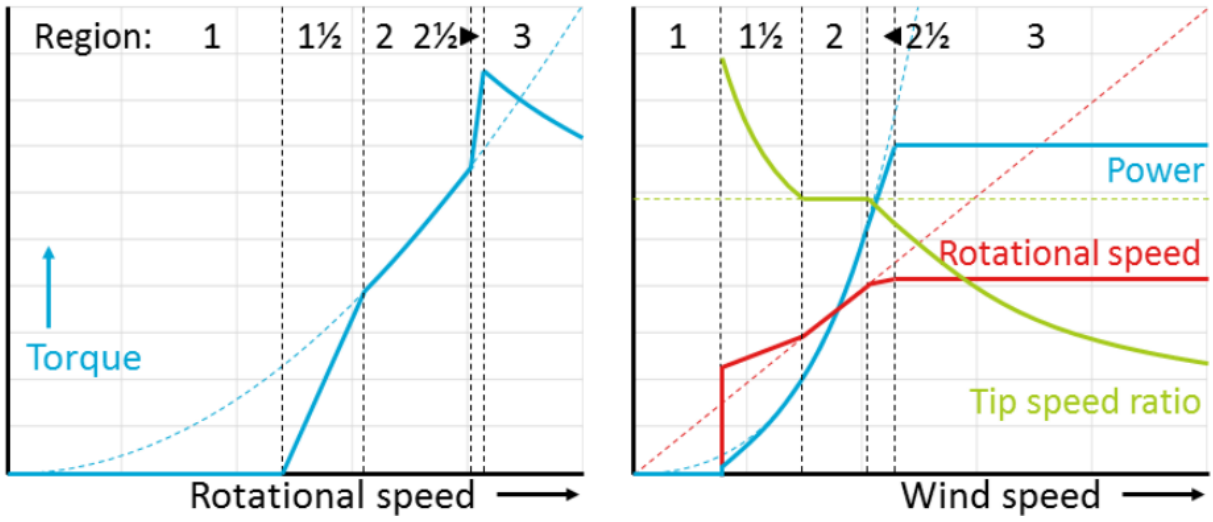

Figure 2.7: Torque-rotational-speed diagram of a modern wind turbine. The dashed curves represent the maximum aerodynamic efficiency [38].

Below the cut-in wind speed (Region 1), the generator is disengaged and the rotor idles with no torque or power production. As wind speed increases, the turbine enters Region 1½: a straight transition curve where generator torque and rotor speed rise together. This path lies to the right of the optimal curve and leads to a higher-than-ideal tip-speed ratio and a small power deficit. In Region 2, the turbine operates in partial-load mode, also called torque control. The torque is applied proportionally to the square of the rotor speed to maintain the optimal tip-speed ratio and extract maximum power. Region 2½ (around rated wind speed) provides a controlled transition toward full-load operation. In Region 3, the turbine sustains its rated power output by regulating the blade pitch to hold the rotor speed constant. Wind gusts can lead to slight overspeeds and are managed along a constant-power curve (torque inversely proportional to speed) until pitch control brings the turbine back to its rated operating point. When the

cut-out wind speed (Region 4) is surpassed, the turbine is taken out of operation by fully feathering the blades to protect structural integrity [38], [51].

When transitioning from fixed to floating offshore platforms, the nature of turbine control becomes more complex due to the additional degrees of freedom introduced by platform motion. The significant translational and rotational motions of FOWTS experience alter the relative inflow experienced by the rotor. This invalidates classical assumptions about wind turbine control, such as rotor speed being determined solely by aerodynamic torque. The controller is both affected by the platform and vice versa (more detail in Subsection 2.1.7). FOWT requires designs that explicitly account for the aero-hydro-servo interaction between the turbine and its floating support structure, while minimising structural loads and maximising the power generation. In response to these challenges, several studies review and classify advanced control strategies for FOWTs [52], [53].

2.1.6. Platform Motions

FOWTs differ fundamentally from offshore bottom-fixed turbines because they are free to move in all six degrees of freedom (DOF): surge, sway, heave, roll, pitch and yaw. Figure 2.8 illustrates 3 translational and 3 rotational DOF and the coordinate system used throughout this thesis. Due to the direction of wind and wave loading, surge (horizontal translation along the wind direction) and pitch (rotation about the lateral axis) and pitch dominate the dynamic behaviour of a FOWT. These motions are highlighted in blue to emphasise their relative importance. The movements in one DOF often influence the reaction in another DOF, leading to a coupled system (more detail in Subsection 2.1.7). To understand this multi-DOF response, the basic platform motions will be discussed in this section [9], [46].

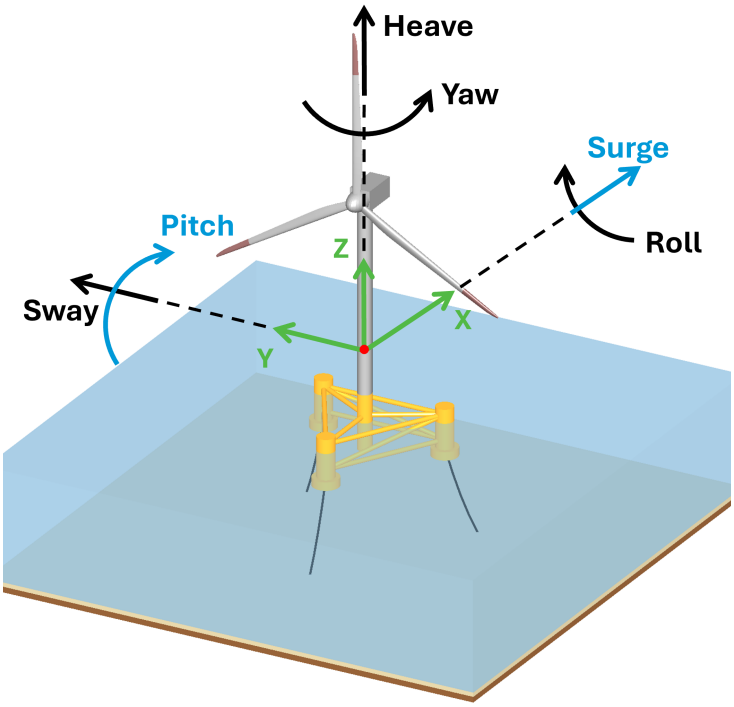

Figure 2.8: The axis system and degree of freedom for a floating offshore wind turbine. The generally most dominant DOFs (surge and pitch) are highlighted in blue. Adapted from [9].

The motions influence both the aerodynamic loads on the rotor and the hydrodynamic loads on the floater. An important metric for the aerodynamic loads is the effective wind speed at the hub, also called the apparent wind speed. The inflow wind speed provides the primary contribution, but can be altered by the platform's translational and rotational motions. As the surge and pitch have the most direct influence on the axial component of the apparent wind speed, they will be discussed in more detail. Figure 2.9 illustrates how a combined surge and pitch motion can either amplify or reduce the relative wind speed experienced at the hub depending on their phase relationship. The apparent wind, V_{app}, speed at the hub can be calculated with Equation 2.1.

$$V_{app} = U - \dot{x}_{\text{surge}} - \dot{\theta}_{\text{pitch}} \cdot h_{\text{nacelle}} \tag{2.1}$$

where V_{app} is the apparent wind speed, calculated by subtracting the floater motions from the free stream wind velocity U. The surge velocity of the hub is equal to the surge velocity of the platform, $\dot{x}_{\text{surge}}$ and the pitch velocity of the hub is calculated by multiplying the platform's pitch velocity $\dot{\theta}_{\text{pitch}}$ with the hub height above the reference point h_{hub}. If the hub moves towards the wind ($\dot{x}_{\text{surge}} < 0$ or $\dot{\theta}_{\text{pitch}} < 0$). the apparent wind speed increases [9].

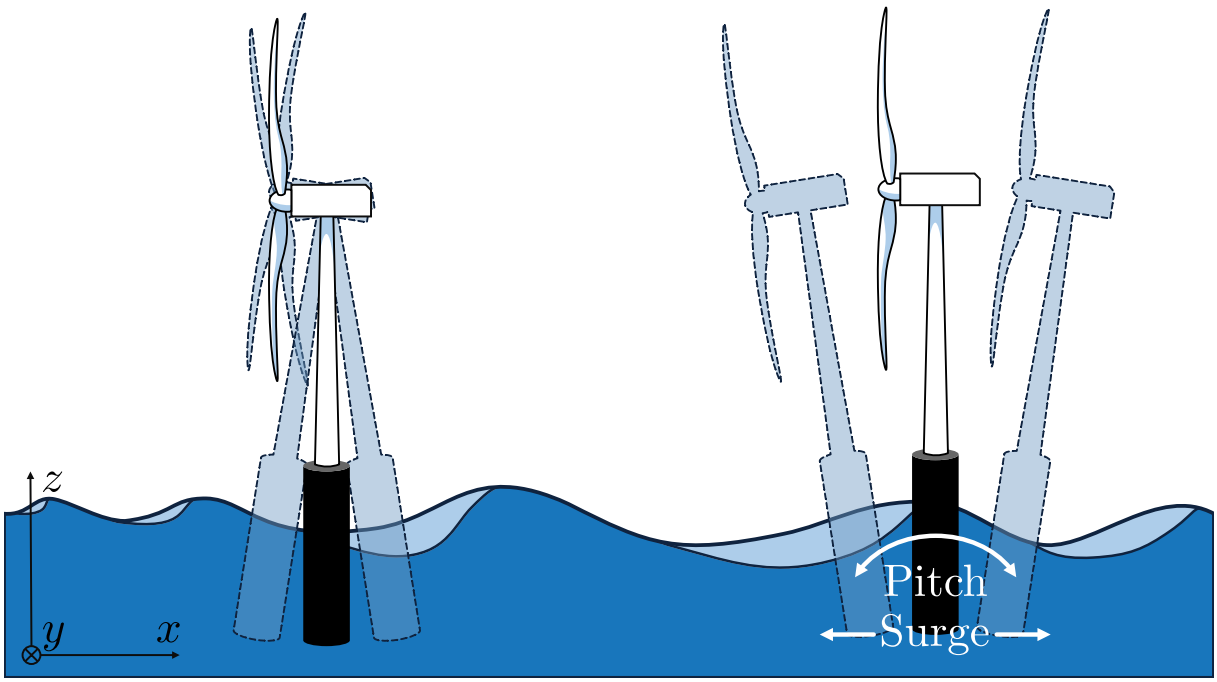

Figure 2.9: The hub motion in a combined pitch and surge motion can be cancelled out or amplified depending on their phase relationship [54].

The overall response of a floating wind turbine depends strongly on the platform concept, which will be discussed in Subsection 2.3.1 in more detail. Figure 2.10 illustrates typical pitch and surge excursions of a 5 MW wind turbine mounted on three different floating foundations. TLPs generally experience the smallest motions due to the high stiffness of the mooring system. The lower hydrostatic restoring forces of spars result in larger motion amplitudes, especially in pitch.

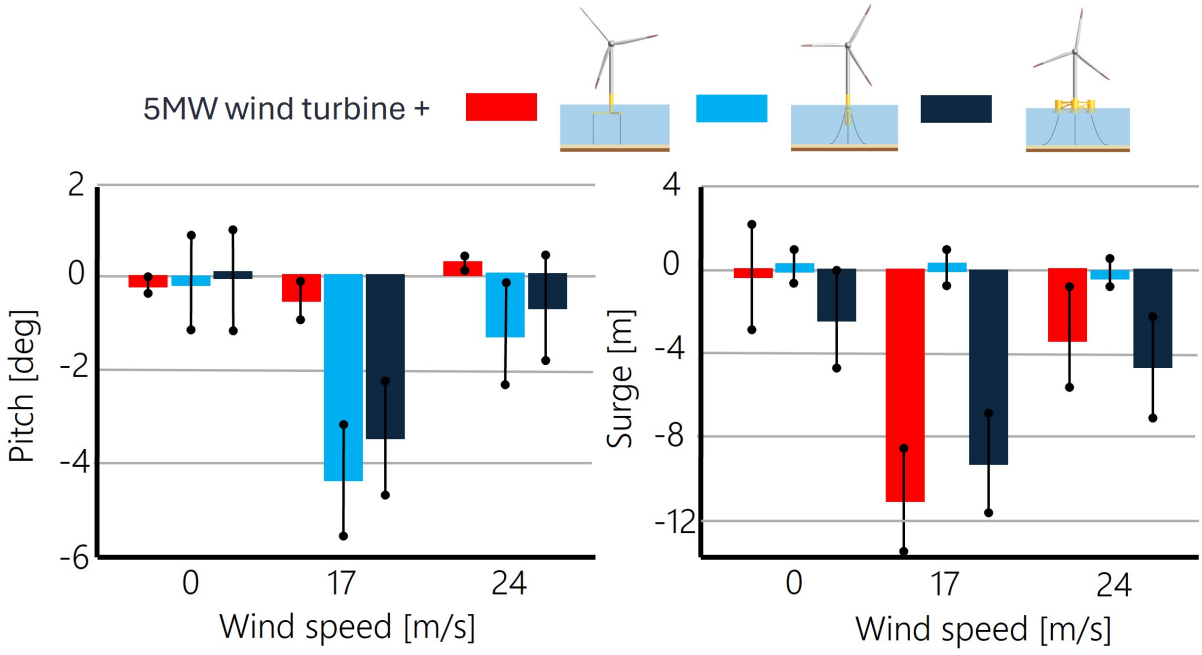

Figure 2.10: Pitch and surge excursion for a 5MW wind turbine combined with a TLP (red), spar buoy (light blue) and semi-submersible (dark blue) for different wind speeds [9].

Surge and pitch primarily affect the magnitude of the apparent wind speed experienced by the rotor. In contrast, other platform motions mainly influence the direction of the incoming flow relative to the rotor plane. Sway and roll produce lateral hub displacements, changing the inflow angle and creating asymmetric loading across the rotor disc. Yaw misalignment decreases the effective axial wind component while enhancing cross-flow effects. Meanwhile, heave motion shifts the rotor vertically within the wind shear profile and leads to minor fluctuations in the perceived inflow velocity.

2.1.7. Coupled Aero-Hydro-Servo-Elastic Behaviour

Aerodynamic, hydrodynamic and gravitational loads affect the behaviour of a FOWT, as illustrated in Figure 2.11. The resulting response is governed by the interaction between the five main subsystems:

- **Aerodynamic subsystem (2.1.1):** Rotor thrust and torque depend on inflow conditions, which are modified by platform surge, pitch and yaw. Aerodynamic forces feed back into platform motion and structural deformation.
- **Structural subsystem (2.1.2):** Blade and tower flexibility change the local angle of attack and thrust direction, modifying aerodynamic loads and interacting with platform pitch, surge and tower dynamics (aeroelastic coupling).
- **Hydrodynamic subsystem (2.1.3):** Wave excitation, radiation, added mass and viscous drag govern platform motions in all six DOFs. These motions alter the apparent wind at the rotor and influence aerodynamic loading and controller response.
- **Mooring subsystem (2.1.4):** Mooring stiffness and damping shape the platform's restoring characteristics and natural frequencies and are dynamically coupled to hydrodynamic loads, aerodynamic thrust and control actions.
- **Control subsystem (2.1.5):** The pitch and torque controller regulates rotor speed but reacts to motion-induced inflow variations. Controller actions introduce reaction forces on the floater and can either damp or amplify platform motions.

Together, these subsystems form a fully coupled aero-hydro-servo-elastic system with multiple DOFs. A disturbance in one DOF can propagate to another DOF and eventually through the entire system. Understanding these interactions is essential for analysing the performance of FOWTs.

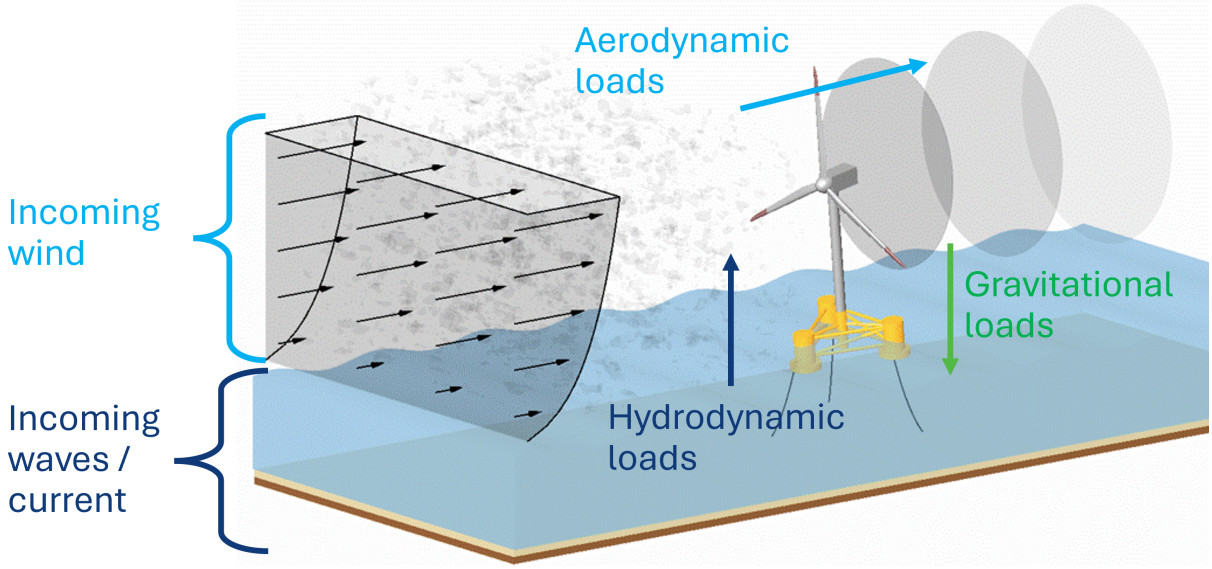

Figure 2.11: The coupled aerodynamic, hydrodynamic and gravitational loads for FOWTs [9].

Interactions among subsystems form feedback paths that can create positive (amplifying) or negative (stabilising) loops, where damping mechanisms play a central role. For example, platform motions alter the apparent wind field at the rotor plane and influence the aerodynamic loads, rotor torque and controller signals. Based on these signals, the controller will pitch the blades or adjust the generator torque. As a result, the aerodynamic forces change, which in turn influence the platform motions. If the controller is poorly tuned, it may amplify oscillations and increase structural loads. In general, aerodynamic damping is stabilising at lower wind speeds but can lead to negative damping above rated conditions: the pitch controller's response to platform-induced inflow variations can increase the oscillations of the platform if reacting in-phase. A recent study proposes modified controllers that mitigate the negative damping instability and still use a standard proportional-integral structure. The controllers avoid additional platform motion measurements, reduce structural loads and improve generator speed regulation [55]. Other unsteady aerodynamic effects, such as dynamic stall, dynamic inflow or wakes, will affect both load magnitude and phase. Mitigation strategies include careful PI gain tuning, motion-compensating control schedules and more advanced feedforward approaches using nacelle accelerations, wave elevation or lidar-based wind preview measurements [9].

In addition to the aerodynamic damping, the hydrodynamic and mooring system forces further contribute to the damping mechanism. Hydrodynamic damping arises from wave radiation, viscous drag on the platform and mooring line drag. Next to the drag, the mooring system adds damping through their stiffness and damping properties. All combined shape the platform's restoring forces and natural frequencies. Stiffer configurations (e.g., taut or tension-leg moorings) suppress motion amplitudes and shorten surge, sway and pitch periods. Thereby, they stabilise rotor inflow and reduce controller activity. This results in improved power quality at the cost of higher line tensions and fatigue loads. In contrast, more flexible catenary systems allow larger excursions that amplify aero-hydro-servo coupling and motion-induced wind variations. Nevertheless, they offer greater damping from geometric effects and line hydrodynamic drag. These trade-offs highlight the need for mooring designs that balance motion control with load management across site-specific wave and wind conditions [56], [57].

The coupled dynamics of a FOWT occur across multiple timescales. Blade aerodynamics, structural vibrations and rapid control occur within seconds, while platform pitch and roll responses to wind and wave loads are more in the order of tens of seconds. There are even slower processes (low-frequency surge drift or quasi-static offsets) that span minutes to hours. Because these timescales influence and are influenced by each other, simplified linear or frequency-domain models would overlook important nonlinear interactions that produce fatigue and power loss. Therefore, accurate design and performance assessment require fully coupled time-domain simulations [9].

2.1.8. Power Curve and Annual Energy Production

To evaluate the performance of a turbine, the power curve is one of the most fundamental tools. It represents the relationship between the free-stream wind speed at hub height and the electrical power output at standardised conditions (left graph Figure 2.12). The power curve is divided into the same four regions as the control curve (Subsection 2.1.5). The four regions are:

- **Region 1 (Below cut-in wind speed):** The turbine produces no power.
- **Region 2 (Partial-load region):** Power increases steeply with wind speed as the turbine operates to maximise aerodynamic efficiency.
- **Region 3 (Rated region):** The turbine maintains constant rated power through pitch regulation.
- **Region 4 (Above cut-out wind speed):** The turbine shuts down for safety.

The foundation of a bottom-fixed offshore wind turbine provides a rigid connection to the seabed and minimize movements of the hub. As a result, the turbine experiences minimal motion-induced variations in apparent wind speed, inflow angle and rotor alignment and the instantaneous power fluctuates only due to atmospheric variability. Consequently, the mean power output follows the idealized power curve and the turbine yields high aerodynamic efficiency with a predictable performance across the operating wind speed range. The bottom-fixed configuration thus serves as a valuable benchmark for comparing different floating offshore wind turbine (FOWT) concepts.

In addition to the aerodynamic losses discussed in Subsection 2.1.1, several environmental and operational factors further reduce the effective power output of a wind turbine. Environmental influences such as rotor misalignment, turbulence-driven inflow variations and site-specific atmospheric conditions can disturb the incoming wind field and lower overall efficiency. Non-ideal control responses and ice formation on the blades in cold climates are examples of operational effects and further contribute to performance reduction. Together, these factors introduce deviations from ideal turbine behaviour and must be accounted for when estimating the expected energy yield.

FOWTS experience additional losses due to the coupled aero-hydro-servo-elastic behaviour (Subsection 2.1.7). Platform motions affect aerodynamic forces and instantaneous power output. Understanding these general losses is essential for accurate prediction of energy yield and for optimising both turbine and floater design [9]. The main floating-specific loss mechanisms are:

- **Apparent wind speed variations**: Platform surge motions change the apparent wind speed at the hub height and the whole rotor plane, which modifies the instantaneous aerodynamic torque.
- **Unsteady inflow effects**: Vertical and lateral platform motions introduce variations in the inflow angle and velocity and create instantaneous deviations from the mean behaviour.
- **Motion-induced rotor misalignment**: Platform pitch and roll cause dynamic tilting of the rotor axis that reduces the effective inflow and shifts the instantaneous operating point.
- **Dynamic pitch-control interactions**: The turbine controller attempts to respond to coupled aerodynamic-hydrodynamic disturbances and deviates from optimal power tracking.

Floating turbines consequently experience a stronger distinction between instantaneous and mean power production. The instantaneous power is highly sensitive to real-time variations in generator torque, rotor speed and platform motion. For FOWTs, more and faster fluctuations can be found than for bottom-fixed turbines. The mean power smooths out these fluctuations by averaging over longer time scales. Despite being reduced due to floating-specific losses, the mean power remains the relevant metric for annual energy production (AEP).

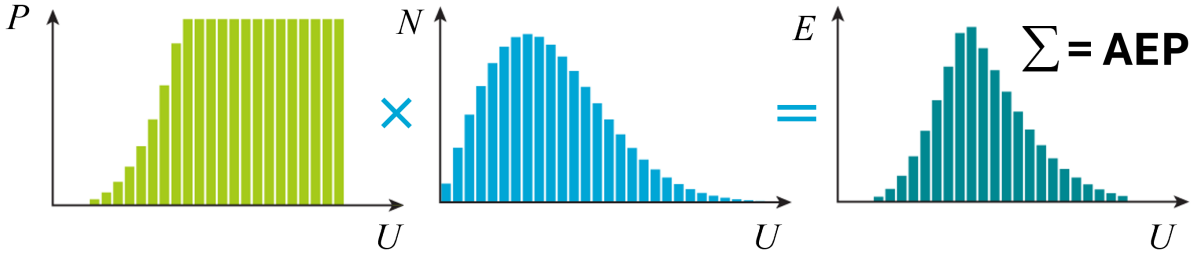

Figure 2.12: The area under the energy curve (E) represents the annual energy production (AEP), obtained by combining the turbine's power curve (P) with the Weibull distribution of wind speeds (U). Adapted from [58].

Figure 2.12 illustrates how the AEP is calculated. The turbine power curve (left) is combined with the site-specific wind speed probability distribution (middle) to arrive at the energy produced at each wind speed bin (right). Integrating the area under this energy curve yields the AEP and represents the expected electrical generation across the full range of wind conditions experienced at a specific site. In practical AEP calculations, several correction factors are applied to include losses due to scheduled and unscheduled maintenance, grid unavailability, curtailment and electrical transmission. Additional uncertainties arise from the wind resource assessment, turbine performance modelling, measurement accuracy and environmental variability [38, 58].

In addition to individual turbine losses, turbines operating within a wind farm are affected by wake-induced losses generated by upstream turbines. These wake effects extend over significant downstream distances and must therefore be taken into account when determining turbine spacing and designing overall wind farm layouts. A comparison of floating-platform types with a bottom-fixed monopile benchmark is shown in Figure 2.13. For equal turbine spacing, floating platforms demonstrate higher wind-farm-level output below rated wind speed due to more scattered wake characteristics [59]. The more rapid wake recovery in these cases reduces downstream velocity deficits and offsets the motion-induced losses. However, when the wind farm layout is optimised for fixed or floating wind turbines, the overall impact on the levelised cost of energy remains limited [60].

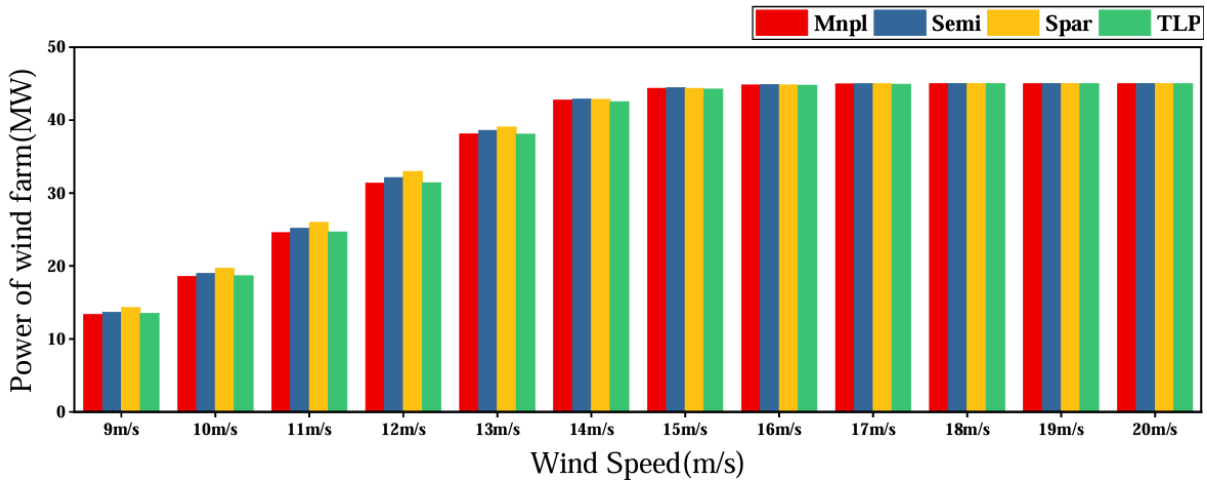

Figure 2.13: The total power output of a wind farm for different platform types at wind speeds ranging from 9 m/s to 20 m/s: Monopile (red), Semi-submersible (blue), spar (yellow) and TLP (green) [59].

2.1.9. Physical Phenomena versus Numerical Representation

The design of FOWTs is challenging because their behaviour arises from a strong coupling between aerodynamic, hydrodynamic and structural dynamics, as can be read in Subsection 2.1.7. Accurately capturing these interactions is difficult in both numerical simulations and physical experiments. Full-scale testing is generally impractical due to the large size and high cost of offshore structures and the limited control over environmental conditions. Consequently, researchers and designers rely on reduced-scale laboratory experiments to reproduce the dominant global motions and load characteristics of the full-scale system. With the help of scaling laws, the governing parameters are expressed in dimensionless form and preserved across the different scales in order to ensure that the key force ratios driving the turbine's behaviour are correctly matched.

For reduced-scale experiments, a fundamental issue arises as aerodynamic and hydrodynamic processes depend on different scaling laws. The aerodynamic forces depend strongly on the Reynolds number, which relates inertial and viscous forces. Scaling down a turbine model leads to a reduction in the characteristic length and a significant reduction in Reynolds number if all other parameters are kept constant. This alters the boundary-layer behaviour, lift, drag and overall turbine performance. In contrast, the hydrodynamic behaviour is dominated by the Froude number, which relates inertial to gravity terms. Wave-basin experiments adopt Froude scaling to maintain realistic platform motion and wave-body interactions. However, matching Froude similarity inevitably leads to incorrect Reynolds scaling; the aerodynamic forces and viscous effects cannot be reproduced exactly. This Reynolds-Froude conflict represents a fundamental limitation in experimental testing of FOWTs and will always cause distortions for force components and dynamic responses in model-scale experiments. [44].

To overcome some of these limitations, numerical models are used to investigate full-scale behaviour without the constraints of similarity laws. Despite this, they introduce their own limitations due to simplifications, assumptions and linearisation. Figure 2.14 illustrates the trade-off for the available models: an increase in the level of fidelity and accuracy comes at a computational cost. Each level of fidelity captures different parts of the physics with varying accuracy and uncertainties arise from turbulence modelling, wave descriptions, coupling approximations and neglected nonlinearities. For example, to solve the aerodynamics of a FOWT you can choose from low-order BEM solvers up to high-order computational fluid dynamics solvers. Each model captures specific aspects of the underlying physics and uncertainties arise from turbulence and wave modelling, coupling approximations and neglected nonlinearities [9]. Even the highest-fidelity models require experimental validation to quantify modelling error.

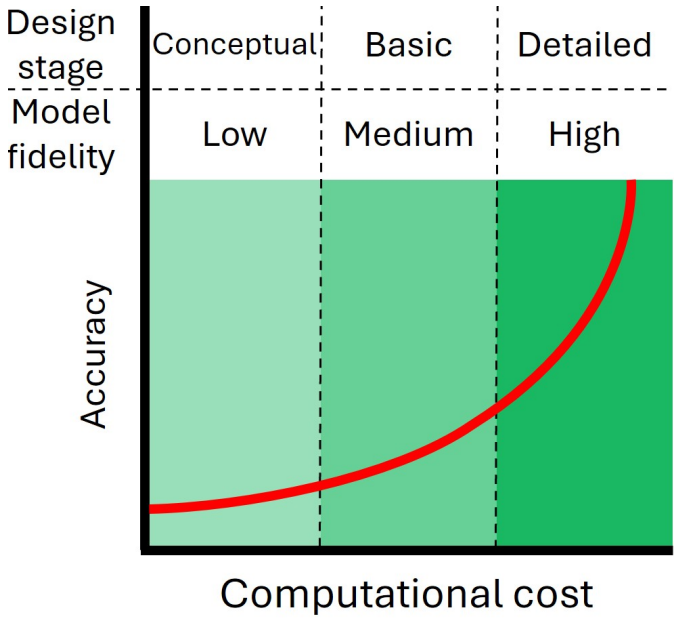

Figure 2.14: Relationship between design stages, model fidelity, accuracy and computational cost of numerical models used in FOWT development. The figure demonstrates how these modelling requirements shift across successive stages of the design process. Based on [61].

To combine the strengths of physical and numerical methods, hybrid testing techniques are increasingly applied. These include wind-tunnel experiments with simulated platform motion, wave-basin tests that use actuators to mimic aerodynamic thrust and hardware-in-the-loop setups where real-time numerical models interact with physical components. Such hybrid methods help recover some of the lost similarity and provide a more representative combined aero-hydro response, although they cannot entirely overcome the inherent scaling mismatch. As a result, reliable assessment of FOWT behaviour relies on the complementary strengths of numerical simulation, scaled experiments and hybrid approaches, with careful interpretation of their respective limitations [9].

2.2. Numerical Modelling and Simulation Tools

For the analysis of FOWTs, reference turbines described in Subsection 2.2.1 provide standardised configurations that enable consistent benchmarking and comparative studies. Accurate prediction of turbine performance requires numerical models that are able to resolve the coupled aero-hydro-servo-elastic behaviour of the full system. A wide range of such simulation tools is available, as reviewed in Subsection 2.2.2. Among these tools, the widely used OpenFAST framework presented in Subsection 2.2.3 integrates dedicated modules for aerodynamics, structural dynamics, hydrodynamics, mooring systems and turbine control. Its accuracy has been verified and validated through several experimental campaigns, summarised in Subsection 2.2.4. Finally, design load cases, outlined in Subsection 2.2.5, define the environmental conditions and load scenarios considered in the simulations. Together, these elements provide the foundation for robust numerical modelling and analysis of floating offshore wind turbines.

2.2.1. Reference Turbine

Reference turbines are standardised models used to benchmark and compare wind turbine performance in simulations and experiments, particularly when evaluating new design concepts or control strategies. They provide openly documented properties to enable consistent and reproducible comparisons across numerical tools, floater concepts and operating conditions. In this way, reference turbines bridge the gap between confidential industrial designs and the academic need for transparent, shareable models [62]. As a result, they provide a common basis for analysing the influence of floating support structures and control strategies across different turbine scales.

The evolution of reference turbines reflects both increasing turbine scale and technological advances, as can be seen in Figure 2.15. The NREL 5 MW turbine [20], developed by the National Renewable Energy Laboratory in 2009, is a three-bladed, upwind, variable-speed, pitch-regulated machine with a traditional geared drivetrain. Designed to represent the first generation of utility-scale offshore turbines, it has been extensively used for code validation and early floating wind studies. Subsequently, the DTU 10 MW reference turbine [21], introduced by the Technical University of Denmark, represented a larger, more modern offshore machine. It provides a baseline for structural and aeroelastic analyses at the 10 MW scale, enabling studies on scalability and control strategies.

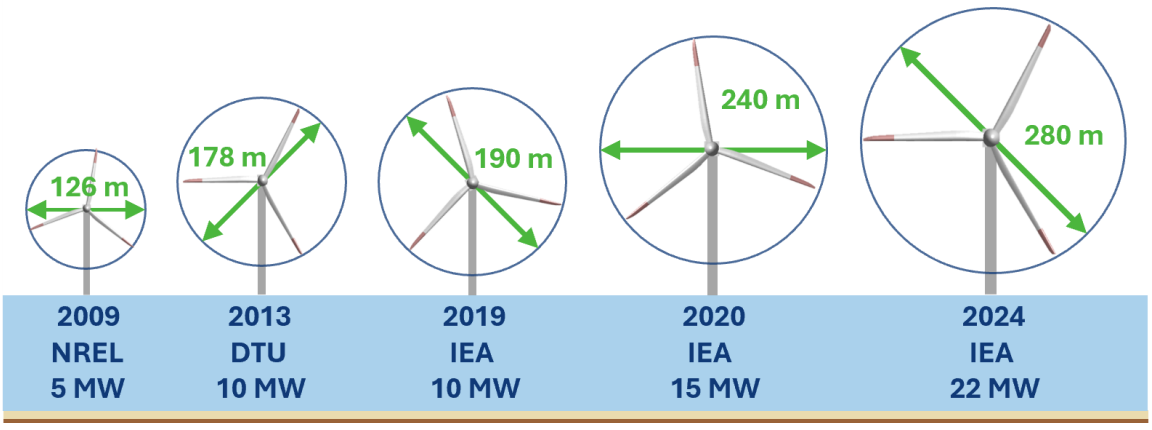

Figure 2.15: Size comparison of the offshore reference turbines.
For each turbine, the rotor diameter, development year and power rating are shown.

Building on these designs, NREL and DTU collaborated within the IEA to develop a family of newer reference turbines: the IEA 10 MW [22], IEA 15 MW [23] and IEA 22 MW [24] reference turbines. These turbines adopt direct-drive technology, reflecting trends in next-generation offshore wind development. The IEA 10 MW turbine serves as an intermediate step between the 5 MW and very large turbines, with complete aerodynamic, structural and controller definitions suitable for system-level and wind farm studies.

The IEA 15 MW turbine extends this concept to the next generation of very large offshore turbines and is explicitly developed for both bottom-fixed and floating applications, which makes it highly relevant for contemporary floating wind research [63]. Most recently, the IEA 22 MW reference turbine has been introduced as a forward-looking design that anticipates ultra-large offshore turbines beyond current commercial sizes. The significantly larger rotor and rated power are intended to test the limits of existing aero-hydro-servo-elastic tools and design practices and to explore how upscaling affects loads, dynamics and controllability [64].

2.2.2. Survey of Simulation Tools

The analysis of floating offshore wind turbines requires numerical simulation tools capable of resolving strongly coupled aero-hydro-servo-elastic behaviour, as discussed in Subsection 2.1.7. These factors interact across different time scales and create a complex, strongly coupled system that requires sophisticated modelling tools to accurately predict turbine performance. As a result, a number of specialised simulation tools, all varying in modelling approach, fidelity and computational cost, have been developed in both academic and industrial contexts [65], [66].

The available tools can be categorised into four main types:

- **Conceptual and frequency-domain models** (e.g. QuLAF, SLOW, WISDEM) are computationally efficient and suitable for early-stage design or optimisation. However, they do not capture full-time-domain dynamics.
- **Mooring- and hydrodynamics-focused solvers** (e.g. OrcaFlex, AQWA) specialise in platform motion and mooring dynamics and therefore do not independently resolve the turbine's aeroelastic response.
- **High-fidelity, time-domain, fully coupled solvers** (e.g. OpenFAST, Bladed, HAWC2) simulate the complete aero-hydro-servo-elastic response of the turbine and floating platform.
- **High-resolution CFD solvers** (e.g. OpenFOAM, STAR-CCM+) model detailed aerodynamic and wake physics, which makes them computationally expensive.

For this thesis, only high-fidelity, time-domain, fully coupled solvers are considered. Hydrodynamics-focused tools are excluded because they require coupling with a separate aeroelastic solver to resolve turbine dynamics. Conceptual and frequency-domain models are not included as they cannot capture the detailed time-domain interactions between the turbine and the floating platform. Similarly, the CFD solvers are excluded due to their expensive computational cost for systematic comparisons of different floater concepts. Focusing on fully coupled solvers ensures accurate representation of the aero-servo-hydro-elastic behaviour central to this study [65], [66].

Although outside the scope of fully coupled aero-hydro-servo-elastic solvers considered in this thesis, OrcaFlex [67] is included as a reference for validated platform and mooring dynamics. It is a widely used commercial solver for floating structures under wave and current loading and extensively benchmarked against experimental measurements. As OrcaFlex does not independently resolve turbine aerodynamics or structural flexibility, it requires integration with an aeroelastic solver for fully coupled simulations.

Bladed [68] and HAWC2 [69] represent established, fully coupled aeroelastic solvers. Bladed, developed by Det Norske Veritas (DNV), integrates aerodynamic, structural and control system models for fatigue and ultimate load calculations and supports offshore and floating wind analyses via coupled hydrodynamic interfaces. HAWC2, developed at DTU, incorporates detailed structural modelling and advanced aerodynamic formulations and has been validated in benchmark studies showing close agreement in predicted dynamic responses.

OpenFAST [70], developed by the NREL, is an open-source, modular time-domain framework combining modules for aerodynamics, structural dynamics, hydrodynamics, mooring systems and control. It has become a standard tool for floating offshore wind turbine research due to its modular architecture, extensive validation against experimental data [71] and commercial codes like HAWC2 [72] and widespread adoption in the academic literature. For this thesis, OpenFAST is selected as the primary simulation environment due to its flexibility, proven accuracy and suitability for systematic comparative studies of different floater concepts.

2.2.3. OpenFAST Framework

OpenFAST is an open-source, time-domain simulation framework widely used for the analysis of wind turbines and their support structures, providing a modular environment for studying their coupled dynamic behaviour [73]. Developed by the National Renewable Energy Laboratory (NREL), it is designed to model the fully coupled aero-hydro-servo-elastic dynamics of both bottom-fixed and floating offshore wind turbines. Its modular architecture, transparency and extensive validation against experimental data and commercial codes (see Subsection 2.2.4) have established OpenFAST as a reference tool in floating wind research.

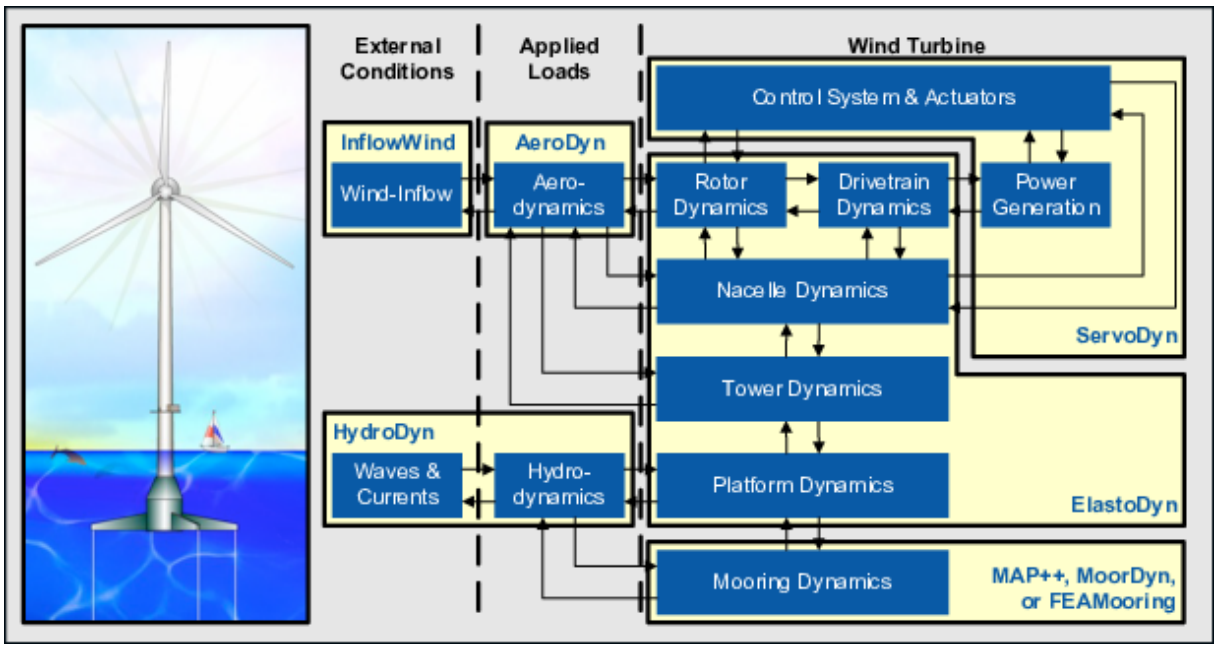

Figure 2.16: Schematic overview of the OpenFAST v4.2.0 modular framework [70].

A schematic overview of OpenFAST framework is shown in Figure 2.16 [70]. The solver consists of a central driver program, often referred to as the glue code, which couples a set of specialised physics modules. At each time step, loads and kinematic responses are exchanged between modules to provide a consistent solution of the strongly coupled system, enabling interactions between aerodynamic loads, hydrodynamic forces, structural flexibility, mooring dynamics and control actions. Such coupling is critical for capturing the complex dynamics of floating offshore wind turbines, as discussed in Subsection 2.1.7.

The OpenFAST modules required for floating offshore wind turbine simulations are summarised below. A more detailed description about each module can be found in the OpenFAST documentation [70].

AeroDyn

AeroDyn calculates aerodynamic loads on the rotor and tower using an actuator-line-based formulation that approximates three-dimensional flow with local two-dimensional aerodynamics at each cross-section. It supports Blade Element Momentum (BEM) theory (see Subsection 2.1.1 for the theoretical background), Dynamic BEM (DBEM) and the cOnvecting LAgrangian Filaments (OLAF) free-vortex wake model. To account for the limitations of classical BEM, AeroDyn includes tip-loss, hub-loss, high-thrust and skewed-wake corrections to improve predictions under yawed and highly loaded conditions. Input files define airfoil polars, blade and tower properties, environmental conditions and tower shadow effects.

InflowWind

InflowWind provides the wind field to AeroDyn by returning undisturbed velocities at specified locations. It supports steady, uniform, power-law and full-field turbulent wind inputs. Key parameters such as mean wind speed, shear and turbulence characteristics are defined to ensure consistency with design load cases and site-specific conditions.

ElastoDyn

ElastoDyn models the structural dynamics of the wind turbine using a reduced-order, mode-shape-based multibody formulation (see Subsection 2.1.2 for the theoretical background). Blade and tower flexibility are represented through a limited set of precomputed eigenmodes that serve as spatial basis functions for bending deformations. The dominant structural modes typically retained are the blade flapwise and edgewise bending modes and the tower fore-aft and side-side bending modes (rotational DOF is fixed). The modal shapes used by ElastoDyn are inputs from dedicated tools and ElastoDyn solves for the corresponding generalised modal coordinates in time. The structural model assumes linear elasticity and small deflections (no geometric nonlinearities), so effects such as large-rotation beam kinematics, geometric stiffening and strong mode coupling are not included. The floating platform is represented by six rigid-body degrees of freedom (surge, sway, heave, roll, pitch, yaw), but platform elastic deformations are not modelled. By coupling the structural responses with the aerodynamic, hydrodynamic and mooring loads, ElastoDyn captures the global dynamics of the turbine-platform system.

HydroDyn + SeaState

HydroDyn calculates the still-water hydrostatics and hydrodynamic loads on support structures due to waves and currents (see Subsection 2.1.3 for the theoretical background). It supports three approaches:

- Linear potential flow theory: external panel-method solvers (e.g. WAMIT) using linear potential flow to solve radiation-diffraction are used to calculate precomputed hydrodynamic coefficients, such as frequency-dependent added mass, radiation damping and hydrostatic stiffness coefficients.
- Morison strip theory: The Morison equation is applied on small strips of a slender structure to calculate the inertia and drag coefficients. The Morison strip theory is valid if the ratio between the characteristic dimension D and wavelength λ is less than 0.2: ($D/\lambda \leq 0.2$).
- Hybrid approach: Both theories are combined to solve the hydromechanics of the large-volume platforms and slender braces or tendons.

The SeaState module defines the inputs of the HydroDyn module. The sea states are described through spectral definitions, (ir)regular waves or measured time series. Wave kinematics are computed using finite-depth dispersion relations that automatically transition between deep-, intermediate- and shallow-water assumptions based on wavelength relative to water depth. This ensures consistent control of the environmental properties within the OpenFAST framework.

MoorDyn

MoorDyn simulates mooring-line dynamics using a lumped-mass approach: each line is discretised into nodes connected by axial spring-damper elements and hydrodynamic force components (see Subsection 2.1.4 for the theoretical background). The model accounts for axial stiffness and damping, segment weight and buoyancy, hydrodynamic drag, added mass and seabed contact forces. It also allows the inclusion of different line types, clump weights, floats and line interconnections to model complex mooring configurations.

Within OpenFAST, MoorDyn computes the dynamic response of the mooring system by solving Newton's second law for each node at every time step. The resulting internal forces are integrated along each line to determine the reaction forces at the fairleads. These fairlead forces are passed to the platform model at every time step and act as external loads on the floating structure. In return, OpenFAST provides the instantaneous fairlead positions and velocities to MoorDyn. This two-way coupling enables fully coupled simulations, allowing the mooring system to contribute realistically to the platform restoring forces and damping.

ServoDyn

ServoDyn implements wind turbine and electrical system control (see Subsection 2.1.5 for the theoretical background), including pitch, torque, yaw and braking systems. It allows both built-in controllers and external dynamic link library (DLL)-based controllers to enable research-oriented strategies such as gain-scheduled proportional-integral (PI) control, individual pitch control, or floating-specific mitigation schemes. Several reference controllers are available in literature, such as the Reference Open-Source Controller (ROSCO) [74]. The control actions influence rotor aerodynamics, which in turn affect platform motions, creating strong controller-structure interactions.

All modules are solved simultaneously within the OpenFAST time-domain framework, exchanging loads, motions and state variables at every time step. This modular, fully coupled architecture allows OpenFAST to accurately capture interactions between aerodynamics, hydrodynamics, structural dynamics, moorings and control. This fully coupled approach is essential for capturing the dynamic behaviour of floating offshore wind turbines, as discussed in Subsection 2.1.7.

2.2.4. OpenFAST Model Verification and Validation

The verification and validation of OpenFAST are essential to ensure reliable predictions of FOWT behaviour. Code verification in OpenFAST is performed using analytical solutions, simplified benchmark problems and unit tests at the module and subroutine level. These include rigid-body dynamics, linear wave loading, structural beam responses and prescribed-motion rotor tests. Together, these tests confirm the correct implementation of numerical schemes, time integration and conservation properties. Early validation of its predecessor FAST against the OC-series experimental campaigns further established confidence in the aeroelastic-hydrodynamic framework and provided the foundation for later floating-wind applications.

In the aerodynamic module, the blade-element-momentum (BEM) formulation has been verified against analytical rotor solutions, high-fidelity models and wind-tunnel measurements, including the UNAFLOW campaigns at Politecnico di Milano [31]. Recent work by Papi et al. [75] shows that the dynamic BEM

implementation captures the dominant trends in thrust and power under prescribed platform motions, though accuracy decreases at high reduced frequencies where wake dynamics and flow separation become more significant, making BEM less reliable in rapidly varying inflow conditions characteristic of highly dynamic floating platforms.

The validation of the hydrodynamics in OpenFAST has been conducted through a wide range of experimental campaigns covering both bottom-fixed and floating configurations. Wave basin tests of the NREL 5-MW reference turbine at the Maritime Research Institute Netherlands (MARIN) have been used to validate platform motions, mooring line tensions and global structural loads. The results showed good agreement in response amplitude operators (RAOs) [29]. Similar validation efforts have been performed for the DTU 10-MW reference turbine [30].

Further confidence in OpenFAST was provided by code-to-code comparisons with commercial solvers such as HAWC2 [69]. A study for the IEA 15 MW reference turbine showed relative differences below 5% in mean values under both uniform and turbulent inflow conditions for the power production, thrust and key blade-root and tower-base loads. The closed-loop dynamics differed more noticeably despite identical controller inputs, which was generally attributed to differences in structural modelling fidelity, including variations in beam theory, mass and stiffness distributions and the treatment of torsion [72].

OpenFAST has also been extensively exercised within large international benchmark projects such as OC3 (spar buoy), OC4 (semi-submersible), OC5 (DeepCwind and Hywind model tests) and OC6 (including TetraSpar) [76]. The most notable is the OC4 project, where more than a dozen software models were compared for OC4 semi-submersible floater [71]. Across these campaigns, the OpenFAST has generally reproduced platform response amplitude operators (RAOs), motion spectra, mooring loads and mean aerodynamic loading within the spread of results produced by other established aeroelastic solvers.However, uncertainties remain for strongly nonlinear hydrodynamics, viscous damping and extreme sea states.

Finally, recent operational validation has further demonstrated OpenFAST's ability to reproduce turbine performance under real atmospheric inflow. A one-to-one aero-servo-elastic validation study using several weeks of SCADA data from a 2.8 MW turbine showed that OpenFAST predicts mean performance quantities with median modelling errors generally within 5-10% across wind speed intervals (beter agreement above rated wind speed) [77].

Taken together, these verification and validation efforts demonstrate that OpenFAST provides a robust and reliable framework for predicting the coupled aero-hydro-servo-elastic behaviour of offshore wind turbines, while also highlighting the remaining challenges associated with unsteady aerodynamics, viscous hydrodynamics and highly nonlinear wave environments.

2.2.5. Design Load Cases

Design load cases (DLCs) define the environmental conditions and operational scenarios used to assess the structural integrity and performance of FOWTs. Wind conditions and sea states are typically represented using statistical spectra: wind turbulence is described by models such as the Kaimal spectra, while wave conditions are characterised by JONSWAP or Pierson-Moskowitz spectra [9]. The parameters for DLCs can be derived either from long-term site measurements or from standardised conditions prescribed in International Electrotechnical Commission (IEC) standards.

Meteorological and oceanographic (metocean) conditions form the basis for DLC definition and describe the combined environmental forcing acting on a FOWT. Individual probability distributions of wind and wave conditions are combined into 3D scatter diagrams to obtain the joint probability distribution of significant wave height (H_s), peak period (T_p) and 1-hour average wind speed ($\overline{U}$), as illustrated in Figure 2.17. This joint distribution is essential for selecting correlated environmental combinations representative of site-specific loading [58].

Wind conditions are defined by several key parameters. The mean wind speed and direction determine the primary energy input and loading direction on the turbine. Turbulence intensity governs short-term fluctuations and contributes to fatigue loading. Wind measurements are typically taken at a reference height and extrapolated to hub height using a vertical wind shear model, such as the power law:

$$U(z) = U_{\text{ref}} \left(\frac{z}{z_{\text{ref}}} \right)^{\alpha} \tag{2.2}$$

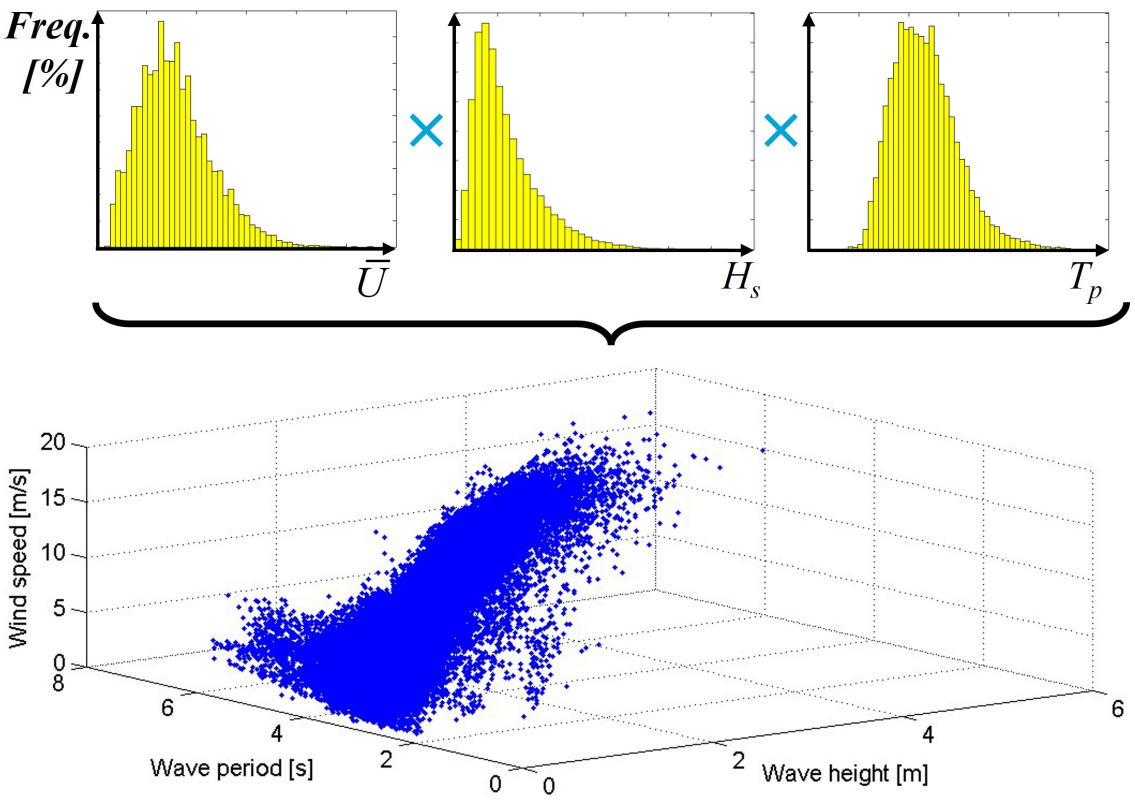

Figure 2.17: 3D scatter diagram of metocean conditions showing joint occurrence of a 1-hour average wind speed $\overline{U}$, significant wave height H_s and peak period T_p, used for correlated DLC selection. Adapted from [58].

where $U(z)$ is the wind speed at height z, U_{ref} is the measured wind speed at reference height z_{ref} and α is the shear exponent, which depends on atmospheric stability and surface roughness [38]. Typical offshore values of α are typically in the order of 0.10-0.20; this repersents relatively low shear due to the smooth sea surface [78],[79]. Additionally, seasonal and geographic variability influence wind resource characteristics, requiring long-term measurements to capture representative conditions.

Wave conditions are described by the wave climate, including significant wave height, peak spectral period and wave direction. These parameters are typically derived from spectral models such as Joint North Sea Wave Project (JONSWAP) for a developing sea (due to limited fetch) or Pierson-Moskowitz for fully developed conditions. Water depth plays a crucial role in wave kinematics and hydrodynamic loading and a distinction is made between deep water, intermediate and shallow water regimes. Floating wind turbines are generally deployed in water depths exceeding approximately 60-200 m. Seabed conditions are also relevant, as they influence mooring system design and anchor performance. Typically frequencies and power spectral density of wind, a developing sea and a fully developed sea can be found in Figure 2.20.

Site conditions are obtained through a combination of measurement techniques. Meteorological masts provide high-accuracy wind data but are limited in offshore deployment. Floating LiDAR systems are increasingly used for wind profiling due to their flexibility and lower cost. Wave and current data are typically measured using buoys equipped with motion sensors, while satellite observations can supplement large-scale assessments. These datasets are combined to develop long-term statistical descriptions of the site [58].

For FOWTs, the relevant load cases are defined in the IEC 61400 series: IEC 61400-1 [80] provides general turbine design load cases, whereas IEC 61400-3-2 [81] specifically addresses floating offshore wind turbines. This includes the additional dynamic effects from platform motion and mooring line interactions. These standards guide the selection of consistent combinations of wind, wave and current conditions for both operational and extreme scenarios to ensure that the coupled aero-hydro-servo-elastic response of the system is adequately captured.

2.3. Floating Platform Concepts

Floating offshore wind turbines rely on specialised platforms that support the turbine while maintaining stability under environmental loads. Over the past decades, numerous floater concepts have been proposed; some are commercially deployed, while others remain under development. Each concept exhibits distinct restoring mechanisms, motion characteristics, mooring requirements and varying suitability for different water depths and turbine sizes [82]. These concepts can be broadly categorised into five families, which are discussed in Subsection 2.3.1. The different floaters will be compared with each other in Subsection 2.3.2 and to bottom-fixed turbines in Subsection 2.3.3. Lastly, Subsection 2.3.4 gives an overview of the currently deployed platform concepts in floating offshore wind farms.

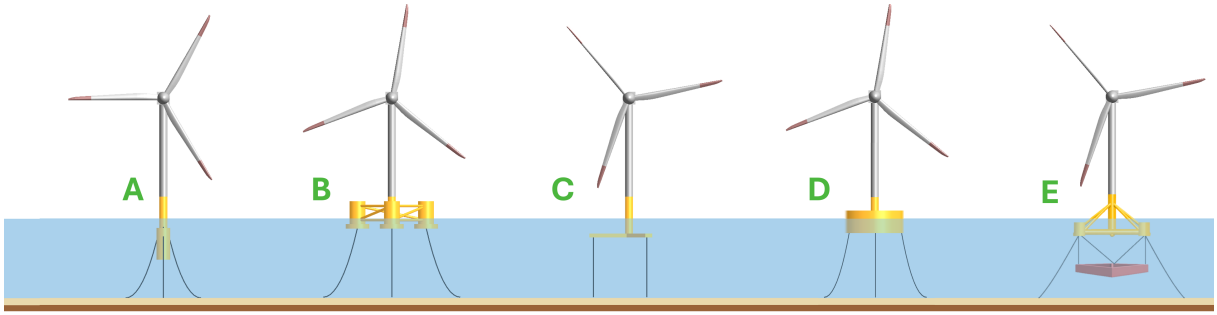

Figure 2.18: Overview of floating wind platform concepts: (A) spar buoy, (B) semi-submersible, (C) tension-leg platform (TLP), (D) barge and (E) hybrid (e.g. TetraSpar). Adapted from [9].

2.3.1. Floater Families and Stability Mechanisms

Floating platforms can be categorised into five main families, as illustrated in Figure 2.18: (A) spar buoy, (B) semi-submersible, (C) tension-leg platform (TLP), (D) barge and (E) hybrid concepts (e.g. TetraSpar) [9],[83],[84]. Within each family, numerous design variations exist that differ slightly in geometry, ballast configuration, column arrangement or mooring layout. However, these variations generally follow the same underlying stability principles. Therefore, the review in this section focuses on the fundamental differences between the five main floater families and minor design variations within each family are not considered in detail. An overview of the key characteristics of the floater families can be found in Table 2.2.

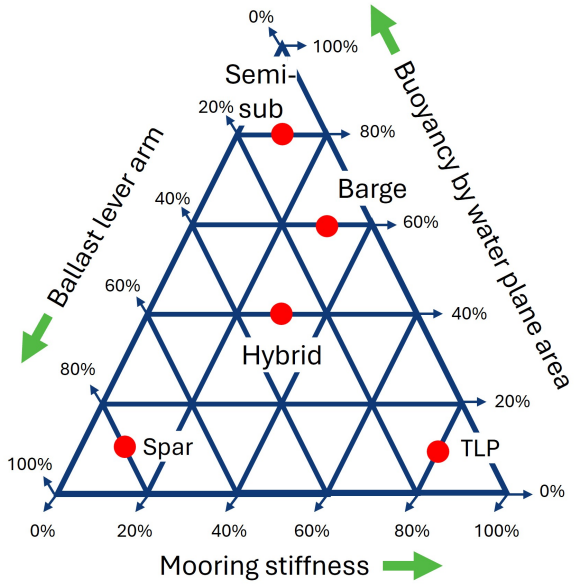

Figure 2.19: Floating triangle showing restoring mechanisms of floating wind turbine concepts. Each corner of the triangle represents a primary restoring mechanism: buoyancy, ballast or mooring. Each concept is positioned within the triangle according to the relative contribution of these mechanisms. Adapted from [25] with additional floater concepts.

Figure 2.19 shows the three restoring mechanisms of floating wind turbine platforms in the form of a triangle. Each corner represents a dominant restoring mechanism: buoyancy, ballast or mooring. A graphical representation of these restoring mechanisms is provided in Figure 2.5. Each floater family relies on a combination of stability mechanisms, although typically one mechanism dominates the overall stability behaviour. The concepts are therefore positioned within the triangle according to the relative contribution of buoyancy, ballast and mooring restoring. This balance of restoring mechanisms strongly influences the characteristic motion response of each platform type under environmental loading, as governed by the hydromechanical principles outlined in Subsection 2.1.3.

A. **Spar buoy**
- **Restoring mechanism (static stability):** Primarily hydrostatic restoring, provided by buoyancy and a large vertical separation between the centre of buoyancy and the centre of gravity due to heavy ballast.
- **Dynamic stability and damping:** Radiation damping from the deep-draft hull; limited viscous damping due to slender geometry.
- **Dominant motions:** Pitch and roll are small; heave is strongly limited by the deep draft; surge motions can be significant.
- **Mooring system:** Catenary mooring lines providing horizontal restoring with minimal vertical stiffness.
- **Challengs:** Large draft complicates port access, assembly and transport. It requires deep-water ports or offshore upending operations.
- **Remarks:** Well suited for deep-water applications, but requires large water depths and substantial ballast mass.

B. **Semi-submersible**
- **Restoring mechanism (static stability):** Hydrostatic restoring through distributed buoyancy and large waterplane area of multiple columns.
- **Dynamic stability and damping:** Significant viscous damping from columns and pontoons; additional radiation damping due to large wetted surface.
- **Dominant motions:** Surge, pitch and roll are dominant; moderate heave motions, but it depends on column spacing and draft.
- **Mooring system:** Catenary or semi-taut mooring lines providing horizontal restoring.
- **Challenges:** The large exposed structure and shallow draft increase wave loading and can lead to higher motions and fatigue loads in harsh sea states.
- **Remarks:** Good motion performance and flexibility in installation and transport.

C. **Tension-leg platform (TLP)**
- **Restoring mechanism (static stability):** Vertical restoring is dominated by high pretension in the tendons; hydrostatic restoring plays a secondary role.
- **Dynamic stability and damping:** Tendon stiffness strongly limits vertical motions; damping is mainly provided by radiation and tendon dynamics.
- **Dominant motions:** Heave is almost fully suppressed; pitch and roll are very small; surge motions remain relevant.
- **Mooring system:** Vertical or near-vertical tensioned tendons anchored to the seabed.
- **Challenges:** The platform is unstable before tendon installation and makes assembly and installation complex. The tendons must withstand very high vertical loads.
- **Remarks:** Excellent motion control, but high structural and installation complexity.

D. **Barge**
- **Restoring mechanism (static stability):** Hydrostatic restoring dominated by large waterplane area and mooring lines.
- **Dynamic stability and damping:** Limited natural damping; additional viscous damping may be introduced through internal damping pools or appendages.
- **Dominant motions:** Significant heave and pitch motions; moderate surge response.
- **Mooring system:** Catenary mooring lines with relatively low stiffness.
- **Challenges:** The pronounced heave and pitch responses in energetic sea states can lead to increased structural loads and reduced turbine performance.
- **Remarks:** Simple geometry and shallow draft, but less favourable motion characteristics in energetic seas.

E. **Hybrid concepts (e.g. TetraSpar):** A combination of features of existing floaters, such as semi-submersibles and spar buoys, to leverage the advantages of multiple designs [85], [86].
- **Restoring mechanism (static stability):** Combination of hydrostatic restoring from buoyancy distribution and mooring-induced restoring.
- **Dynamic stability and damping:** Enhanced viscous damping through truss structures and appendages; additional damping from mooring system dynamics.
- **Dominant motions:** Reduced surge, pitch and roll compared to conventional semi-submersibles; controlled heave response.
- **Mooring system:** Catenary or taut mooring systems, depending on design and water depth.
- **Challenges:** The structural complexity of the novel configurations increases design, fabrication and certification challenges compared to established floater concepts.
- **Remarks:** Emerging designs aiming to reduce mass, cost and installation complexity while maintaining favourable motion performance.

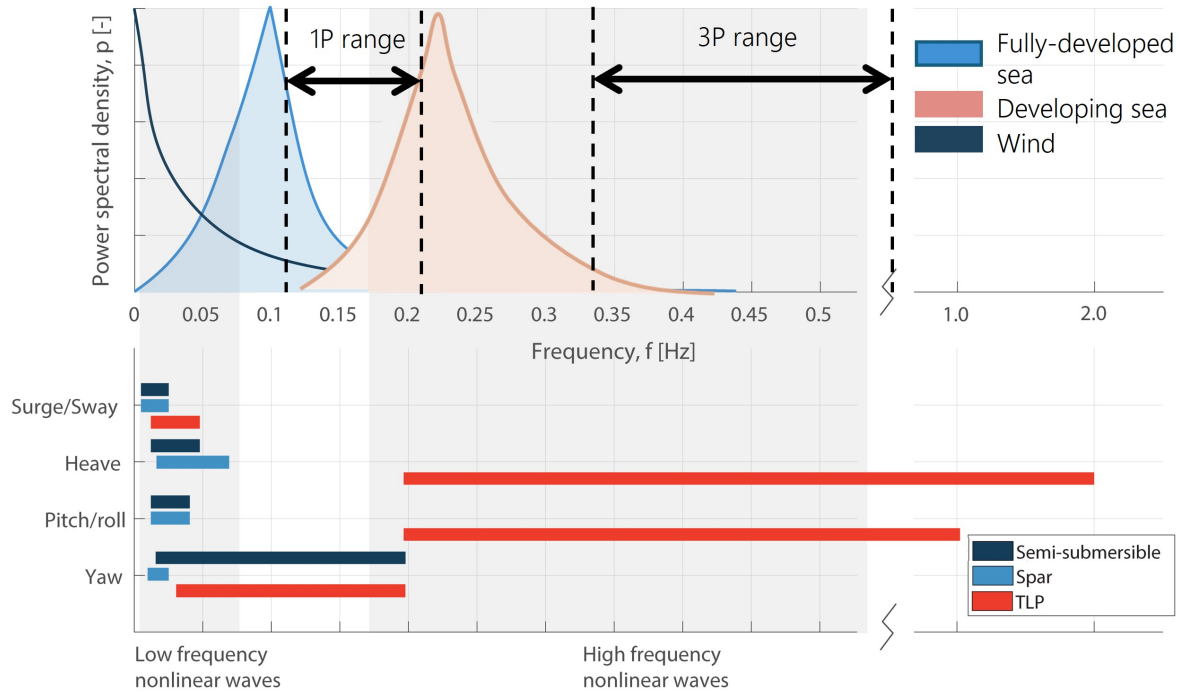

Figure 2.20: Natural frequencies for floater families relative to the wind and wave frequencies [9].

Figure 2.20 illustrates the typical natural frequency ranges of different floater families relative to the dominant wind and wave excitation frequencies. The low-frequency range is governed by wind-drive drift forces and mooring-system stiffness, while the high-frequency range is associated with rotor-induced cyclic loading (e.g. 3P) and structural dynamics. Between these lies the wave-frequency band of a fully developed sea state, where direct hydrodynamic excitation from incident waves is most energetic. Successful floater designs position their natural frequencies outside this energetic wave-frequency band and rotor-related frequencies to avoid resonance. Spar buoys exhibit the lowest natural frequencies across all degrees of freedom due to their deep draft, high inertia and catenary mooring system. Semi-submersibles benefit from distributed buoyancy and multi-column geometry, which generally results in low natural frequencies as well; only yaw often lies within the wave-frequency band because of the large waterplane area and corresponding sensitivity to incident waves. In contrast, TLPs feature significantly elevated heave and pitch natural frequencies due to the high vertical stiffness of the pretensioned tendons. However, their yaw stiffness remains low and results in a wider distribution of natural frequencies across degrees of freedom [9], [47].

The main characteristics of the different floater families are summarised in Table 2.2.

Table 2.2: Summary of key characteristics of different floater families [9], [47].

Property	Spar buoy	Semi-submersible	TLP	Barge	Hybrid
Dominant motions	Surge	Surge, pitch	Surge	Heave, pitch	Balanced
Restoring principle	Ballast + Buoyancy	Buoyancy	Mooring	Buoyancy	Buoyancy + Mooring
Typical periods: surge / pitch	>20s / 25s	10-20s / 15-25s	15-30s / 2-5s	8-15s / 10-20s	15-25s / 15-25s
Draft range	80-200 m	20-50 m	30-60 m	10-25 m	30-70 m
Mooring type	Catenary	Catenary / semi-taut	Tension-leg	Catenary	Catenary/taut
Key challenge	Port access & assembly	Wave exposure	Installation stability	Poor damping	Complexity

2.3.2. Comparison of Different Floater Concepts

Comparative studies of floating offshore wind platform concepts primarily focus on stability characteristics, natural frequencies and operational performance for small to medium-sized turbines. Early systematic comparisons have largely been conducted using reference turbines such as the NREL 5 MW turbine

[25], [26], [27] and, more recently, the DTU 10 MW turbine [28]. As a result, most available results reflect trends for earlier-generation turbine sizes and may not directly extrapolate to contemporary large-scale designs.

The thesis study of Matha [25], studies by Jonkman and Matha [26] and Robertson and Jonkman [27] compare spar buoy, semi-submersible, TLP and barge concepts in terms of dynamic response, stability and fatigue. Their results indicate that spar-buoy platforms exhibit low heave motions due to their deep draft and ballast-based restoring, while semi-submersibles benefit from increased viscous damping but experience larger surge and pitch motions. TLP concepts show significantly reduced heave and pitch responses owing to the high vertical stiffness provided by the tendons, at the cost of increased mooring system complexity. Lastly, the barge concept is shown to be more strongly influenced by wave excitation than by aerodynamic loading, resulting in excessive pitch and roll motions. Consequently, it experiences the highest structural loads in the turbine components among the concepts considered.

More recent benchmarking studies, such as Ramzanpoor et al. [28], extend these comparisons to the larger 10 MW DTU reference turbine. Their results confirm that platform natural frequencies and motion amplitudes are strongly influenced by draft, displacement and mooring stiffness. Figure 2.21 highlights the differences in power production across floating concepts. The four concepts (semi-sumbersible, spar, tension-leg buoy (TLB) and tension-leg platform (TLP)) were tested above rated wind speed for a severe sea state. While the mean power varies by only a few percent, larger differences are observed in power fluctuations (standard deviation). Deep-draft platforms generally offer improved stability but require greater installation depths, whereas shallow-draft concepts allow simpler installation at the expense of increased wave-induced motions.

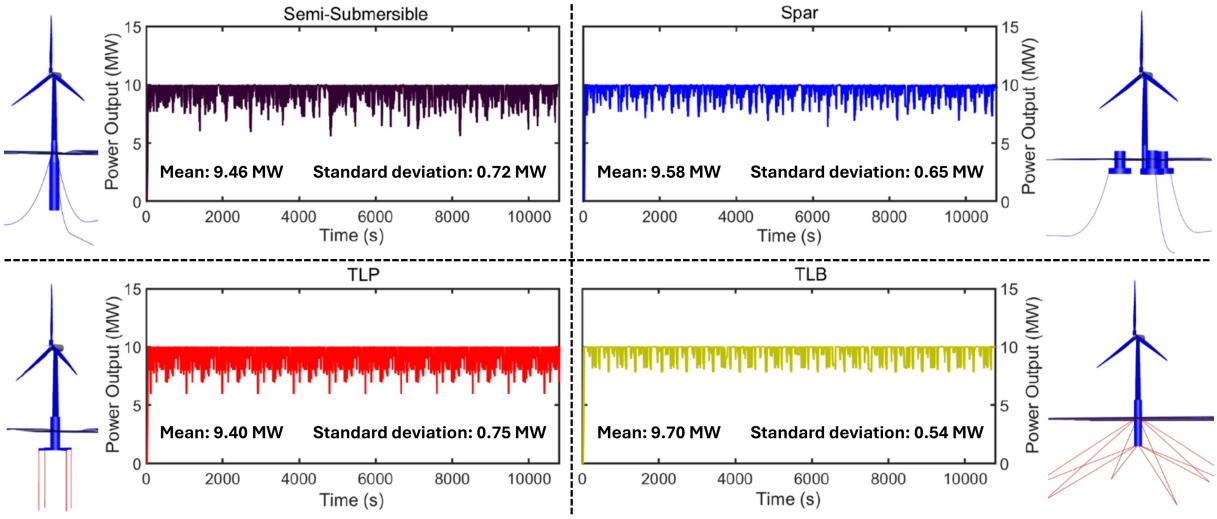

Figure 2.21: Power output over time for four floating wind turbine concepts using the DTU 10 MW reference turbine at above-rated wind speed under a severe sea state. The mean power output and standard deviation are indicated. From top left clockwise: semi-submersible, spar, tension-leg buoy (TLB) and tension-leg platform (TLP). Adapted from [28].

In addition to numerical benchmarking studies, experimental tests were conducted at the MARIN wave basin to compare multiple floating wind platform concepts [87]. The tests provided valuable insight into platform motion behaviour, hydrodynamic damping and restoring mechanisms under controlled wave conditions. The results generally confirmed trends observed in numerical studies, such as reduced heave for deep-draft platforms and increased damping for multi-column concepts. Although the experiments used scaled and simplified models, they significantly improved understanding of floating offshore wind systems and offered partial validation of numerical simulation tools.

Across the literature, mooring system complexity emerges as a key differentiator between floater families. Catenary-based systems used for spars and semi-submersibles are comparatively simple but provide limited horizontal stiffness, while tension-leg systems employed by TLPs offer superior motion control at higher design and installation complexity. Semi-taut and taut mooring systems combine the other two systems but are less commonly employed. Motion-induced power losses are generally reported to be small for well-designed platforms but increase for concepts with larger pitch and surge responses, particularly under severe sea states.

Overall, these comparative studies provide valuable insights into the relative advantages and trade-offs of different floater concepts. All platform concepts try to resist the motion in pitch, surge and heave motion in order to minimise the motion-induced losses on the turbine power generation. However, the applicability of the reported results to modern large-scale floating wind turbines remains limited, highlighting the need for updated analyses using contemporary turbine ratings and platform designs.

2.3.3. Comparison of Floater Concepts to Monopiles

The loads on FOWTs are often compared to land-based turbines [25], [26], [27]. However, FOWT differ from land-based and bottom-fixed systems not only in their structural behaviour but also in the environments in which they can be deployed. Bottom-fixed foundations are limited to shallow water depths up to 50-60 m. This constrains development to near-shore continental shelves, where wind conditions are typically less consistent than those found farther offshore. Studies comparing floating and bottom-fixed platforms show that most research to date has focused on load differences, yet these structural comparisons occur within fundamentally different resource environments [88].

Floating offshore wind technology removes this depth restriction by allowing turbines to be deployed in waters well beyond 60 m. It is reported that over 80% of the global offshore wind resource lies in waters deeper than 60 m [6], [7]. This capability unlocks access to deep-water regions where winds are stronger, steadier and less turbulent and makes FOWTs essential for tapping into the majority of available offshore wind potential. These deep-water sites typically yield higher capacity factors: around 45-60% for floating turbines compared to 40-55% for bottom-fixed systems [89], [90]. Consequently, floating turbines are not just structurally distinct; they enable access to higher-quality wind resources that bottom-fixed designs cannot reach.

2.3.4. Overview of Deployed Floating Wind Platform Concepts

All major floating wind platform families introduced in Subsection 2.3.1 have now reached full-scale demonstration. This reflects a high level of technological maturity and a clear transition toward early commercial deployment. Demonstration and pilot projects over the past 15 years provide valuable insights into platform performance, scalability and practical deployment constraints.

Spar buoys are represented by Equinor's Hywind projects, progressing from the first FOWT prototype (2009: 1 $\times$ 2.3 MW) [11] to the the world's first commercial floating wind farm Hywind Scotland (2017: 5 $\times$ 6 MW) [91]. Hywind Tampen (2022: 11 $\times$ 8.6 MW) [13] currently stands as the largest operational floating wind project. Spar concepts exhibit excellent motion characteristics and proven reliability, but their deep draft requirements restrict fabrication and assembly to a limited number of suitable deep-water ports.

Semi-submersible platforms, particularly Principle Power's WindFloat concept, have shown a strong pathway toward commercial scaling. After the initial prototype (2011: 1 x 2.0 MW) [12], the concept has been applied in multi-turbine projects: WindFloat Atlantic (2020: 3 $\times$ 8.4 MW) [92], WindFloat Kincardine (2021: 5 $\times$ 9.5 MW) [93] and the EFGL project (2025: 3 $\times$ 10.0 MW) [94]. Their shallow draft and compatibility with port-based assembly make them well suited for large-scale deployment.

Barge-type floaters with moonpool configurations have been demonstrated by BW Ideol through the FloatGen project (2018: 1 $\times$ 2 MW) [95] and the nearly constructed EolMed project (2026: 3 $\times$ 10 MW) [96]. These platforms offer compact footprints and simplified hull geometry but have yet to demonstrate scalability comparable to semi-subs.

TLPs have reached full-scale validation with Provence Grand Large (2025) [97]. Hybrid concepts are represented by the TetraSpar demonstrator (2021: 1 $\times$ 3.6 MW) [98], which combines modular construction with favourable hydrodynamic performance and has achieved a reported capacity factor of 63% in 2024 [99]. These concepts confirm technical feasibility but have seen more limited uptake to date.

Looking ahead, several large-scale floating wind farms are under development. For example, the Green Volt (2029: 35 $\times$ 16.0 MW) [100] and Cenos (2030-2035: <95 $\times$ 15-21 MW) [101] wind farms are being developed in Scotland. These projects illustrate the industry's rapid shift toward very large turbine ratings; however, the specific floater concepts to be deployed have not yet been finalised. Overall, the global project pipeline indicates that all major floater families have reached a high level of technological maturity, with semi-submersibles and spar buoys currently leading early commercial scaling. Looking forward, the next phase of sector growth will require standardisation in floater concepts in order to accelerate industrialisation and reduce the cost of deployement.

3

Simulation Framework for Floating IEA 15 MW Wind Turbine Concepts

This chapter presents the OpenFAST simulation model setup for the IEA 15 MW floating offshore wind turbine. It begins with an introduction of the reference turbine and the floating platform concepts considered in this study (Section 3.1). The subsequent section, Section 3.2, describes the OpenFAST model configuration, operational design limits, the modelling assumptions and environmental conditions applied throughout the analyses. Next, Section 3.3 introduces the baseline workflow to evaluate behaviour and annual energy production of the investigated floater concepts. Finally, Section 3.4 outlines the sensitivity analyses performed.

3.1. Reference Turbine and Floater Concept Selection

For the thesis study, the IEA 15 MW reference turbine [23] was selected as the baseline turbine model for all simulations. This choice is motivated by three considerations. First, this turbine, representing the next generation of large-scale offshore wind turbines, reflects the size of machines currently being ordered for offshore wind farms and is therefore commercially relevant [4]. Second, studies comparing multiple floaters have already been conducted for smaller turbines, including the NREL 5 MW reference turbine [26, 27] and the DTU 10 MW reference turbine [28], but similar analyses for larger turbines remain limited. Last, although the IEA 22 MW reference turbine has been developed and represents the future step in upscaling, publicly available floater designs are not currently provided, preventing comparable studies. Technical details about the IEA 15 MW reference turbine are presented in Subsection 3.1.1 and a description of the available floaters is provided in Subsection 3.1.2.

3.1.1. The IEA 15 MW Reference Turbine

The IEA 15 MW reference turbine (see Figure 3.1) was developed by an International Energy Agency (IEA) task force to supply offshore wind developers with a publicly available benchmark. The turbine has a rotor diameter of 240 m and a hub height of 150 m, representative of next-generation large-scale offshore wind turbines. Figure 3.2 shows the power curve and the cut-in, rated and cut-out wind speeds, which are 3, 10.59 and 25 m/s. An overview of other relevant parameters of the turbine can be found in Table 3.1. The reference turbine aims to advance the offshore wind development by bridging the gap between the industry and academics [23]. Moreover, the publicly available data facilitates standardised performance comparisons for different floaters.

A broad range of validation studies has been conducted for the IEA 15 MW reference turbine to validate the aerodynamic, structural and floating offshore applications. Numerous benchmarking campaigns have evaluated steady-state performance, blade eigenfrequencies and monopile and tower mass properties across different aeroelastic modelling tools. HAWC2 and OrcaFlex consistently demonstrated close agreement with the OpenFAST reference implementation [72], [102]. In addition to numerical comparisons, the turbine has also been validated experimentally in a 1:70-scale campaign at the University of Maine's with a performance-matched semisubmersible configuration [103]. The measurements showed strong correspondence with OpenFAST predictions and confirmed accurate modelling of the hydrodynamic behaviour and aero-servo-elastic response of the floating system. Overall, these studies highlight the suitability of the IEA 15 MW reference turbine as a reliable basis for validating numerical models and assessing different floating platform designs.

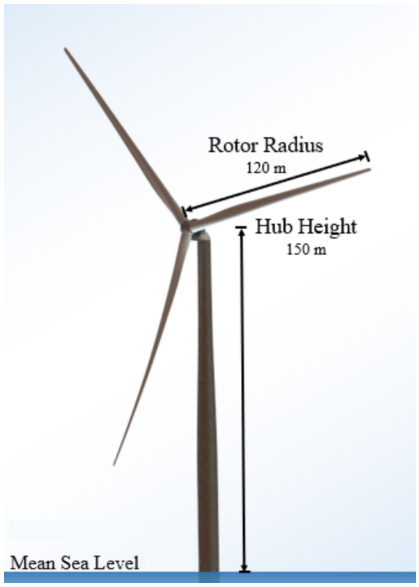

Figure 3.1: Illustration of the IEA 15 MW reference turbine. Adapted from [23].

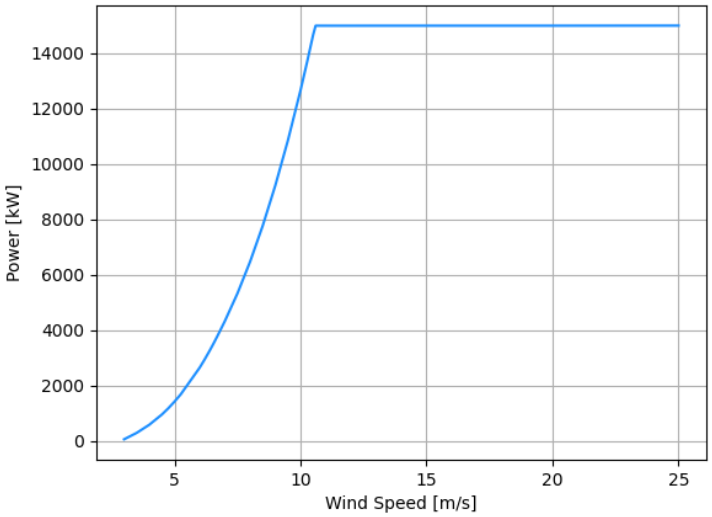

Figure 3.2: Power curve of the IEA 15 MW reference turbine [23].

Table 3.1: Key parameters for the IEA Wind 15-MW turbine. Relevant parameters selected from [23].

Parameter	Unit	Value
Power rating	MW	15
Turbine class	-	IEC Class 1B
Configuration	-	Upwind, 3 blades
Control	-	Variable speed Collective pitch
Drivetrain	-	Low speed direct drive
Cut-in, rated & cut-out wind speed	m/s	3, 10.59, 25
Rated thrust	MN	2.4
Min, max rotor speed	rpm	5.0, 7.56
Design tip-speed ratio	-	5.9
Maximum tip speed	m/s	95

Parameter	Unit	Value
Rotor diameter	m	240
Hub height	m	150
Hub diameter	m	7.94
Hub overhang	m	11.35
Shaft tilt angle	deg	6
Rotor precone angle	deg	-4.0
Blade prebend	m	4
Blade mass	t	65
RNA mass[1]	t	1017
Tower mass[2]	t	860

[1] RNA = Rotor nacelle assembly
[2] Tower mass varies with floater concept

3.1.2. Selected Floater Concepts

This thesis analyses the four publicly available floater concepts developed for the IEA 15 MW reference turbine. These platforms represent three of the five principal floater families introduced in Section 2.3. The COREWIND project provides two of the concepts: the spar-buoy platform WindCrete (Figure 3.3) and the semi-submersible ActiveFloat (Figure 3.4) [32]. A second semi-submersible design, the VolturnUS-S (Figure 3.5), was developed by the University of Maine [33]. Finally, a reference TLP (Figure 3.6) for multiple water depths was created by Hall et al. [34]. At the time of writing, no barge or hybrid floaters (e.g. TetraSpar-type designs) have been developed for this turbine. So these four platforms constitute the complete set of models available for comparison in this thesis.

The four platforms differ primarily in their stability mechanism and mooring system design. Together with the mass distribution, these characteristics govern the dynamic response under wind and wave loading. An overview of their main characteristics is presented in Table 3.2.

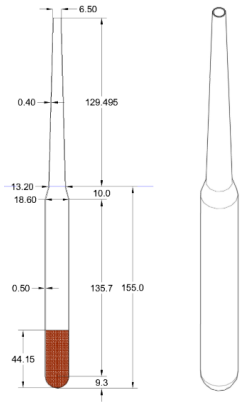

Figure 3.3: Illustration of the spar buoy platform WindCrete [32].

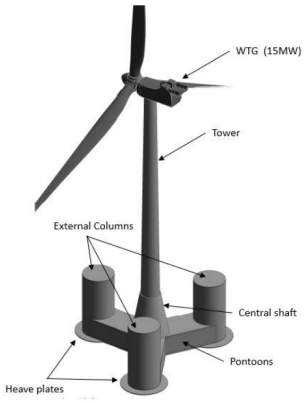

Figure 3.4: Illustration of the semi-submersible ActiveFloat [32].

Figure 3.5: Illustration of the semi-submersible VolturnUS-S [33].

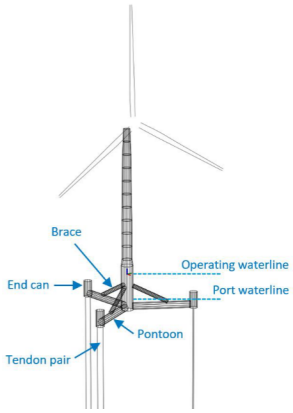

Figure 3.6: Illustration of the reference TLP [34].

Table 3.2: Overview of the four floaters designed for the IEA 15 MW reference floater [32], [33], [34].

Parameter	WindCrete	ActiveFloat	VolturnUS-S	Reference TLP
Platform type	Spar buoy	Semi-submersible	Semi-submersible	Tension-leg platform
Platform material	Reinforced concrete	Reinforced concrete	Steel	Steel
Radius [m][1]	9.4	46.5	51.75	63.5
Draft [m]	155	26.5	20	36
Water depth [m]	200	200	200	200-1500
COG platform [m][2]	-113.1	-17.37	-14.94	-26.3
Platform mass [t]	36550	34487	17839	4030
Ballast mass [t]	25070	6360	13840	0
Displacement [m^3]	40540	36431	20206	14216
Pitch inertia round COG [$kg * m^2$]	55.9 * 10^9	15.7 * 10^9	12.5 * 10^9	3.16 * 10^9
Hub height [m]	135	135	150	150
Mooring type	Catenary	Catenary	Catenary	Tension-leg
# of mooring lines	3	3	3	6 (3 pairs)
Depth to fairleads / anchors [m]	-90.0 / -200.0	-15.0 / -200.0	-14.0 / -200.0	-36.0 / -200.0
Radius to fairleads / anchors [m]	9.3 / 600.0	42.5 / 600.0	58.0 / 837.6	63.5 / 63.5
Mooring mass density [$kg * m^{-1}$]	561.25	561.25	685.00	26.00
Mooring diameter [m]	0.160	0.160	0.333	0.184
Mooring stiffness [N]	2.304 * 10^9	2.304 * 10^9	3.27 * 10^9	2.39 * 10^9
OpenFAST version	V2.1 (2018)	V2.1 (2018)	V4.0.0 (2024)	V4.0.3 (2024)
Remarks	Tower is integrated into the floater. Iron ore used as ballast.	Seawater can be used as active ballast.	Fixed and fluid (seawater) ballast are used.	Design varies with water depth.

[1] For the semi-submersible and tension-leg platforms, the radius is defined as the distance from the centre of the platform to the end of one of the legs.
[2] Vertical centre of gravity (COG) from the still water level (SWL).

The three different stability mechanisms (see Figure 2.19) can be clearly identified per floater. The spar buoy concept WindCrete achieves stability through its deep draft (155 m) and low centre of gravity due to extra ballast at the keel. ActiveFloat and VolturnUS-S, both semi-submersible platforms, rely instead on a wide footprint (46.5 m and 51.75 m radius, respectively) and large water-plane area that provide geometric restoring through buoyancy changes during heave and pitch. At the opposite triangle, the Reference TLP represents the opposite extreme and derives nearly all stability from the vertical tendons; the combined tendon pretension corresponds to approximately 57% of the platform's total buoyancy. This yields exceptionally low pitch and surge excursions.

Among the platform properties, the most relevant for this comparison are platform mass, platform geometry, hub height and mooring type. Material differences (reinforced concrete versus steel) are not analysed explicitly in this thesis, but they indirectly affect mass and stiffness and therefore influence the platform dynamics. Another difference can be found for the hub height; the WindCrete and ActiveFloat have a reduced hub height of 135 m (vs. 150 m IEA 15 MW reference turbine) to lower the centre of gravity and reduce loads (details in Subsection 3.2.1). The model fidelity also varies across concepts and will impact the interpretation of results. The VolturnUS-S includes first and second-order hydrodynamic coefficients generated by the external panel-method solvers WAMIT, while WindCrete and ActiveFloat only use first-order coefficients. The reference TLP is most limited and has no WAMIT files entirely; its hydrodynamic behaviour will be analysed by the Morison strip theory (valid for $D/\lambda \leq 0.2$).

The mooring stiffness values in Table 3.2 represent the axial line stiffness of the mooring lines, determined by the line's elastic and geometric properties. The WindCrete and ActiveFloat share an identical stiffness of $2.304 * 10^9 N$, but will have different horizontal restoring characteristics due to the differences in geometry and layout (e.g. bridles for WindCrete). The reference TLP has a similar stiffness ($2.39 * 10^9 N$), but tendons mainly affect the vertical motions. The VolturnUS-S has a significantly higher stiffness ($3.27 * 10^9 N$) than the other platforms. The mooring stiffness also indirectly influences pitch through the vertical lever arm between the fairlead and the platform COG, which determines the pitch-restoring moment generated by horizontal mooring forces. It has to be noted that for catenary platforms, pitch restoring remains dominated by hydrostatic effects.

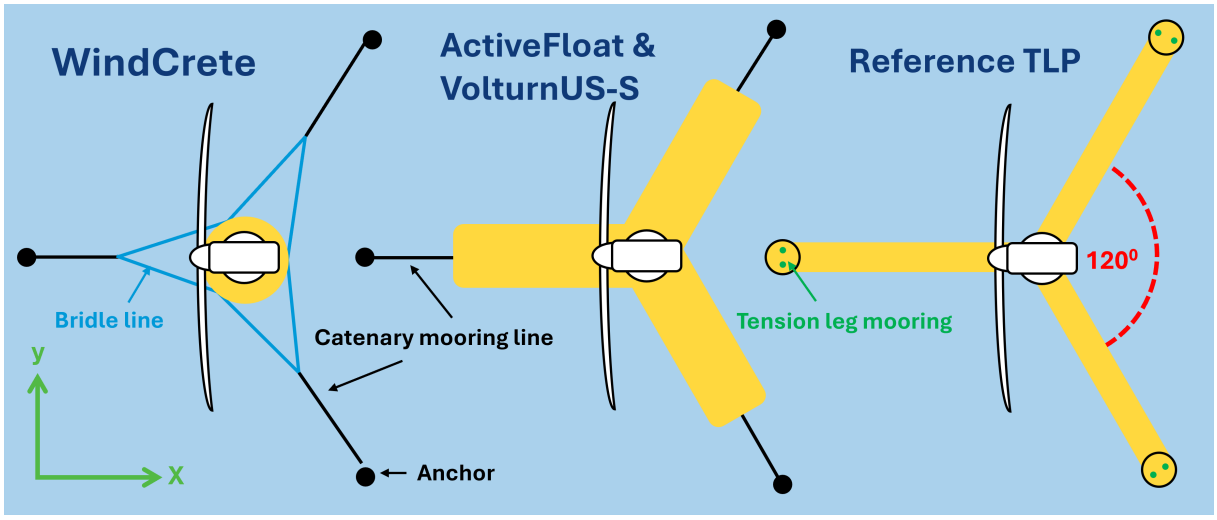

Figure 3.7: Schematic representation of the floater orientation and mooring layout of the analysed floaters. The mooring lines and wind turbines are not to scale. From left to right: WindCrete, ActiveFloat & VolturnUS-S, Reference TLP.

Figure 3.7 illustrates the resulting floater layouts and mooring configurations with respect to incoming wind and waves (propagating in the positive x direction). For the ActiveFloat, VolturnUS-S and Reference TLP, the turbine is located in the centre between three legs (also called pontoons) spaced 120° apart. As can be seen, all floaters have one of the legs orientated upwind. The Reference TLP uses six tension leg moorings (vertical tendons anchored to the sea floor) and the ActiveFloat and VolturnUS-S use a simple catenary mooring system attached to the end of the legs which spaces the mooring lines 120° apart. The WindCrete uses an adapted catenary mooring system which splits into two bridle lines 48 m from the floater to provide extra yaw stability to the platform [32]. The six bridle lines connect to three attachment points at the floater, also 120° spaced apart.

The WindCrete, ActiveFloat and VolturnUS-S platforms employ hybrid ballast systems combining fixed and fluid components to optimise for their specific geometry and stability requirements. The WindCrete uses fixed ballast to achieve the required hydrostatic stiffness in pitch and roll DOF. The ActiveFloat uses fluid ballast in the pontoons to reduce the differential pressure of the water as they are fully submerged. The radial columns at the end of the legs are partially filled and can be used for an active ballast system [32]. The VolturnUS-s uses fluid ballast in the pontoons and equally diveded fixed ballast in the radial columns [33] to improve stability.

The TLP is a reference design intended for a wide range of water depths (200 m - 1500 m). For shallower depths than 1100 m, the design is largely driven by the requirement to remain stable in port during installation and operations. This harbour-stability constraint is the primary reason the TLP is oversized for shallow water depths. Moreover, fewer load cases (such as the wind step test) have been tested for the TLP. In combination with the less complete hydrodynamic data, the results should be interpreted with particular caution. The TLP serves best as a stiffly moored concept rather than as a fully validated industrial design. These modelling limitations are therefore an important consideration when interpreting platform pitch, tower loads or power output, as the TLP's response may appear less dynamic than that of the spar buoy and semi-submersible concepts [34].

These differences represent the main design difference of each floater family (detailed overview in Subsection 2.3.1) and directly affect the pitch and surge response, mooring loads, control interaction and most importantly, the power output of the turbine.

3.2. OpenFAST Model Setup

For all simulations in this study, OpenFAST was selected as the modelling tool, following its modular capabilities and demonstrated accuracy as described in Subsection 2.2.3 and Subsection 2.2.4. The four selected floaters all had an OpenFAST setup available but were implemented in different OpenFAST versions. To be able to compare all floaters, the inputs had to be made as similar as possible without adjusting the floater's design. Before any modifications were applied, each original OpenFAST model was first run and compared against the results reported in the corresponding reference paper. This served as a baseline verification step to confirm that the published configuration was implemented correctly and that the starting point for the subsequent updates was consistent with the original study. A more detailed overview of the verification steps taken, can be found in Subsection 2.2.4. Subsection 3.2.4 summarizes all changes made to the floater models.

The second step was to update all designs to OpenFAST 4.2.0. With the help of the change log on the OpenFAST Github repository [104] and OpenFAST documentation [70], all input files were updated and, if required, new were created. The outputs were compared for 12 runs (combinations of different wave heights for regular and irregular waves with below/above rated wind speed as seen in Table 3.6) to make sure no errors were made during this version update. The behaviour was nearly identical, but small differences were observed in the power output. For the floaters updated from OpenFAST 4.0.x to 4.2.0, the Normalised Root Mean Square Difference (NRMSD) was on average 0.059% with a maximum of 0.243%, while for those updated from version 2.1.0 to 4.2.0, NRMSD's of up to 4.91% were found but the average NRMSD stayed at 1.21%. The detailed overview can be found in Subsection 2.2.4 and Table 3.6. These deviations are considered negligible and are attributed to model and solver updates between versions.

After the version update, the second step standardised the turbine model, boundary conditions and simulation settings across all floaters. This involved iterative updates to ElastoDyn, AeroDyn15, ServoDyn, HydroDyn, InflowWind, MoorDyn and SeaState inputs. The iterative updates were used to align with the latest IEA 15 MW reference turbine specifications released after the older OpenFAST 2.1.0 models and quantify the influence of each updated parameter. Key changes included RNA mass and position dimensions (e.g., TipRad from 120 m to 120.97 m, HubRad from 3 m to 3.97 m), generator efficiency (96.55%→95.756%), gravity (9.8065→9.81 m/s²) and SeaState waveseed and discretisation (5 m half-width to prevent memory issues). Equalizing of the hub height has a major influence on the power output and will be discussed in more detail in Subsection 3.2.1. These updates ensured identical turbine properties without altering floater designs, with verification showing minimal impact on outputs.

The last step implemented a unified controller: the Reference Open-Source Controller (ROSCO) tuned for the IEA 15 MW reference turbine and tested on the VolturnUS-S (UMaine semisubmersible) platform. ROSCO [74] is a modular, Bladed-style DLL controller providing baseline industry-standard features like proportional-integral (PI) pitch control for generator speed regulation, torque control modes (e.g. $k^2\omega^2$

below rated), notch filtering for platform motion (fore-aft and generator speed), individual pitch control (IPC) for 1P/2P load reduction, wind estimation and floating-specific platform pitch feedback to reduce motions by up to 30%. ROSCO replaced the controllers from the OpenFAST v2.1.0 models, which exhibited numerical instabilities for certain load cases as illustrated in Figure 3.8. The stability issue made the controller unstable for the systematic analysis. As the ROSCO controller was already in use for the VolturnUS-S and Reference TLP, it was extended to all platforms and used as the controller for the rest of this thesis. Using a consistent controller across all platforms reduces the influence of controller differences on the comparative results.

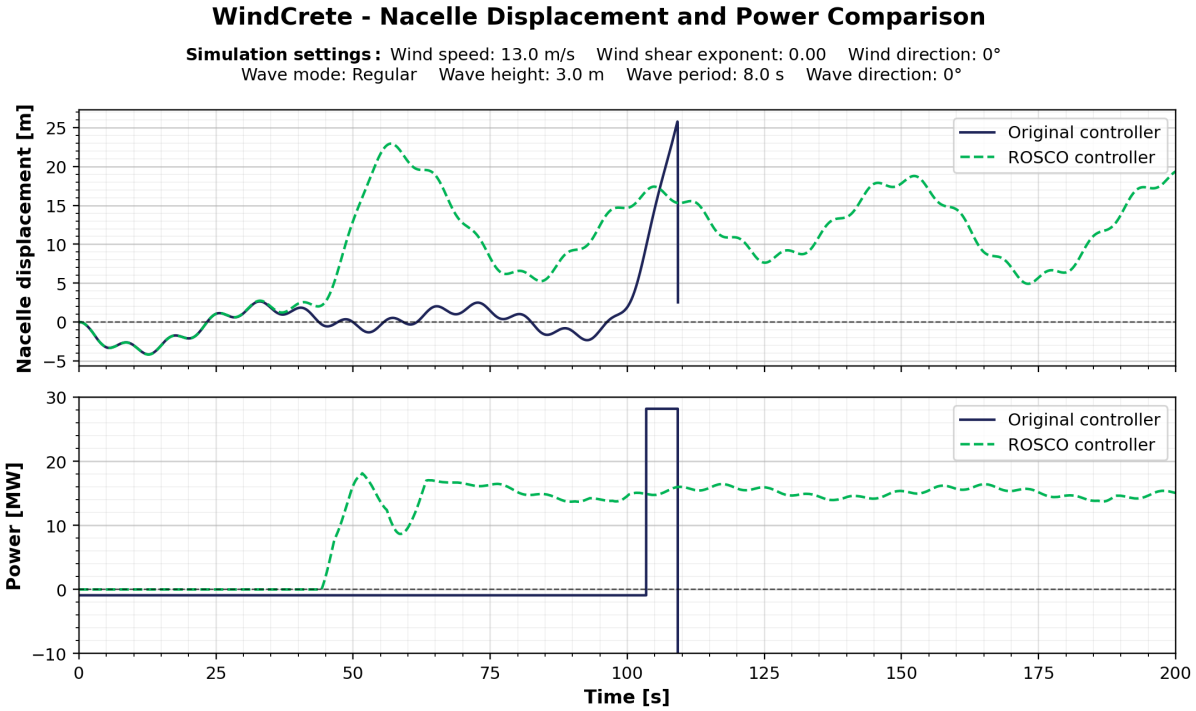

Figure 3.8: Numerical instability of the original OpenFAST v2.1.0 controller for the WindCrete platform. The nacelle acceleration and power output exhibit unphysical behaviour around 105s and make the controller unsuitable for a systematic analysis.

3.2.1. Incorporation Hub Height Difference for the WindCrete and ActiveFloat

As shown in Table 3.2, both the ActiveFloat and WindCrete designs feature a reduced hub height of 135 m compared to the baseline 150 m configuration. The reduced hub height decreases the overall loads and leads to a lighter and more cost-effective structure. The 135 m was determined with constraints from the IEC 61400-3-2 standard for the height and clearance of the access platform [32]. To enable fair comparisons with other floaters, both hub height variants (135 m and 150 m) are analysed in this study. The four configurations are designated as '*ActiveFloat_135m*', '*ActiveFloat_150m*', '*WindCrete_135m*' and '*WindCrete_150m*' for analysis.

For the 150 m version, the `TowerHt` in ElastoDyn was increased from 129.495 m to 144.386 m. However, the mode shapes of the tower were kept unchanged. ElastoDyn automatically scaled tower strength and weight per unit height based on this fractional adjustment. This led to an increase in tower weight and, as the platform was not adjusted, a static heave offset for the floaters. The resulting offsets are approximately 0.15 m for ActiveFloat and 2.5 m for WindCrete. For ActiveFloat, this offset is considered negligible. For WindCrete, the 2.5 m offset is more significant and may influence the results; however, correcting it would require retuning the platform ballast, which is outside the scope of this study. The offset is therefore acknowledged as a modelling limitation for the WindCrete 150 m variant and its potential influence should be kept in mind when interpreting the corresponding results.

The tower diameters in AeroDyn were originally defined for the baseline 135 m hub height configuration (`TowerHt = 129.495 m`). For the extended 150 m hub height (`TowerHt = 144.386 m`), the intermediate tower stations (`TwrElev`) were scaled proportionally from 135 m to 150 m elevations while preserving the fixed base diameter and top diameter. Both the original (135 m) and scaled (150 m) tower dimensions can be found in Table 3.3 and visualised in Figure 3.9.

Table 3.3: Parameters for the scaling of the WindCrete and ActiveFloat tower for AeroDyn module.

WindCrete			ActiveFloat		
Tower elevation: 135 m vs 150 m hub height [m]		Tower diameter [m]	Tower elevation: 135 m vs 150 m hub height [m]		Tower diameter [m]
15.000	15.000	12.42	9.000	9.000	10
25.000	28.251	11.90295	21.050	23.651	9.65
35.000	39.552	11.38589	33.099	37.189	9.3
45.000	50.853	10.86884	45.149	50.728	8.95
55.000	62.153	10.35179	57.198	64.267	8.6
65.000	73.454	9.834734	69.248	77.805	8.25
75.000	84.754	9.317681	81.297	91.344	7.9
85.000	96.055	8.800628	93.347	104.882	7.55
95.000	107.356	8.283575	105.396	118.421	7.2
105.000	118.656	7.766522	117.446	131.960	6.85
115.000	129.957	7.249469	129.495	144.386	6.5
125.000	141.257	6.732415			
129.495	144.386	6.5			

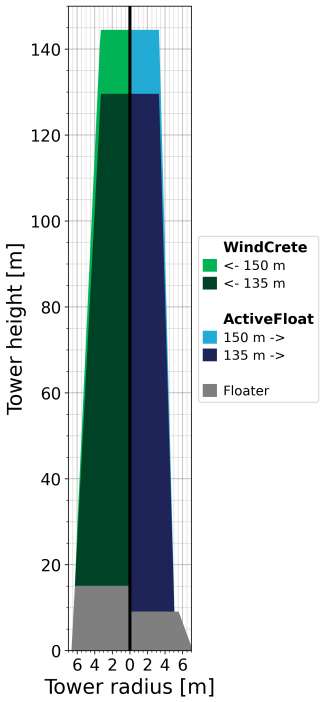

Figure 3.9: Illustration of the scaling of the WindCrete and ActiveFloat towers for AeroDyn module.

The implementation was verified using a uniform wind profile without wind shear. As expected, the 150 m hub height variants exhibited increased mean platform pitch compared to the 135 m variants. This is consistent with the longer moment arm between the hub and the platform centre of gravity. At below-rated wind speed (8 m/s), this increased platform motion resulted in a slight reduction in mean power output, while at above-rated wind speed (13 m/s) the pitch controller maintained rated power for both variants. This behaviour is physically consistent and confirms the correct implementation of the hub height increase. The effect is quantified in Table 3.4 for both WindCrete and ActiveFloat. For the ActiveFloat, the corresponding time series of nacelle displacement and power output are shown in Figure 3.10 and Figure 3.11.

Table 3.4: Mean nacelle displacement and power output for the 135 m and 150 m hub height variants of WindCrete and ActiveFloat at below-rated (8 m/s) and above-rated (13 m/s) wind speeds with an irregular wave(JONSWAP: H_s = 1.5 m and T_p = 8.0 s). Mean values are computed over the steady-state period from 300 s to 1200 s, excluding the initial transient.

		WindCrete		ActiveFloat	
Wind speed	Mean steady-state period	_135m	_150m	_135m	_150m
Below rated: 8 m/s	Platform pitch [deg]	2.26	2.73	2.80	3.70
	Nacelle displacement [m]	11.24	13.20	16.50	18.53
	Power output [MW]	6.57	6.54	6.55	6.50
Above rated: 13 m/s	Platform pitch [deg]	2.48	3.01	3.10	4.15
	Nacelle displacement [m]	12.22	14.50	18.03	20.44
	Power output [MW]	15.00	15.00	15.00	15.00

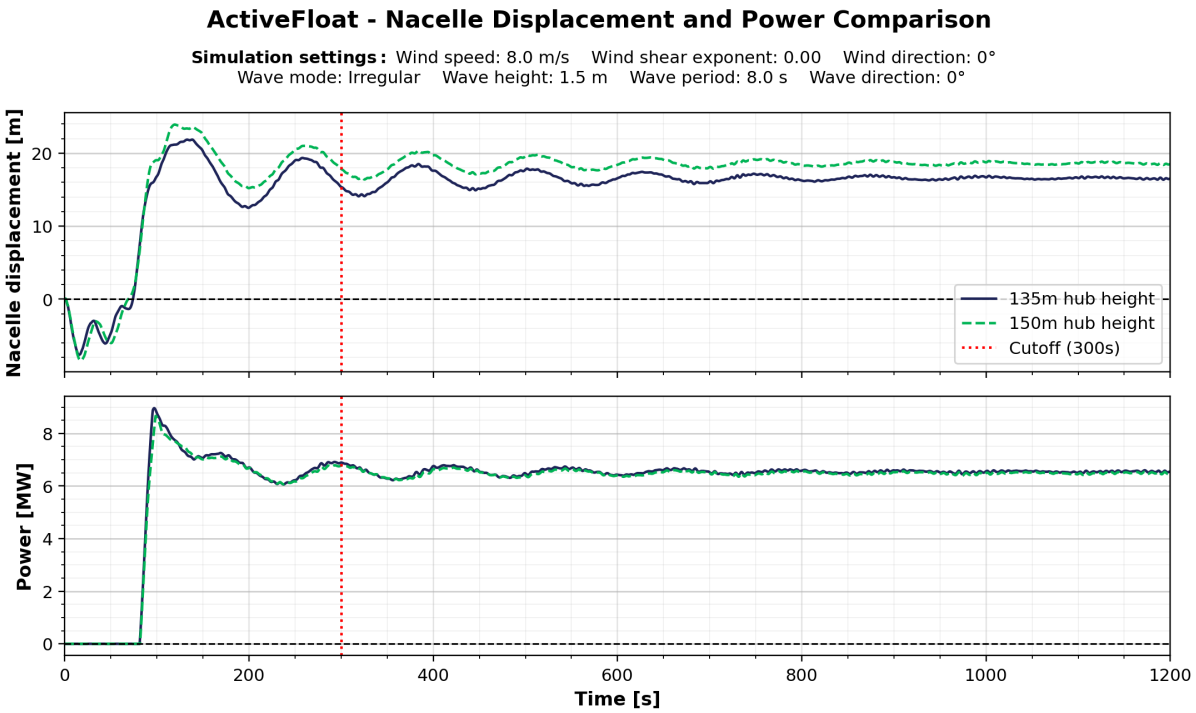

Figure 3.10: Time series of nacelle displacement and power for the ActiveFloat 135 m and 150 m hub height variants under below-rated wind speed. The 150 m variant exhibits increased nacelle displacement and a slight reduction in mean power output.

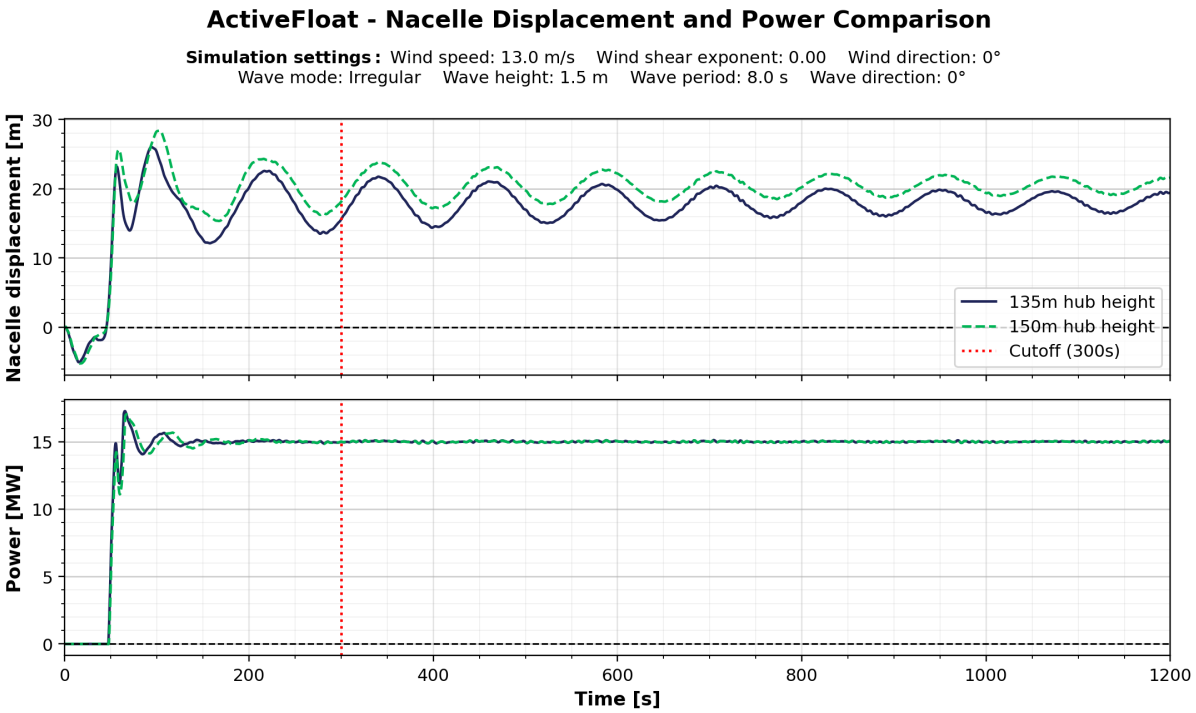

Figure 3.11: Time series of nacelle displacement and power for the ActiveFloat 135 m and 150 m hub height variants under above-rated wind speed. Despite the increased nacelle displacement for the 150 m variant, the pitch controller maintains rated power output for both configurations.

3.2.2. Simulation Assumptions and Limits

The numerical simulations conducted in this study focused on the power output during normal operational conditions. Extreme-load performance of the floaters has been addressed in the respective design studies. Consequently, no fatigue calculations are included; instead, the analysis relies exclusively on maximum motion values and on the 10-minute standard deviations σ of the platform degrees of freedom. These limits serve as operational boundaries for acceptable floater behaviour and are based on the criteria adopted in the CoreWind Project [32],[105] and in the IEA Wind Task 39 design-limit development [106].

Table 3.5: Floater motion and acceleration limits for operational conditions used in OpenFAST simulations [32], [105], [106].

Degree of freedom	Maximum	10 min σ
Surge limit	$\leq$ 30.0 m	-
Pitch warning	[- 5.0° , + 5.0°]	-
Pitch limit	[- 7.0° , + 7.0°]	$\leq$1.0°
Roll limit	[- 2.0° , + 2.0°]	$\leq$0.4°
Yaw limit	[-15.0°, +15.0°]	$\leq$3.0°
Nacelle acceleration	$\leq 0.3g$[1]	-

[1] $g = 9.81\ \mathrm{m/s^2}$

Table 3.5 shows the motion limits applied to surge, pitch, roll, yaw and nacelle acceleration. For pitch, a warning interval of ±5° is introduced to signal expected operational boundaries. However, exceeding this range does not automatically invalidate the simulation if the behaviour remains physically plausible. A strict cut-off is imposed at ±7°. Any simulation surpassing one of the thresholds is excluded from power performance calculations. The limits are only applicable for aligned wind and wave conditions (both propagating in the positive x-direction). No limits are put on the heave or sway, as they are generally low for this condition.

The turbine controller incorporates an additional safety measure based on blade pitch. If the blade pitch exceeds 22.56° (0.39386 rad), the controller initiates a feather-mode shutdown to protect the structural integrity of the turbine. In feather mode, the blades rotate to 90° and fully stall the rotor. This behaviour is illustrated in Figure 3.12, which compares the blade pitch evolution for two pitch limit strategies under a high wind speed scenario of 24.5 m/s for the VolturnUS-S platform. The left panel shows the full simulation, where the baseline controller enforces the 22.56° limit (the horizontal dashed line) while the extended configuration allows up to 25.00°. The right panel zooms in on the first 25 seconds, clearly capturing the moment the blade pitch rapidly feathers to 90° once the limit is exceeded. To prevent unintended cut-offs due to blade pitch peaks during the transient start-up phase at high wind speeds, the simulations were initially performed with a higher pitch limit. The maximum pitch after the transient behaviour (after cut-off) was then checked to ensure compliance with operational boundaries.

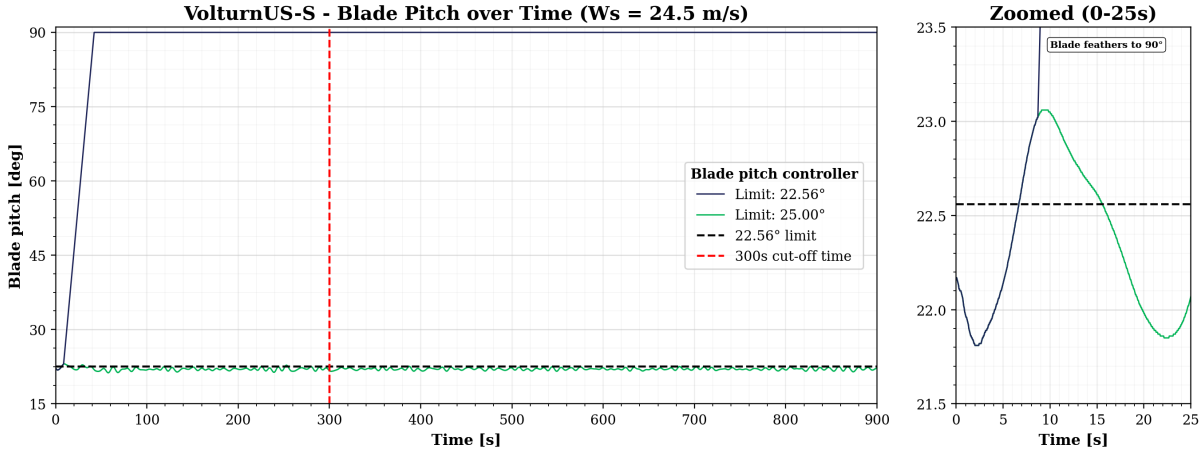

Figure 3.12: Blade pitch response for VolturnUS-S at 24.5 m/s wind speed showing both the basic (22.56° limit) and extra pitch control (25.00° limit) strategies. Left: Full simulation duration (0–900 s). Right: Zoom on the first 25 seconds, highlighting the feathering of the blade to 90 ° after the blade pitch limit is exceeded.

The hydrodynamic modelling applied in OpenFAST reflects the level of data available for each platform. The VolturnUS-S is the only concept for which second-order potential-flow data are available. This enables the inclusion of low-frequency drift and difference-frequency effects through the HydroDyn WAMIT module. The WindCrete and ActiveFloat platforms rely solely on first-order hydrodynamic coefficients. Their responses are captured using linear potential-flow theory. For the Reference TLP, no panel-method hydrodynamic data are available. Therefore, it's loads are computed using Morison-strip theory. These differing levels of hydrodynamic fidelity follow directly from the available datasets and represent intentional modelling choices rather than inconsistencies in the analysis.

The active ballast system of the ActiveFloat platform is not enabled in this study. Since the ballast configuration cannot be adjusted dynamically during an OpenFAST simulation, it would be impractical to redefine the ballast distribution for every individual run. To ensure that all simulations start from identical initial conditions and remain directly comparable, a fixed ballast setup is used. The total ballast mass is evenly distributed across all tanks, providing one consistent parameter set for every simulation.

The mooring system details of the Reference TLP are available for all waterdepths in RAFT; only the 800-m case had been implemented in OpenFAST. To extend the analysis to 200 m, the RAFT and OpenFAST input files for the 800-m depths were compared and the 200-m conditions were translated accordingly into the OpenFAST model.

The nacelle yaw DOF (`YawDOF = False`) was disabled to eliminate controller-induced instabilities during decay tests and modal analysis. The tower torsion is not modelled in OpenFAST, resulting in zero torsional displacement. Consequently, nacelle yaw motion equals platform yaw motion. The floater is modelled as a rigid body and the dynamic high-voltage power cable is neglected. Past studies have shown that the contribution of the dynamic cable to global floater motion is minimal for this type of platform configuration, supporting its omission from the model [48].

The environmental parameters in this research focused exclusively on wind and wave-induced loads. Effects from currents and tidal variations are intentionally excluded. Although tidal variations can modify mooring line pretension and effective system stiffness, these effects fall outside the scope of this thesis. Wind and waves are assumed to be perfectly aligned and atmospheric turbulence is excluded from the simulations. The simulations can include a wind shear profile that follows a power-law formula in Equation 2.2.The shear exponent α is based on site-specific measurements.

The wind-farm interactions and wake losses are not considered. Only single-turbine behaviour is evaluated and any potential influence of turbine motion on array-level wake losses is neglected. This is supported by existing literature, which indicates that difference in wake effects between bottom-fixed and floating wind farms is typically small [60].

Lastly, the annual energy production assessment assumes continuous turbine availability; there is no downtime due to maintenance, environmental restrictions or unforeseen events (e.g. bird migration curtailment). However, wind variability is accounted for through a Weibull distribution and will include wind speeds outside the turbine's operational range.

3.2.3. Verification of the Simulation Setup

The simulation setup was verified through a series of targeted checks, covering OpenFAST version consistency, turbine model updates, controller differences and simulation duration. Each step is discussed below.

Definition of Normalised Root Mean Square Difference

To verify the impact of model updates on simulation consistency, representative load cases from the reference database were re-run and compared using the Normalised Root Mean Square Difference (NRMSD). The NRMSD is defined as:

$$\mathrm{NRMSD} = \frac{\sqrt{\frac{1}{N}\sum_i \left(x_i - y_i\right)^2}}{\frac{1}{N}\sum_i y_i} \cdot 100\% \tag{3.1}$$

where x_i are the values from the updated version, y_i the reference values and N the number of time-series samples. Normalising by the mean of the reference signal ensures the metric is independent of the absolute magnitude of the output, allowing meaningful comparison across different floaters and load cases.

OpenFAST Baseline Validation Against Reference Database

As a first verification step, the OpenFAST implementation was validated against a publicly available open-source simulation database for the NREL 5 MW reference turbine on the OC4 semi-submersible platform [107]. This serves to confirm that the OpenFAST setup is correctly configured and that the automated input file generation and simulation workflow function as intended, before applying the same setup to the floating platforms of interest.

The same input files from the reference database were adopted [108] and compared to the corresponding simulation reference outputs [109]. The reference database was produced with OpenFAST version 3.5.3, while this work used OpenFAST 4.2.0. From the 1000 available load cases in the database, a representative subset was selected based on the following criteria: steady wind conditions, wind speeds either below or above the rated wind speed of the turbine, no wind direction changes and operational conditions only.

The comparison yields a high correlation between the reproduced and reference results as seen in Table 3.6. The NRMSD of the power output is below 0.6% for all selected load cases, with an average of 0.173%. The agreement is strongest for above-rated wind speeds and for load cases with lower wave periods. While the floating platform simulations themselves provide stronger evidence that the model behaves correctly under the specific conditions of this study, this baseline comparison confirms that the OpenFAST implementation and toolchain are functioning as expected.

OpenFAST Version Update

To ensure consistency across the simulation campaign, the influence of updating the OpenFAST version was assessed by re-running a set of representative load cases and computing the NRMSD. The same cases from the reference database were used.

The results are summarised in Table 3.6. NRMSD values remain low across all floaters and load cases. The highest average NRMSD is observed for WindCrete (1.58%), followed by ActiveFloat (0.85%), while the Reference TLP (0.111%) and VolturnUS-S (0.006%) show negligible differences. The larger NRMSD values for WindCrete and ActiveFloat occur predominantly under regular wave conditions with larger wave heights, suggesting that the version update has a greater influence when wave-induced platform motions are more pronounced.

Table 3.6: Normalised Root Mean Square Difference (NRMSD) for OpenFAST version updates per load case per floater.

Run time [s]	Wind speed [m/s]	Wave mode	Wave height [m]	Wave period [s]	NRMSD OC4 Semisub	NRMSD OpenFAST version update			
						Wind-Crete	Active-Float	Volturn-US-S	Reference TLP
600	8.0	Regular	3.0	8.0	0.164%	0.63%	0.38%	0.013%	0.119%
600	13.0	Regular	3.0	8.0	0.102%	1.27%	0.63%	0.006%	0.074%
600	8.0	Regular	6.0	10.0	0.350%	1.55%	0.70%	0.014%	0.243%
600	13.0	Regular	6.0	10.0	0.159%	2.89%	0.91%	0.005%	0.168%
600	8.0	Regular	9.0	12.0	0.566%	2.44%	1.91%	0.005%	0.222%
600	13.0	Regular	9.0	12.0	0.173%	4.91%	3.10%	0.003%	0.212%
1200	8.0	Irregular	1.5	8.0	0.087%	0.30%	0.27%	0.003%	0.019%
1200	13.0	Irregular	1.5	8.0	0.040%	1.20%	0.40%	0.001%	0.013%
1200	8.0	Irregular	3.0	10.0	0.136%	0.46%	0.36%	0.006%	0.060%
1200	13.0	Irregular	3.0	10.0	0.045%	1.17%	0.43%	0.003%	0.044%
1200	8.0	Irregular	4.5	12.0	0.196%	0.75%	0.58%	0.007%	0.094%
1200	13.0	Irregular	4.5	12.0	0.055%	1.42%	0.50%	0.003%	0.070%
				Average:	0.173%	1.58%	0.85%	0.006%	0.111%

As shown in Figure 3.13, the updated OpenFAST version (4.2.0) produces slightly higher peaks and troughs in the power output compared to version 2.1.0 for the highest-difference load case. The version jump from 2.1.0 to 4.2.0 encompasses a large number of changes across multiple modules, including updates to the aerodynamic, hydrodynamic and structural solvers, making it difficult to attribute the difference to a single cause. Nevertheless, the mean response and general time-series character remain

consistent between versions. This indicates that the update does not alter the underlying physics in a meaningful way. The NRMSD differences are therefore considered acceptable and the version update is not expected to have a significant influence on the conclusions drawn from the simulation results.

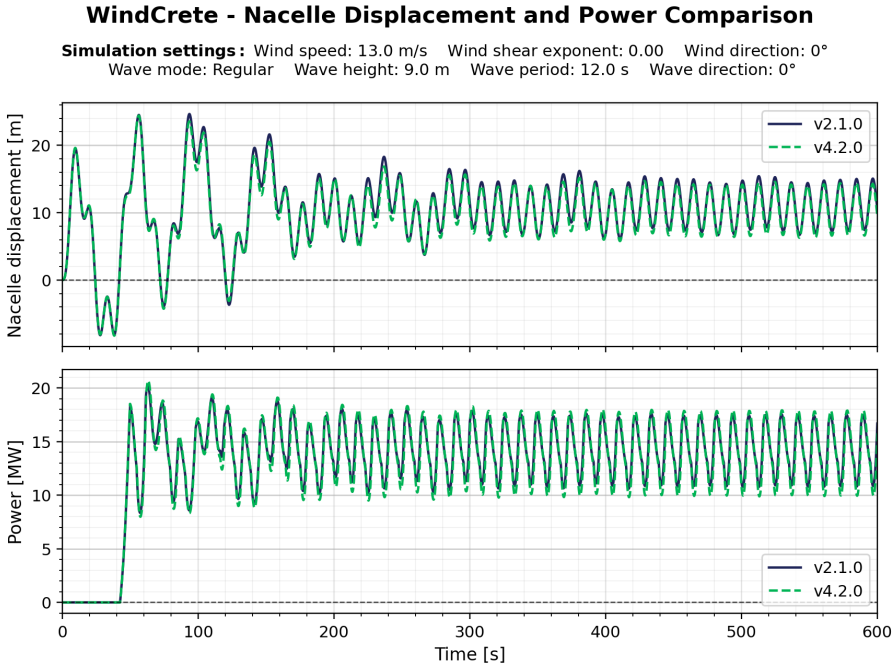

Figure 3.13: Power output time series for WindCrete under the load case with the highest NRMSD, comparing the 2.1.0 and 4.2.0 OpenFAST versions.

Turbine Model Update

The turbine model was updated across all floating platforms, with an overview of all changes in Subsection 3.2.4. To verify that the update does not introduce unphysical behaviour, the NRMSD was computed between the original and updated model for all floaters across the representative load case set.

The turbine update resulted in significantly larger NRMSD values compared to the OpenFAST version update, primarily due to phase shifts in the time-series response rather than changes in overall dynamic behaviour. As shown in Figure 3.14, the mean power output and general response character remain consistent between the two model versions, confirming that the update does not alter the underlying physics in a meaningful way. The updated turbine model is therefore accepted for use in the main simulation campaign.

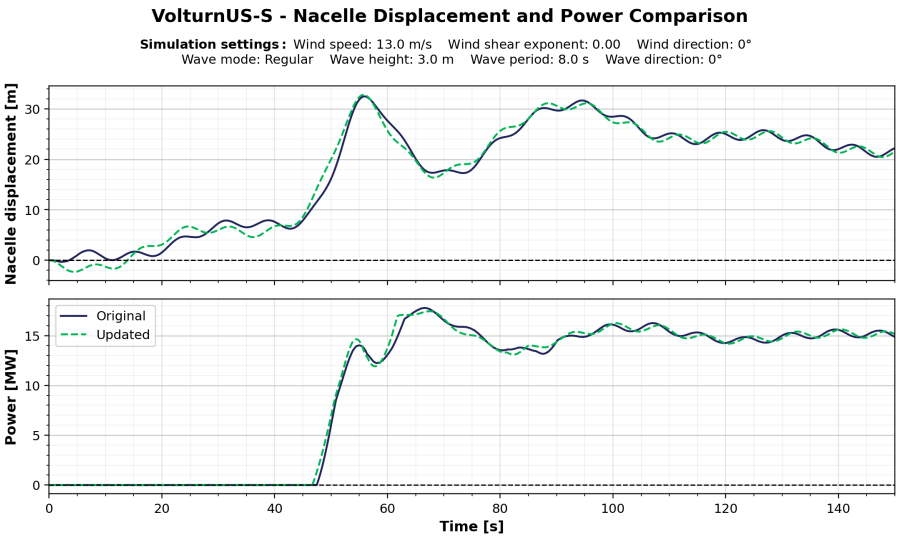

Figure 3.14: Power output time series comparing the original and updated turbine model for the VolturnUS-S under a representative load case.

Simulation Duration: 10-Minute versus 3-Hour Runs

The main simulation campaign uses 15-minute runs with the first 5 minutes discarded as transient, yielding 10 minutes of usable data per load case. This duration is standard practice in offshore wind simulations [58] and was adopted to reduce computational cost. To verify that this duration does not introduce significant statistical bias, a full 3-hour simulation was conducted for the VolturnUS-S; the remaining floaters were only analysed around cut-in, rated and cut-out wind speed. The resulting AEP differed by only 0.007% compared to the 10-minute runs, confirming that the shorter simulation duration is sufficient for the purposes of this study. The full results of the 3-hour run comparison are discussed in Subsection 4.3.2.

Visual Inspection and Physical Limit Checks

In addition to the quantitative checks described above, all simulations were screened visually by inspecting time-series plots of key output channels: wave elevation, power output, rotor speed, platform motions, blade pitch and deflection and tower deflections. For the power, mean and standard deviation were plotted to check results. Furthermore, the physical limits defined in Subsection 3.2.2 were applied as automated checks to flag any load cases exhibiting unphysical behaviour. Lastly, the fixed turbine was used as baseline the spot unphysical results of the floating turbines.

3.2.4. Simulation Setup Overview

Table 3.7 summarises the updates applied to the floater models. These include changes to the turbine, aerodynamic and structural input parameters, sea-state discretisation, controller settings and the overall model configuration. The sea-state model used a reduced spatial discretisation of 5 m in both horizontal directions with default water depth to limit memory usage. The input files per floater used for the remainder of this thesis can be found in a GitHub repository [110].

Table 3.7: Summary of updated model parameters.

Variable	Unit	Value	Variable	Unit	Value
AeroDyn15			**SeaState**		
TwrShadow	-	1	X_HalfWidth	m	5
IntegrationMethod	-	3	Y_HalfWidth	m	5
Elastodyn			Z_Depth	m	Default
TipRad	m	120.97	NX	-	2
HubRad	m	3.97	NY	-	2
Overhang	m	-12.098	NZ	-	15
NacCMxn	m	-5.125	Wavemod	-	2
NacCMzn	m	4.315	WvLowCOff	rad/s	0.111527
TowerHt[a]	m	129.495	WvHiCOff	rad/s	3.2
TowerHt[b]	m	144.386	WaveSeed(1)	-	123456789
NcIMUxn	m	0.0	WaveSeed(2)	-	”RANLUX”
NcIMUzn	m	0.0	**ServoDyn**		
Twr2Shft	m	4.3495	TechNPol	-	100
NacMass	kg	644857	YawSpr	N-m/rad	6009291301.0
YawBrMass	kg	28249	YawDamp	N-m/(rad/s)	4811254.0
DTTorSpr	N-m/rad	69737644900.0	YawManRat	deg/s	0.25
DTTorDmp	N-m/(rad/s)	49418406.0	GenEff	%	95.756
IEA-15-240-RWT input folder			DLL_Ramp	-	False
ROSCO controller: VolturnUS-S version			**.fst**		
Update input folder turbine[c]			Gravity	m/s^2	9.81

[a] Tower height for the WindCrete and ActiveFloat 135 m variants.
[b] Tower height for the WindCrete 150 m variant, VolturnUS-S, Reference TLP and fixed turbine.
[c] The input folder contains airfoil data, AeroDyn15_blade.dat, BeamDyn_blade.dat, ElastoDyn_blade.dat files.

3.2.5. OpenFAST Modules and Software Setup

For automation of the OpenFAST simulation, the available Python toolbox was used to generate load cases and run the OpenFAST executable in batch mode. The simulations used the following software configuration:

- OpenFAST v4.2.0 (released January 27, 2026) [104]
- ROSCO v2.9.4 [111]
- Python toolbox for Openfast for automatisation [112]
- Python v3.14

3.3. AEP Baseline Analysis for the 15 MW Floater Concepts

This section outlines the full procedure used to analyse and compare the dynamic behaviour and power performance of the four floating platform concepts supporting the IEA 15 MW reference wind turbine. All simulations are performed with a fixed time step of 0.0125 s, consistent with recommended values in existing OpenFAST validation studies. Steady, turbulence-free wind is applied from a single direction, unless stated otherwise. This approach follows insights from Karimirad and Moan [113], who demonstrate that mean power in floating systems remains unaffected by turbulence versus constant wind; turbulence in the wind would only increase power fluctuations below rated wind speed.

3.3.1. Free Decay Tests

Free decay simulations are performed to identify the natural frequencies and damping characteristics of each platform in all six rigid-body DOFs. Wave excitation is disabled and the AeroDyn module is turned off to isolate hydrodynamic restoring and mooring forces. For each degree of freedom, the platform is displaced from its equilibrium position by a prescribed initial displacement and then released. Four initial displacement magnitudes are applied per degree of freedom, as listed in Table 3.8. The different initial displacements are applied to verify consistency and avoid artefacts caused by numerical noise or nonlinearities. Each simulation is run for approximately five times the expected natural period of the corresponding DOF, based on literature values, to ensure sufficient decay while limiting computational cost.

The natural period is determined from the time between successive peaks in the response signal. Peak identification is manually verified to avoid misinterpretation due to numerical noise. The damping ratio is extracted by fitting the free decay response to an exponentially decaying harmonic model:

$$x(t) = x_0 + Ae^{-\zeta\omega_n t}\sin\left(\omega_d t + \phi\right), \tag{3.2}$$

where A is the amplitude, ζ is the damping ratio, ω_n is the natural frequency, $\omega_d = \omega_n\sqrt{1-\zeta^2}$ is the damped natural frequency, ϕ is the phase and x_0 is the offset. The unknown parameters are identified using nonlinear least-squares optimisation.

Damping characteristics may vary with the initial displacement amplitude, as reported for the VolturnUS-S platform [33]. Therefore, the range of initial displacements is used to evaluate amplitude-dependent damping behaviour for each DOF. The quality of the curve fit is assessed through visual comparison with the original time-domain signal. Figure 4.3 shows an example of such a curve fit to a decaying signal.

Table 3.8: Initial displacements and simulation durations used for the free decay tests per degree of freedom.

DOF	Unit	Initial displacement				Simulation duration [s]
Surge (1)	**[m]**	7.5	15.0	22.5	30.0	750
Sway (2)	**[m]**	7.5	15.0	22.5	30.0	750
Heave (3)	**[m]**	1.25	2.50	3.75	5.00	150
Roll (4)	**[deg]**	2.5	5.0	7.5	10.0	150
Pitch (5)	**[deg]**	2.5	5.0	7.5	10.0	150
Yaw (6)	**[deg]**	5.0	10.0	15.0	-	500

3.3.2. Representative Load Case Determination

For each discrete wind speed, an initial “no-wave” simulation is first carried out. These runs used wind without shear and prescribed rotational speed and blade-pitch values from the IEA 15 MW definition report to avoid unrealistic transient start-up behaviour. Each initial-condition simulation ran for 600s of which the first 300s are discarded to remove transient behaviour. The mean values over the remaining 300s (tower and blade deflection, rotor speed, blade pitch and platform offsets) are extracted and used as the initial state for all subsequent wave-inclusive simulations to reduce the computational load.

Each wind-and-wave simulation ran for a total of 900 s as discussed in Subsection 2.2.4. The first 300 s were discarded to eliminate transient effects caused by wave introduction and the final 600 s (10 minutes) were used for the analysis of the mean power production, standard deviation of power and platform motions.

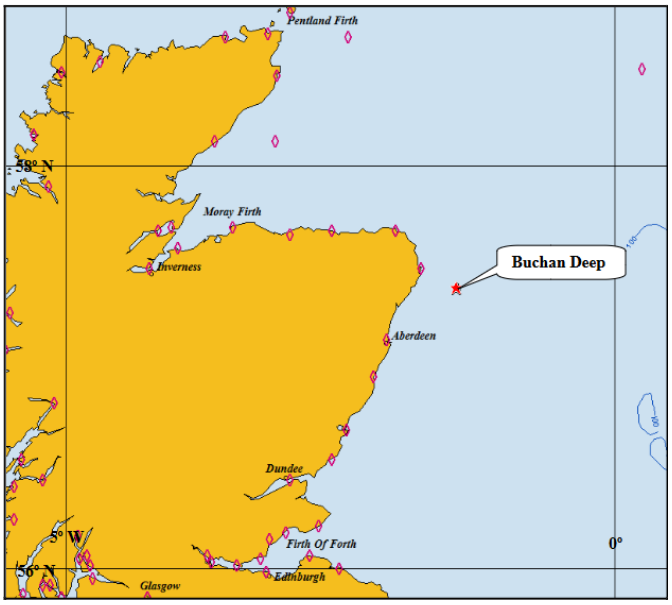

Figure 3.15: Map showing position of Hywind Scotland floating wind farm site at Buchan Deep, northeast of Aberdeen (Scotland) [35].

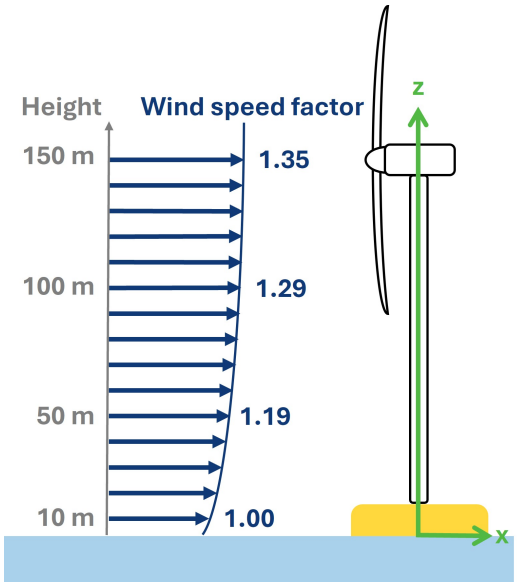

Figure 3.16: Wind speed factor at different height for a shear factor $\alpha = 0.11$.

Wind and wave statistics are derived from the Buchan Deep region, northeast of Scotland in the North Sea. This area hosts the Hywind Scotland floating wind farm and its location is shown in Figure 3.15. The long-term wind data is generated by the Nora10 hindcast model operated by the Norwegian Meteorological Institute based on data from 1958 to 2010 [35]. The wind speed occurrence is determined using a Weibull distribution at a 10 m height with values. The Weibull plot uses a shape factor of 2.235, a scale factor of 10.03 and a location factor of 0.0. Figure 3.19 shows the Weibull plot based on these parameters.

The input wind speed was assumed to be steady (no turbulence) and was extrapolated to different heights with Equation 2.2. A shear exponent of α = 0.11 aligns well with the height-dependent variation observed in the dataset and values found in literature. The value was used for all simulations with wind shear included. Figure 3.16 illustrates the wind speed factor to scale the wind speed to different heights for heights between 10 m (measurement height) and 150 m (hub height).

Wave conditions were selected using coupled wind-wave scatter information from the Hywind dataset. To model irregular waves, the JONSWAP wave spectrum (limited fetch at the North Sea) was selected. Due to the limited influence of the wave height and period, for simplicity and to reduce computational burden, one representative significant wave height H_s and peak period T_p are used per wind speed. A sensitivity analysis for multiple wave heights is performed separately (see Subsection 3.4.3). The wind speed was recalculated to a 100 m height in order to be able to calculate the H_s with the use of the empirical equation in Figure 3.18. A corresponding peak period is derived using ’mean’ line of the empirical in Figure 3.18. The final step in the simulation setup involved discretising the wind speed distribution in wind speed bins as shown in Figure 3.19. Simulations were conducted from 1.0 m/s below the cut-in wind speed to 1.0 m/s above the cut-out wind speed to make sure the operational range was fully simulated. Within this range, the mean wind speed of each bin was used as the simulation input. Next to the limits discussed in Table 3.5, simulations which generated less than 0.5% of rated power (P < 75 kW for the 15 MW turbine)

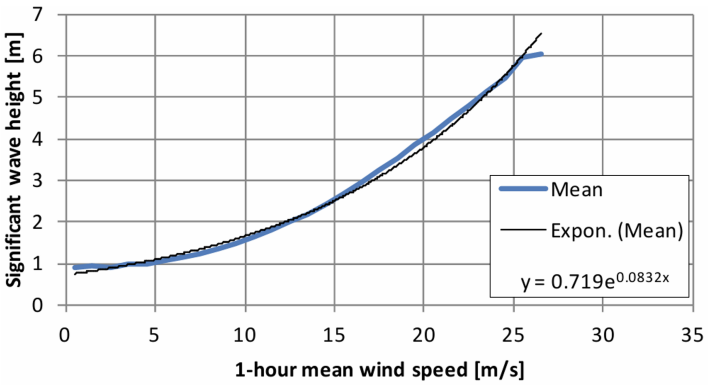

Figure 3.17: Significant wave height H_s as a function of 1-hour mean wind speed at 100 m above sea level at Buchan Deep. The black line shows an exponential function fit to the data [35].

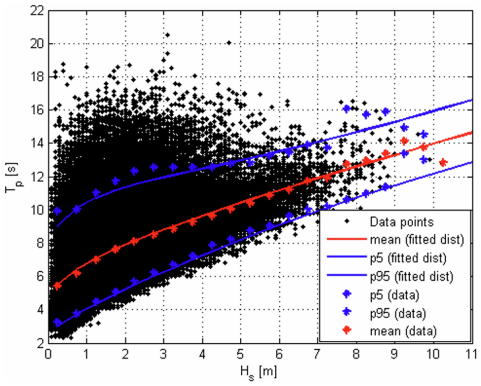

Figure 3.18: Spectral peak period T_p for given significant wave height H_s at Buchan Deep [35].

were excluded. An overview of the operational conditions and occurrence frequency per wind speed bin is provided in Table 3.9, with full details of the bin boundaries and wind speeds at different hub heights given in Table B.1 in the Appendix. The discretised PDF sums to 0.9998 rather than 1.00, as the infinite upper tail of the Weibull distribution extends far beyond the cut-out wind speed. This 0.02% (= 2 hrs) falls outside the operational range and does not affect the results.

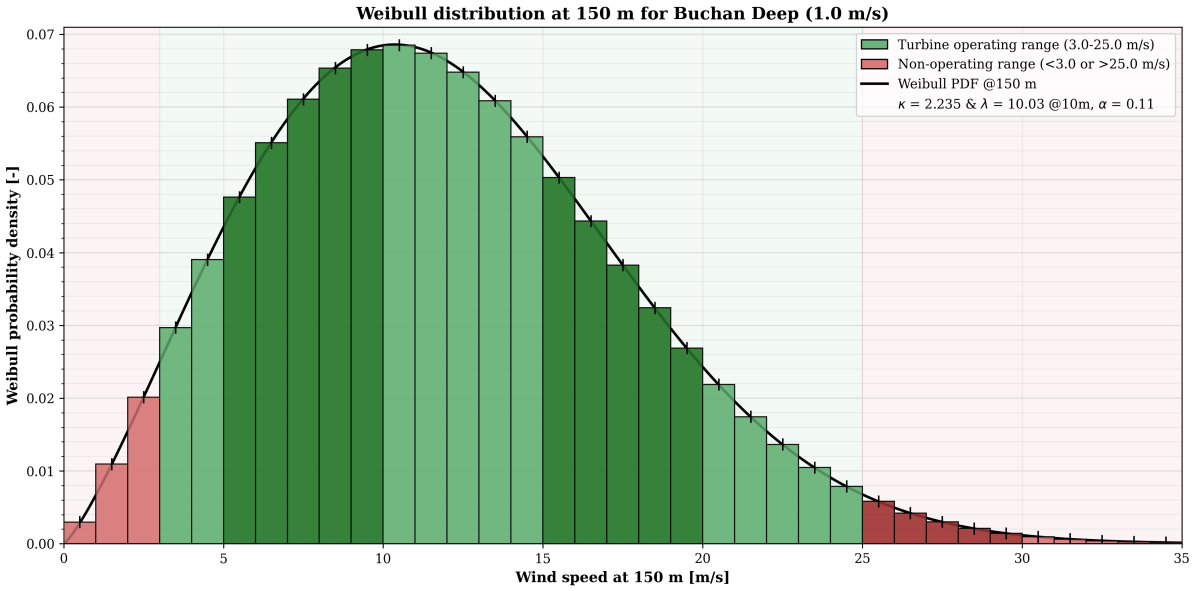

Figure 3.19: Weibull distribution at 150 m height at Buchan Deep. The distribution is defined by shape parameter $\kappa = 2.235$ and scale parameter $\lambda = 10.03m/s$, both specified at 10 m height. Wind speeds are extrapolated to 150 m using the power law with a shear exponent $\alpha = 0.11$. A default bin size of 1.0 m/s is applied. Shading intervals change every 5 m/s for improved visual clarity. An enlarged figure can be found in Figure B.1 and the detailed data for the figure can be found in Table B.1.

3.3.3. Comparative Analysis with Baseline Scenario: a Fixed Turbine

To isolate platform-induced dynamic effects, each floating turbine's performance is compared against a fixed, rigidly mounted version of the IEA 15 MW reference turbine. The tower base is fully constrained in all six DOFs with wave excitation disabled. While this is not physically representative of bottom-fixed offshore turbines, this configuration provides the clearest baseline for evaluating the aerodynamic performance differences and motion-induced power variability.

A direct bottom-fixed comparison is not feasible, as it would require relocating all floaters to a shallow-water site (50-60 m depth, current depth limit for bottom-fixed turbines). In this area, only the semisubmersible could operate with a redesigned mooring system. While floating turbines theoretically access superior deep-water wind resources inaccessible to bottom-fixed concepts (see Subsection 2.3.3), this study uses the rigid baseline as the closest practical analogue at the 200 m deep Buchan Deep site. This approach maintains metocean consistency across all platforms while isolating platform motion effects.

Table 3.9: Wind speed bins and environmental conditions for simulations at Buchan Deep (150 m Weibull distribution shown in Figure 3.19). The default binning is 1.0 m/s. The row shading changes every 5 m/s for clarity. A more comprehensive overview of bin boundaries, wind speed at different heights, bin occurrence and operational conditions is provided in Table B.1.

150 m height			Significant	Spectral	PDF [-]	Operational	
Lower limit [m/s]	Upper limit [m/s]	Wind speed [m/s]	wave height [m]	peak period [s]		time [hrs]	envelope
0.0	1.0	0.5	0.75	6.66	0.0030	26	FALSE
1.0	2.0	1.5	0.81	6.72	0.0109	96	FALSE
2.0	3.0	2.5	0.88	6.78	0.0201	176	TRUE
3.0	4.0	3.5	0.95	6.85	0.0297	260	TRUE
4.0	5.0	4.5	1.03	6.93	0.0390	342	TRUE
5.0	6.0	5.5	1.11	7.01	0.0476	417	TRUE
6.0	7.0	6.5	1.21	7.09	0.0551	483	TRUE
7.0	8.0	7.5	1.31	7.19	0.0611	535	TRUE
8.0	9.0	8.5	1.41	7.29	0.0654	573	TRUE
9.0	10.0	9.5	1.53	7.40	0.0679	594	TRUE
10.0	11.0	10.5	1.66	7.52	0.0685	600	TRUE
11.0	12.0	11.5	1.80	7.64	0.0674	591	TRUE
12.0	13.0	12.5	1.94	7.78	0.0648	568	TRUE
13.0	14.0	13.5	2.10	7.93	0.0609	533	TRUE
14.0	15.0	14.5	2.28	8.08	0.0559	490	TRUE
15.0	16.0	15.5	2.47	8.25	0.0503	441	TRUE
16.0	17.0	16.5	2.67	8.44	0.0443	388	TRUE
17.0	18.0	17.5	2.89	8.63	0.0383	335	TRUE
18.0	19.0	18.5	3.13	8.84	0.0324	284	TRUE
19.0	20.0	19.5	3.39	9.07	0.0269	236	TRUE
20.0	21.0	20.5	3.67	9.31	0.0219	192	TRUE
21.0	22.0	21.5	3.98	9.57	0.0174	153	TRUE
22.0	23.0	22.5	4.31	9.84	0.0136	120	TRUE
23.0	24.0	23.5	4.66	10.13	0.0105	92	TRUE
24.0	25.0	24.5	5.05	10.45	0.0079	69	TRUE
25.0	26.0	25.5	5.47	10.78	0.0058	51	TRUE
26.0	27.0	26.5	5.92	11.13	0.0042	37	FALSE
27.0	28.0	27.5	6.41	11.50	0.0030	26	FALSE
28.0	29.0	28.5	6.94	11.90	0.0021	18	FALSE
29.0	30.0	29.5	7.52	12.31	0.0014	12	FALSE
30.0	31.0	30.5	8.14	12.75	0.0010	8	FALSE
31.0	32.0	31.5	8.82	13.21	0.0006	5	FALSE
32.0	33.0	32.5	9.55	13.68	0.0004	4	FALSE
33.0	34.0	33.5	10.34	14.18	0.0003	2	FALSE
34.0	35.0	34.5	11.19	14.69	0.0002	1	FALSE
				Total:	0.9998	8758	-

3.3.4. Annual Energy Production and Power Fluctuations

Annual energy production is calculated by multiplying the mean power output $\overline{P}_i$ from each wind speed bin i with its corresponding occurrence probability O_i and the hours in a year (8760 hr) following the method in Subsection 2.1.8.

$$\text{AEP} = 8760 \sum_i \overline{P}_i \cdot O_i \quad [\text{kWh}] \tag{3.3}$$

Platform motion induces power fluctuations quantified by the coefficient of variation (CoV). Power variability is a critical metric for two reasons: it affects grid stability, as rapid fluctuations challenge frequency regulation and may require costly balancing measures. Furthermore, it does serve as a measure for structural fatigue loading as oscillating aerodynamic and drivetrain forces associated with power swings accumulate cyclic stress on the rotor, shaft and tower. The CoV is quantified by the following equation:

$$\text{CoV}_i = \frac{\sigma_{P_i}}{\overline{P}_i} \tag{3.4}$$

where σ_{P_i} is the standard deviation in bin i (600 s analysis period, conditional on active power production). The total CoV across the wind distribution is weighted by each bin's AEP contribution:

$$\text{CoV}_{\text{total}} = \sum_i \frac{\sigma_{P_i}}{\overline{P}_i} \cdot \frac{\overline{P}_i \cdot O_i}{\sum_i (\overline{P}_i \cdot O_i)} \tag{3.5}$$

This ensures the aggregate metric reflects operational reality, with high-power bins (near rated) dominating total variability. Load cases below 0.5% of rated power ($P < 75$ kW for the 15 MW turbine) are excluded. Startup transients at low wind speeds produce unrealistically high relative fluctuations unrelated to steady-state platform dynamics.

3.4. Sensitivity Analyses for the 15MW Floater Concepts

Sensitivity analyses systematically vary key parameters to assess their impact on floater performance at the representative wind speed of 9.5 m/s (detailed in Subsection 3.4.1). The following subsections describe the parameters, simulation procedures and conditions used in the analyses. The baseline case assumes aligned wind and wave directions ($0°$) and is characterised by a significant wave height of $H_s = 1.53$ m and a peak period of $T_p = 7.40$ s. Unless otherwise specified, all parameters maintain baseline conditions. An overview of all parameters per sensitivity analysis is given in Table 3.12.

3.4.1. Selected Wind Speed for Sensitivity Analyses

A wind speed of 9.5 m/s at hub heigt is selected for the sensitivity analyses as it is found to be representative for several reasons:

- The wind speed lies below the rated wind speed where the turbine operates at peak aerodynamic efficiency and power scales quadratically. Both amplify sensitivity to wind variations.
- The wind speed coincides with the site's peak Weibull distribution frequency (see Figure 3.19). This maximises its influence on annual energy production.
- The wind speed falls within the ROSCO Individual Pitch Control ramp-up range of 8.592-10.74 m/s. As the controller gradually activates the Individual Pitch Control, it prevents abrupt control transitions and load spikes during partial-to-full loading.

As this region exhibits strong sensitivity to platform-aerodynamic interactions and control system behaviour, it is ideal for comparing floating support structure performance. While cut-in and cut-out conditions may show pronounced platform motions, their limited contribution to annual energy production renders them less critical for the AEP.

3.4.2. Sensitivity Analysis: Wind Speed Bins Size

To quantify the accuracy of the AEP calculation, a finer bin resolution (e.g., 0.5 or 0.25 m/s) has been applied between cut-in (3 m/s) and rated wind speed (10.59 m/s) and around the cut-out wind speed (25 m/s). A comprehensive overview of bin boundaries, wind speed at different heights, bin occurrence and operational conditions is provided in Appendix B, with both a Weibull plot and an overview table for each wind speed bin sizing.

3.4.3. Sensitivity Analysis: Wave Height and Period

For the selected wind speed of 9.5 m/s at hub height (corresponding to 9.09 m/s at 100 m and 7.04 m/s at 10 m), significant wave heights of 0 to 5 m occur as shown in Table 3.10. This table presents filtered data from the full wind-wave data at Buchan Deep found in Appendix A.

Table 3.10: Joint occurrence probabilities of significant wave height (H_s) bins and wind speeds at 100 m for the Buchan Deep. Data extracted from the full scatter Table A.1. Values indicate percentage occurrence of each H_s bin for the given wind speed, with total wind speed occurrence shown in the final column.

	H_s [m]						Occurence
Ws @100 m	**0-1**	**1-2**	**2-3**	**3-4**	**4-5**	**5-6**	**windspeed**
8.5 m/s	27.47%	58.72%	12.60%	1.14%	0.07%	0.00%	7.55%
9.5 m/s	16.15%	66.63%	14.92%	2.12%	0.18%	0.00%	7.50%

Wave-height bins are defined based on occurrence frequency: finer resolution of 0.5 m steps for frequent low waves (0-3 m) and coarser 1 m steps for rarer high waves (3-5 m). For each H_s, three peak periods (T_p) are tested (5th percentile (P5), mean and 95th percentile (P95)) with statistics provided in Table 3.11. Each floater concept is simulated for the complete set of 24 sea states; each simulation with the same initial conditions.

Table 3.11: Peak period (T_p) statistics for each significant wave height (H_s) bin at 9.5 m/s wind speed. Columns show 5th percentile (P5), mean and 95th percentile (P95) T_p values derived from the H_s-T_p scatter distribution (Figure 3.18).

	T_p [s]		
H_s [m]	**P5**	**Mean**	**P95**
0.5	3.55	6.42	10.36
1.0	4.12	6.90	10.65
1.5	4.67	7.37	10.93
2.0	5.22	7.83	11.22
2.5	5.75	8.28	11.50
3.0	6.26	8.73	11.79
4.0	7.26	9.58	12.37
5.0	8.21	10.41	12.95
1.53	-	**7.40**	-

3.4.4. Sensitivity Analysis: Mooring Stiffness

Mooring stiffness sensitivity analyses are conducted by scaling the baseline mooring stiffness values from Table 3.2 by factors of 0.25, 0.50, 0.75, 1.00, 1.25, 1.50, 1.75 and 2.00. Two distinct simulation types isolate the mooring effects:

- **Free decay tests** (Subsection 3.3.1) established natural periods and damping ratios across all DOFs per mooring stiffness.
- **Power generation simulations** quantified the operational performance.

For the power generation simulations, only aerodynamic and structural initial conditions (rotor speed, tower deflections and blade deformations) are taken from baseline runs. The platform is initialised at zero offset displacement to isolate mooring-restoring force effects. In order to fully remove the transient behaviour of the simulation, they are extended to 1200 s and only the last 600 seconds are analysed.

3.4.5. Sensitivity Analysis: Wind-Wave Misalignment

Wind-wave misalignment was assessed by independently rotating wind and wave directions in 15 ° increments up to 60 ° with respect to the platform orientation as can be seen in Figure 3.20. The platform motion limits and nacelle were rotated to the same angle to match the wind direction. With the nacelle yaw DOF disabled (`YawDOF = False`), as previously described, the nacelle remains fixed relative to the platform throughout all simulations. The wave direction (`WaveDir` - SeaState) and nacelle yaw (`NacYaw` - ElastoDyn) are equal but opposite in sign compared to incoming wind (`PropagationDir` - InflowWind) due to a difference in sign convention. Only aerodynamic and structural DOF initial conditions (rotor speed, tower deflections and blade deformations) are taken from baseline runs. The platform is initialised at zero offset displacement to isolate mooring restoring force effects and the simulations are extended to 1200 s to take the transient behaviour in account.

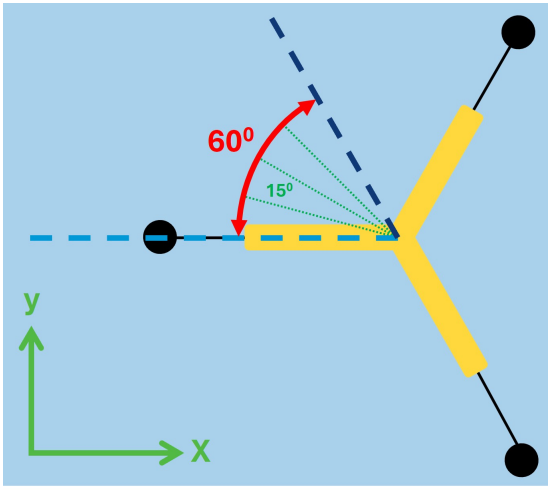

Figure 3.20: Overview of the wind-wave misalignment used for the sensitivity check. The wind and waves are rotated in steps of 15° up to a 60° angle. For the wind direction (`PropagationDir`) a clockwise rotation is positive. For the nacelle yaw (`NacYaw`) and wave direction (`WaveDir`), a counter-clockwise rotation is positive.

Testing all wind-wave combinations up to 60° wind misalignment captures the full 360° directional response of the floater as they are all 120°-axis symmetric. The 60° case positions one mooring line and platform leg downwind (vs. upwind in baseline) to reveal distinct hydrodynamic and restoring responses for the floater orientation. For the VolturnUS-S, second-order WAMIT effects are excluded due to unavailable data for rotated wave directions.

3.4.6. Baseline and Sensitivity Analyses Overview

To give an overview of the simulation setup described throughout this chapter, Table 3.12 provides a structured overview of the external parameters used across the AEP baseline analysis and the four sensitivity analyses. The AEP baseline analysis sweeps the full operational wind speed range from cut-in to cut-out, with representative wave conditions derived empirically from the Buchan Deep metocean dataset. Each sensitivity analysis isolates a single parameter while keeping all others at baseline values. This allows its individual effect on floater performance to be assessed independently. The selected wind speed of 9.5 m/s is used across all sensitivity cases for the reasons outlined in Subsection 3.4.1. The results from these simulations are presented Chapter 4 and discussed in Chapter 5.

Table 3.12: Overview of load cases for the main baseline run and sensitivity analyses. Mooring stiffness is expressed as a multiplier of the baseline values from Table 2.2.

	AEP	**Sensitivity analyses**			
Parameter	**baseline analysis**	**Wind speed bin size**	**Wave height & period**	**Mooring stiffness**	**Wind-wave misalignment**
Wind speed [m/s]	3-25 (1 m/s bins)	Bin size: 0.25/0.5m/s	9.5	9.5	9.5
Wind direc. [deg]	0	0	0	0	0, 15, 30, 45, 60
Wind shear [-]	0.11	0.11	0.11	0.11	0.11
Wave height H_s [m]	Empirical (Fig. 3.17)	Empirical (Fig. 3.17)	0 - 5 (Stepsize in Tab. 3.11)	1.53	1.53
Wave peak period T_p [s]	Empirical mean per H_s (Fig. 3.18)	Empirical mean per H_s (Fig. 3.18)	Empirical P5, mean, P95 per H_s (Fig. 3.18)	7.40	7.40
Wave direc. [deg]	0	0	0	0	0, 15, 30, 45, 60
Mooring stiffness [-]	1.00 × baseline	1.00 × baseline	1.00 × baseline	0.25-2.00 × baseline	1.00 × baseline

4

Simulation Results for Floating IEA 15 MW Wind Turbine Concepts

Following the OpenFAST modelling framework and simulation setup established in Chapter 3, this chapter presents OpenFAST simulation results for the IEA 15 MW reference wind turbine mounted on the WindCrete concrete spar, ActiveFloat and VolturnUS-s semi-submersible and Reference TLP platforms, compared against a bottom-fixed baseline turbine. Results address platform dynamics, operational motions, power production characteristics and sensitivity to environmental and modelling parameters through four main sections. The baseline performance characterisation begins with Section 4.1, which establishes inherent platform dynamics through free decay tests across all degrees of freedom. Following, Section 4.2 quantifies six-DOF responses under representative wind and wave loading. Section 4.3 then integrates these dynamics into turbine performance metrics: power curves, production variability and AEP comparisons. Finally, Section 4.4 systematically evaluates robustness through bin sizing, wave influence, mooring stiffness and wind-wave misalignment effects. These results establish the foundation for the interpretation and platform comparison presented in Chapter 5.

For consistent visualisation across all comparisons, a standardised colour scheme is applied. Figure 4.1 shows the floater-specific colours and markers used when comparing the several floaters and the fixed baseline case. When analysing individual floater performance, such as degrees of freedom (DOF), power output, or coefficient of variation, the base floater colour is combined with parameter-specific shading patterns shown in Figure 4.2.

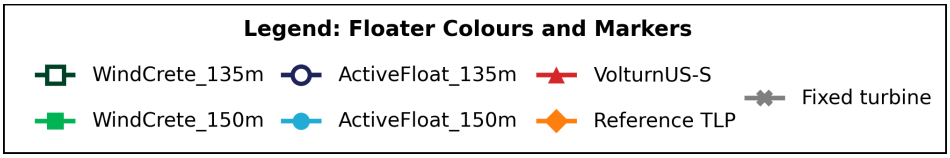

Figure 4.1: Colour and marker conventions for platform comparisons. WindCrete_135m/_150m (dark / light green), ActiveFloat_135m/_150m (dark / light blue), VolturnUS-S (red), Reference TLP (orange) and fixed baseline (grey).

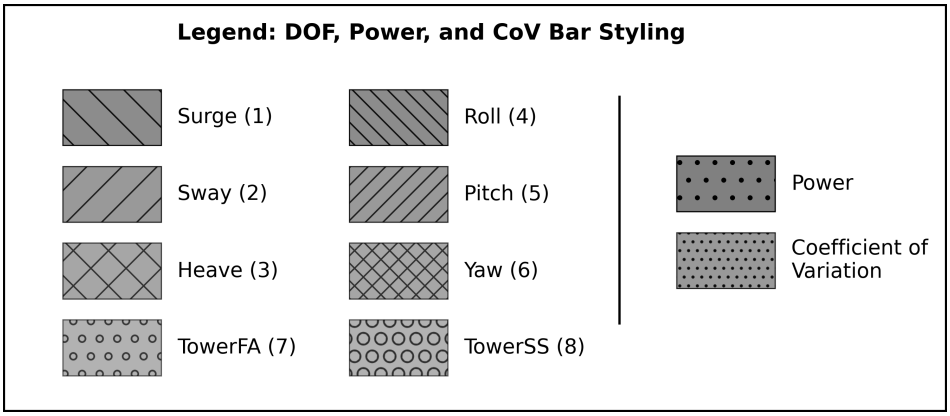

Figure 4.2: Shading patterns for degrees of freedom (DOF), power output (P) and coefficient of variation (CoV) when analysing individual platform performance.

4.1. Natural Periods and Damping Characteristics

This section presents free decay test results establishing natural periods and damping ratios for all six degrees of freedom (surge, sway, heave, roll, pitch, yaw) for all floating platforms. The results were derived using the methodology described in Subsection 3.3.1. An example of the curve-fitting procedure used to extract the natural period and damping ratio is shown in Figure 4.3.

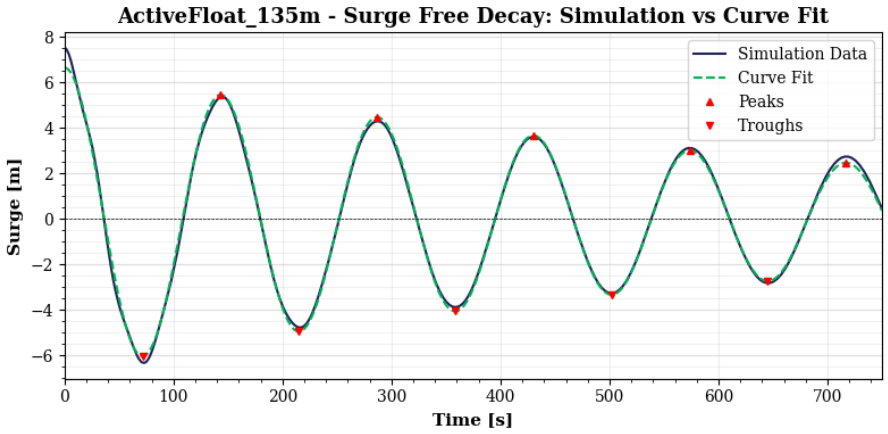

Figure 4.3: Example of the curve-fitting used to determine the natural period and damping ratio from a free-decay test response.

Natural periods per DOF are visualised in Figure 4.4 with numerical values in Table 4.1. The semi-submersibles (ActiveFloat, VolturnUS-S) show the longest surge (up to 143.3 s), sway (up to 144.3 s) and yaw periods (around 80-90 s), while the Reference TLP exhibits the shortest periods across all DOFs (e.g., heave 2.6 s, surge 37.8 s). The WindCrete has the highest roll and pitch periods at 45.6 s.

Table 4.1: Natural periods of the floaters per degree of freedom. Values not reported in the literature are marked with '-'.

	Natural period [s] (thesis result / literature)					
DOF	**WindCrete 135m**	**WindCrete 150m**	**ActiveFloat 135m**	**ActiveFloat 150m**	**Volturn-US-S**	**Reference TLP**
Surge (1)	76.3 / 81.9	78.8 / -	143.3 / 163.9	143.6 / -	137.3 / 142.9	37.8 / 37.7
Sway (2)	76.1 / -	78.8 / -	143.9 / -	144.3 / -	137.7 / 142.9	37.8 / -
Heave (3)	33.9 / 32.77	34.0 / -	18.4 / 18.2	18.5 / -	20.7 / 20.4	2.6 / 2.7
Roll (4)	41.3 / 40.97	45.6 / -	29.8 / 32.7	33.7 / -	28.9 / 27.8	4.1 / -
Pitch (5)	41.2 / -	45.6 / -	29.9 / -	33.8 / -	28.9 / 27.8	4.2 / 4.0
Yaw (6)	11.2 / 10.92	11.6 / -	82.6 / 81.9	82.8 / -	90.8 / 90.9	22.6 / 22.7

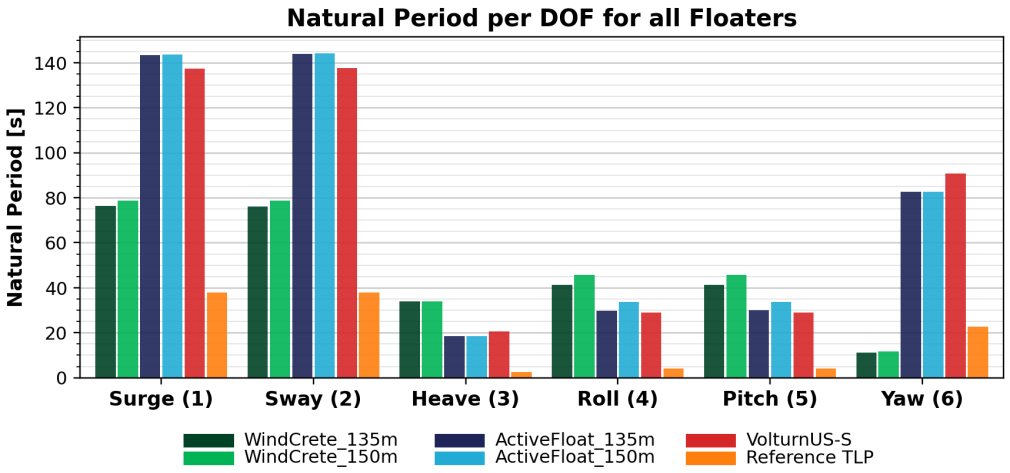

Figure 4.4: Natural periods per degree of freedom for all platforms from free decay tests. Full data: Table 4.1.

Damping ratios derived from curve-fit analyses for a single initial displacement are reported in Table 4.2. As the damping ratio depends on the initial displacement amplitude, the dataset for multiple initial displacements is provided in Table C.1. Figure 4.5 shows the surge and pitch damping ratio for multiple initial displacements (overview for all DOF given in Figure C.1).

Surge damping is found to be comparable for WindCrete and ActiveFloat, whereas VolturnUS-S exhibits the highest surge damping at low initial displacements. WindCrete shows the highest yaw damping ratio, reaching a value of 0.178. All floating platforms demonstrate lower pitch damping than the reference TLP, which displays a rapid increase in both roll and pitch damping. However, accurate determination of TLP roll and pitch damping ratios is challenging due to pronounced signal noise at the start of the simulations, smaller oscillations superimposed on the primary response and a rapid initial decay followed by persistent residual oscillations beyond 40-60 cycles in the time-series data. In contrast, damping decay is consistently identifiable for the remaining DOFs of the TLP and for all DOFs of the other floaters.

The summary in Table 4.2 facilitates floater-to-floater comparisons, while comparisons between DOFs are better assessed using the damping ratios for multiple initial displacements Table C.1 and Figure C.1. Together with the natural periods, these damping characteristics define the dynamic baseline for the operational response simulations presented in Section 4.2.

Table 4.2: Damping ratio for each floater per degree of freedom for a single initial displacement. The data for all initial displacements can be found in Table C.1.

		Damping ratio [-]					
DOF	**Initial disp.**	**WindCrete 135m**	**WindCrete 150m**	**ActiveFloat 135m**	**ActiveFloat 150m**	**Volturn-US-S**	**Reference TLP**
Surge (1)	**7.5 m**	0.030	0.032	0.031	0.032	0.052	0.036
Sway (2)	**7.5 m**	0.028	0.031	0.032	0.032	0.053	0.036
Heave (3)	**5.0 m**	0.010	0.014	0.239	0.242	0.048	0.324
Roll (4)	**5.0°**	0.017	0.015	0.075	0.074	0.019	0.039
Pitch (5)	**5.0°**	0.017	0.015	0.081	0.080	0.022	0.377
Yaw (6)	**10.0°**	0.178	0.178	0.028	0.028	0.069	0.077

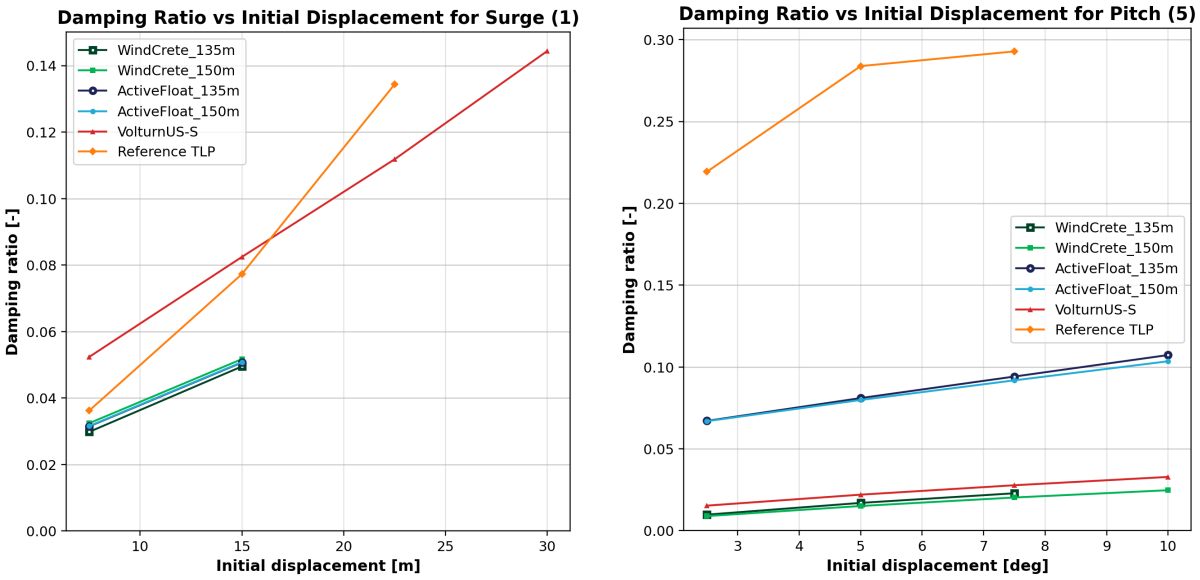

(a) Surge (1)

(b) Pitch (5)

Figure 4.5: Damping ratios as a function of initial displacement for (a) surge and (b) pitch across all platforms. The corresponding damping ratios for all degrees of freedom and all initial displacements are provided in Table C.1, while an overview of all DOFs is shown in Figure C.1.

4.2. Platform Motions under Operational Conditions

This section presents the platform motion response under the full operational wind speed range. Platform motions are evaluated using the mean response and corresponding standard deviation, providing a compact representation of both the average behaviour and variability induced by changing wind conditions. The analysed degrees of freedom include surge, sway, heave, roll, pitch, yaw and tower fore-aft and side-side displacement. While summary plots are shown for surge and pitch, Appendix D provides the complete set of statistics for all DOFs and wind speed bins.

Figure 4.6 illustrates the post-processing approach applied to all time-domain simulations, using the VolturnUS-S surge response at a wind speed of 7.5 m/s as an example. Each simulation is initialised with a transient period (300 s) that is excluded from the statistical analysis; only the steady-state portion of the signal is retained. The mean and standard deviation are then computed from this steady-state segment and are used throughout this section to characterise platform response. This procedure is applied consistently across all platforms, wind speed bins and sea states.

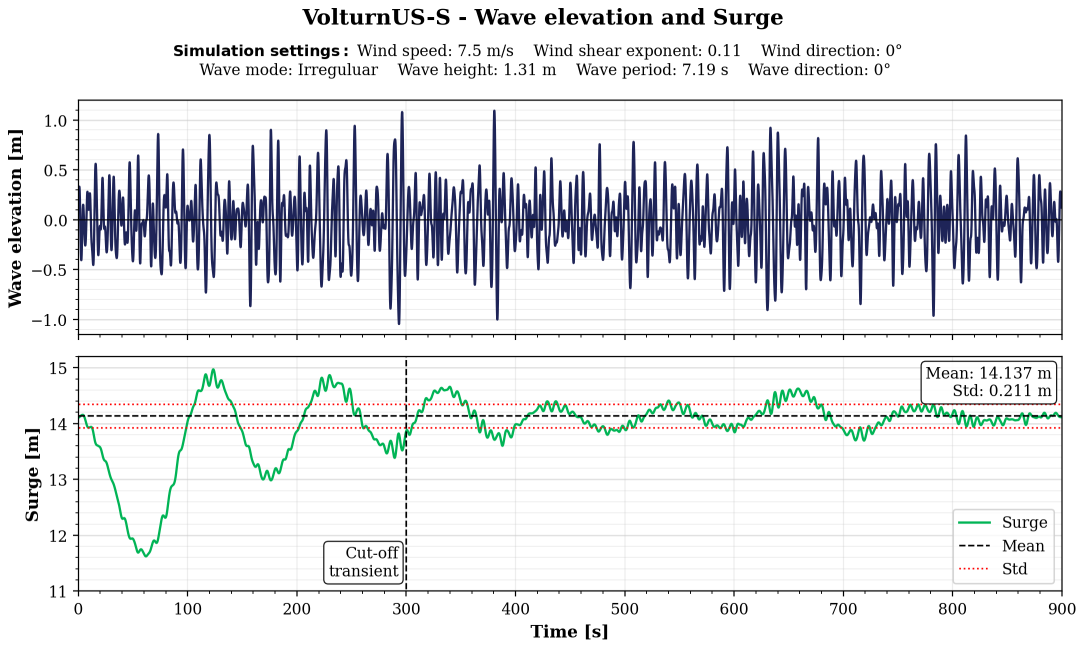

Figure 4.6: Example time-domain trace of wave elevation and surge motion for the VolturnUS-S at a wind speed of 7.5 m/s. The cut-off moment, mean and standard deviation are indicated in the figure.

Figures 4.7-4.11 show the mean platform motions in surge and pitch together with the corresponding standard deviations across all operational wind speeds. Translational surge motions and rotational pitch motions dominate the operational response envelope, while sway, heave, roll and yaw remain comparatively small for all floating platforms. The fixed reference structure exhibits zero platform motions in all translational and rotational DOFs. Tower fore-aft and side-side displacements for the fixed turbine remain within approximately ±0.4 m and ±0.15 m, respectively.

Around cut-in wind speed, all floating platforms show near-zero mean surge and pitch responses. For some configurations, slightly negative mean values are observed. As wind speed increases, all floaters exhibit increasing mean surge and pitch motions and reach maximum values around rated wind speed. Beyond rated conditions, both mean surge and pitch motions decrease and subsequently level off. The standard deviation of the pitch motion increases after rated wind speed, indicating enhanced variability in platform pitch response under higher wind speeds.

Among the floating platforms, the VolturnUS-S exhibits the largest mean surge displacement across the operational wind speed range, whereas the TLP shows the smallest surge response. For both the WindCrete and ActiveFloat platforms, the *_135m* and *_150m* configurations exhibit very similar motion behaviour; therefore, only the *_150m* variants are shown here. Results for the corresponding *_135m* configurations are provided in the appendix (see Figure D.2 and Figure D.4). The primary differences between the *_135m* and *_150m* configurations are a slight increase in pitch motion and tower side-side displacement. Additionally, the WindCrete_150m configuration exhibits a consistently negative mean heave offset of approximately 2.5 m across the operational wind speed range.

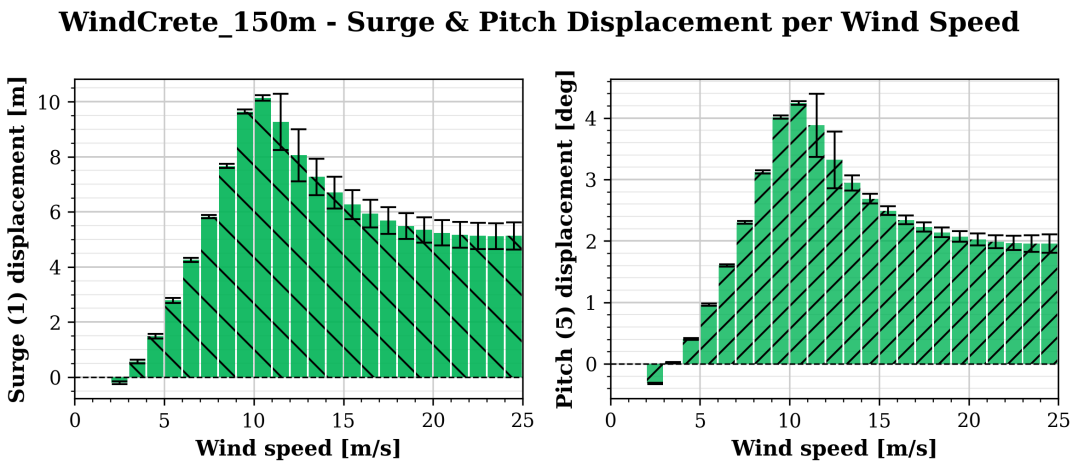

Figure 4.7: Mean platform motions and corresponding standard deviations for surge and pitch across all operational wind speeds for the WindCrete_150m. A full overview of all degrees of freedom is provided in Figure D.3.

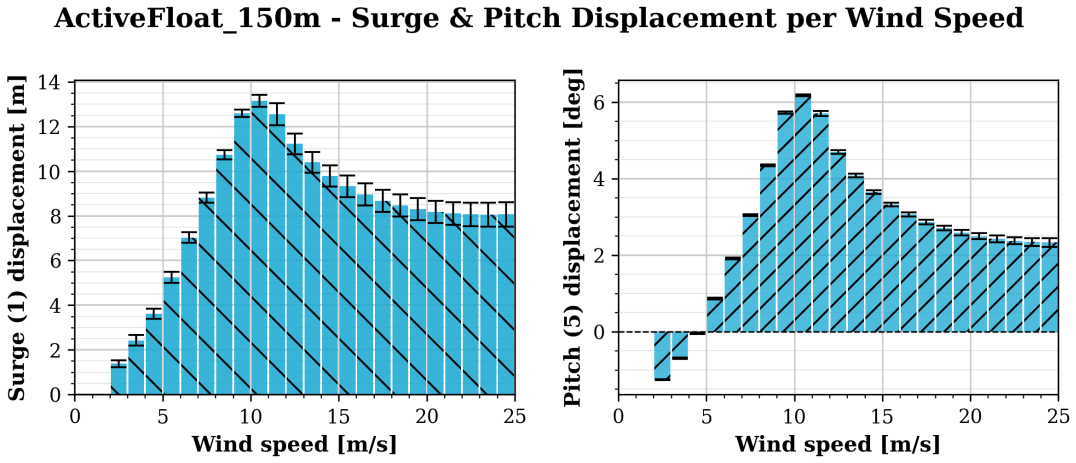

Figure 4.8: Mean platform motions and corresponding standard deviations for surge and pitch across all operational wind speeds for the ActiveFloat_150m. A full overview of all degrees of freedom is provided in Figure D.5.

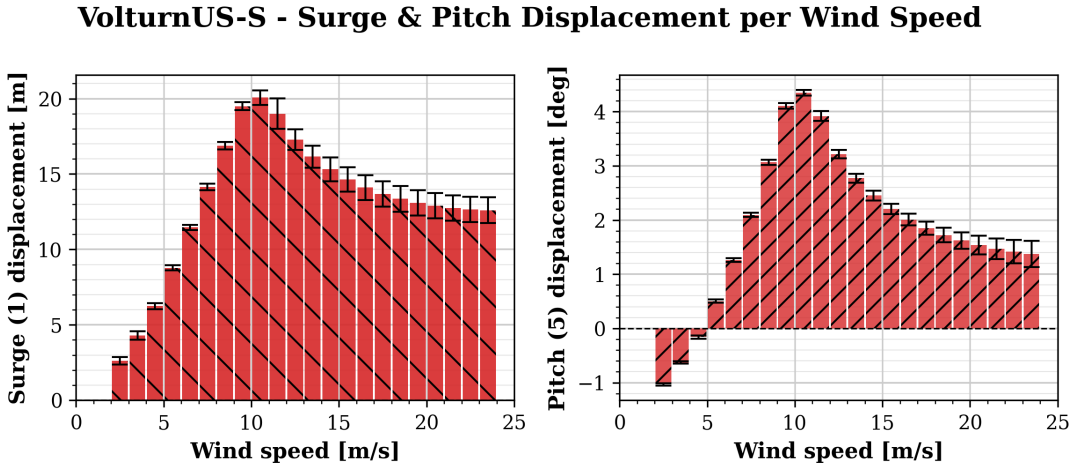

Figure 4.9: Mean platform motions and corresponding standard deviations for surge and pitch across all operational wind speeds for the VolturnUS-S. A full overview of all degrees of freedom is provided in Figure D.6.

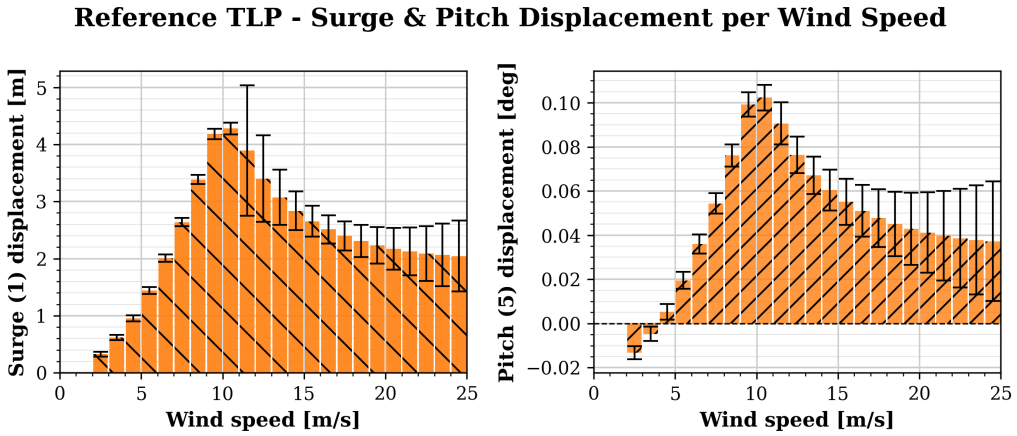

Figure 4.10: Mean platform motions and corresponding standard deviations for surge and pitch across all operational wind speeds for the Reference TLP. A full overview of all degrees of freedom is provided in Figure D.7.

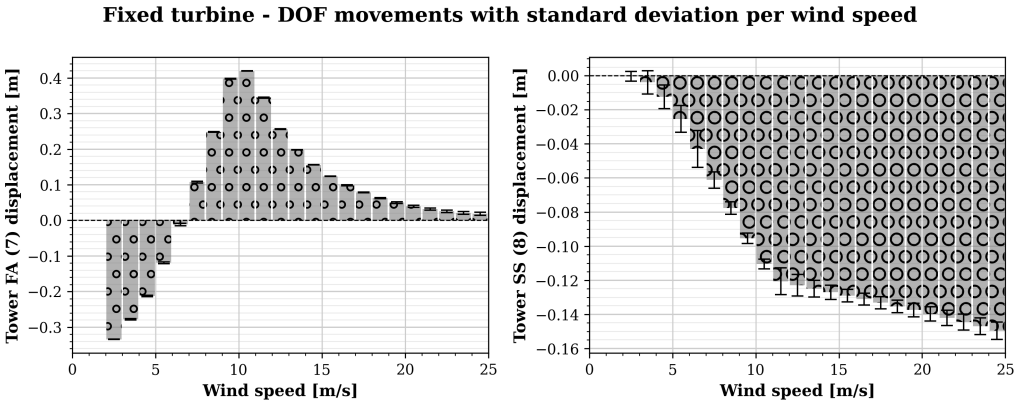

Figure 4.11: Mean tower fore-aft and side-side motions and associated standard deviations across the full operational wind speed range for the fixed reference turbine.

4.3. Power Production, Coefficient of Variation and Annual Energy Production

This section presents the power production characteristics of the floating platforms and the fixed reference turbine across the full operational wind speed range. The analysis focuses on mean power output, power variability expressed through the coefficient of variation (CoV), coefficient of performance (C_p) and the resulting annual energy production (AEP).

Figure 4.12 illustrates the post-processing approach applied to derive power statistics from the time-domain simulations, using the VolturnUS-S at 7.5 m/s as an example. Following each simulation, an initial transient period (300 s) is excluded and the mean power and standard deviation are computed from the remaining steady-state signal. The coefficient of variation is then obtained as the ratio of the standard deviation to the mean power. This procedure is applied consistently across all platforms and wind speed bins. The resulting per-bin mean power values are subsequently combined with the Weibull-distributed wind speed probabilities at the Buchan Deep site to compute the annual energy production. Table 4.3 summarises total AEP, C_p and CoV for all configurations. The fixed turbine and Reference TLP achieve the highest AEP (92.31 GWh). All other floating platforms exhibit a reduction in AEP relative to the fixed case, with total values ranging from 90.63 GWh to 91.48 GWh (<2% reduction). Among the floating concepts, the TLP shows the highest AEP and coefficient of performance ($C_p = 0.7025$), while the VolturnUS-S yields the lowest total energy production (C_p=0.6898).

Across all floating configurations, increased power variability compared to the fixed turbine is observed, as reflected by higher CoV values. The fixed reference turbine exhibits the lowest overall CoV of 0.0693%, whereas the floating platforms show CoV values between 0.38% and 1.13%. The WindCrete configurations exhibit the highest power variability, while the ActiveFloat platforms show the lowest CoV among the floating concepts.

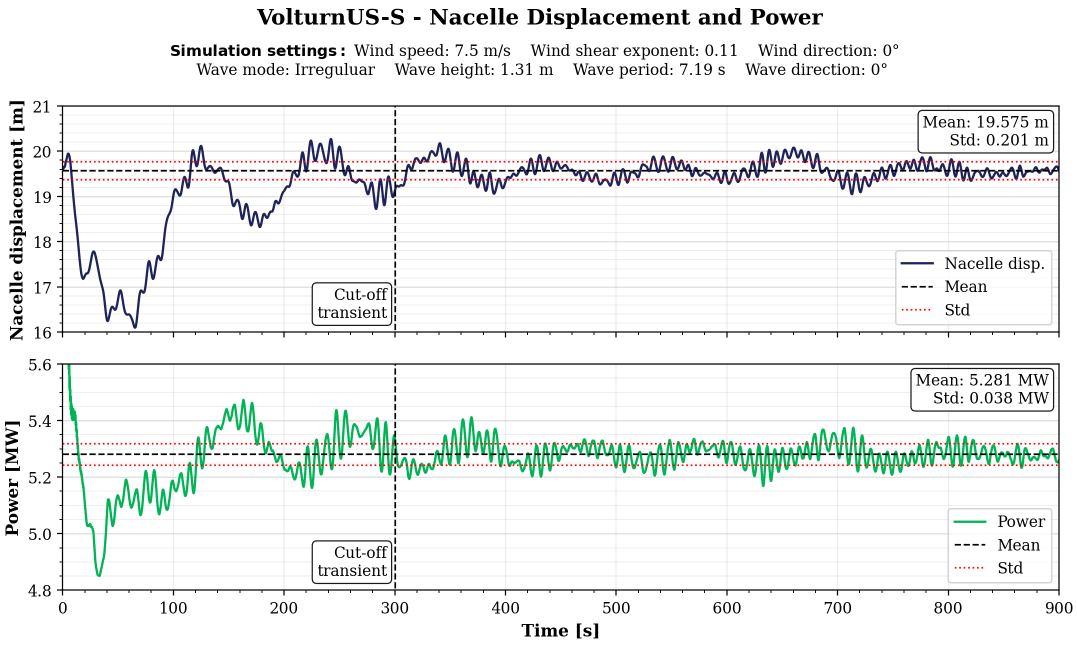

Figure 4.12: Example time-domain trace of nacelle displacement and power output for the VolturnUS-S at a wind speed of 7.5 m/s. The cut-off moment, mean and standard deviation are indicated in the figure.

Figure 4.13 presents the percentage difference in AEP relative to the fixed turbine and total CoV, highlighting inter-platform differences more clearly. All floating platforms show a modest reduction in annual energy production, generally below 2%, demonstrating that overall energy yield remains close to that of the fixed reference despite platform motion. In contrast, the increase in power variability is more pronounced.

Table 4.3: Annual energy production (AEP), coefficient of performance (C_p) and coefficient of variation (CoV) for different floaters and the fixed turbine.

	WindCrete 135m	WindCrete 150m	ActiveFloat 135m	ActiveFloat 150m	Volturn-US-S	Reference TLP	Fixed turbine
AEP [GWh]	90.94	91.48	90.79	91.31	90.63	92.31	92.31
C_p [-]	0.6921	0.6962	0.6909	0.6949	0.6898	0.7025	0.7025
CoV [-]	0.9942%	1.1256%	0.4221%	0.3835%	0.6534%	0.7745%	0.0693%

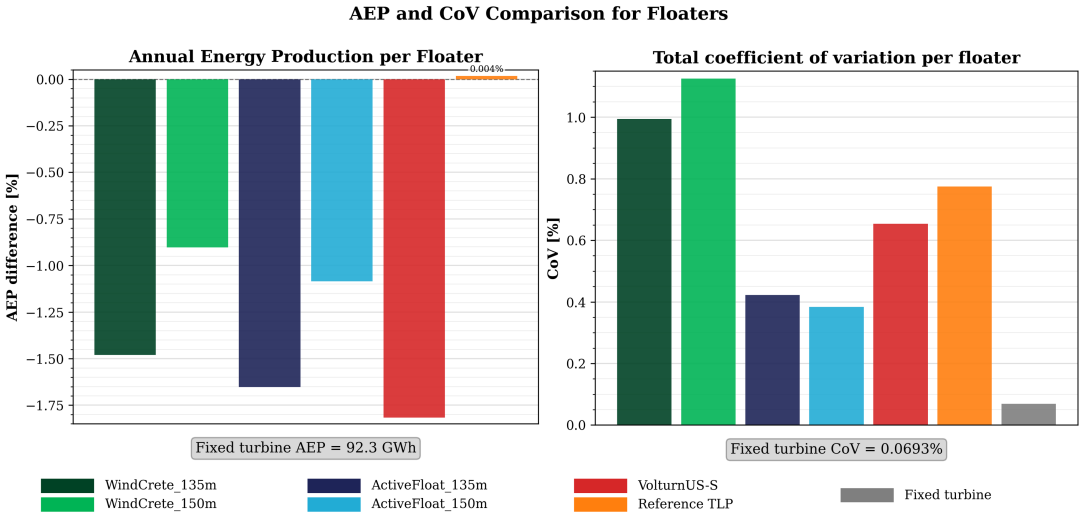

Figure 4.13: Percentage difference in annual energy production (AEP) relative to the fixed turbine and coefficient of variation (CoV) for all floating platforms.

4.3.1. Power Production Metrics per Wind Speed Bin

Detailed power production metrics per operational wind speed bin are provided in Appendix E. This includes turbine power (Table E.1), coefficient of variation (Table E.2), coefficient of performance and AEP (Table E.3) per wind speed for each platform. Figures E.1-E.7 visualise the data for each individual floater.

The power output per wind speed bin and AEP per wind speed bin for the fixed turbine are shown in Figure 4.14 and Figure 4.15. This serves as the reference against which all floating platforms are compared with. The percentage difference in AEP relative to the fixed turbine and the coefficient of variation (CoV) per wind speed bin are shown for all platforms in Figure 4.16.

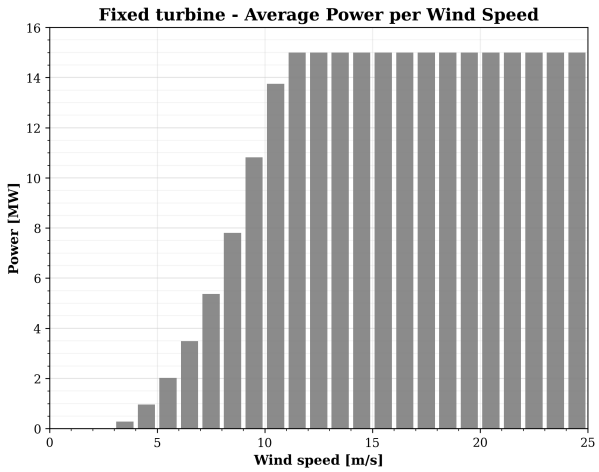

Figure 4.14: Power per wind speed bin for the fixed turbine.

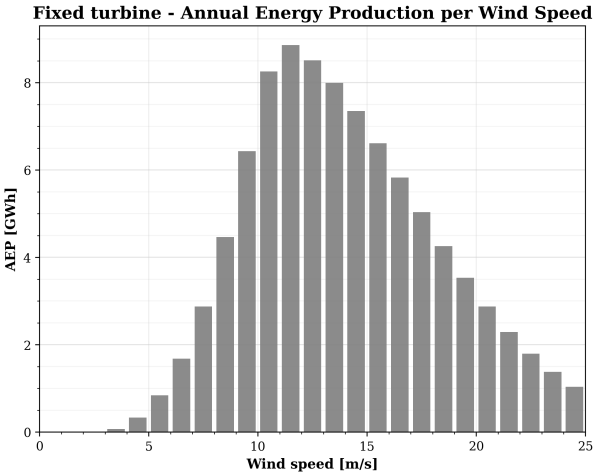

Figure 4.15: Annual energy production (AEP) per wind speed bin for the fixed turbine.

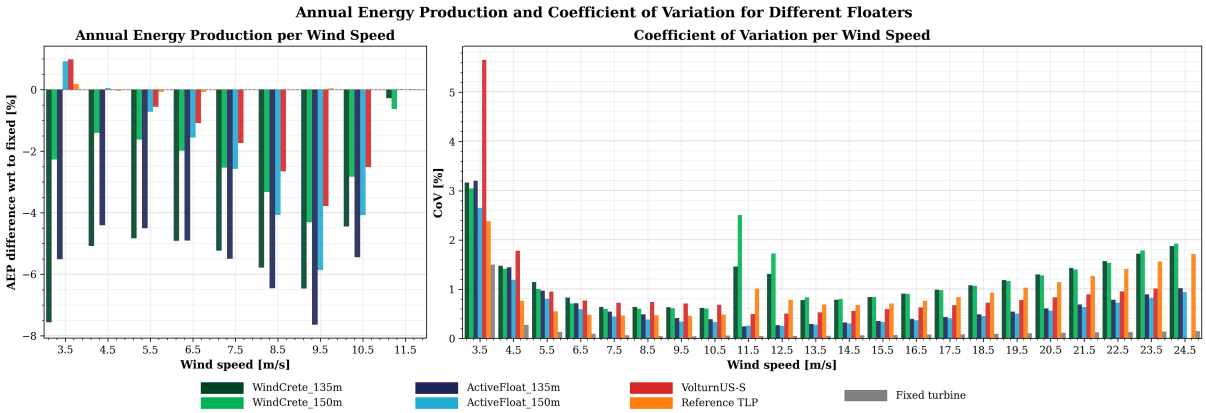

Figure 4.16: Percentage difference in annual energy production (AEP) relative to the fixed turbine and coefficient of variation (CoV) for all floating platforms per wind speed bin. As all floaters produce the same rated power of 15MW from 12 m/s until 25 m/s wind speed, the wind speeds have been cut off the power graph. Only the VolturnUS-S cut-off at 24 m/s on produces no power in the last wind speed bin.

The AEP split between below-rated and above-rated wind speeds is summarised in Table 4.4. Above rated wind speeds ($U > 11$ m/s), all floating platforms produce the same AEP as the fixed turbine (67.36 GWh), with the exception of the VolturnUS-S, which yields 66.32 GWh due to a blade pitch-limit exceedance at the 24-25 m/s wind speed bin. This exceedance occurs for 0.25 s (0.042% of the run duration); if the affected bin were included, the above-rated AEP would be 67.36 GWh and the total AEP 91.67 GWh, matching the other platforms.

Below rated wind speeds ($U \leq 11$ m/s), differences between platforms are more pronounced. The fixed turbine and Reference TLP produce the highest below-rated AEP at 24.95 GWh, while the other floating platforms show reductions ranging from 0.64 GWh (VolturnUS-S, 24.31 GWh) to 1.52 GWh (ActiveFloat 135m, 23.43 GWh) relative to the fixed turbine. The 150m hub height variants of both WindCrete and ActiveFloat consistently outperform their 135m counterparts below rated wind speed, producing 24.17 GWh and 23.95 GWh respectively compared to 23.62 GWh and 23.43 GWh.

Table 4.4: Annual energy production (AEP) for below-rated, above-rated and all wind speeds combined, using 1 m/s wind speed bins. The rated wind speed of 10.59 m/s falls within the 10 - 11 m/s bin (below-rated region = U $\leq$ 11m/s, above-rated = U > 11 m/s).

AEP [GWh]	WindCrete 135m	WindCrete 150m	ActiveFloat 135m	ActiveFloat 150m	Volturn-US-S	Reference TLP	Fixed turbine
$\leq$ 11.0 m/s	23.62	24.17	23.43	23.95	24.31	24.95	24.95
> 11.0 m/s	67.33	67.31	67.36	67.36	66.32 [a]	67.36	67.36
Total	90.94	91.48	90.79	91.31	90.63	92.31	92.31

[a] This wind-speed bin is affected by the blade pitch-limit cutoff. The limit is exceeded for 0.25 s (0.042% of the run); If the bin was included, the resulting total AEP would be 67.36 GWh above rated and 91.67 GWh in total.

4.3.2. Verification of Simulation Duration

The results of the simulation duration comparison, as described in Subsection 3.2.3, are presented in this subsection. A full comparison for the VolturnUS-S across all wind speed bins is provided in Figure 4.17 with the numerical data inTable F.1. For all platforms selected wind speed bins around cut-in, rated and cut-out wind speed, the numerical data is given in Table F.2 and Table F.3.

The total AEP for the VolturnUS-S changes by only -0.007% between the 10-minute and 3-hour runs (90,634.6 MWh to 90,628.6 MWh), as shown in Table F.1. Differences in mean power output are small across all platforms and wind speed bins (Figure 4.17), with the largest relative differences occurring at low wind speeds (3-5 m/s), reaching up to -1.4% for the Reference TLP at 3-4 m/s. From 9 m/s onwards, power differences remain below 0.05% for all platforms.

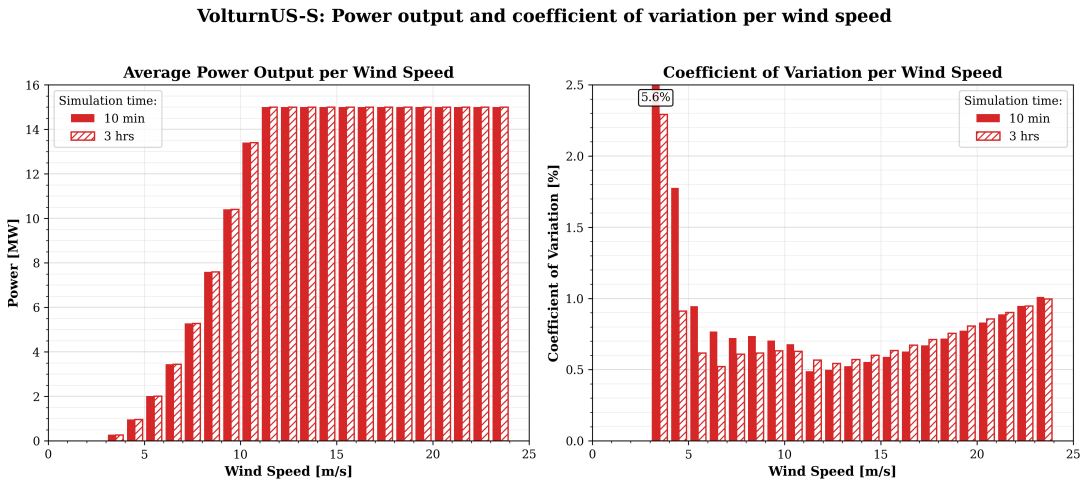

Figure 4.17: Turbine average power and coefficient of variation per wind speed for the VolturnUS-S for both 10-minute and 3-hour simulation runs (excluding the 5-minute transient period at the start). Numerical values can be found in Table F.1.

The CoV shows greater sensitivity to simulation duration than the mean power (Table F.3). Below rated wind speed, the CoV is systematically lower in the 3-hour runs, with differences reaching up to -61% for ActiveFloat at 4-5 m/s. This is attributed to the slow sinusoidal surge motion that is not fully damped out within the 5-minute transient period at low wind speeds, as illustrated in Figure 4.18. Above rated wind speed, CoV differences are smaller and decrease further with increasing wind speed.

For the VolturnUS-S, the pitch limit is exceeded for a total of 36.5 s (0.338% of the run duration) in the 24-25 m/s bin, consistent with the exclusion of this bin applied in the standard setup. Both WindCrete platforms exceed the blade pitch limit during the 3-hour runs in a manner not captured within the 10-minute simulations. WindCrete 135 m exceeds the limit for 0.5 s (0.005% of the run duration) and WindCrete 150 m for 4.7 s (0.044%), resulting in zero power output in the 24-25 m/s bin for both variants. Individual exceedances last between 0.5 and 2 seconds.

The 10-minute simulation duration is considered sufficient for the purposes of this study. The total AEP difference of 0.007% for the VolturnUS-S confirms statistical convergence of the mean power output. While the CoV shows greater sensitivity to simulation duration at low wind speeds, these bins contribute negligibly to the total AEP. The pitch limit exceedances observed only in the 3-hour runs needs further investigation to determine their influence on platform performance.

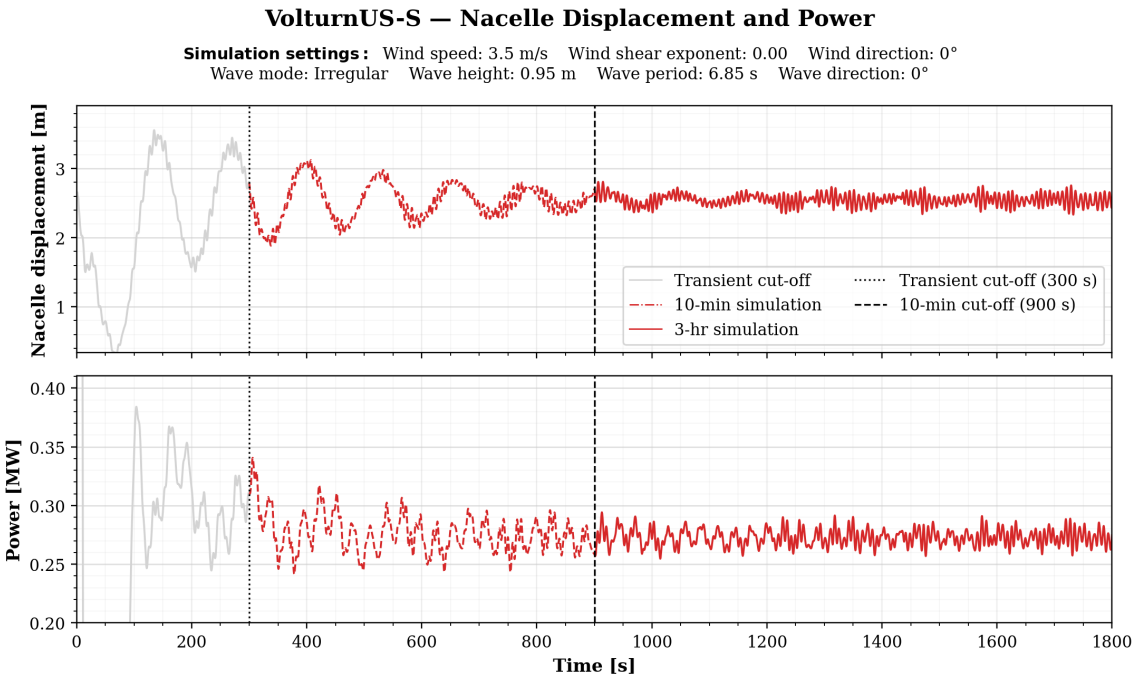

Figure 4.18: Nacelle displacement and power output for the VolturnUS-S at 3.5 m/s wind speed. Only the first 1800 s of the 3-hour simulation are shown to improve clarity; the transient period (0-300 s) is shaded in grey.

4.4. Results of Sensitivity Analyses

This section presents a series of sensitivity analyses conducted to assess the robustness of the platform motion and power production results with respect to key modelling and environmental parameters. The investigated sensitivities include wind speed bin sizing, wave influence, mooring stiffness variation and wind-wave misalignment. The analyses aim to identify which parameters have a meaningful impact on platform dynamics and turbine performance and which effects remain secondary within the investigated operating range.

The sensitivity analyses have been performed for a wind speed of 9.5 m/s at hub height, for which the mean surge and pitch motions with corresponding standard deviations are shown in Figure 4.19.The figure illustrates the relative magnitude and variability of surge and pitch motions between platforms under identical inflow conditions. This baseline case assumes aligned wind and wave directions ($0°$) and is characterised by a significant wave height of $H_s = 1.53$ m and a peak period of $T_p = 7.40$ s.

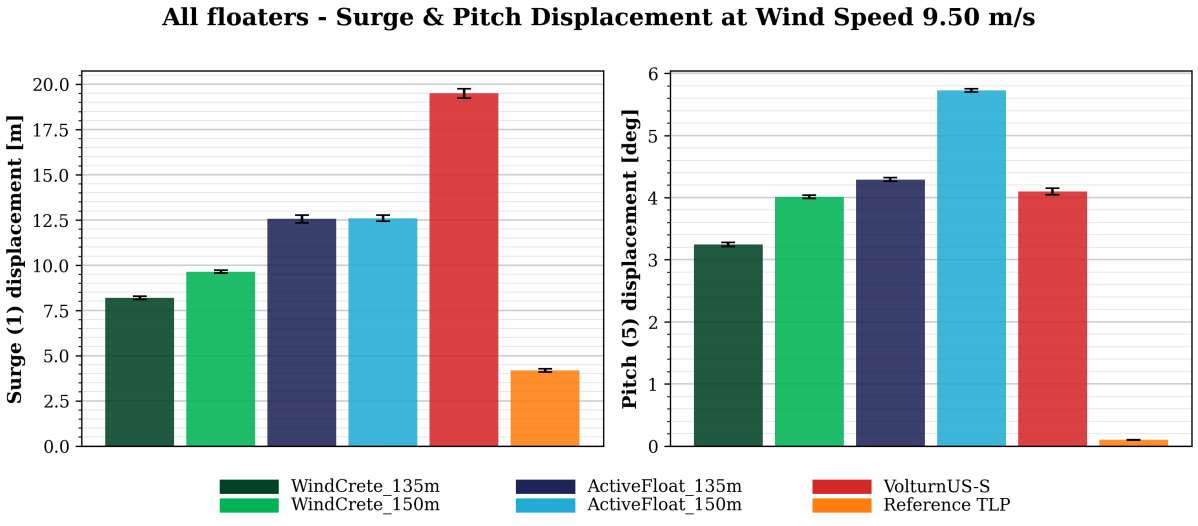

Figure 4.19: Surge and pitch motions across all platforms at 9.5 m/s wind speed, demonstrating relative platform response characteristics. The full 8-DOF comparison can be found in Figure D.8.

4.4.1. Sensitivity to Wind Speed Bin Size

This subsection investigates the sensitivity of the annual energy production (AEP) and power variability to the choice of wind speed bin size used (1.0 m/s, 0.5 m/s and 0.25 m/s) for the operational simulations. The total AEP and corresponding coefficient of variation (CoV) for all platforms and bin sizes are summarised in Table 4.5. The differences in AEP with respect to fixed turbine and total CoV per wind speed bin sizing are illustrated in Figure 4.20.

Across all floating platforms and the fixed reference turbine, variations in annual energy production (AEP) due to changes in wind speed bin size remain below 1% for all configurations. The VolturnUS-S exhibits the largest AEP increase, with a maximum rise of approximately +0.7% for a bin size of 0.5 m/s. In contrast, the WindCrete 150 m configuration and the reference TLP show the largest AEP reductions, amounting to approximately −0.4% for the 0.5 m/s bin size. For a bin size of 0.25 m/s, the WindCrete, ActiveFloat 150 m and TLP configurations also exhibit small reductions in AEP. The fixed turbine is the least sensitive to bin-size variation and remains largely unaffected.

Changes in the coefficient of variation (CoV) are between +2% and -3%. For most platforms, CoV values remain effectively unchanged across the investigated bin sizes. The WindCrete 135 m and ActiveFloat 135 m configurations show increases in CoV exceeding 1% for both reduced bin sizes. In contrast, the WindCrete 150 m configuration exhibits the largest CoV reduction, with decreases of approximately 3.0% for the 0.5 m/s bin size and 3.6% for the 0.25 m/s bin size. Overall, while small numerical fluctuations occur, the magnitude of power variability and the trends between platforms remain consistent across all bin sizes.

Below rated wind speed ($\leq$11.0 m/s), AEP has only marginal increases of up to 0.08 GWh observed. Above rated wind speed ($>$11.0 m/s), larger deviations emerge at smaller bin sizes: at 0.5 m/s, WindCrete 150 m and the Reference TLP show reductions of 0.47 GWh and 0.48 GWh respectively, while at 0.25 m/s similar reductions are observed across several platforms. As discussed below, these differences are driven by shifts in the cut-out bin boundary rather than power curve resolution.

The dominant source of AEP variation across bin sizes is the position of the last active wind speed bin. As the bin size decreases, the upper bin boundary shifts, either capturing or excluding high-energy occurrences near 25 m/s. This effect is most pronounced for the VolturnUS-S, whose last active bin shifts from 23.0-24.0 m/s at 1.0 m/s to 24.0-24.5 m/s at 0.5 m/s and 0.25 m/s, capturing approximately 1 GWh of additional energy and producing the largest AEP increase of +0.7%. Conversely, WindCrete 150 m and the Reference TLP lose the upper portion of the 24-25 m/s interval at finer bin sizes, resulting in reductions of approximately -0.4%. The last active bin per platform and bin size is listed in Table 4.5.

The CoV shows modest sensitivity to bin size, with changes between +2% and -4% relative to the 1.0 m/s reference. Most platforms are largely unaffected. WindCrete 135 m and ActiveFloat 135 m show small CoV increases just above 1%, while WindCrete 150 m exhibits the largest reduction (-3.0% at 0.5 m/s, -3.6% at 0.25 m/s), consistent with its shift in cut-out bin. The relative ranking of platforms by CoV is preserved across all bin sizes.

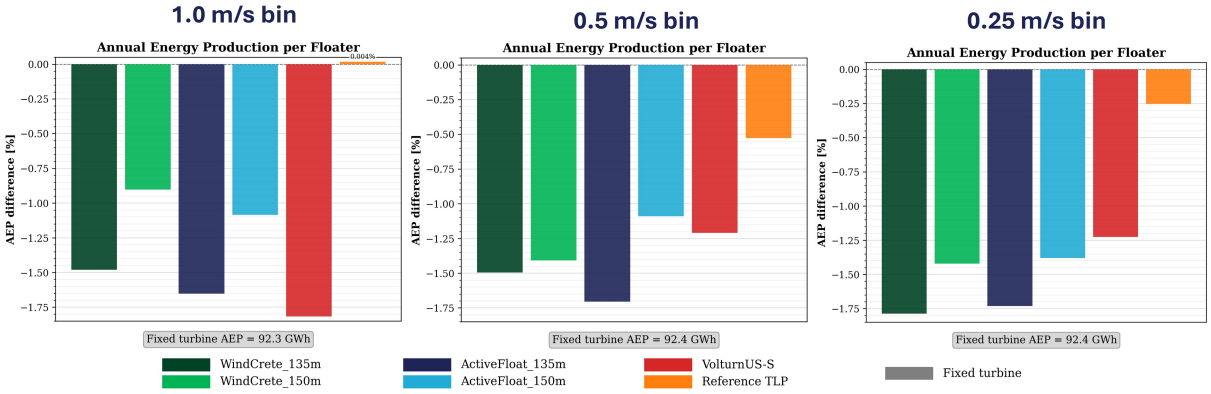

Figure 4.20: Relative difference in annual energy production (AEP) compared to the fixed turbine for all floating platforms per wind speed bin size. Numerical data is given in Table 4.5.

Table 4.5: Annual energy production (AEP), coefficient of variation (CoV) and cut-out wind speed bin for different wind speed bin sizes. The cut-out bin is the highest wind speed bin producing power.

Wind speed bin size [m/s]		WindCrete 135m	WindCrete 150m	ActiveFloat 135m	ActiveFloat 150m	Volturn-US-S	Reference TLP	Fixed turbine
AEP	1.0	23.62	24.17	23.43	23.95	24.31	24.95	24.95
$\leq$ 11.0 m/s	0.5	23.68	24.24	23.48	24.01	24.38	25.01	25.02
[GWh]	0.25	23.69	24.25	23.50	24.03	24.39	25.03	25.04
AEP	1.0	67.33	67.31	67.36	67.36	66.32	67.36	67.36
> 11.0 m/s	0.5	67.32	66.84	67.32	67.36	66.88	66.88	67.36
[GWh]	0.25	67.05	66.84	67.29	67.09	66.87	67.13	67.36
Total	1.0	90.94	91.48	90.79	91.31	90.63	92.31	92.31
AEP	0.5	91.00	91.08	90.80	91.37	91.26	91.89	92.38
[GWh]	0.25	90.75	91.08	90.80	91.12	91.26	92.16	92.40
CoV [%]	1.0	0.994	1.126	0.422	0.384	0.653	0.774	0.0693
	0.5	1.006	1.092	0.429	0.383	0.657	0.771	0.0691
	0.25	1.014	1.085	0.427	0.386	0.659	0.765	0.0693
Cut-out	1.0	24.0-25.0	24.0-25.0	24.0-25.0	24.0-25.0	23.0-24.0	24.0-25.0	24.0-25.0
bin	0.5	24.5-25.0	24.0-24.5	24.5-25.0	24.5-25.0	24.0-24.5	24.0-24.5	24.5-25.0
[m/s]	0.25	24.5-24.75	24.25-24.5	24.75-25.0	24.5-24.75	24.25-24.5	24.5-24.75	24.75-25.0

4.4.2. Sensitivity to Wave Influence

This subsection investigates the influence of wave conditions on platform motions and turbine power production at a fixed wind speed of 9.5 m/s. The analysis focuses on changes in platform response and power variability as a function of increasing significant wave height while maintaining aligned wind and wave directions.

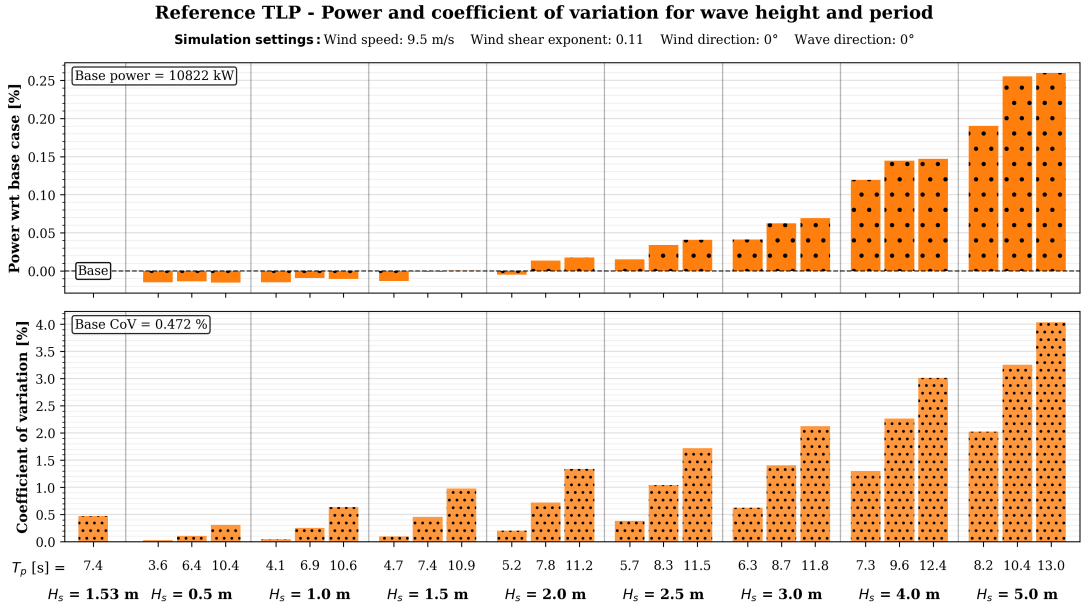

Figure 4.21: Influence of significant wave height and peak period on mean turbine power output and coefficient of variation for the reference TLP at a wind speed of 9.5 m/s with aligned wind and wave directions.

An example of the wave-height and peak period sensitivity is shown in Figure 4.21; all floaters have a similar behaviour. For an increasing wave height results in a gradual increase in power variability, expressed by a higher coefficient of variation. However, the mean power output remains largely unaffected across the investigated wave heights. Similar trends are observed for all floating platforms.

A complete overview of wave-height-dependent platform motions and power metrics is provided in Appendix G. This includes motion responses for all eight degrees of freedom as well as power output and coefficient of variation results (Figures **??**-**??**). The corresponding numerical data are summarised in Table G.1 and Table G.2.

4.4.3. Sensitivity to Mooring Stiffness: Natural Period and Damping

This subsection focuses on the influence of mooring stiffness on natural periods and damping ratio. Overview figures of the natural periods and damping ratios for each floater as a function of mooring stiffness are provided in Appendix H (Figures H.1-H.6).

Figure 4.22 illustrates the influence of mooring stiffness on the surge, sway and yaw natural periods for all floating platforms. As the sway natural period closely follows the surge response, it is not shown separately. Variations in the heave, pitch and roll natural periods remain comparatively limited across the investigated stiffness range. Increasing mooring stiffness leads to a consistent reduction in the natural periods of surge, sway and yaw, reflecting the enhanced horizontal restoring forces. The corresponding numerical values for surge and sway are provided in Table H.1, while yaw natural periods are listed in Table H.2.

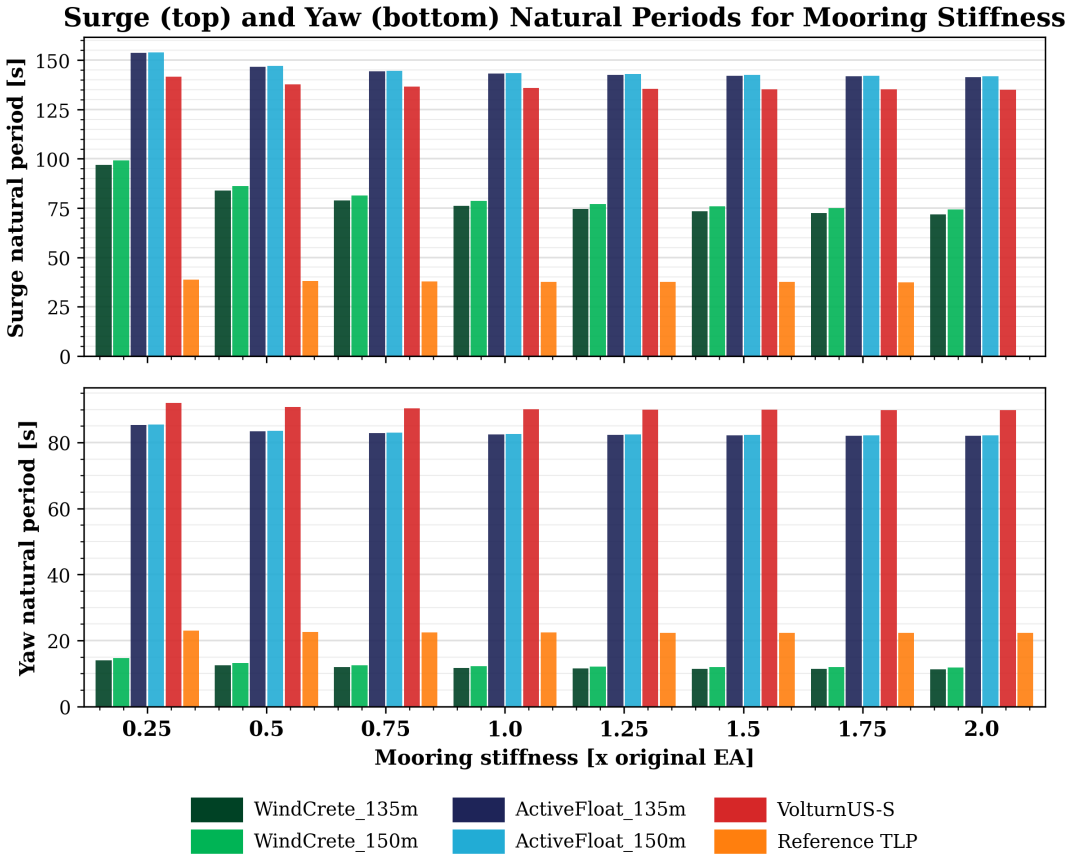

Figure 4.22: Surge and yaw natural period per mooring stiffness. The sway natural period closely follows the surge response and is not shown separately. The data for the surge and sway can be found in Table H.1 and for yaw in Table H.2.

Figure 4.23 illustrates the influence of mooring stiffness on the surge, sway and heave damping ratio for all floating platforms. For the ActiveFloat and VolturnUS-S platforms, changes in damping ratios across the investigated stiffness range remain small (<2.0%) for all considered degrees of freedom. These platforms therefore exhibit limited sensitivity of damping behaviour to mooring stiffness.

In contrast, the WindCrete platform shows more changes in damping, particularly in the heave degree of freedom. Increasing mooring stiffness leads to higher heave damping ratios and a visible shift in the equilibrium position, reflected by a larger initial offset in the free-decay responses. This behaviour indicates that increased vertical restoring stiffness substantially influences the heave dynamics of the WindCrete platform, although the absolute heave damping ratios remain small compared to those of the other floaters. A similar mechanism is observed for the reference TLP, where damping changes are again most evident in heave, with additional but smaller effects in surge and sway at the lowest tendon

stiffness. Pitch and roll responses exhibit a general tendency toward increased damping with stiffer tendons. However, due to significant signal noise, no definitive quantitative trend can be established for these modes.

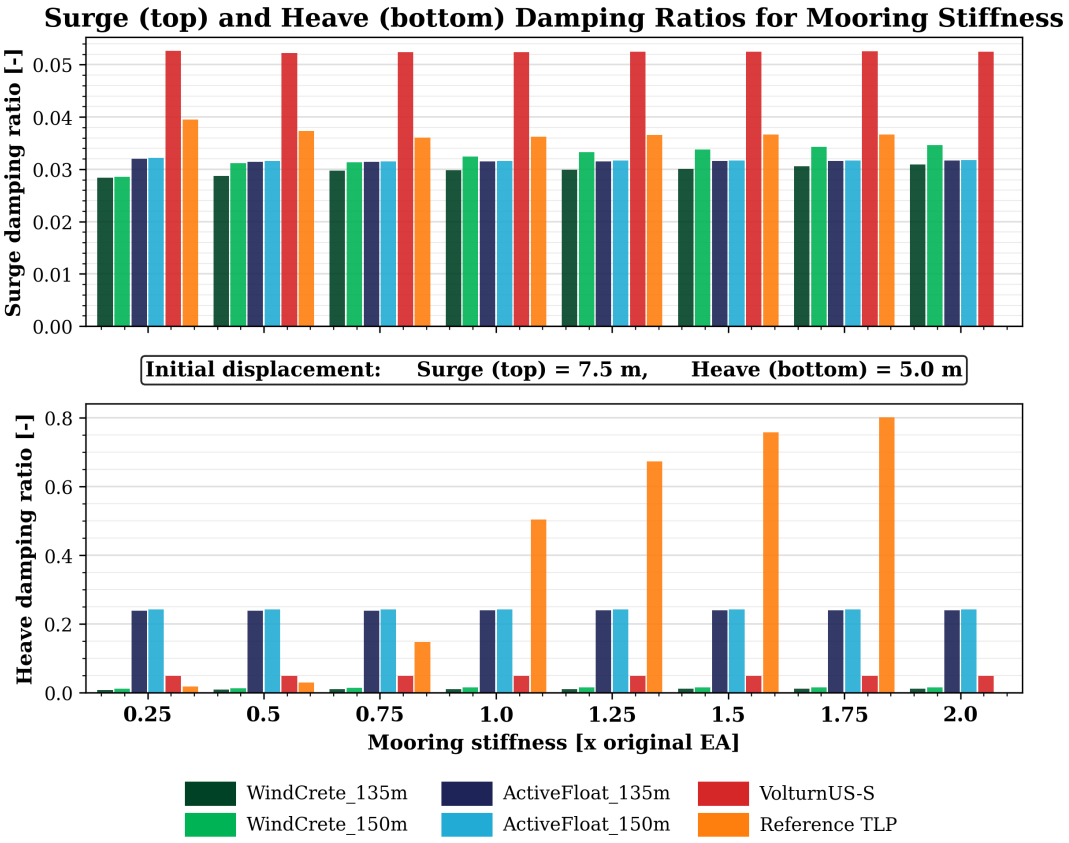

Figure 4.23: Surge and heave damping ratio per mooring stiffness. The sway damping ratio closely follows the surge response and is not shown separately. Simulations for the TLP at *2.0* × *EA* failed to converge and are excluded from the results.

4.4.4. Sensitivity to Mooring Stiffness: Power Metrics

This subsection examines change in power output and coefficient of variation per mooring stiffness. A complete overview of mooring stiffness-dependent platform motions and power metrics is provided in Appendix I. This includes motion responses for all eight degrees of freedom as well as power output and coefficient of variation results (Figures I.1-I.6).

Figure 4.24 illustrates an example of the sensitivity of turbine power output and coefficient of variation to mooring stiffness, shown here for the reference TLP. Across all floating platforms, increasing mooring stiffness above the baseline configuration (EA = 1.0) generally results in a reduction in mean power output, whereas reduced stiffness leads to a small increase in power. The magnitude of these power differences remains limited for all platforms. The ActiveFloat platform forms an exception in that it shows slightly increased power for stiffness values below the baseline, while remaining largely insensitive to stiffness increases above the baseline. The quantitative power differences relative to the baseline stiffness are summarised in Table 4.6 and remains below 0.01% for floaters.

The coefficients of variation per mooring stiffness are given in Table 4.7. For the WindCrete platform, the CoV reaches a minimum close to the baseline mooring stiffness. For the ActiveFloat and TLP platforms, CoV decreases slightly with increasing stiffness, indicating a modest reduction in power variability. In contrast, the VolturnUS-S exhibits an increase in CoV with increasing stiffness. Despite these differences, the overall changes in variability remain small.

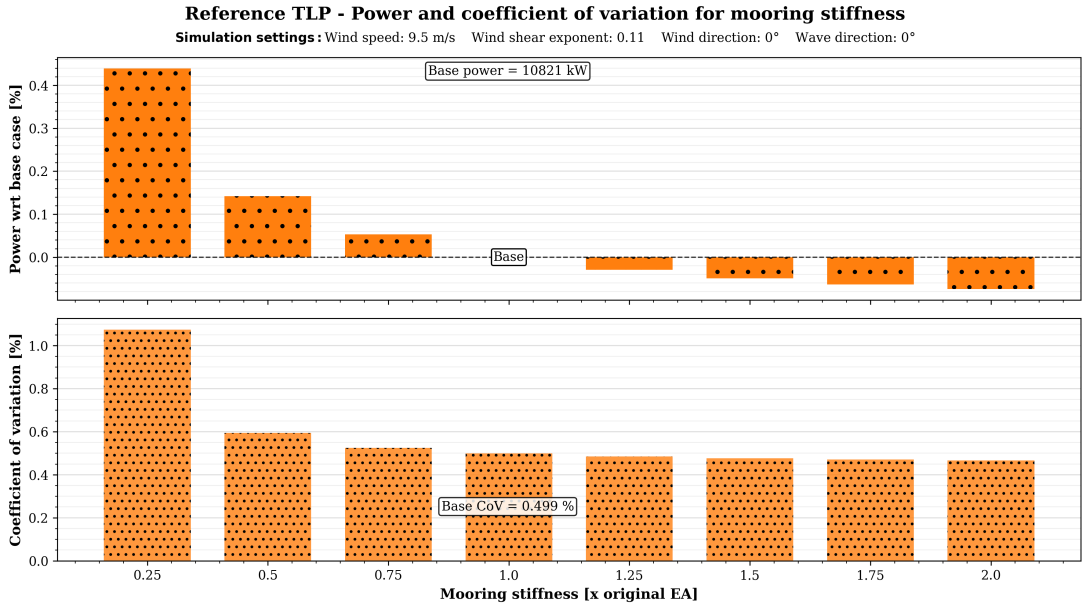

Figure 4.24: Influence of mooring stiffness on mean turbine power output and coefficient of variation for the reference TLP. Numerical values for all platforms are listed in Table 4.6 and Table 4.7.

Table 4.6: Turbine power difference for different mooring stiffnesses.

	Turbine power difference vs base (EA = 1.0 x)					
EA x	**WindCrete 135m**	**WindCrete 150m**	**ActiveFloat 135m**	**ActiveFloat 150m**	**Volturn-US-S**	**Reference TLP**
0.25	0.080%	0.052%	0.059%	0.042%	0.009%	0.439%
0.50	0.017%	0.026%	0.015%	0.010%	0.006%	0.142%
0.75	0.012%	-0.017%	0.004%	0.002%	0.002%	0.053%
1.00	**10122 kW**	**10358 kW**	**9990 kW**	**10182 kW**	**10406 kW**	**10821 kW**
1.25	-0.022%	-0.006%	-0.002%	-0.001%	-0.002%	-0.030%
1.50	-0.035%	-0.013%	-0.002%	-0.001%	-0.003%	-0.049%
1.75	-0.040%	-0.021%	-0.002%	-0.001%	-0.003%	-0.064%
2.00	-0.042%	-0.028%	-0.002%	-0.001%	-0.004%	-0.074%

Table 4.7: Coefficient of variation (CoV) for different mooring stiffnesses.

	Coefficient of variation					
EA x	**WindCrete 135m**	**WindCrete 150m**	**ActiveFloat 135m**	**ActiveFloat 150m**	**Volturn-US-S**	**Reference TLP**
0.25	0.868%	0.986%	0.507%	0.490%	0.671%	1.073%
0.50	0.828%	0.971%	0.493%	0.486%	0.685%	0.594%
0.75	0.864%	0.942%	0.478%	0.467%	0.693%	0.525%
1.00	**0.812%**	**0.922%**	**0.480%**	**0.464%**	**0.698%**	**0.499%**
1.25	0.796%	0.945%	0.484%	0.465%	0.702%	0.485%
1.50	0.810%	0.959%	0.489%	0.468%	0.704%	0.477%
1.75	0.816%	0.955%	0.493%	0.470%	0.706%	0.471%
2.00	0.813%	0.945%	0.496%	0.472%	0.707%	0.467%

4.4.5. Sensitivity to Wind-Wave Misalignment

This subsection presents turbine power output and coefficient of variation (CoV) under wind-wave misalignment for a wind speed of 9.5 m/s. Figure 4.25 shows mean power difference and CoV for wind-wave aligned cases across platforms, as wind-wave misalignment produces only small changes relative to wind direction effects. The numerical data for the power difference can be found in Table 4.8 and CoV in Table 4.9.

All floating platforms exhibit power reductions (<0.2%) from the aligned reference direction ($0°$), with semi-submersibles showing the largest differences. An increase in wind-wave misalignment produces a mean power reduction across all platforms. In contrast, the CoV values prove lowest at $0°$ and $60°$ directions across platforms. The values are in general smaller for a larger difference between the wind and wave directions despite the reduction in power. Only the Reference TLP shows negligible reaction to directional changes.

A comprehensive overview of platform motions and power metrics for all wind-wave direction combinations is provided in Appendix J. The complete numerical datasets for all wind-wave direciton combinations are listed in Table J.1 and Table J.2. The 8-DOF motion responses and corresponding power and CoV results are shown in Figures J.1-J.6).

Table 4.8: Turbine power difference for different wind-wave aligned cases. Results for all wind and wave direction cases can be found in Table J.1.

		Turbine power difference vs base (Wind = wave direction = $0°$)					
Wind direction	**Wave direction**	**WindCrete 135m**	**WindCrete 150m**	**ActiveFloat 135m**	**ActiveFloat 150m**	**Volturn-US-S**	**Reference TLP**
0°	**0°**	**10122 kW**	**10358 kW**	**9990 kW**	**10182 kW**	**10406 kW**	**10821 kW**
15°	**15°**	-0.004%	-0.001%	-0.003%	-0.017%	-0.011%	0.000%
30°	**30°**	-0.028%	-0.008%	-0.043%	-0.085%	-0.070%	0.001%
45°	**45°**	-0.016%	-0.025%	-0.075%	-0.146%	-0.088%	0.001%
60°	**45°**	-0.035%	-0.030%	-0.083%	-0.167%	-0.087%	0.000%

Table 4.9: Coefficient of variation (CoV) for different wind-wave aligned cases. Results for all wind and wave direction cases can be found in Table J.2.

		Coefficient of Variation					
Wind direction	**Wave direction**	**WindCrete 135m**	**WindCrete 150m**	**ActiveFloat 135m**	**ActiveFloat 150m**	**Volturn-US-S**	**Reference TLP**
0°	**0°**	**0.812%**	**0.922%**	**0.480%**	**0.464%**	**0.667%**	**0.499%**
15°	**15°**	0.856%	0.936%	0.479%	0.458%	0.721%	0.496%
30°	**30°**	0.919%	1.025%	0.560%	0.539%	0.747%	0.493%
45°	**45°**	0.812%	0.972%	0.597%	0.579%	0.725%	0.491%
60°	**60°**	0.812%	0.971%	0.549%	0.530%	0.662%	0.491%

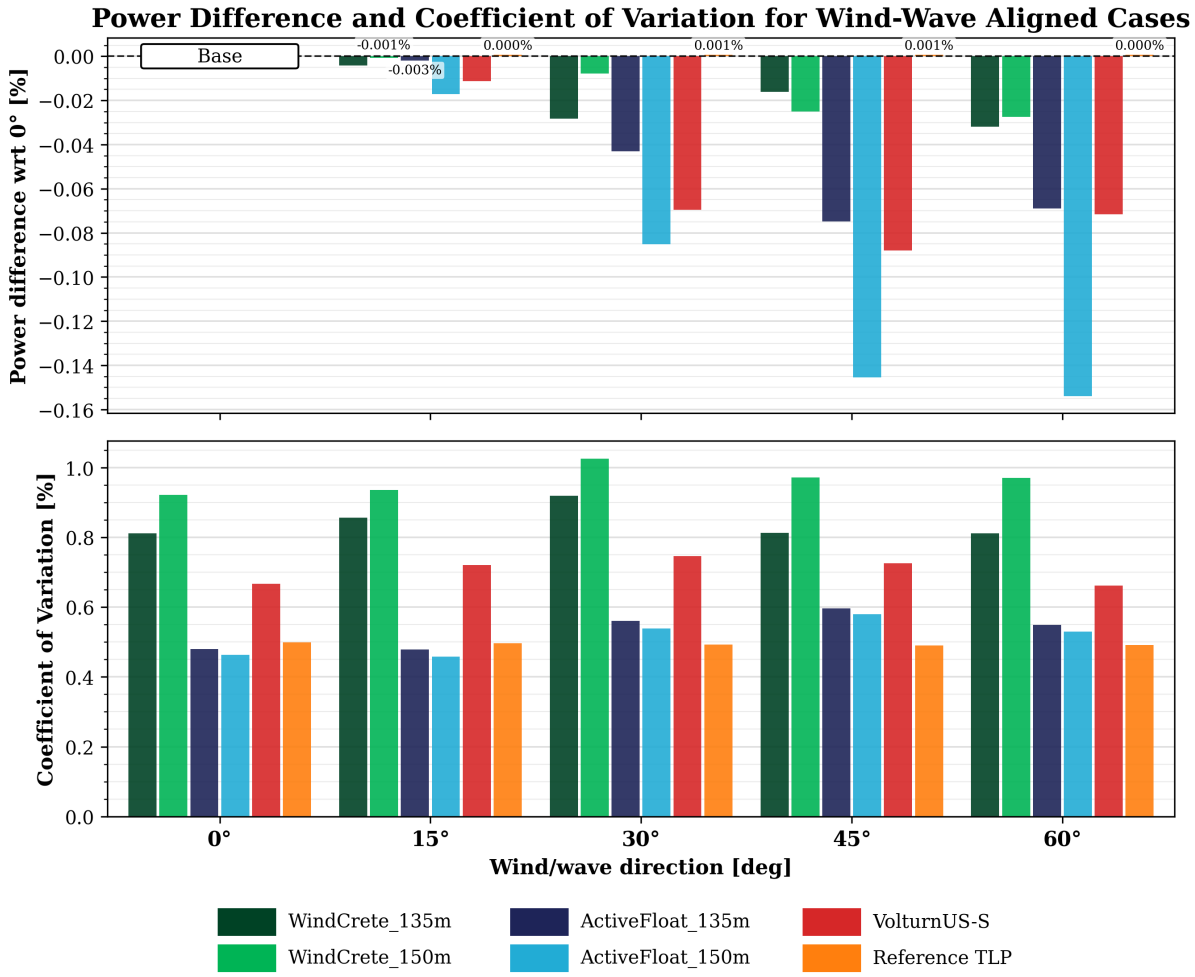

Figure 4.25: Power difference and coefficient of variation of wind-wave aligned cases for all floaters. Data for the power output can be found in Table 4.8 and for the CoV Table 4.9.

5

Discussion

Building on the OpenFAST simulation results presented in Chapter 4, this chapter discusses and interprets the findings with the objective of answering the central research question of this thesis. The interpretation of intrinsic platform dynamics derived from free-decay tests is presented in Section 5.1. Section 5.2 then examines operational six-DOF motions under wind-wave loading and their coupling with turbine control. The impact of these dynamics on turbine performance, including power variation and annual energy production, is analysed in Section 5.3. The robustness of the results is assessed in Section 5.4, where the influence of wind speed bin sizing, wave conditions, mooring stiffness variation and wind-wave misalignment is evaluated. A system-level comparison of the floating platform concepts is subsequently discussed in Section 5.5, highlighting trade-offs between motion behaviour, power stability and energy yield without identifying a single optimal concept. Finally, the limitations of the study are addressed in Section 5.6, followed by a discussion of the implications of the findings for floating wind turbine design in Section 5.7. These interpretations provide the foundation for conclusions and design recommendations in Chapter 6.

5.1. Interpretation of Intrinsic Platform Dynamics

The free-decay analyses presented in Section 4.1 provide insight into the intrinsic dynamic characteristics of the floating platforms, independent of wind excitation and turbine control effects. As the free-decay simulations focus exclusively on hydromechanical behaviour, only the mass and inertia of the turbine and tower are accounted for, while aerodynamic loading and aerodynamic damping are deliberately excluded. This allows the fundamental restoring and damping properties of the platform-mooring system to be isolated.

The obtained natural periods show close agreement with values reported in the design papers of each floating platform concept. The ordering of natural periods across the different floater families follows expected trends based on their dominant restoring mechanisms. Platforms relying primarily on hydrostatic restoring, such as the spar and semi-submersibles, exhibit longer surge and pitch periods, while the reference TLP shows substantially shorter heave, pitch and roll periods due to the high pretension in the tendons. This agreement with prior studies supports the validity of the baseline dynamic characterisation.

A minor discrepancy is noted for the ActiveFloat and WindCrete platforms, whose simulated free-decay responses differ slightly from their respective design documents. Repeating the simulations using the original input files yields the same results. This confirmed the discrepancy is not introduced by the current modelling setup and remains unresolved. For the VolturnUS-S, the surge stiffness was provided as a frequency of 0.007 Hz; small variations in this input (0.0065–0.0074 Hz) can produce a notable shift in the predicted surge natural period, introducing a degree of uncertainty that should be kept in mind when comparing absolute values with the literature.

Quantitative comparison of damping ratios is more limited, as most design papers did not include the analysis. In the present work, damping ratios of the VolturnUS-S platform are lower than reported values, which is expected given that the study accounted for additional aerodynamic damping contributions from the rotating rotor and tower-aerodynamic interaction. Aerodynamic damping is known to significantly increase overall system damping, particularly in surge and pitch and its exclusion in the free-decay simulations therefore leads to conservative damping estimates. Nevertheless, relative differences in damping behaviour between platforms remain informative, as all configurations are assessed under the same modelling assumptions.

An increase in damping ratio with larger initial displacement amplitudes is observed for several degrees of freedom, consistent with the VolturnUS-S design paper. This behaviour reflects the nonlinear nature of hydrodynamic damping, where viscous drag and geometric effects become more pronounced at larger motion amplitudes. The dependence of damping on initial displacement highlights that reported damping ratios should be interpreted as amplitude-dependent estimates rather than constant system properties.

A notable result is the relatively high yaw damping observed for the WindCrete platform. Although the spar has limited intrinsic rotational resistance due to its slender geometry, the mooring system layout plays a key role in yaw behaviour. The WindCrete bridle mooring lines connect to the platform at a radial distance of approximately 48 m from the platform centre. This bridle system generates a significant yaw-restoring moment even for small angular displacements. This distance is of similar magnitude to the effective mooring radii of the semi-submersible platforms. However, the semi-submersibles possess substantially larger rotational inertia due to their wide footprint and distributed mass, which reduces the relative impact of mooring-induced yaw damping. As a result, WindCrete exhibits comparatively high yaw damping despite its lower structural rotational inertia.

Overall, the free-decay results establish a consistent dynamic baseline for the subsequent operational analyses. They confirm that the dominant differences between the floating platforms arise from their stability mechanisms, mass distribution and mooring configurations. This provides a physically grounded explanation for the motion characteristics observed under wind and wave loading in later sections.

5.2. Interpretation of Operational Platform Response

The operational platform responses presented in Section 4.2 reflect the combined effect of hydromechanical restoring mechanisms, mass and inertia properties, mooring system layouts and coupling with aerodynamic loading and turbine control. Interpreting these responses requires linking the observed motion trends to the intrinsic dynamic characteristics established through the free-decay analyses.

At low wind speeds, several floating configurations exhibit a small negative mean pitch angle. This behaviour is primarily caused by the static moment induced by the rotor-nacelle assembly positioned forward of the tower centreline. In the absence of significant aerodynamic thrust at low wind speeds, the gravitational contribution of the rotor and nacelle dominates. As wind speed increases and aerodynamic thrust becomes the dominant load component, this offset is progressively overcome and the mean pitch response shifts accordingly.

Differences in surge and pitch motions between the floating platforms can be directly linked to their dominant restoring mechanisms and mass distribution. Platforms relying primarily on hydrostatic restoring, such as the WindCrete spar and semi-submersible (ActiveFloat and VolturnUS-S) concepts, exhibit larger surge excursions due to their relatively low horizontal stiffness. In particular, platforms with broader waterplane areas and lower effective mooring stiffness show larger mean surge motions accompanied by increased variation. This behaviour reflects both the reduced horizontal restoring force and the interaction between low-frequency surge motion and aerodynamic loading.

In contrast, the Reference TLP exhibits minimal surge and pitch motions with limited variation across the operational wind speed range. This is a direct consequence of the high pretension in the vertical tendons. The resulting stiff system suppresses large-amplitude motions and limits the coupling between platform response and rotor aerodynamics. Consequently, the TLP displays the smallest mean excursions and lowest motion variability among the floating concepts.

The fixed reference turbine provides a clear baseline for this analysis, as it exhibits no rigid-body motion in any of the six platform degrees of freedom. Only tower fore-aft and side-side deformations are present and are driven solely by aerodynamic loading. This rigid reference therefore isolates the additional dynamics introduced by floating support structures. These motion characteristics form the physical basis for the differences in power variation and energy yield discussed in the subsequent sections.

5.3. Impact of Platform Dynamics on Power Production

The annual energy production results presented in Section 4.3 reflect the combined influence of platform motion, aerodynamic inflow variations and turbine control behaviour. Differences between floating and fixed configurations are therefore best understood by linking platform dynamics to changes in apparent wind conditions at the rotor and the resulting controller response. Across all floating platforms, the impact on mean power output and annual energy production is relatively small ($<$2%) when compared to the fixed reference turbine.

The dominant mechanism behind power fluctuations for floating platforms is the coupling between platform motion and rotor inflow. Surge and pitch motions modify the apparent wind speed and direction at the rotor disc, leading to short-term deviations from the ideal operating point. In particular, surge motion directly influences the axial inflow component, while pitch motion alters both the effective inflow angle and rotor area perpendicular to the wind speed. These motion-induced inflow variations result in fluctuations in aerodynamic torque and trigger controller actions, which manifest as increased power variation.

The coefficient of variation (CoV) provides a clear measure of these effects and shows strong consistency with the relative magnitude of platform motions identified in the operational response analysis. Platforms exhibiting larger surge and pitch motions also display higher CoV values, whereas stiffer configurations with limited motion show reduced power variation. This confirms that floating platforms primarily influence power stability rather than long-term energy yield. The mean power output is only weakly affected, while short-term fluctuations increase noticeably with platform compliance.

An apparent inconsistency worth noting is that the Reference TLP achieves the highest AEP among all floating platforms but does not exhibit the lowest CoV. The high AEP results from the TLP's stiff mooring system, which suppresses large surge and pitch excursions and keeps the rotor well aligned with the incoming wind. This minimises motion-induced power losses. The elevated CoV, however, is explained by the short natural periods of the tendon system: the stiff tendons drive higher-frequency platform oscillations that produce more rapid variations in rotor inflow and controller response. Larger short-term power peaks and troughs are the results and thus a higher standard deviation and CoV.

Controller interaction plays a key role in shaping this behaviour. The ROSCO controller responds to motion-induced inflow variations by adjusting blade pitch and generator torque to maintain rotor speed and limit loads. Near rated wind speed, where controller activity is highest, this interaction amplifies power variation. Nevertheless, the controller effectively limits sustained power losses, contributing to the small differences observed in AEP and coefficient of performance between floating configurations.

The comparison between floating platforms and the fixed reference turbine further highlights these effects. The fixed turbine experiences no rigid-body motion and is therefore exposed only to aerodynamic variation, resulting in minimal power fluctuations and the lowest CoV. Floating platforms introduce additional low-frequency power variation through platform motion, but this does not translate into a proportionally large reduction in energy yield. This distinction underscores that platform motion predominantly affects short-term power quality rather than cumulative energy production.

The aggregated performance metrics summarised in Table 4.3 further support these observations. The reduction in C_p relative to the fixed turbine is consistent with increased rotor misalignment and unsteady inflow caused by platform motion. However, differences in C_p between floating platforms remain small and indiciates comparable aerodynamic efficiency under operational conditions.

Overall, the power production analysis demonstrates that while floating support structures introduce increased power variation through platform motion and aero-servo-elastic coupling, their impact on mean energy yield remains limited. This reinforces the conclusion that floater selection and mooring design are more critical for power stability and load mitigation than for maximising annual energy production.

5.4. Interpretation of Sensitivity Analyses

This section interprets the sensitivity analyses presented in Section 4.4. Each sensitivity study is discussed individually to assess its physical relevance, its influence on platform dynamics and power performance and its implications for modelling robustness and floater concept selection.

5.4.1. Sensitivity to Wind Speed Bin Size

The sensitivity analysis on wind speed bin sizing, presented in Subsection 4.4.1, demonstrates that AEP is only weakly dependent on the chosen bin resolution, with differences remaining below 1% for all platforms and bin sizes investigated. The dominant source of variation is not power curve resolution below rated wind speed but the position of the cut-out wind speed bin. This behaviour indicates that bin-size sensitivity is primarily numerical rather than physical, as the turbine power curve is smooth across the operational range and platform motion characteristics do not change abruptly for small wind speed changes.

The weak sensitivity to bin size provides confidence in the use of a 1.0 m/s bin width as a suitable compromise between computational efficiency and accuracy. This choice significantly reduces the number of required simulations while preserving the fidelity of AEP estimates, which is particularly relevant for comparative studies involving multiple floating concepts or extended sensitivity analyses. However, the abrupt cut-out behaviour modelled in this study does not reflect the soft cut-out strategies employed in modern wind turbines, where power is gradually reduced above rated wind speed to avoid sudden shutdowns. Incorporating a more realistic cut-out control strategy would improve the fidelity of AEP estimates in the high wind-speed region and is recommended for future studies.

5.4.2. Sensitivity to Wave Conditions

The sensitivity to wave conditions, discussed in Subsection 4.4.2, shows that wave excitation primarily affects short-term power variation rather than mean power output. Across all floating platforms, increasing wave height and peak period results in higher standard deviations of surge, pitch and heave motions, while the corresponding changes in mean power remain limited.

This behaviour can be explained by the frequency content of wave excitation relative to the platforms' natural periods and dominant wind-induced loading. Under operational conditions, wind loading and aerodynamic thrust dominate the mean equilibrium of the system, whereas wave excitation contributes mainly to oscillatory motion around this equilibrium. As a result, wave effects manifest more clearly in variation metrics such as CoV than in mean power output.

For some configurations, a slight reduction in mean pitch angle is observed at higher wave heights and longer wave periods, which can marginally increase power production by improving rotor alignment with the incoming wind. However, such severe wave conditions occur infrequently at the Buchan Deep site and their contribution to long-term AEP is therefore negligible. Nevertheless, across all floating configurations, wave-induced effects remain secondary compared to wind-induced responses under the investigated operational conditions. This indicates that wave conditions play a limited role in determining AEP, although they may be more relevant for fatigue loading and power quality considerations.

5.4.3. Sensitivity to Mooring Stiffness: Natural Period and Damping

The influence of mooring stiffness on natural periods and damping characteristics, as presented in Subsection 4.4.3, reveals clear and platform-dependent effects on the intrinsic dynamics of the floating systems. Increasing mooring stiffness primarily affects restoring-force-dominated degrees of freedom, resulting in shorter natural periods and increased damping. This effect is particularly evident in heave, where higher stiffness leads to increased damping and a downward shift of the static equilibrium position for the WindCrete platform and, most prominently, for the reference TLP. In contrast, the ActiveFloat and VolturnUS-S platforms exhibit only limited sensitivity to stiffness variations. This reflects their inertia-dominated response and reliance on hydrostatic restoring.

For the reference TLP, changes in natural periods and damping with increasing stiffness remain modest overall, despite the pronounced heave-damping response. This behaviour is explained by the platform's inherently stiff station-keeping system, in which vertical tendon pretension already dominates the restoring mechanism. As a result, further increases in mooring stiffness yield diminishing returns in terms of additional dynamic response modification. This highlights that mooring stiffness variations primarily influence equilibrium position and damping, rather than altering the platform's dynamic characteristics.

5.4.4. Sensitivity to Mooring Stiffness: Power Metrics

The sensitivity of turbine power output and variation to mooring stiffness, discussed in Subsection 4.4.4, confirms that power production is only weakly affected by stiffness variations within the investigated range. Changes in mean power output remain small for all floating platforms, even when stiffness is varied between 0.25 and 2.0 times the original stiffness.

The coefficient of variation shows only minor changes with stiffness adjustment and the highest mean

power values are consistently obtained for the lowest mooring stiffness. Quantitatively, the VolturnUS-S platform exhibits the smallest sensitivity, with maximum power changes on the order of 0.001%. The ActiveFloat and WindCrete platforms show slightly larger variations, with maximum changes around 0.01%, while the reference TLP displays the largest relative sensitivity, with power differences of up to approximately 0.4%. Despite these differences, all observed variations remain small in absolute terms.

This limited sensitivity arises from the indirect relationship between mooring stiffness and power production. While increased stiffness reduces platform motions, the resulting changes in apparent wind speed and rotor inflow are generally too small to cause a substantial change in mean aerodynamic power. It should be noted that the smaller observed variations are of comparable magnitude to the modelling uncertainties inherent in the simulation framework. The small differences in power metrics across stiffness values should therefore be interpreted with caution, as they may partly reflect numerical sensitivity rather than physically meaningful trends.

It should be noted that the baseline mooring stiffness of the VolturnUS-S platform is approximately 40% higher than that of the other floater concepts. This elevated baseline stiffness partly explains the reduced relative sensitivity observed for this platform. Nevertheless, the overall conclusion remains that turbine power production is robust to reasonable variations in mooring stiffness and that stiffness primarily influences platform motions and power stability rather than mean energy yield.

5.4.5. Sensitivity to Wind-Wave Misalignment

The wind-wave misalignment sensitivity analysis presented in Subsection 4.4.5 indicates that directional misalignment has a limited impact on turbine power performance under the investigated operational conditions. Variations in mean power output are small (< 0.2%) and changes in CoV remain modest.

The results show that wind direction dominates power performance, while wave direction plays a secondary role. This is expected, as aerodynamic loading governs the mean operating point of the turbine, whereas wave loading primarily introduces oscillatory motion. Consequently, misalignment affects the mean power output slightly through changes in apparent wind direction and rotor alignment but does not strongly influence short-term power variation.

Platform symmetry and mooring layout also influence the observed trends. For configurations where one mooring leg faces upwind or downwind, slightly higher power output and lower CoV values are observed. Conversely, when a leg is positioned downwind, small reductions in power may occur. From a practical perspective, the limited sensitivity to wind-wave misalignment suggests that, under normal operational conditions, misalignment effects are unlikely to be a primary driver of energy yield. Instead, they may be more relevant for detailed load analysis, yaw strategy optimisation, or wind farm layout considerations.

5.4.6. Relative Importance of Sensitivity Parameters

Taken together, the sensitivity analyses allow a clear ranking of the relative importance of the investigated parameters (see Table 5.1 for overview). Wind-speed bin sizing primarily affects numerical accuracy rather than physical behaviour and has a small influence on annual energy production. Wave conditions mainly influence power variation, while their impact on mean power output and AEP remains limited under operational conditions. Mooring stiffness strongly affects platform motions and damping characteristics, but only weakly affects mean energy yield. Wind-wave misalignment introduces small changes in mean power output, with minimal influence on power variation. Overall, these results demonstrate that floating wind turbine energy yield is robust to a wide range of environmental and modelling parameters, while power stability and motion response are more sensitive to platform and mooring design choices.

Table 5.1: Relative importance of investigated sensitivity parameters on platform dynamics, power variation and annual energy production.

Parameter	Platform motions	Power variation (CoV)	AEP
Wind-speed bin sizing	None[a]	None	Very low[b]
Wave conditions	Moderate	Low to moderate	Very low
Mooring stiffness	High[c]	Low	Very low
Wind-wave misalignment	Low	Very low	Very low

[a] No physical influence; only affects numerical resolution of the power curve.
[b] Sensitivity primarily governed by discretisation of the cut-out wind speed.
[c] Influence through restoring forces and damping characteristics.

5.5. Comparison of Floater Concepts

The comparative analysis of the floating platform concepts demonstrates that no single floater outperforms the others across all evaluated metrics. Instead, each concept exhibits distinct trade-offs between platform stability, motion response, power variation and energy yield, which must be evaluated in relation to site-specific conditions and design priorities.

It should be noted that the platforms investigated in this study were designed under different philosophies and structural objectives. The WindCrete and ActiveFloat concepts use concrete, while the VolturnUS-S and Reference TLP reflect steel semi-submersible and tension-leg design traditions. These differing design philosophies result in distinct mass distributions, mooring configurations and hydrodynamic characteristics, meaning that observed performance differences reflect both inherent concept trade-offs and platform-specific design choices rather than concept type alone.

The spar-buoy WindCrete platform exhibits relatively large surge motions and a slower rotational response due to its deep draft and inertia-dominated behaviour. This results in increased low-frequency motion and higher power variation compared to the TLP, while the overall impact on annual energy production remains small. However, the large draft also constrains deployment to deep-water sites, limiting the feasible installation regions compared to shallower-moored concepts.

The semi-submersible platforms, ActiveFloat and VolturnUS-S, occupy an intermediate position between the spar and TLP concepts. Their wide footprint and large water-plane area provide stronger hydrostatic restoring than the spar, resulting in reduced pitch amplitudes, while surge motion remains relatively large. These platforms display moderate motion amplitudes and power variation while maintaining AEP values comparable to the other floating concepts. Differences between the two semi-submersibles are mainly attributed to variations in baseline mooring stiffness and mass distribution rather than fundamental differences in stability mechanisms.

The reference TLP consistently exhibits the smallest surge and pitch motions and the lowest motion variability, owing to the high vertical and rotational stiffness provided by its tension-leg mooring system. The combined tendon pretension corresponds to approximately 57% of the platform's total buoyancy, resulting in very strong station-keeping capability and effectively suppressing platform excursions. This also explains why the TLP achieves the highest AEP among all floating platforms: by limiting surge and pitch excursions, the rotor remains well-aligned with the incoming wind across the full operational range, minimising motion-induced power losses. While this configuration is advantageous from a power-stability and energy-yield perspective, it entails increased mooring complexity, high tendon loads and more demanding installation requirements.

Across all concepts, the fixed reference turbine serves as a clear benchmark, exhibiting no rigid-body motion and the lowest power variation. Comparison with this baseline highlights that floating support structures primarily increase power variation rather than significantly reducing energy yield. Consequently, floater selection is less critical for maximising AEP than for controlling platform motions, limiting power fluctuations and managing structural loads.

Overall, the results indicate that floater selection involves a balance between motion suppression, system complexity and operational robustness. While the TLP offers superior motion control, more flexible moored concepts such as spars and semi-submersibles achieve competitive energy yield with reduced design and installation constraints. The optimal choice therefore depends on system-level considerations and site-specific requirements rather than energy yield alone.

5.6. Limitations of the Study

The results presented in this thesis are subject to a number of modelling and methodological limitations that should be considered when interpreting the findings.

First, all simulations were performed using OpenFAST, which relies on reduced-order aerodynamic and hydrodynamic models. Aerodynamic loading is modelled using blade element momentum (BEM) theory, which does not fully capture three-dimensional flow effects, dynamic stall or wake-motion interaction at higher motion frequencies. Similarly, hydrodynamic loading is treated primarily within a linear framework based on first-order potential-flow theory, except for the VolturnUS-S platform where second-order effects are included. Nonlinear wave effects, viscous phenomena and wave breaking are therefore not fully represented.

Second, the environmental conditions are limited in scope. The analysis focuses on one offshore site and a representative set of wind and wave conditions. While sensitivity analyses were performed for wave height, mooring stiffness and wind-wave misalignment, extreme sea states, broader directional wind and wave spreading and turbulence in the wind speed were not considered. Moreover, fatigue and ultimate loads were not evaluated load cases.

Third, turbine control behaviour is based on a single, fixed controller tuning. Although the ROSCO controller is representative of industry-standard practice, controller tuning for each floater's properties can significantly influence platform damping, power variation and aero-servo-elastic coupling. Given the small differences in AEP observed between floater concepts, platform-specific controller tuning could potentially shift the relative ranking of concepts. The adoption of alternative or floating-specific control strategies could therefore alter some of the observed trends and warrants further investigation.

Fourth, the floating platforms were originally designed for their respective hub heights and structural configurations. In the present study, comparisons are made across platforms with different hub heights without updating the structural design of each platform to account for the resulting changes in overturning moment and mass distribution. This introduces a degree of inconsistency in the comparison, as increased hub height alters both the aerodynamic loading and the platform pitch response in ways that were not originally accounted for in the platform designs.

Finally, the analysis is limited to single-turbine simulations. Wake effects, wind-farm-level interactions and array control strategies are not considered. While previous studies suggest that motion-induced wake effects are generally small for isolated turbines, their cumulative impact at the wind-farm scale remains uncertain. These limitations do not invalidate the comparative trends observed between floater concepts, but they do define the scope within which the conclusions of this study should be applied.

5.7. Implications for Floating Wind Design

The results of this study provide several insights relevant to the early-stage design and selection of floating offshore wind turbine concepts.

First, the comparison between floater types indicates that platform dynamics primarily affect power variation rather than mean annual energy production. All investigated floating platforms achieve AEP values close to that of the fixed reference turbine, despite marked differences in surge and pitch response. This suggests that, for well-designed floating concepts, energy yield alone may not constitute a decisive criterion for floater selection. Instead, considerations related to power stability, structural loads and controller interaction become increasingly important.

Second, mooring system design plays a central role in shaping platform dynamics. Increased mooring stiffness systematically reduces surge and pitch motions and shortens natural periods, particularly for platforms relying on hydrostatic restoring mechanisms. However, the influence of mooring stiffness on mean power output remains limited. This highlights a trade-off between motion control and system complexity, where stiffer mooring configurations improve platform stability but may increase installation demands and structural loading without substantially improving energy yield.

Third, the results underline the importance of integrated controller-floater design. Floating platforms with larger low-frequency motions exhibit higher power variation, indicating stronger coupling between platform dynamics and turbine control actions. Control strategies capable of mitigating motion-induced power fluctuations may therefore offer tangible benefits, particularly for more flexible moored floating concepts. Given the sensitivity of AEP comparisons to controller tuning, platform-specific controller optimisation should be considered in future comparative studies.

Finally, the absence of a single clearly optimal floater across all performance metrics reinforces the context-dependent nature of floater selection. Spar, semi-submersible and tension-leg platforms each present distinct trade-offs between motion characteristics, power stability and design complexity. The suitability of a given floater type should therefore be assessed in relation to site conditions, installation constraints and system-level performance objectives rather than energy yield alone.

6

Conclusion & Recommendations

This chapter summarises the main findings of the thesis and formulates conclusions and recommendations based on the results presented and discussed in Chapters 4 and 5. The conclusions directly address the central research question and its sub-questions, while the recommendations outline implications for floating wind turbine design and suggest directions for future research.

6.1. Conclusion

The objective of this thesis was to investigate how floater type and mooring stiffness influence the energy yield of a floating offshore wind turbine. This was addressed using comparative OpenFAST simulations of the IEA 15 MW reference turbine mounted on four floating platform concepts (WindCrete spar buoy, ActiveFloat and VolturnUS-S semi-submersibles and a reference tension-leg platform) together with a fixed reference turbine baseline.

The free-decay analyses show that intrinsic platform dynamics are primarily governed by the dominant restoring mechanisms and mass distribution of each floater concept. Platforms relying on hydrostatic restoring exhibit longer natural periods and lower damping, whereas the reference TLP shows substantially shorter heave and pitch periods due to tendon pretension. The agreement of natural periods and qualitative damping trends with literature confirms the consistency of the modelling approach.

Under operational wind and wave conditions, platform response is dominated by surge and pitch motions. More flexible moored platforms display larger mean motions and increased variation, while the TLP exhibits minimal excursions due to its stiff station-keeping system. The fixed reference turbine serves as a useful baseline to isolate the additional dynamics introduced by floating support structures.

Despite these differences in platform dynamics, the impact on mean power output and annual energy production is limited. Across all floating configurations, total AEP remains within 2% of the fixed reference case. The results demonstrate that floating platforms primarily affect power stability rather than long-term energy yield. Surge and pitch motions introduce additional power fluctuations through variations in apparent wind speed and controller response, but these effects largely average out over time.

Sensitivity analyses confirm that numerical choices such as wind-speed bin sizing have a negligible effect on AEP and that wave conditions and wind-wave misalignment primarily influence short-term power variation rather than mean energy yield. Mooring stiffness significantly affects natural periods, damping and platform motions, particularly for restoring-force-dominated degrees of freedom. However, its influence on mean power output is limited. Increased stiffness reduces motion amplitudes and power variation but does not lead to substantial gains in AEP. The strongest sensitivity of power output to stiffness is observed for the TLP, although absolute changes remain small.

In conclusion, the central research question can be answered as follows: floater type and mooring stiffness have a strong influence on platform dynamics and power variation, but only a limited influence on annual energy production for well-designed floating wind turbine systems. No single floater concept can be identified as universally superior based on energy yield alone. Energy yield is robust across different floating concepts, while design choices primarily affect power stability and operational behaviour. Floater selection and mooring design are therefore more critical for controlling platform motions and limiting power fluctuations than for maximising annual energy production. The selection involves trade-offs between motion control, mooring complexity, installation requirements and power variation.

6.2. Recommendations

This section outlines recommendations derived from the findings of this thesis, addressing both practical implications for floating wind turbine design in the industry and directions for future academic research.

6.2.1. Recommendations for Design and Industry

Based on the findings of this thesis, several recommendations can be made for FOWT design:

- **Base floater selection on power stability and operational robustness, not energy yield alone.** AEP differences between well-designed floating concepts are small ($<$2%), so platform motions, power variation, structural loading, installation constraints and site suitability should be taken into account for concept selection in early-stage design.
- **Tune mooring stiffness primarily to control platform motions and power variation.** Increasing stiffness beyond a threshold yields diminishing returns in dynamic response while raising mooring loads, tendon pretension requirements and system complexity, without proportionally improving energy yield.
- **Optimise control strategies for each floater type.** Motion-induced power fluctuations play a key role in floating wind turbine performance. Floating-specific controller optimisation is particularly important for more flexibly moored semi-submersible and spar concepts. Controller tuning should therefore be integrated into the floater design process rather than treated as a separate post-design step.
- **Use wind-wave-aligned load cases for early-stage and comparative annual energy production studies.** Wind-wave misalignment was found to have a limited impact on energy yield under operational conditions. Aligned load cases from a single dominant direction are therefore generally sufficient for comparative AEP assessments, reserving misalignment analyses for detailed load and yaw strategy studies.

6.2.2. Recommendations for Future Research

Several opportunities for further research arise from the scope and limitations of this study:

- **Compare floater concepts designed from a common philosophy and equal constraints.** The platforms investigated here were developed under differing structural philosophies, hub heights and design objectives. A more meaningful future comparison would design all concepts from the same specification to eliminate the influence of design philosophy and isolate the effect of the stability mechanism.
- **Analyse floater performance across multiple offshore sites.** Restricting the analysis to a single site (Buchan Deep) limits the generalisability of the AEP conclusions. Future studies should evaluate how shifts in the Weibull wind speed distribution and wind shear exponent alter the relative ranking of floater concepts.
- **Investigate wind and wave directional spreading.** The sensitivity study considered discrete misalignment angles between collinear wind and wave directions. Realistic sea states exhibit directional spreading in both wind and waves; the effect of this spreading on platform response and power variation warrants dedicated investigation, including assessment of whether standard controller architectures can handle the resulting multi-directional loading.
- **Extend to a broader set of design load cases.** The analysis is limited to operational power production conditions. Extension to extreme sea states, fault cases and fatigue-driving load cases is needed to assess long-term structural integrity and to determine whether the motion rankings established here hold under non-operational conditions.
- **Incorporate higher-fidelity hydrodynamic modelling.** Linear potential-flow theory and Morison-element representations do not fully capture viscous drag, nonlinear wave loads and large-amplitude responses. Including second-order hydrodynamic effects uniformly across all floater concepts would reduce modelling inconsistency and improve the accuracy of predicted motion amplitudes and damping ratios.
- **Evaluate mooring stiffness sensitivity across the full wind speed range.** Assessing how stiffness variations affect platform motions and power output at different wind speed bins would yield more physically interpretable trends and guide mooring design more directly.
- **Optimise turbine control strategies for each floater type.** Given that the small AEP differences observed between floater concepts are sensitive to controller tuning, platform-specific controller optimisation should be included in future comparative studies. This includes retuning of the proportional-integral blade pitch controller gain schedule, exploration of active platform-damping feedback loops and evaluation of model-predictive control strategies.

AI statement

For this thesis, artificial intelligence tools were used to support text editing and code development. To improve textual clarity and readability, ChatGPT and Perplexity were used as an editorial aid to provide feedback on grammar, sentence structure and logical flow. The prompts were explicitly limited to language refinement and consistency checks, rather than content generation. In addition, QuillBot AI was used to paraphrase repetitive sentences to enhance readability. For code development and clarification, Microsoft Copilot was used within Visual Studio Code to assist with code generation and explanation. The content from both the text and code remains the sole responsibility of the author.

References

[1] National Renewable Energy Laboratory (NREL), *NREL Floats New Offshore Wind Cost Optimization Vision*, May 2025. [Online]. Available: https://www.nrel.gov/news/detail/program/2020/nrel-floats-new-offshore-wind-cost-optimization-tool.

[2] United Nations Framework Convention on Climate Change (UNFCCC), *The Paris Agreement*. [Online]. Available: https://unfccc.int/process-and-meetings/the-paris-agreement.

[3] International Energy Agency (IEA), *Net Zero Roadmap: A Global Pathway to Keep the 1.5 °C Goal in Reach*, Sep. 2023. [Online]. Available: https://www.iea.org/reports/net-zero-roadmap-a-global-pathway-to-keep-the-15-c-goal-in-reach.

[4] WindEurope, "Wind energy in Europe: 2024 Statistics and the outlook for 2025-2030," WindEurope, Tech. Rep., Feb. 2025. [Online]. Available: https://windeurope.org/data/products/wind-energy-in-europe-2024-statistics-and-the-outlook-for-2025-2030/.

[5] WindEurope, "Wind energy in Europe: 2025 Statistics and the outlook for 2026-2030," WindEurope, Tech. Rep., Feb. 2026. [Online]. Available: https://windeurope.org/data/products/wind-energy-in-europe-2025-statistics-and-the-outlook-for-2026-2030/.

[6] National Renewable Energy Laboratory (NREL) and Energy Industries Council (EIC), "Global Offshore Wind Report 2019: Norway/Equinor Internal Analysis," National Renewable Energy Laboratory / Energy Industries Council, Tech. Rep., 2019.

[7] R. James and M. C. Ros, "Floating Offshore Wind: Market and Technology Review," The Carbon Trust, commissioned by the Scottish Government, Tech. Rep., Jun. 2015. [Online]. Available: https://www.carbontrust.com/sites/default/files/documents/resource/public/Floating%20Offshore%20Wind%20Market%20Technology%20Review%20-%20REPORT.pdf.

[8] A. Al Mowafy, S. Lotfian, and F. Brennan, "Decommissioning Offshore Wind Fixed Steel Pile Foundations: A Critical Review," *Energies*, vol. 17, no. 21, Nov. 2024. DOI: 10.3390/en17215460.

[9] A. Viré and D. De Tavernier, *AE4W31 Floating Offshore Wind Energy, TU Delft*, 2024.

[10] Blue H Engineering, *Historical development*. [Online]. Available: https://www.bluehengineering.com/historical-development.html.

[11] J. Madslien, *Floating wind turbine launched*, Jun. 2009. [Online]. Available: http://news.bbc.co.uk/2/hi/business/8085551.stm.

[12] Principle Power, *Projects: WindFloat 1*. [Online]. Available: https://www.principlepower.com/projects/windfloat1.

[13] Equinor, *Hywind Tampen*. [Online]. Available: https://www.equinor.com/energy/hywind-tampen.

[14] RenewableUK, *Global floating wind project pipeline grows by 9% over last 12 months*, Oct. 2024. [Online]. Available: https://www.renewableuk.com/news-and-resources/press-releases/global-floating-wind-project-pipeline-grows-by-9-over-last-12-months.

[15] GE Vernova News, *GE's Haliade-X 14.7 MW-220 turbine obtains full DNV type certificat*, Dec. 2022. [Online]. Available: https://www.gevernova.com/news/press-releases/ge-haliade-x-14-7mw-220-turbine-obtains-full-dnv-type-certificate.

[16] A. Memija, *Dongfang Installs 'World's Largest Single-Capacity' Offshore Wind Turbine for Testing*, Sep. 2025. [Online]. Available: https://www.offshorewind.biz/2025/09/03/dongfang-installs-worlds-largest-single-capacity-offshore-wind-turbine-for-testing/.

[17] Topsector energie, *Standardisation Over Size - The Future of Offshore Wind Turbines*, Feb. 2019. [Online]. Available: https://topsectorenergie.nl/en/knowledge-base/standardisation-over-size-the-future-of-offshore-wind-turbines/.

[18] NedZero, *De North Seas Standard*. [Online]. Available: https://www.nedzero.nl/nl/kennisproducten-wind-op-zee/de-north-seas-standard.

[19] Ørsted, *Offshore Wind Energy*. [Online]. Available: https://orsted.com/en/what-we-do/renewable-energy-solutions/offshore-wind.

[20] J. Jonkman, S. Butterfield, W. Musial, and G. Scott, "Definition of a 5-MW Reference Wind Turbine for Offshore System Development," National Renewable Energy Labratory, Tech. Rep., Feb. 2009. DOI: 10.2172/947422. [Online]. Available: https://www.osti.gov/biblio/947422.

[21] C. Bak et al., “The DTU 10-MW Reference Wind Turbine,” Tech. Rep., 2013. [Online]. Available: https://backend.orbit.dtu.dk/ws/portalfiles/portal/55645274/The_DTU_10MW_Reference_Turbine_Christian_Bak.pdf.

[22] P. Bortolotti et al., “Systems Engineering in Wind Energy - WP2.1 Reference Wind Turbines,” International Energy Agency, Tech. Rep., May 2019. [Online]. Available: https://docs.nrel.gov/docs/fy19osti/73492.pdf?.

[23] E. Gaertner et al., “Definition of the IEA Wind 15-Megawatt Offshore Reference Wind Turbine Technical Report,” International Energy Agency, Tech. Rep., Mar. 2020. [Online]. Available: www.nrel.gov/publications.

[24] F. Zahle et al., “Definition of the IEA Wind 22-Megawatt Offshore Reference Wind Turbine,” International Energy Agency, Tech. Rep., Apr. 2024. DOI: 10.11581/DTU.00000317.

[25] D. Matha, J. Jonkman, and T. Fischer, “Model Development and Loads Analysis of a Wind Turbine on a Floating Offshore Tension Leg Platform,” Ph.D. dissertation, Jan. 2009.

[26] J. M. Jonkman and D. Matha, “Dynamics of offshore floating wind turbines-analysis of three concepts,” *Wind Energy*, vol. 14, no. 4, pp. 557–569, May 2011. DOI: 10.1002/we.442.

[27] A. Robertson and J. Jonkman, *Loads Analysis of Several Offshore Floating Wind Turbine Concepts*, Jan. 2011.

[28] I. Ramzanpoor, M. Nuernberg, and L. Tao, “Benchmarking study of 10 MW TLB floating offshore wind turbine,” *Journal of Ocean Engineering and Marine Energy*, vol. 10, no. 1, pp. 1–34, 2024. DOI: 10.1007/s40722-023-00295-w.

[29] P. Anant et al., “FAST Code Verification of Scaling Laws for DeepCwind Floating Wind System Tests,” Jun. 2012. [Online]. Available: https://docs.nrel.gov/docs/fy12osti/54221.pdf.

[30] H. Ahn and H. Shin, “Experimental and numerical analysis of a 10 MW floating offshore wind turbine in regular waves,” *Energies*, vol. 13, no. 10, May 2020. DOI: 10.3390/en13102608.

[31] R. Bergua et al., “OC6 project Phase III: validation of the aerodynamic loading on a wind turbine rotor undergoing large motion caused by a floating support structure,” *Wind Energy Science*, vol. 8, no. 4, pp. 465–485, Apr. 2023. DOI: 10.5194/wes-8-465-2023. [Online]. Available: https://docs.nrel.gov/docs/fy23osti/86250.pdf.

[32] M. Y. Mahfouz et al., “Public design and FAST models of the two 15MW floater-turbine concepts,” Corewind, Tech. Rep., Apr. 2020.

[33] C. Allen et al., “Definition of the UMaine VolturnUS-S Reference Platform Developed for the IEA Wind 15-Megawatt Offshore Reference Wind Turbine,” International Energy Agency, Tech. Rep., Jul. 2020. [Online]. Available: www.nrel.gov/publications..

[34] M. Hall, S. Housner, and L. Carmo, “A Reference Tension-Leg Platform for a 15-MW Floating Wind Turbine,” Jun. 2025. DOI: 10.1115/OMAE2025-157544.

[35] M. Mathiesen, A. K. Meyer, and B. Kvingedal, “Hywind Buchan Deep Metocean Design Basis RE2014-002,” May 2014. [Online]. Available: https://marine.gov.scot/sites/default/files/metocean_design_basis_hywind_buchan_deep_mdb_rev2_0.pdf.

[36] A. Betz, “Das Maximum der theoretisch möglichen Ausnützung des Windes durch Windmotoren,” *Zeitschrift für das gesamte Turbinenwesen*, vol. 26, pp. 307–309, 1920. DOI: 10.1260/0309-524X.37.4.441.

[37] A. Betz, “The Maximum of the Theoretically Possible Exploitation of Wind by Means of a Wind Motor,” *Wind Engineering*, vol. 37, no. 4, pp. 441–446, Aug. 2013. DOI: 10.1260/0309-524X.37.4.441.

[38] M. Zaayer and A. Viré, *AE4W02TU Introduction to Wind Turbines: Physics and Technology, TU Delft*, 2023.

[39] C. Simao Ferreira, *AE4135 Rotor / wake Aerodynamics, TU Delft*, 2023.

[40] N. Jenkins, T. Burton, E. Bossanyi, D. Sharpe, and M. Graham, *Wind Energy Handbook 3e*. Nov. 2021, ISBN: 9781119451143. DOI: 10.1002/9781119451143.

[41] E. Branlard, “Tip-Losses with Focus on Prandlt’s Tip Loss Factor,” in 2017, pp. 227–245. DOI: https://doi.org/10.1007/978-3-319-55164-7{_}13.

[42] C. J. S. Ferreira, *AE4W21-14 Wind Turbine Aeroelasticity, TU Delft*, 2024.

[43] Q. Van Suijlen, “Floating to Floating Installation of a Full 15 MW Wind Turbine on a Tension Leg Platform with a Semi-Submersible Crane Vessel,” TU Delft, Tech. Rep., Apr. 2023. [Online]. Available: https://resolver.tudelft.nl/uuid:2ca9baa7-55f4-4f67-a3a0-d0c5a8a1e4d6.

[44] D. Fiscaletti, *OE44150 Marine Hydromechanics, TU Delft*, 2025.

[45] P. Wellens and P. Naaijen, *MT44021 Motions & Loading of Structures in Waves, TU Delft*, 2024.

[46] *Guide to a floating offshore wind farm | An informative resource for floating offshore wind*. [Online]. Available: https://guidetofloatingoffshorewind.com/.

[47] Z. Jiang, "Mooring design for floating wind turbines: A review," *Renewable and Sustainable Energy Reviews*, vol. 212, p. 115 231, Apr. 2025. DOI: 10.1016/j.rser.2024.115231.

[48] P. Trubat et al., "D1.6 Design Recommendations and Impact of Mooring and Dynamic Cables Into Integrated Modelling and Structural Design," Corewind, Tech. Rep., Mar. 2023.

[49] B. Cerfontaine, S. Gourvenec, and D. White, "Specificities of floating offshore wind turbines for risk and safety evaluation of anchoring systems," in *Geotechnical Engineering Challenges to Meet Current and Emerging Needs of Society*, London: CRC Press, Sep. 2024, pp. 154–166. DOI: 10.1201/9781003431749-10.

[50] O. Apata and D. T. Oyedokun, "An overview of control techniques for wind turbine systems," *Scientific African*, vol. 10, Nov. 2020. DOI: 10.1016/j.sciaf.2020.e00566.

[51] D. L. Contreras, J. M. Canedo, and D. P. Montoya, "A modified power flow algorithm in power systems with renewable energy sources," in *2017 North American Power Symposium (NAPS)*, IEEE, Sep. 2017, pp. 1–6. DOI: 10.1109/NAPS.2017.8107242.

[52] H. Namik and K. Stol, "A Review of Floating Wind Turbine Controllers," pp. 415–441, Jan. 2013. DOI: 10.1007/978-3-642-41080-2{_}13.

[53] D. Stockhouse et al., "Sink or Swim: A Tutorial on the Control of Floating Wind Turbines," in *2023 American Control Conference (ACC)*, 2023, pp. 2512–2529. DOI: 10.23919/ACC55779.2023.10155920.

[54] D. Van Den Berg, D. De Tavernier, and J. W. Van Wingerden, "The dynamic coupling between the pulse wake mixing strategy and floating wind turbines," *Wind Energy Science*, vol. 8, no. 5, pp. 849–864, May 2023. DOI: 10.5194/wes-8-849-2023.

[55] A. Hegazy, P. Naaijen, and J.-W. Van Wingerden, "Control design for floating wind turbines," *Wind Energy Science Discussions*, 2025. DOI: 10.5194/wes-2025-68.

[56] D. Qiao and J. Ou, "Mooring Line Damping Estimation for a Floating Wind Turbine," *The Scientific World Journal*, vol. 2014, pp. 1–10, Aug. 2014. DOI: 10.1155/2014/840283.

[57] J. Pan, S. Witter, M. Cardaun, T. Reichartz, R. Schelenz, and G. Jacobs, "Dynamic behavior and damping effects of catenary mooring lines for a floating offshore wind turbine," *Ocean Engineering*, vol. 339, p. 122 017, Jul. 2025. DOI: 10.1016/j.oceaneng.2025.122017.

[58] W. Bierbooms, *AE4W13 Site Conditions for Wind Turbine Design, TU Delft*, 2024.

[59] J. Cui et al., "Research on the Power Output of Different Floating Wind Farms Considering the Wake Effect," *Journal of Marine Science and Engineering*, vol. 12, no. 9, p. 1475, Aug. 2024. DOI: 10.3390/jmse12091475.

[60] V. Gupta, "Evaluating the Impact of FOWT Displacement on Energy Yield for Wind Farm Optimization," Ph.D. dissertation, TU Delft, Oct. 2024.

[61] A. Lauria, P. Loprieno, A. Francone, E. Leone, and G. Tomasicchio, "Recent advances in understanding the dynamic characterization of floating offshore wind turbines," *Ocean Engineering*, vol. 307, p. 118 189, Sep. 2024. DOI: 10.1016/j.oceaneng.2024.118189.

[62] U.S. Department of Energy, *New Reference Turbine Model Accelerates Development of Larger, Cost-Competitive Offshore Wind Systems | Department of Energy*, Jul. 2020. [Online]. Available: https://www.energy.gov/eere/wind/articles/new-reference-turbine-model-accelerates-development-larger-cost-competitive.

[63] N. Mendoza et al., "Verification and Validation of Model-Scale Turbine Performance and Control Strategies for the IEA Wind 15 MW Reference Wind Turbine," *Energies*, vol. 15, no. 20, p. 7649, Oct. 2022. DOI: 10.3390/en15207649.

[64] W. Collier et al., "Aeroelastic code comparison using the IEA 22MW reference turbine," 5, vol. 2767, Jun. 2024, p. 052 042. DOI: 10.1088/1742-6596/2767/5/052042.

[65] M. Maali Amiri, M. Shadman, and S. F. Estefen, "A Review of Numerical and Physical Methods for Analyzing the Coupled Hydro-Aero-Structural Dynamics of Floating Wind Turbine Systems," *Journal of Marine Science and Engineering*, vol. 12, no. 3, p. 392, Feb. 2024. DOI: 10.3390/jmse12030392.

[66] E. Faraggiana, G. Giorgi, M. Sirigu, A. Ghigo, G. Bracco, and G. Mattiazzo, "A review of numerical modelling and optimisation of the floating support structure for offshore wind turbines," *Journal of Ocean Engineering and Marine Energy*, vol. 8, no. 3, pp. 433–456, Aug. 2022. DOI: 10.1007/s40722-022-00241-2.

[67] Orcina, *OrcaFlex - dynamic analysis software for offshore marine systems*. [Online]. Available: https://www.orcina.com/orcaflex/.

[68] Det Norske Veritas (DNV), *Bladed - wind turbine design software*. [Online]. Available: https://www.dnv.com/software/services/bladed/.

[69] Danmarks Tekniske Universitet (DTU), *HAWC2: An aeroelastic code*. [Online]. Available: https://www.hawc2.dk/.

[70] National Renewable Energy Laboratory (NREL), *OpenFAST Documentation - v4.1.2*, Nov. 2025. [Online]. Available: https://openfast.readthedocs.io/en/dev/index.html.

[71] A. Robertson et al., "Offshore Code Comparison Collaboration, Continuation within IEA Wind Task 30: Phase II Results Regarding a Floating Semisubmersible Wind System," Tech. Rep., 2014.

[72] J. Rinker et al., "Comparison of loads from HAWC2 and OpenFAST for the IEA Wind 15 MW Reference Wind Turbine," in *Journal of Physics: Conference Series*, vol. 1618, IOP Publishing Ltd, Sep. 2020. DOI: 10.1088/1742-6596/1618/5/052052.

[73] National Renewable Energy Laboratory (NREL), *Wind research: OpenFAST*. [Online]. Available: https://www.nrel.gov/wind/nwtc/openfast.

[74] N. J. Abbas, D. S. Zalkind, L. Pao, and A. Wright, "A reference open-source controller for fixed and floating offshore wind turbines," *Wind Energy Science*, vol. 7, no. 1, pp. 53–73, Jan. 2022. DOI: 10.5194/wes-7-53-2022.

[75] F. Papi, J. Jonkman, A. Robertson, and A. Bianchini, "Going beyond BEM with BEM: an insight into dynamic inflow effects on floating wind turbines," *Wind Energy Science*, vol. 9, no. 5, pp. 1069–1088, May 2024. DOI: 10.5194/wes-9-1069-2024.

[76] G. Stewart and M. Muskulus, "A Review and Comparison of Floating Offshore Wind Turbine Model Experiments," *Energy Procedia*, vol. 94, pp. 227–231, Sep. 2016. DOI: 10.1016/j.egypro.2016.09.228.

[77] K. Brown et al., "One-to-one aeroservoelastic validation of operational loads and performance of a 2.8 MW wind turbine model in OpenFAST," *Wind Energy Science*, vol. 9, no. 8, pp. 1791–1810, Aug. 2024. DOI: 10.5194/WES-9-1791-2024.

[78] A. Viselli, N. Faessler, and M. Filippelli, "Analysis of Wind Speed Shear and Turbulence LiDAR Measurements to Support Offshore Wind in the Northeast United States," in *ASME 2018 1st International Offshore Wind Technical Conference*, American Society of Mechanical Engineers, Nov. 2018, ISBN: 978-0-7918-5197-5. DOI: 10.1115/IOWTC2018-1003.

[79] A. Viselli, N. Faessler, and M. Filippelli, "LiDAR Measurements of Wind Shear Exponents and Turbulence Intensity Offshore the Northeast United States," *Journal of Offshore Mechanics and Arctic Engineering*, vol. 144, no. 4, Aug. 2022. DOI: 10.1115/1.4053583.

[80] NEN (Dutch Standardisation Institute), *Wind Turbines - Part 1: General Requirements*, 2019.

[81] NEN (Dutch Standardisation Institute), *Wind Turbines - Part 3-2: Design Requirements for Floating Offshore Wind Turbines*, 2025.

[82] ABSG Consulting Inc., "Floating Offshore Wind Turbine Development Assessment: Final Report and Technical Summary," ABSG Consulting Inc., Tech. Rep., Mar. 2021.

[83] M. Maktabi and E. Rusu, "A Review of Perspectives on Developing Floating Wind Farms," *Inventions*, vol. 9, no. 2, p. 24, Feb. 2024. DOI: 10.3390/inventions9020024.

[84] International Renewable Energy Agency (IRENA), "Floating Offshore Wind Outlook," IRENA, Tech. Rep., Jun. 2024. [Online]. Available: https://www.irena.org/-/media/Files/IRENA/Agency/Publication/2024/Jul/IRENA_G7_Floating_offshore_wind_outlook_2024.pdf.

[85] R. Bergua et al., "OC6 project Phase IV: Validation of numerical models for novel floating offshore wind support structures," *Wind Energy Science*, vol. 9, no. 4, pp. 1025–1051, Apr. 2024. DOI: 10.5194/wes-9-1025-2024.

[86] H. Darling et al., "OC6 Phase IV: Validation of CFD Models for Stiesdal TetraSpar Floating Offshore Wind Platform," *Wind Energy*, vol. 28, no. 1, Jan. 2025. DOI: 10.1002/we.2966.

[87] A. N. Robertson et al., "Summary of Conclusions and Recommendations Drawn From the DeepCwind Scaled Floating Offshore Wind System Test Campaign," in *Volume 8: Ocean Renewable Energy*, American Society of Mechanical Engineers, Jun. 2013, ISBN: 978-0-7918-5542-3. DOI: 10.1115/OMAE2013-10817.

[88] J. Jonkman and W. Musial, "Offshore Code Comparison Collaboration (OC3) for IEA Wind Task 23 Offshore Wind Technology and Deployment," National Renewable Energy Laboratory (NREL), Tech. Rep., Dec. 2010. DOI: 10.2172/1004009.

[89] *Fixed versus floating offshore wind | Guide to a floating offshore wind farm*. [Online]. Available: https://guidetofloatingoffshorewind.com/fixed-versus-floating-offshore-wind/.

[90] Modern Power Systems, *Outstanding load factor performance from the world's first floating wind farm*. [Online]. Available: https://www.modernpowersystems.com/analysis/outstanding-load-factor-performance-from-the-worlds-first-floating-wind-farm-6151857/.

[91] Equinor, *Hywind Scotland - the world's first floating wind farm - Equinor*. [Online]. Available: https://www.equinor.com/energy/hywind-scotland.

[92] *Windfloat Atlantic*. [Online]. Available: https://windfloat-atlantic.com/.

[93] Principle Power, *Projects: Kincardine Offshore Wind Farm*. [Online]. Available: https://www.principlepower.com/projects/kincardine-offshore-wind-farm.

[94] *Projet Ferme Eolienne flottante marine au Golfe du Lion*. [Online]. Available: https://info-efgl.fr/.

[95] BW Ideol, *Floatgen*. [Online]. Available: https://www.bw-ideol.com/en/floatgen-demonstrator.

[96] BW Ideol, *EolMed Project*. [Online]. Available: https://www.bw-ideol.com/en/eolmed-project.

[97] Provence Grand Large, *Provence Grand Large*. [Online]. Available: https://provencegrandlarge.fr/en/home/.

[98] Stiesdal Offshore, *The TetraSpar Demonstrator*. [Online]. Available: https://stiesdaloffshore.com/projects/the-tetraspar-full-scale-demonstration-project/.

[99] A. Memija, *TetraSpar Demonstrator Floating Wind Turbine Hits 63 Pct Capacity Factor in Norway*, May 2024. [Online]. Available: https://www.offshorewind.biz/2024/05/27/tetraspar-demonstrator-floating-wind-turbine-hits-63-pct-capacity-factor-in-norway/.

[100] Green Volt, *Green Volt - Floating Wind At Scale*. [Online]. Available: https://greenvoltoffshorewind.com/.

[101] Cenos, *Cenos Floating Offshore Wind Farm*. [Online]. Available: https://cenosoffshorewind.com/.

[102] Orcina, "Comparison of loads from OrcaFlex and OpenFAST for the IEA 15 MW RWT," [Online]. Available: www.orcina.com.

[103] M. Fowler et al., "Wind/Wave Testing of a 1:70-Scale Performance-Matched Model of the IEA Wind 15 MW Reference Wind Turbine with Real-Time ROSCO Control and Floating Feedback," *Machines*, vol. 11, no. 9, Sep. 2023. DOI: 10.3390/machines11090865.

[104] *OpenFAST Github*. [Online]. Available: https://github.com/OpenFAST/openfast.

[105] F. Vigara et al., "D1.2 Design basis," Corewind, Tech. Rep., Dec. 2019.

[106] M. Hall et al., "The IEA Wind Task 49 Reference Floating Wind Array Design Basis," International Energy Agency, Tech. Rep., Jun. 2024. [Online]. Available: https://docs.nrel.gov/docs/fy24osti/89709.pdf#page=52.29.

[107] A. B. Krishna Pribadi, A. Al-Ghuwaidi, and E. Lataire, "Open-access simulation dataset of the floating wind turbine DeepCwind OC4 in wind and waves," *Journal of Physics: Conference Series*, vol. 3131, no. 1, p. 012 024, Oct. 2025. DOI: 10.1088/1742-6596/3131/1/012024.

[108] A. B. K. Pribadi and E. Lataire, *Deliverable 1.1.1.1 BEL-Float project | Dataset containing the results of numerical simulations (motions, forces) of the operational performance analysis - Input files*, Oct. 2024. DOI: 10.5281/zenodo.13940284.

[109] A. B. K. Pribadi and E. Lataire, *Deliverable 1.1.1.1 BEL-Float project | Report describing the dataset containing the results of numerical simulations (motions, forces) of the operational performance analysis*, Nov. 2024. DOI: 10.5281/zenodo.14223737.

[110] O. Grootes, *Floater_data_thesis_2026*, Version: commit abc1234, 2026. [Online]. Available: https://github.com/ogrootes/FloaterThesisData-2026.git.

[111] *ROSCO Github*. [Online]. Available: https://github.com/NatLabRockies/ROSCO.

[112] *OpenFAST Toolbox Github*. [Online]. Available: https://github.com/OpenFAST/openfast_toolbox/blob/main/openfast_toolbox/case_generation/examples/Example_Parametric.py.

[113] M. Karimirad and T. Moan, "Wave-and Wind-Induced Dynamic Response of a Spar-Type Offshore Wind Turbine," 2012. DOI: 10.1061/(ASCE)WW.1943-5460.

A

Hywind Buchan Deep Metocean Data

The metocean data used throughout this thesis originates from the NORA10 hindcast dataset (1958-2010) for the Buchan Deep region northeast of Scotland, coinciding with the Hywind Scotland pilot farm location. Figure A.1 presents the scatter plot of 1-hour mean wind speed at 100 m height and significant wave height.

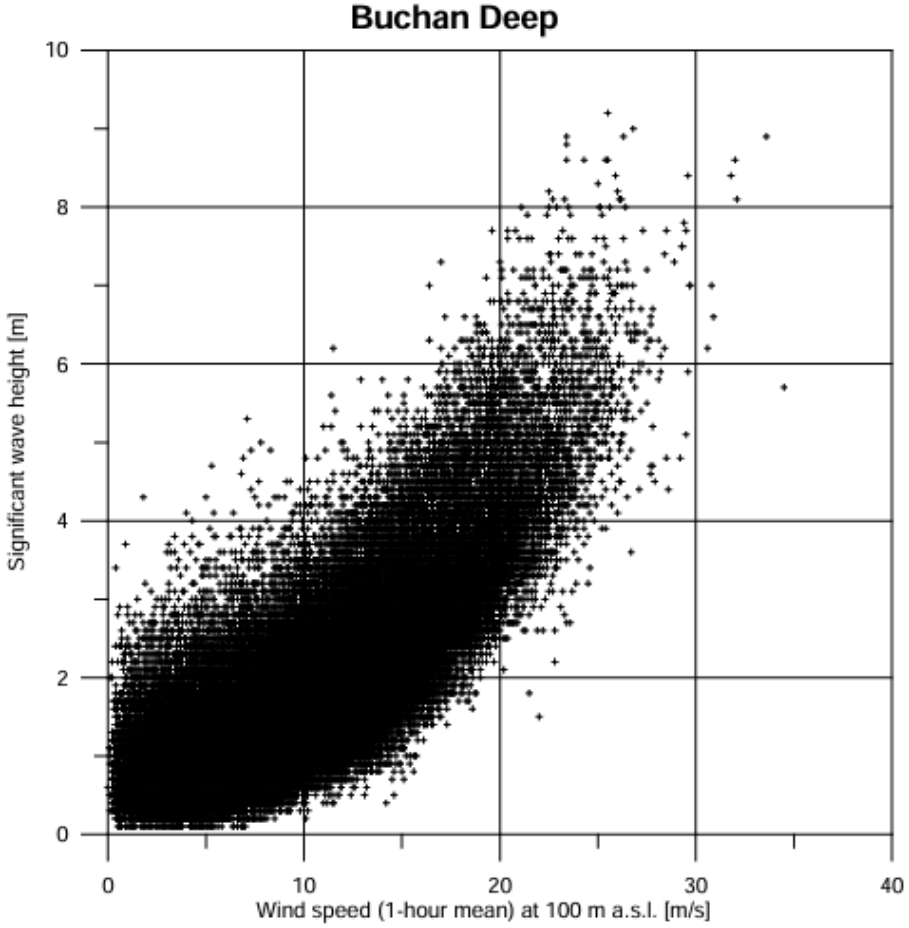

Figure A.1: Significant wave height versus 1-hour mean wind speed at 100 m height at Buchan Deep. Data: Nora 10 hindcast data for the period 1958 - 2010 [35].

Table A.1 provides the complete scatter table showing joint occurrence frequencies across 1 m/s wind speed and 1 m wave height bins (values represent occurrence counts).

Table A.1: Scatter table of significant wave height versus 1-hour mean wind speed (Wspd) at 100 m above sea level at Buchan Deep. Data: Nora 10 hindcast data for the period 1958-2010 [35].

Wspd	Significant wave height [m]										
[m/s]	0-1	1-2	2-3	3-4	4-5	5-6	6-7	7-8	8-9	9-10	Sum
0.5	391	208	28	2	0	0	0	0	0	0	629
1.5	1161	649	77	2	1	0	0	0	0	0	1890
2.5	1899	1014	122	4	0	0	0	0	0	0	3039
3.5	2260	1427	170	17	0	0	0	0	0	0	3874
4.5	2586	1799	263	22	2	0	0	0	0	0	4672
5.5	2632	2268	333	25	3	0	0	0	0	0	5261
6.5	2668	2876	421	51	3	0	0	0	0	0	6019
7.5	2374	3422	604	63	5	2	0	0	0	0	6470
8.5	1880	4018	862	78	5	0	0	0	0	0	6843
9.5	1097	4527	1014	144	12	0	0	0	0	0	6794
10.5	593	4634	1397	217	17	0	0	0	0	0	6858
11.5	292	4029	1789	333	24	5	1	0	0	0	6473
12.5	84	3309	2126	508	58	3	0	0	0	0	6088
13.5	35	2264	2355	673	88	5	0	0	0	0	5420
14.5	13	1214	2447	746	163	12	0	0	0	0	4595
15.5	4	509	2282	868	256	26	0	0	0	0	3945
16.5	0	170	1587	897	290	48	2	1	0	0	2995
17.5	0	38	959	969	342	83	8	1	0	0	2400
18.5	0	14	490	922	353	122	23	0	0	0	1924
19.5	0	0	166	747	342	170	30	2	0	0	1457
20.5	0	0	52	466	351	145	41	7	0	0	1062
21.5	0	1	9	195	302	125	42	12	1	0	687
22.5	0	1	4	72	232	105	54	8	4	0	480
23.5	0	0	4	22	130	86	40	16	5	0	303
24.5	0	0	0	7	38	86	38	12	1	0	182
25.5	0	0	0	2	12	48	29	9	7	1	108
26.5	0	0	0	1	9	22	17	9	5	1	64
27.5	0	0	0	0	5	5	12	2	0	0	24
28.5	0	0	0	0	2	2	3	3	0	0	10
29.5	0	0	0	0	1	2	0	6	1	0	10
30.5	0	0	0	0	0	0	2	1	0	0	3
31.5	0	0	0	0	0	0	0	0	1	0	1
32.5	0	0	0	0	0	0	0	0	2	0	2
33.5	0	0	0	0	0	0	0	0	1	0	1
34.5	0	0	0	0	0	1	0	0	0	0	1
Sum	19969	38391	19561	8053	3046	1103	342	89	28	2	90584
Mean	5.64	8.99	12.7	15.91	18.52	2064	22.43	23.99	25.74	26.15	
Std	2.59	3.31	3.52	3.39	3.2	2.97	2.72	2.87	3.19	0.65	

B

Wind speed bin sizes for simulations

The annual energy production assessment uses the Buchan Deep Weibull distribution at hub height (150 m) with shape factor $= 2.235$, scale factor $= 10.03$ m/s and location factor of $= 0.0$ m/s (extrapolated from 10 m NORA10 hindcast data using $\alpha = 0.11$ shear) [35].

To compute bin occurrence probabilities for AEP, the continuous Weibull PDF is discretised into wind speed bins. The probability for each bin is divided by bin width to compute the probability density for the figures in this appendix. The discretised PDF does not sum 1.00, as the infinite upper tail of the Weibull distribution extends far beyond the cut-out wind speed. The missing percentage falls outside the operational range and does not affect the results.

The Weibull graph has been plotted with finer bins between cut-in (3 m/s) and rated (10.59 m/s) and around cut-out (25 m/s) to capture transitions accurately. The different bin sizes are: 1.0 m/s (Figure B.1), 0.5 m/s (Figure B.2) and 0.25 m/s (Figure B.3). Detailed simulation parameters (mean wind speed, occurrence, wave height and peak spectral period) are given in Table B.1-B.3.

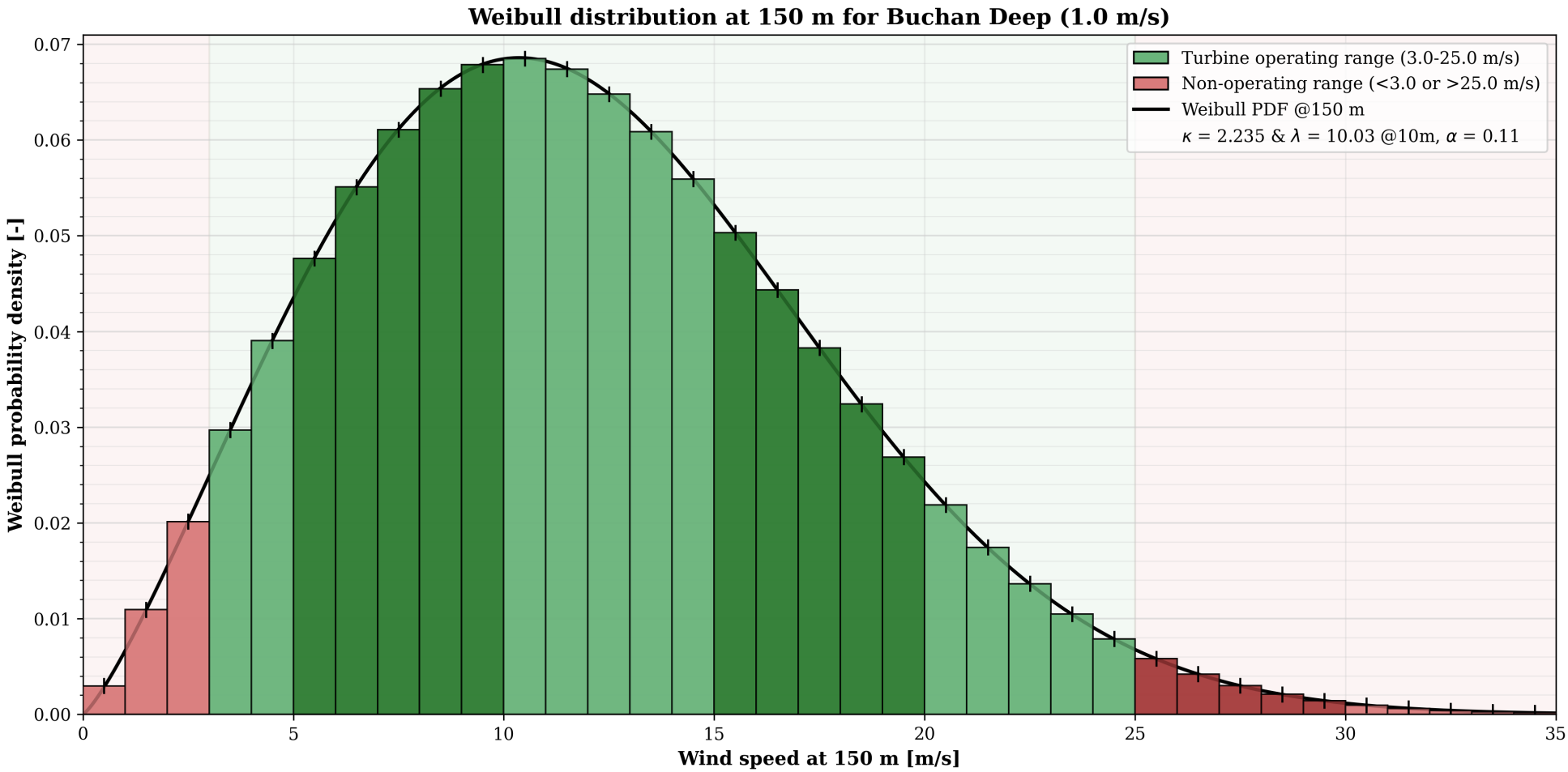

Figure B.1: Weibull distribution at 150 m height at Buchan Deep. The distribution is defined by shape parameter κ = 2.235 and scale parameter λ = 10.03 m/s, both specified at 10 m height. Wind speeds are extrapolated to 150 m using the power law with a shear exponent α = 0.11. A default bin size of 1.0 m/s is applied. Shading intervals change every 5 m/s for improved visual clarity. The detailed data for the figure can be found in Table B.1.

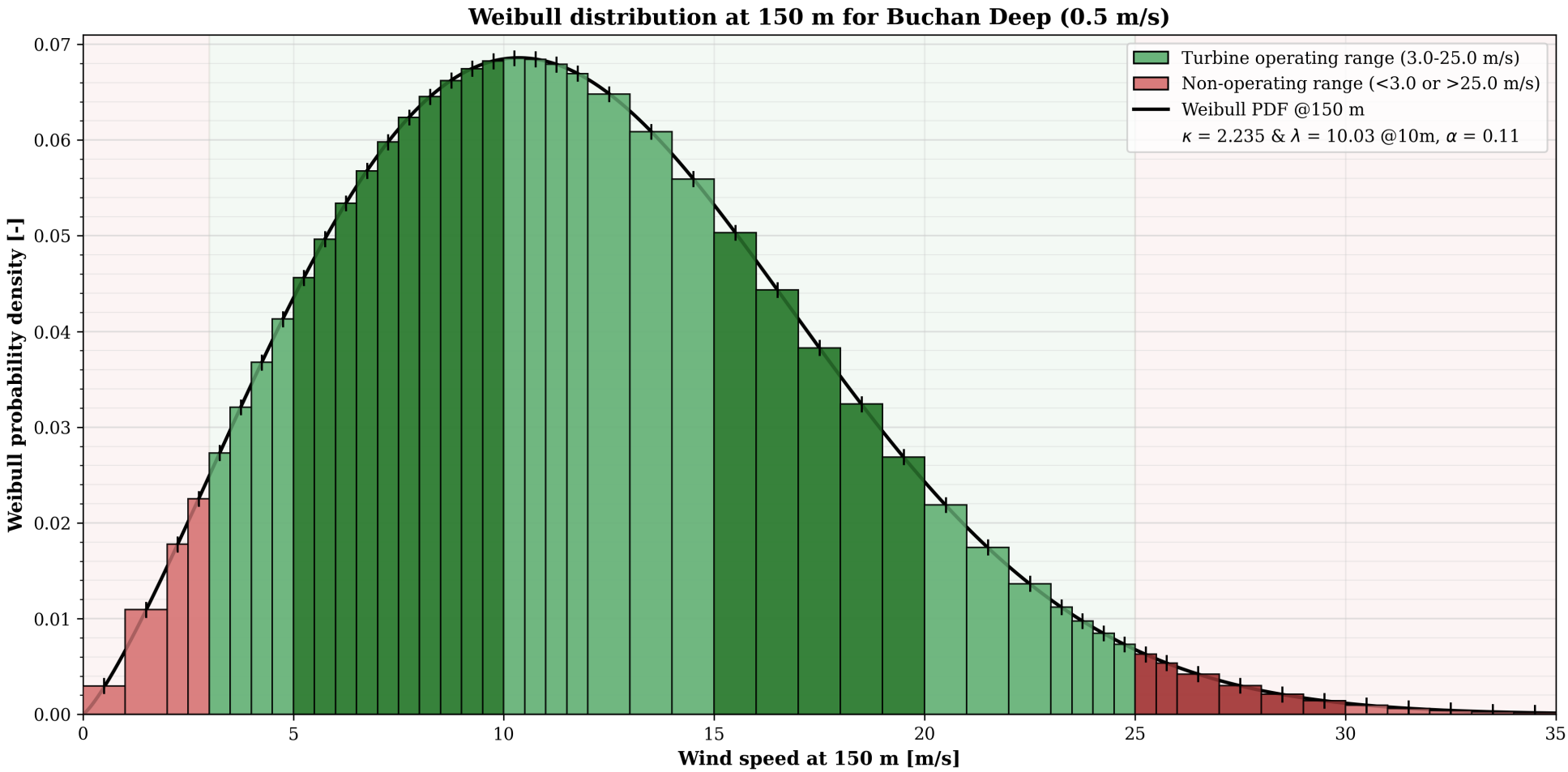

Figure B.2: Weibull distribution at 150 m height at Buchan Deep. The distribution is defined by shape parameter κ = 2.235 and scale parameter λ = 10.03 m/s, both specified at 10 m height. Wind speeds are extrapolated to 150 m using the power law with a shear exponent α = 0.11. A default bin size of 1.0 m/s is applied. Between cut-in and rated wind speeds and in the vicinity of the cut-out wind speed, a finer bin size of 0.5 m/s is used. Shading intervals change every 5 m/s for improved visual clarity. The detailed data for the figure can be found in Table B.2.

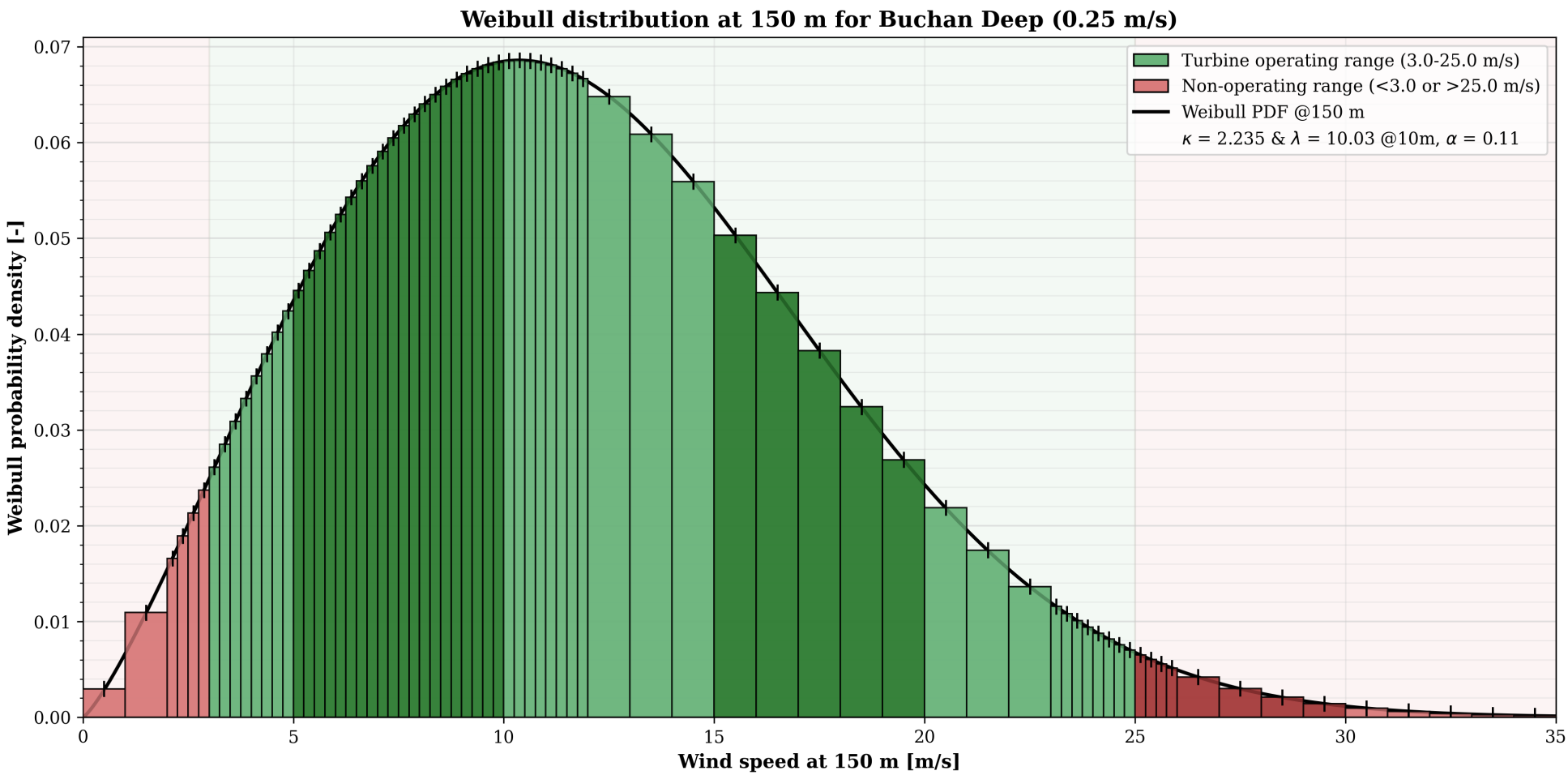

Figure B.3: Weibull distribution at 150 m height at Buchan Deep. The distribution is defined by shape parameter κ = 2.235 and scale parameter λ = 10.03 m/s, both specified at 10 m height. Wind speeds are extrapolated to 150 m using the power law with a shear exponent α = 0.11. A default bin size of 1.0 m/s is applied. Between cut-in and rated wind speeds and in the vicinity of the cut-out wind speed, a finer bin size of 0.25 m/s is used. Shading intervals change every 5 m/s for improved visual clarity. The detailed data for the figure can be found in Table B.3.

Table B.1: Wind speed bins and environmental conditions for simulations at Buchan Deep (150 m Weibull distribution shown in Figure B.1). The default binning is 1.0 m/s. The row shading changes every 5 m/s for clarity.

150 m height				100 m height	Significant wave height [m]	Spectral peak period [s]	10 m height			PDF [-]	CDF [-]	Operational time [hrs]	Operational envelope
Lower limit [m/s]	Upper limit [m/s]	Bin size [m/s]	Wind speed [m/s]	Wind speed [m/s]			Lower limit [m/s]	Upper limit [m/s]	Wind speed [m/s]				
0.0	1.0	1.0	0.5	0.48	0.75	6.66	0.00	0.74	0.37	0.0030	0.0030	26	FALSE
1.0	2.0	1.0	1.5	1.43	0.81	6.72	0.74	1.48	1.11	0.0109	0.0139	96	FALSE
2.0	3.0	1.0	2.5	2.39	0.88	6.78	1.48	2.23	1.86	0.0201	0.0340	176	TRUE
3.0	4.0	1.0	3.5	3.35	0.95	6.85	2.23	2.97	2.60	0.0297	0.0637	260	TRUE
4.0	5.0	1.0	4.5	4.30	1.03	6.93	2.97	3.71	3.34	0.0390	0.1028	342	TRUE
5.0	6.0	1.0	5.5	5.26	1.11	7.01	3.71	4.45	4.08	0.0476	0.1504	417	TRUE
6.0	7.0	1.0	6.5	6.22	1.21	7.09	4.45	5.20	4.83	0.0551	0.2055	483	TRUE
7.0	8.0	1.0	7.5	7.17	1.31	7.19	5.20	5.94	5.57	0.0611	0.2666	535	TRUE
8.0	9.0	1.0	8.5	8.13	1.41	7.29	5.94	6.68	6.31	0.0654	0.3319	573	TRUE
9.0	10.0	1.0	9.5	9.09	1.53	7.40	6.68	7.42	7.05	0.0679	0.3998	594	TRUE
10.0	11.0	1.0	10.5	10.04	1.66	7.52	7.42	8.17	7.80	0.0685	0.4683	600	TRUE
11.0	12.0	1.0	11.5	11.00	1.80	7.64	8.17	8.91	8.54	0.0674	0.5357	591	TRUE
12.0	13.0	1.0	12.5	11.95	1.94	7.78	8.91	9.65	9.28	0.0648	0.6005	568	TRUE
13.0	14.0	1.0	13.5	12.91	2.10	7.93	9.65	10.39	10.02	0.0609	0.6614	533	TRUE
14.0	15.0	1.0	14.5	13.87	2.28	8.08	10.39	11.14	10.76	0.0559	0.7173	490	TRUE
15.0	16.0	1.0	15.5	14.82	2.47	8.25	11.14	11.88	11.51	0.0503	0.7676	441	TRUE
16.0	17.0	1.0	16.5	15.78	2.67	8.44	11.88	12.62	12.25	0.0443	0.8120	388	TRUE
17.0	18.0	1.0	17.5	16.74	2.89	8.63	12.62	13.36	12.99	0.0383	0.8503	335	TRUE
18.0	19.0	1.0	18.5	17.69	3.13	8.84	13.36	14.11	13.73	0.0324	0.8827	284	TRUE
19.0	20.0	1.0	19.5	18.65	3.39	9.07	14.11	14.85	14.48	0.0269	0.9096	236	TRUE
20.0	21.0	1.0	20.5	19.61	3.67	9.31	14.85	15.59	15.22	0.0219	0.9314	192	TRUE
21.0	22.0	1.0	21.5	20.56	3.98	9.57	15.59	16.33	15.96	0.0174	0.9489	153	TRUE
22.0	23.0	1.0	22.5	21.52	4.31	9.84	16.33	17.07	16.70	0.0136	0.9625	120	TRUE
23.0	24.0	1.0	23.5	22.47	4.66	10.13	17.07	17.82	17.45	0.0105	0.9730	92	TRUE
24.0	25.0	1.0	24.5	23.43	5.05	10.45	17.82	18.56	18.19	0.0079	0.9809	69	TRUE
25.0	26.0	1.0	25.5	24.39	5.47	10.78	18.56	19.30	18.93	0.0058	0.9867	51	TRUE
26.0	27.0	1.0	26.5	25.34	5.92	11.13	19.30	20.04	19.67	0.0042	0.9909	37	FALSE
27.0	28.0	1.0	27.5	26.30	6.41	11.50	20.04	20.79	20.42	0.0030	0.9939	26	FALSE
28.0	29.0	1.0	28.5	27.26	6.94	11.90	20.79	21.53	21.16	0.0021	0.9960	18	FALSE

Continued on next page

Table B.1 – continued from previous page

150 m height				100 m height	Significant	Spectral	10 m height			PDF [-]	CDF [-]	Operational	Operational
Lower limit [m/s]	Upper limit [m/s]	Bin size [m/s]	Wind speed [m/s]	Wind speed [m/s]	wave height [m]	peak period [s]	Lower limit [m/s]	Upper limit [m/s]	Wind speed [m/s]			time [hrs]	envelope
29.0	30.0	1.0	29.5	28.21	7.52	12.31	21.53	22.27	21.90	0.0014	0.9974	12	FALSE
30.0	31.0	1.0	30.5	29.17	8.14	12.75	22.27	23.01	22.64	0.0010	0.9983	8	FALSE
31.0	32.0	1.0	31.5	30.13	8.82	13.21	23.01	23.76	23.39	0.0006	0.9990	5	FALSE
32.0	33.0	1.0	32.5	31.08	9.55	13.68	23.76	24.50	24.13	0.0004	0.9994	4	FALSE
33.0	34.0	1.0	33.5	32.04	10.34	14.18	24.50	25.24	24.87	0.0003	0.9996	2	FALSE
34.0	35.0	1.0	34.5	33.00	11.19	14.69	25.24	25.98	25.61	0.0002	0.9998	1	FALSE
									Total:	0.9998	-	8758	-

Table B.2: Wind speed bins and environmental conditions for simulations at Buchan Deep (150 m Weibull distribution shown in Figure B.2). The default binning is 1.0 m/s; refined to 0.5 m/s between rated-cut-out and around cut-out speeds (bold). The row shading changes every 5 m/s for clarity.

150 m height				100 m height	Significant	Spectral	10 m height			PDF [-]	CDF [-]	Operational	Operational
Lower limit [m/s]	Upper limit [m/s]	Bin size [m/s]	Wind speed [m/s]	Wind speed [m/s]	wave height [m]	peak period [s]	Lower limit [m/s]	Upper limit [m/s]	Wind speed [m/s]			time [hrs]	envelope
0.0	1.0	1.0	0.5	0.48	0.75	6.66	0.00	0.74	0.37	0.0030	0.0030	26	FALSE
1.0	2.0	1.0	1.5	1.43	0.81	6.72	0.74	1.48	1.11	0.0109	0.0139	96	FALSE
2.0	2.5	0.5	2.3	2.15	0.86	6.77	1.48	1.86	1.67	0.0089	0.0228	78	FALSE
2.5	3.0	0.5	2.8	2.63	0.89	6.80	1.86	2.23	2.04	0.0113	0.0340	99	TRUE
3.0	3.5	0.5	3.3	3.11	0.93	6.83	2.23	2.60	2.41	0.0137	0.0477	120	TRUE
3.5	4.0	0.5	3.8	3.59	0.97	6.87	2.60	2.97	2.78	0.0160	0.0637	141	TRUE
4.0	4.5	0.5	4.3	4.06	1.01	6.91	2.97	3.34	3.16	0.0184	0.0821	161	TRUE
4.5	5.0	0.5	4.8	4.54	1.05	6.95	3.34	3.71	3.53	0.0206	0.1028	181	TRUE
5.0	5.5	0.5	5.3	5.02	1.09	6.99	3.71	4.08	3.90	0.0228	0.1256	200	TRUE
5.5	6.0	0.5	5.8	5.50	1.14	7.03	4.08	4.45	4.27	0.0248	0.1504	217	TRUE
6.0	6.5	0.5	6.3	5.98	1.18	7.07	4.45	4.83	4.64	0.0267	0.1771	234	TRUE
6.5	7.0	0.5	6.8	6.46	1.23	7.12	4.83	5.20	5.01	0.0284	0.2055	249	TRUE
7.0	7.5	0.5	7.3	6.93	1.28	7.16	5.20	5.57	5.38	0.0299	0.2354	262	TRUE
7.5	8.0	0.5	7.8	7.41	1.33	7.21	5.57	5.94		0.0312	0.2666	273	TRUE
8.0	8.5	0.5	8.3	7.89	1.39	7.26	5.94	6.31	6.12	0.0323	0.2988	283	TRUE

Continued on next page

Table B.2 – continued from previous page

150 m height				100 m height	Significant wave height [m]	Spectral peak period [s]	10 m height			PDF [-]	CDF [-]	Operational time [hrs]	Operational envelope
Lower limit [m/s]	Upper limit [m/s]	Bin size [m/s]	Wind speed [m/s]	Wind speed [m/s]			Lower limit [m/s]	Upper limit [m/s]	Wind speed [m/s]				
8.5	9.0	0.5	8.8	8.37	1.44	7.32	6.31	6.68	6.50	0.0331	0.3319	290	TRUE
9.0	9.5	0.5	9.3	8.85	1.50	7.37	6.68	7.05	6.87	0.0337	0.3657	295	TRUE
9.5	10.0	0.5	9.8	9.32	1.56	7.43	7.05	7.42	7.24	0.0341	0.3998	299	TRUE
10.0	10.5	0.5	10.3	9.80	1.63	7.49	7.42	7.80	7.61	0.0343	0.4341	300	TRUE
10.5	11.0	0.5	10.8	10.28	1.69	7.55	7.80	8.17	7.98	0.0342	0.4683	300	TRUE
11.0	11.5	0.5	11.3	10.76	1.76	7.61	8.17	8.54	8.35	0.0339	0.5022	297	TRUE
11.5	12.0	0.5	11.8	11.24	1.83	7.68	8.54	8.91	8.72	0.0335	0.5357	293	TRUE
12.0	13.0	1.0	12.5	11.95	1.94	7.78	8.91	9.65	9.28	0.0648	0.6005	568	TRUE
13.0	14.0	1.0	13.5	12.91	2.10	7.93	9.65	10.39	10.02	0.0609	0.6614	533	TRUE
14.0	15.0	1.0	14.5	13.87	2.28	8.08	10.39	11.14	10.76	0.0559	0.7173	490	TRUE
15.0	16.0	1.0	15.5	14.82	2.47	8.25	11.14	11.88	11.51	0.0503	0.7676	441	TRUE
16.0	17.0	1.0	16.5	15.78	2.67	8.44	11.88	12.62	12.25	0.0443	0.8120	388	TRUE
17.0	18.0	1.0	17.5	16.74	2.89	8.63	12.62	13.36	12.99	0.0383	0.8503	335	TRUE
18.0	19.0	1.0	18.5	17.69	3.13	8.84	13.36	14.11	13.73	0.0324	0.8827	284	TRUE
19.0	20.0	1.0	19.5	18.65	3.39	9.07	14.11	14.85	14.48	0.0269	0.9096	236	TRUE
20.0	21.0	1.0	20.5	19.61	3.67	9.31	14.85	15.59	15.22	0.0219	0.9314	192	TRUE
21.0	22.0	1.0	21.5	20.56	3.98	9.57	15.59	16.33	15.96	0.0174	0.9489	153	TRUE
22.0	23.0	1.0	22.5	21.52	4.31	9.84	16.33	17.07	16.70	0.0136	0.9625	120	TRUE
23.0	23.5	0.5	23.3	22.24	4.57	10.06	17.07	17.45	17.26	0.0056	0.9681	49	TRUE
23.5	24.0	0.5	23.8	22.71	4.76	10.21	17.45	17.82	17.63	0.0049	0.9730	43	TRUE
24.0	24.5	0.5	24.3	23.19	4.95	10.37	17.82	18.19	18.00	0.0042	0.9772	37	TRUE
24.5	25.0	0.5	24.8	23.67	5.15	10.53	18.19	18.56	18.37	0.0037	0.9809	32	TRUE
25.0	25.5	0.5	25.3	24.15	5.36	10.69	18.56	18.93	18.75	0.0031	0.9840	27	TRUE
25.5	26.0	0.5	25.8	24.63	5.58	10.86	18.93	19.30	19.12	0.0027	0.9867	23	FALSE
26.0	27.0	1.0	26.5	25.34	5.92	11.13	19.30	20.04	19.67	0.0042	0.9909	37	FALSE
27.0	28.0	1.0	27.5	26.30	6.41	11.50	20.04	20.79	20.42	0.0030	0.9939	26	FALSE
28.0	29.0	1.0	28.5	27.26	6.94	11.90	20.79	21.53	21.16	0.0021	0.9960	18	FALSE
29.0	30.0	1.0	29.5	28.21	7.52	12.31	21.53	22.27	21.90	0.0014	0.9974	12	FALSE
30.0	31.0	1.0	30.5	29.17	8.14	12.75	22.27	23.01	22.64	0.0010	0.9983	8	FALSE
31.0	32.0	1.0	31.5	30.13	8.82	13.21	23.01	23.76	23.39	0.0006	0.9990	5	FALSE

Continued on next page

Table B.2 – continued from previous page

150 m height				100 m height	Significant	Spectral	10 m height			PDF [-]	CDF [-]	Operational	Operational
Lower limit [m/s]	Upper limit [m/s]	Bin size [m/s]	Wind speed [m/s]	Wind speed [m/s]	wave height [m]	peak period [s]	Lower limit [m/s]	Upper limit [m/s]	Wind speed [m/s]			time [hrs]	envelope
32.0	33.0	1.0	32.5	31.08	9.55	13.68	23.76	24.50	24.13	0.0004	0.9994	4	FALSE
33.0	34.0	1.0	33.5	32.04	10.34	14.18	24.50	25.24	24.87	0.0003	0.9996	2	FALSE
34.0	35.0	1.0	34.5	33.00	11.19	14.69	25.24	25.98	25.61	0.0002	0.9998	1	FALSE
									Total:	0.9998	-	8758	-

Table B.3: Wind speed bins and environmental conditions for simulations at Buchan Deep (150 m Weibull distribution shown in Figure B.3). The default binning is 1.0 m/s; refined to 0.25 m/s between rated-cut-out and around cut-out speeds (bold). The row shading changes every 5 m/s for clarity.

150 m height				100 m height	Significant	Spectral	10 m height			PDF [-]	CDF [-]	Operational	Operational
Lower limit [m/s]	Upper limit [m/s]	Bin size [m/s]	Wind speed [m/s]	Wind speed [m/s]	wave height [m]	peak period [s]	Lower limit [m/s]	Upper limit [m/s]	Wind speed [m/s]			time [hrs]	envelope
0.00	1.00	1.00	0.5	0.48	0.75	6.66	0.000	0.742	0.37	0.0030	0.0030	26	FALSE
1.00	2.00	1.00	1.5	1.43	0.81	6.72	0.742	1.485	1.11	0.0109	0.0139	96	FALSE
2.00	2.25	0.25	2.1	2.03	0.85	6.76	1.485	1.670	1.58	0.0041	0.0180	36	FALSE
2.25	2.50	0.25	2.4	2.27	0.87	6.77	1.670	1.856	1.76	0.0047	0.0228	41	FALSE
2.50	2.75	0.25	2.6	2.51	0.89	6.79	1.856	2.042	1.95	0.0053	0.0281	47	TRUE
2.75	3.00	0.25	2.9	2.75	0.90	6.81	2.042	2.227	2.13	0.0059	0.0340	52	TRUE
3.00	3.25	0.25	3.1	2.99	0.92	6.83	2.227	2.413	2.32	0.0065	0.0406	57	TRUE
3.25	3.50	0.25	3.4	3.23	0.94	6.84	2.413	2.598	2.51	0.0071	0.0477	62	TRUE
3.50	3.75	0.25	3.6	3.47	0.96	6.86	2.598	2.784	2.69	0.0077	0.0554	68	TRUE
3.75	4.00	0.25	3.9	3.71	0.98	6.88	2.784	2.970	2.88	0.0083	0.0637	73	TRUE
4.00	4.25	0.25	4.1	3.95	1.00	6.90	2.970	3.155	3.06	0.0089	0.0726	78	TRUE
4.25	4.50	0.25	4.4	4.18	1.02	6.92	3.155	3.341	3.25	0.0095	0.0821	83	TRUE
4.50	4.75	0.25	4.6	4.42	1.04	6.94	3.341	3.526	3.43	0.0100	0.0922	88	TRUE
4.75	5.00	0.25	4.9	4.66	1.06	6.96	3.526	3.712	3.62	0.0106	0.1028	93	TRUE
5.00	5.25	0.25	5.1	4.90	1.08	6.98	3.712	3.898	3.80	0.0111	0.1139	98	TRUE
5.25	5.50	0.25	5.4	5.14	1.10	7.00	3.898	4.083	3.99	0.0117	0.1256	102	TRUE
5.50		0.25	5.6	5.38	1.12	7.02	4.083	4.269	4.18	0.0122	0.1377	107	TRUE
	6.00	0.25	5.9	5.62	1.15	7.04	4.269	4.454	4.36	0.0127	0.1504	111	TRUE
6.00	6.25	0.25	6.1	5.86	1.17	7.06	4.454	4.640	4.55	0.0131	0.1635	115	TRUE

Continued on next page

Table B.3 – continued from previous page

150 m height				100 m height	Significant wave height [m]	Spectral peak period [s]	10 m height			PDF [-]	CDF [-]	Operational time [hrs]	Operational envelope
Lower limit [m/s]	Upper limit [m/s]	Bin size [m/s]	Wind speed [m/s]	Wind speed [m/s]			Lower limit [m/s]	Upper limit [m/s]	Wind speed [m/s]				
6.25	6.50	0.25	6.4	6.10	1.19	7.08	4.640	4.826	4.73	0.0136	0.1771	119	TRUE
6.50	6.75	0.25	6.6	6.34	1.22	7.11	4.826	5.011	4.92	0.0140	0.1911	123	TRUE
6.75	7.00	0.25	6.9	6.58	1.24	7.13	5.011	5.197	5.10	0.0144	0.2055	126	TRUE
7.00	7.25	0.25	7.1	6.81	1.27	7.15	5.197	5.382	5.29	0.0148	0.2202	129	TRUE
7.25	7.50	0.25	7.4	7.05	1.29	7.18	5.382	5.568	5.48	0.0151	0.2354	132	TRUE
7.50	7.75	0.25	7.6	7.29	1.32	7.20	5.568	3	5.66	0.0154	0.2508	135	TRUE
7.75	8.00	0.25	7.9	7.53	1.35	7.23	3	5.939	5.85	0.0157	0.2666	138	TRUE
8.00	8.25	0.25	8.1	7.77	1.37	7.25	5.939	6.125	6.03	0.0160	0.2826	140	TRUE
8.25	8.50	0.25	8.4	8.01	1.40	7.28	6.125	6.310	6.22	0.0163	0.2988	142	TRUE
8.50	8.75	0.25	8.6	8.25	1.43	7.30	6.310	6.496	6.40	0.0165	0.3153	144	TRUE
8.75	9.00	0.25	8.9	8.49	1.46	7.33	6.496	6.681	6.59	0.0166	0.3319	146	TRUE
9.00	9.25	0.25	9.1	8.73	1.49	7.36	6.681	6.867	6.77	0.0168	0.3487	147	TRUE
9.25	9.50	0.25	9.4	8.97	1.52	7.38	6.867	7.053	6.96	0.0169	0.3657	148	TRUE
9.50	9.75	0.25	9.6	9.21	1.55	7.41	7.053	7.238	7.15	0.0170	0.3827	149	TRUE
9.75	10.00	0.25	9.9	9.44	1.58	7.44	7.238	7.424	7.33	0.0171	0.3998	150	TRUE
10.00	10.25	0.25	10.1	9.68	1.61	7.47	7.424	7.609	7.52	0.0171	0.4169	150	TRUE
10.25	10.50	0.25	10.4	9.92	1.64	7.50	7.609	7.795	7.70	0.0171	0.4341	150	TRUE
10.50	10.75	0.25	10.6	10.16	1.67	7.53	7.795	7.981	7.89	0.0171	0.4512	150	TRUE
10.75	11.00	0.25	10.9	10.40	1.71	7.56	7.981	8.166	8.07	0.0171	0.4683	150	TRUE
11.00	11.25	0.25	11.1	10.64	1.74	7.59	8.166	8.352	8.26	0.0170	0.4853	149	TRUE
11.25	11.50	0.25	11.4	10.88	1.78	7.63	8.352	8.537	8.44	0.0169	0.5022	148	TRUE
11.50	11.75	0.25	11.6	11.12	1.81	7.66	8.537	8.723	8.63	0.0168	0.5190	147	TRUE
11.75	12.00	0.25	11.9	11.36	1.85	7.69	8.723	8.909	8.82	0.0167	0.5357	146	TRUE
12.00	13.00	1.00	12.5	11.95	1.94	7.78	8.909	9.651	9.28	0.0648	0.6005	568	TRUE
13.00	14.00	1.00	13.5	12.91	2.10	7.93	9.651	10.393	10.02	0.0609	0.6614	533	TRUE
14.00	15.00	1.00	14.5	13.87	2.28	8.08	10.393	11.136	10.76	0.0559	0.7173	490	TRUE
15.00	16.00	1.00	15.5	14.82	2.47	8.25	11.136	11.878	11.51	0.0503	0.7676	441	TRUE
16.00	17.00	1.00	16.5	15.78	2.67	8.44	11.878	12.621	12.25	0.0443	0.8120	388	TRUE
17.00	18.00	1.00	17.5	16.74	2.89	8.63	12.621	13.363	12.99	0.0383	0.8503	335	TRUE
18.00	19.00	1.00	18.5	17.69	3.13	8.84	13.363	14.105	13.73	0.0324	0.8827	284	TRUE

Continued on next page

Table B.3 – continued from previous page

150 m height				100 m height	Significant wave height [m]	Spectral peak period [s]	10 m height			PDF [-]	CDF [-]	Operational time [hrs]	Operational envelope
Lower limit [m/s]	Upper limit [m/s]	Bin size [m/s]	Wind speed [m/s]	Wind speed [m/s]			Lower limit [m/s]	Upper limit [m/s]	Wind speed [m/s]				
19.00	20.00	1.00	19.5	18.65	3.39	9.07	14.105	14.848	14.48	0.0269	0.9096	236	TRUE
20.00	21.00	1.00	20.5	19.61	3.67	9.31	14.848	15.590	15.22	0.0219	0.9314	192	TRUE
21.00	22.00	1.00	21.5	20.56	3.98	9.57	15.590	16.332	15.96	0.0174	0.9489	153	TRUE
22.00	23.00	1.00	22.5	21.52	4.31	9.84	16.332	17.075	16.70	0.0136	0.9625	120	TRUE
23.00	23.25	0.25	23.1	22.12	4.53	10.02	17.075	17.260	17.17	0.0029	0.9654	25	TRUE
23.25	23.50	0.25	23.4	22.36	4.62	10.10	17.260	17.446	17.35	0.0027	0.9681	24	TRUE
23.50	23.75	0.25	23.6	22.59	4.71	10.17	17.446	17.632	17.54	0.0025	0.9706	22	TRUE
23.75	24.00	0.25	23.9	22.83	4.81	10.25	17.632	17.817	17.72	0.0024	0.9730	21	TRUE
24.00	24.25	0.25	24.1	23.07	4.90	10.33	17.817	18.003	17.91	0.0022	0.9752	19	TRUE
24.25	24.50	0.25	24.4	23.31	5.00	10.41	18.003	18.188	18.10	0.0020	0.9772	18	TRUE
24.50	24.75	0.25	24.6	23.55	5.10	10.49	18.188	18.374	18.28	0.0019	0.9791	17	TRUE
24.75	25.00	0.25	24.9	23.79	5.20	10.57	18.374	18.560	18.47	0.0018	0.9809	15	TRUE
25.00	25.25	0.25	25.1	24.03	5.31	10.65	18.560	18.745	18.65	0.0016	0.9825	14	TRUE
25.25	25.50	0.25	25.4	24.27	5.42	10.74	18.745	18.931	18.84	0.0015	0.9840	13	TRUE
25.50	2	0.25	25.6	24.51	5.52	10.82	18.931	19.116	19.02	0.0014	0.9854	12	FALSE
2	26.00	0.25	25.9	24.75	5.64	10.91	19.116	19.302	19.21	0.0013	0.9867	11	FALSE
26.00	27.00	1.00	26.5	25.34	5.92	11.13	19.302	20.044	19.67	0.0042	0.9909	37	FALSE
27.00	28.00	1.00	27.5	26.30	6.41	11.50	20.044	20.787	20.42	0.0030	0.9939	26	FALSE
28.00	29.00	1.00	28.5	27.26	6.94	11.90	20.787	21.529	21.16	0.0021	0.9960	18	FALSE
29.00	30.00	1.00	29.5	28.21	7.52	12.31	21.529	22.272	21.90	0.0014	0.9974	12	FALSE
30.00	31.00	1.00	30.5	29.17	8.14	12.75	22.272	23.014	22.64	0.0010	0.9983	8	FALSE
31.00	32.00	1.00	31.5	30.13	8.82	13.21	23.014	23.756	23.39	0.0006	0.9990	5	FALSE
32.00	33.00	1.00	32.5	31.08	9.55	13.68	23.756	24.499	24.13	0.0004	0.9994	4	FALSE
33.00	34.00	1.00	33.5	32.04	10.34	14.18	24.499	25.241	24.87	0.0003	0.9996	2	FALSE
34.00	35.00	1.00	34.5	33.00	11.19	14.69	25.241	25.984	25.61	0.0002	0.9998	1	FALSE
									Total:	0.9998	-	8758	-

C

Damping Characteristics for all Degree of Freedom

Damping ratios across all initial displacements (complete dataset: Table C.1). Six-DOF overview in Figure C.1. The plot uses consistent colour conventions from Figure 4.1.

Table C.1: Damping ratio for each floater and degree of freedom for different initial displacements (data from Figure C.1). Empty cells indicate simulations that failed to converge.

		Damping ratio [-]					
DOF	**Initial disp.**	**WindCrete 135m**	**WindCrete 150m**	**ActiveFloat 135m**	**ActiveFloat 150m**	**Volturn-US-S**	**Reference TLP**
Surge (1)	**7.5 m**	0.030	0.032	0.031	0.032	0.052	0.036
	15.0 m	0.050	0.052	0.051	0.051	0.082	0.077
	22.5 m					0.102	0.134
	30.0 m					0.144	
Sway (2)	**7.5 m**	0.028	0.031	0.032	0.032	0.053	0.036
	15.0 m	0.045	0.047	0.050	0.050	0.082	0.077
	22.5 m					0.111	0.135
	30.0 m					0.146	
Heave (3)	**1.25 m**	0.001	0.008	0.169	0.173	0.023	0.023
	2.50 m	0.005	0.010	0.191	0.194	0.033	0.100
	3.75 m	0.007	0.012	0.214	0.218	0.041	0.248
	5.00 m	0.010	0.014	0.239	0.242	0.048	0.324
Roll (4)	**2.50°**	0.009	0.009	0.060	0.060	0.012	0.005
	5.00°	0.017	0.015	0.075	0.074	0.019	0.039
	7.50°	0.023	0.021	0.089	0.087	0.026	0.125
	10.00°	0.029	0.026	0.103	0.099	0.031	
Pitch (5)	**2.50°**	0.010	0.009	0.067	0.067	0.015	
	5.00°	0.017	0.015	0.081	0.080	0.022	0.377
	7.50°	0.023	0.020	0.094	0.092	0.028	0.362
	10.00°		0.025	0.107	0.103	0.033	
Yaw (6)	**5.00°**	0.155	0.159	0.017	0.018	0.046	0.035
	10.00°	0.178	0.178	0.028	0.028	0.069	0.077
	15.00°	0.193	0.191	0.037	0.037	0.090	0.132

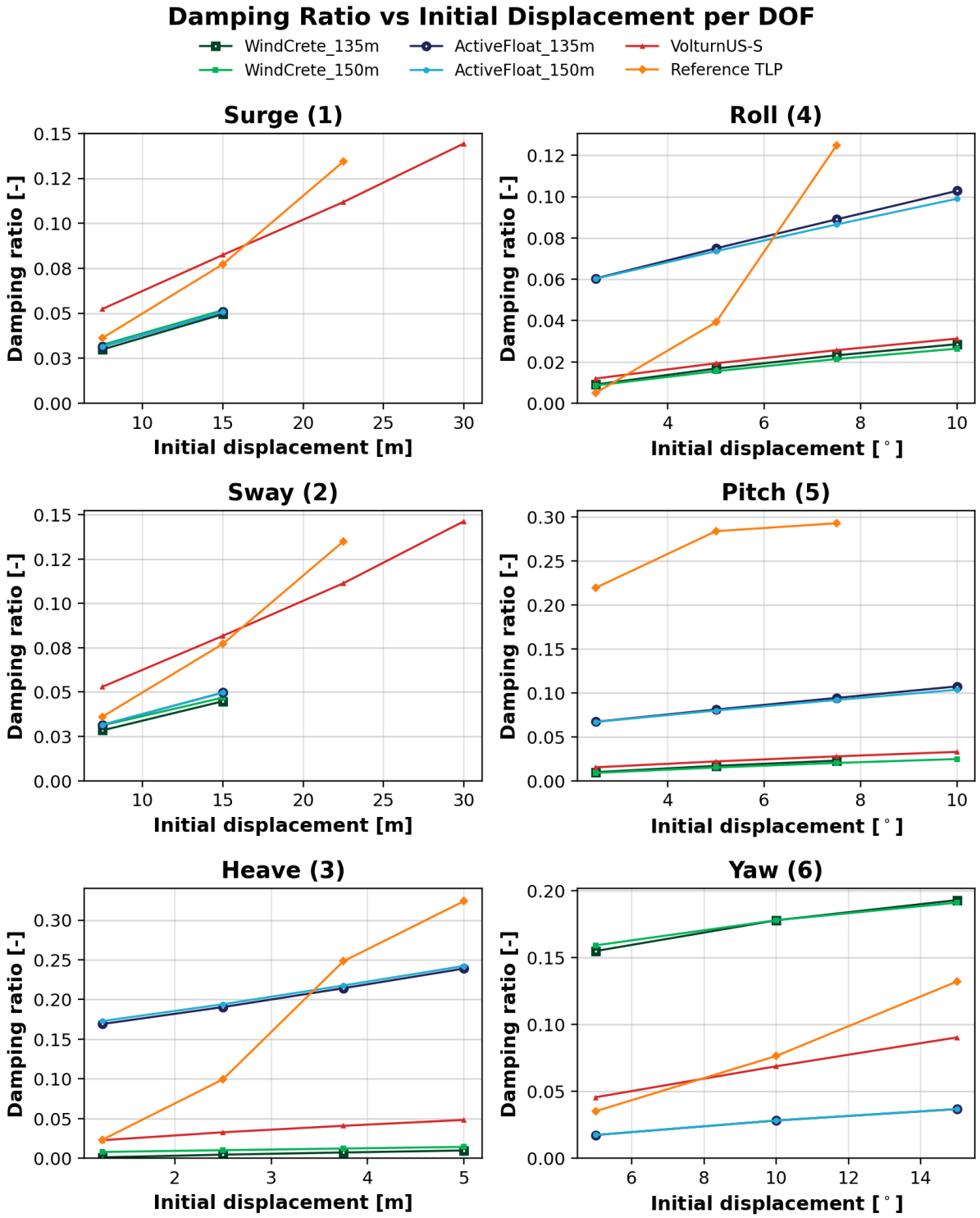

Figure C.1: Damping ratio for the different DOF of all floaters (data from Table C.1). Non-converged simulations are omitted from the plot.

D

Platform Motions per Wind Speed

The average displacement and standard deviation of the degrees of freedom (surge, sway, heave, roll, pitch, yaw and tower fore-aft and side-side displacement) is shown for each operational wind speed. Figure D.1 shows the bottom-fixed baseline followed by the figures for the floaters (Figures D.2-D.7). Figure D.8 shows the displacement at a wind speed of 9.5 m/s. All plots use consistent colour conventions from Figure 4.1 and Figure 4.2.

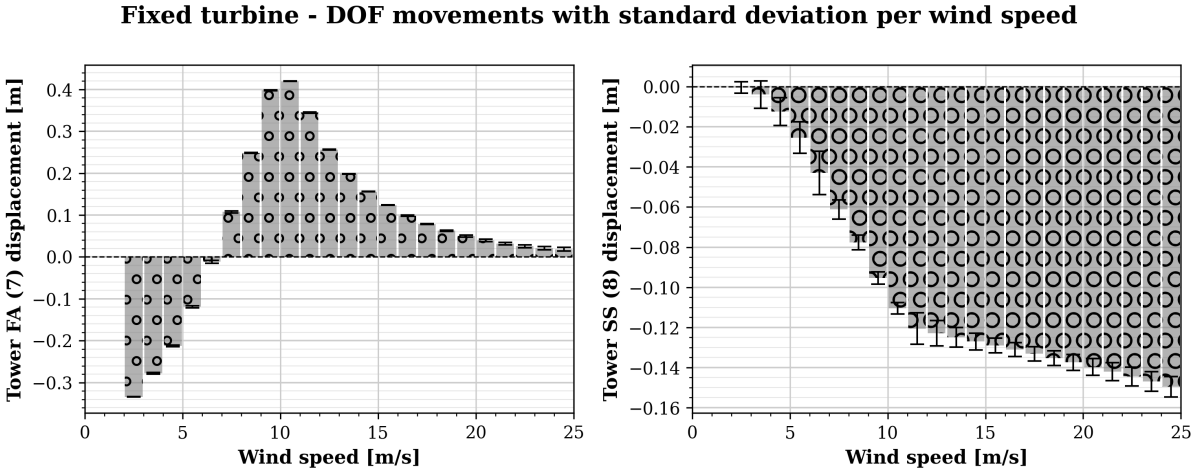

Figure D.1: Fixed turbine: Tower fore-aft and side-side motions for all operational wind speeds.

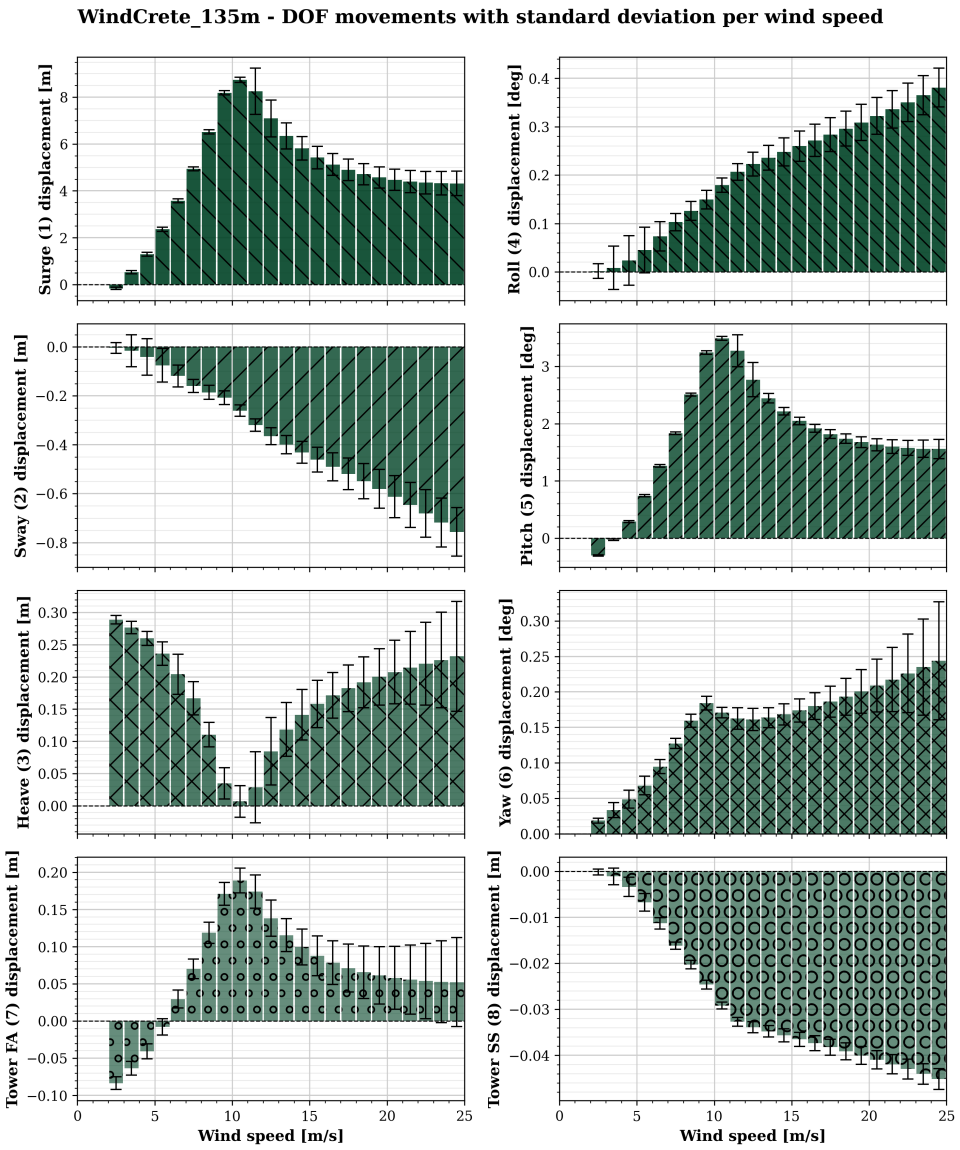

Figure D.2: WindCrete_135m: 8-DOF motions for all operational wind speeds.

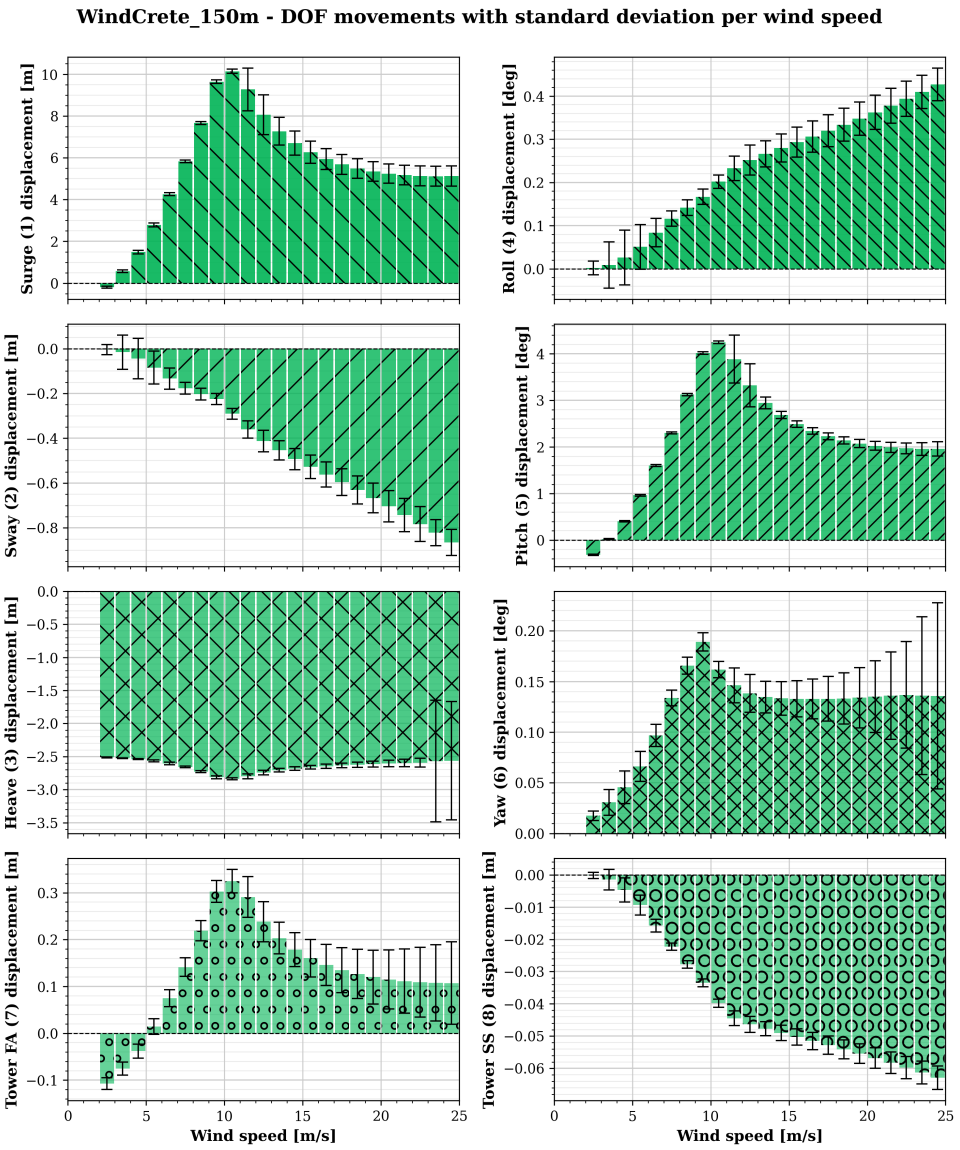

Figure D.3: WindCrete_150m: 8-DOF motions for all operational wind speeds.

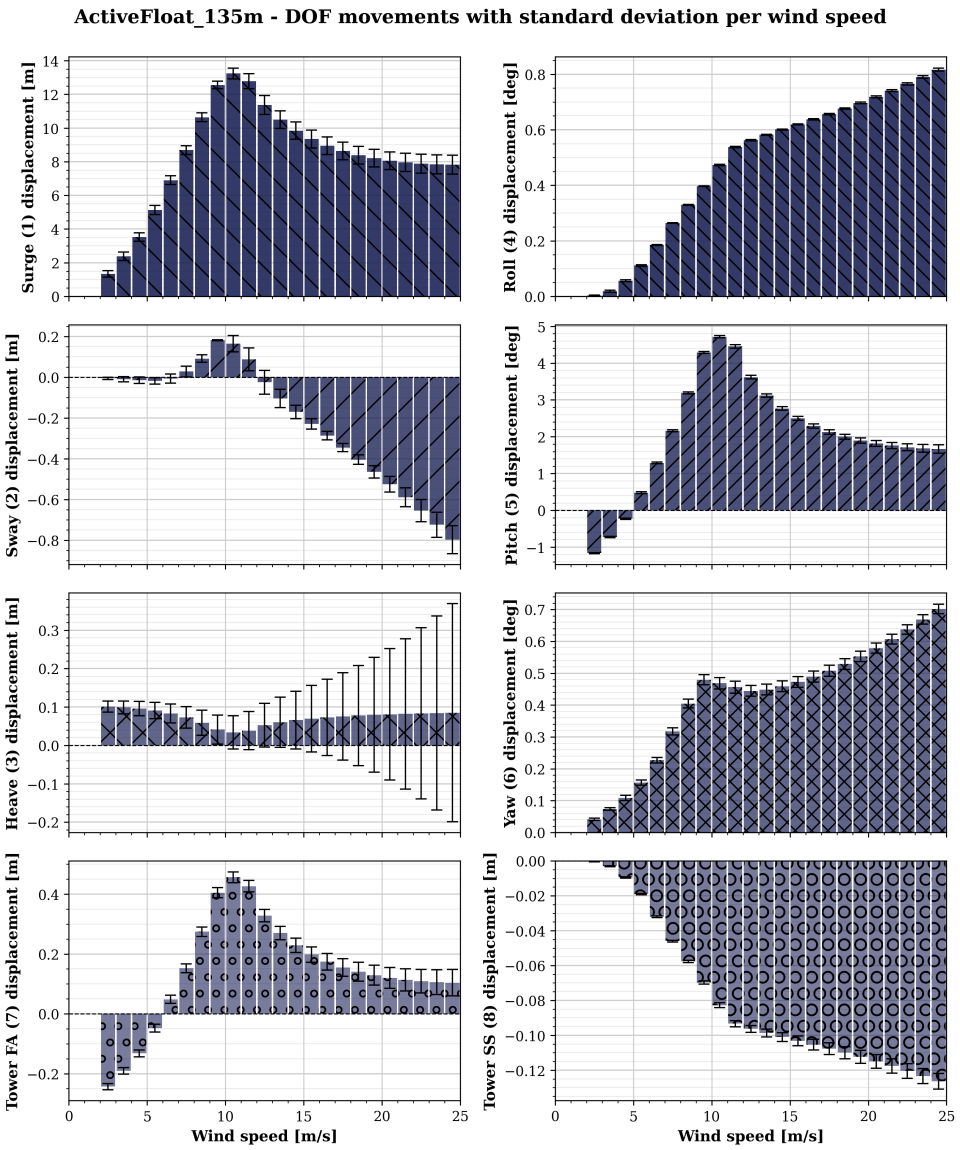

Figure D.4: ActiveFloat_135m: 8-DOF motions for all operational wind speeds.

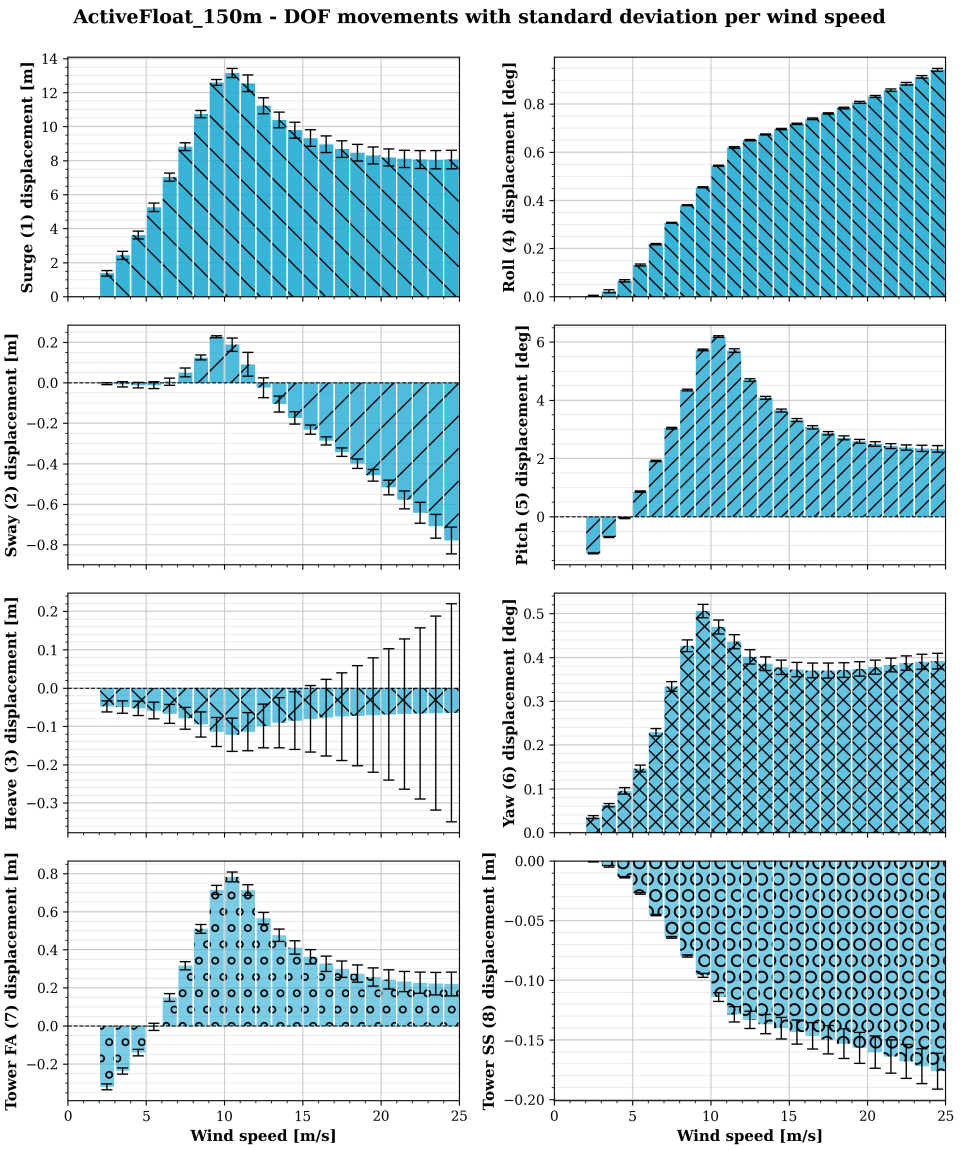

Figure D.5: ActiveFloat_150m: 8-DOF motions for all operational wind speeds.

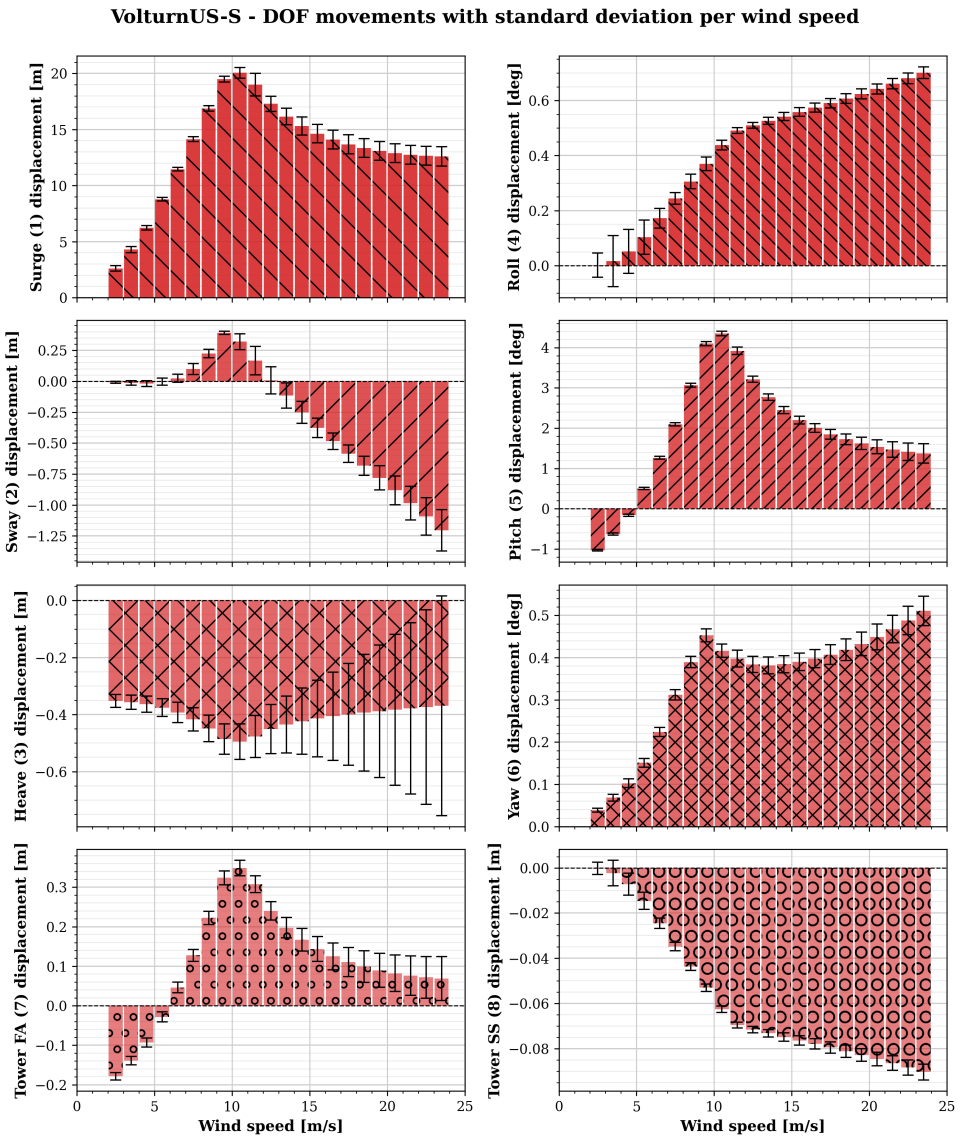

Figure D.6: VolturnUS-S: 8-DOF motions for all operational wind speeds.

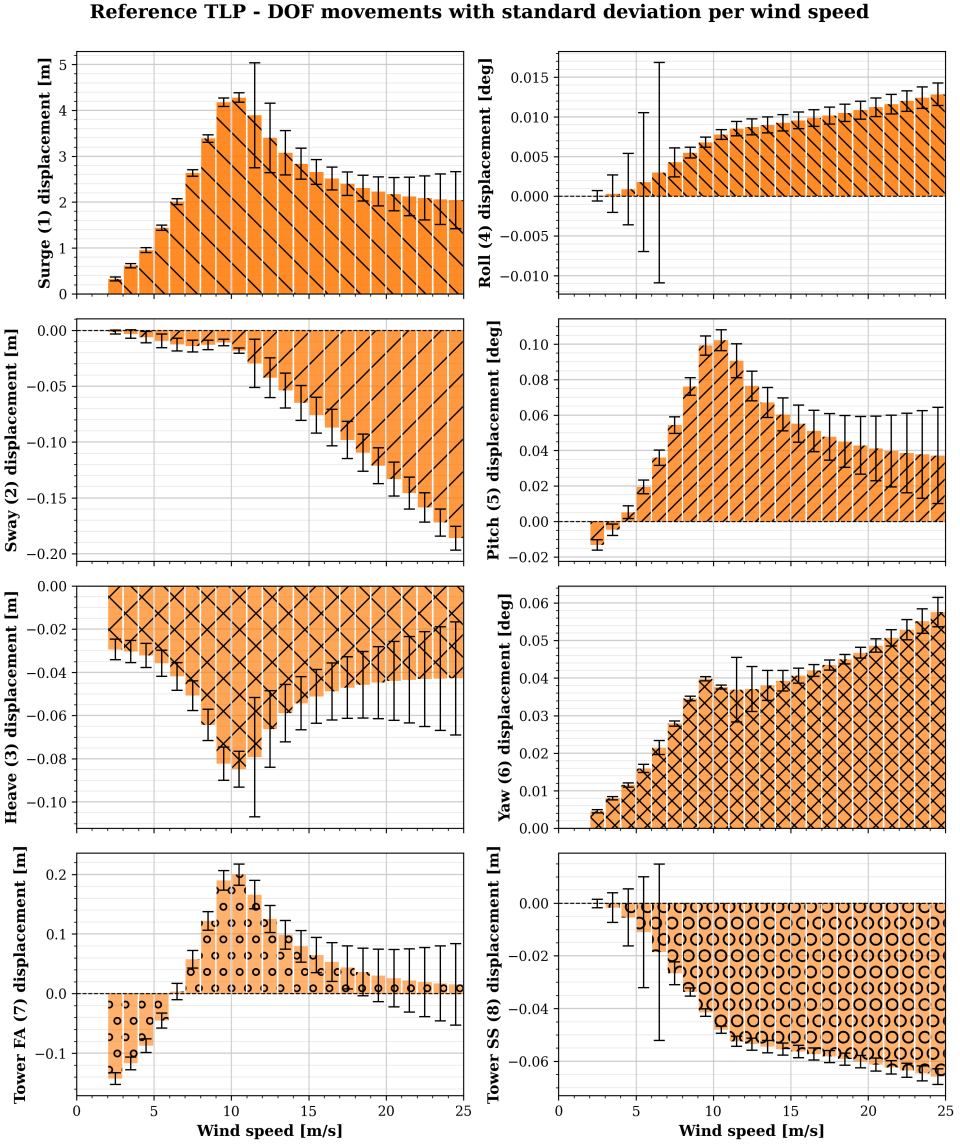

Figure D.7: Reference TLP: 8-DOF motions for all operational wind speeds.

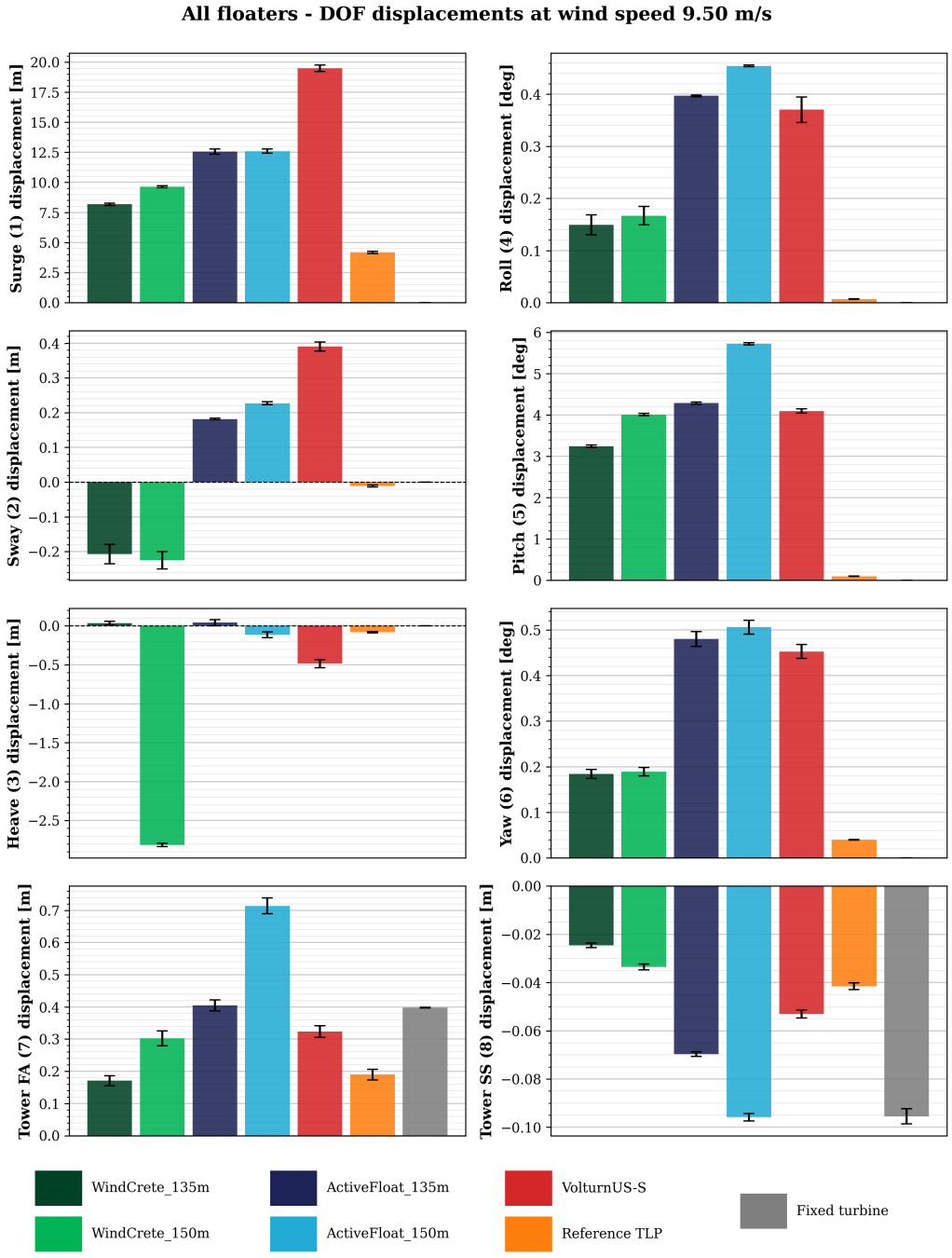

Figure D.8: 8-DOF motions across all platforms at 9.5 m/s wind speed, demonstrating relative platform response characteristics.

E

AEP and Power Production Metrics

The power curve (Table E.1), coefficient of variation (CoV) (Table E.2), annual energy production (AEP) (Table E.3) and coefficient of performance C_p metrics for all platforms across operational wind speeds. The individual platform results appear in Figures E.1-E.7. Colour conventions follow Figure 4.1.

Table E.1: Turbine power per wind speed bin.

	Turbine power [kW]						
Wind speed	**WindCrete 135m**	**WindCrete 150m**	**ActiveFloat 135m**	**ActiveFloat 150m**	**Volturn-US-S**	**Reference TLP**	**Fixed turbine**
0-1 m/s	0	0	0	0	0	0	0
1-2 m/s	0	0	0	0	0	0	0
2-3 m/s	0	0	0	0	0	0	0
3-4 m/s	253	267	258	276	276	274	274
4-5 m/s	916	952	923	966	965	965	966
5-6 m/s	1924	1989	1930	2007	2010	2020	2021
6-7 m/s	3313	3415	3313	3429	3446	3481	3484
7-8 m/s	5093	5238	5079	5236	5281	5373	5374
8-9 m/s	7350	7542	7298	7484	7595	7803	7801
9-10 m/s	10120	10353	9992	10184	10410	10824	10819
10-11 m/s	13144	13366	13006	13195	13409	13754	13755
11-12 m/s	14959	14906	15000	15000	14999	14997	15000
12-13 m/s	14999	15009	15000	15000	15000	15002	15000
13-14 m/s	14998	15003	15000	15000	15000	15002	15000
14-15 m/s	14998	15002	15001	15000	15001	15002	15000
15-16 m/s	14999	15001	15001	15001	15001	15002	15000
16-17 m/s	14999	15001	15001	15001	15001	15002	15001
17-18 m/s	14999	15001	15001	15001	15001	15002	15001
18-19 m/s	14999	15001	15001	15001	15001	15001	15001
19-20 m/s	15000	15001	15001	15001	15001	15001	15001
20-21 m/s	15000	15001	15001	15001	15001	15001	15001
21-22 m/s	15000	15001	15001	15001	15001	15001	15001
22-23 m/s	15000	15001	15001	15001	15001	15002	15001
23-24 m/s	15000	14999	15001	15001	15002	15002	15001
24-25 m/s	15000	15000	15001	15001	0	15002	15001
25-26 m/s	0	0	0	0	0	0	0

Table E.2: Coefficient of variation per wind speed bin.

	Coefficient of variation						
Wind speed	**WindCrete 135m**	**WindCrete 150m**	**ActiveFloat 135m**	**ActiveFloat 150m**	**Volturn-US-S**	**Reference TLP**	**Fixed turbine**
0-1 m/s	-	-	-	-	-	-	-
1-2 m/s	-	-	-	-	-	-	-
2-3 m/s	-	-	-	-	-	-	-
3-4 m/s	3.1604%	3.0388%	3.1924%	2.6424%	5.6436%	2.3721%	1.4958%
4-5 m/s	1.4718%	1.4071%	1.4414%	1.1838%	1.7758%	0.7622%	0.2720%
5-6 m/s	1.1415%	1.0010%	0.9631%	0.8021%	0.9460%	0.5451%	0.1249%
6-7 m/s	0.8270%	0.7051%	0.7114%	0.5912%	0.7675%	0.4735%	0.0914%
7-8 m/s	0.6340%	0.5956%	0.5412%	0.4397%	0.7213%	0.4601%	0.0613%
8-9 m/s	0.6347%	0.5989%	0.4836%	0.3792%	0.7369%	0.4646%	0.0452%
9-10 m/s	0.6314%	0.6114%	0.4123%	0.3348%	0.7053%	0.4571%	0.0399%
10-11 m/s	0.6160%	0.5995%	0.3833%	0.3326%	0.6796%	0.4805%	0.0550%
11-12 m/s	1.4570%	2.4964%	0.2424%	0.2553%	0.4885%	1.0114%	0.0443%
12-13 m/s	1.3056%	1.7181%	0.2680%	0.2521%	0.4991%	0.7807%	0.0479%
13-14 m/s	0.7730%	0.8321%	0.2908%	0.2737%	0.5241%	0.6839%	0.0528%
14-15 m/s	0.7812%	0.7950%	0.3185%	0.2995%	0.5546%	0.6734%	0.0593%
15-16 m/s	0.8341%	0.8370%	0.3507%	0.3291%	0.5889%	0.7062%	0.0663%
16-17 m/s	0.9028%	0.8998%	0.3884%	0.3636%	0.6277%	0.7627%	0.0744%
17-18 m/s	0.9835%	0.9761%	0.4324%	0.4037%	0.6708%	0.8359%	0.0827%
18-19 m/s	1.0743%	1.0631%	0.4833%	0.4502%	0.7184%	0.9229%	0.0915%
19-20 m/s	1.1782%	1.1619%	0.5400%	0.5018%	0.7739%	1.0242%	0.1005%
20-21 m/s	1.2942%	1.2727%	0.6065%	0.5621%	0.8308%	1.1390%	0.1097%
21-22 m/s	1.4230%	1.3958%	0.6854%	0.6341%	0.8888%	1.2671%	0.1187%
22-23 m/s	1.5640%	1.5302%	0.7788%	0.7196%	0.9481%	1.4069%	0.1280%
23-24 m/s	1.7146%	1.7788%	0.8882%	0.8201%	1.0110%	1.5561%	0.1374%
24-25 m/s	1.8713%	1.9213%	1.0142%	0.9357%	-	1.7113%	0.1469%
25-26 m/s	-	-	-	-	-	-	-
Totaal	0.9942%	1.1256%	0.4221%	0.3835%	0.6534%	0.7745%	0.0693%

Table E.3: Annual energy production (AEP) per wind speed bin.

	Annual energy production [GWh]						
Wind speed	**WindCrete 135m**	**WindCrete 150m**	**ActiveFloat 135m**	**ActiveFloat 150m**	**Volturn-US-S**	**Reference TLP**	**Fixed turbine**
0-1 m/s	0.00	0.00	0.00	0.00	0.00	0.00	0.00
1-2 m/s	0.00	0.00	0.00	0.00	0.00	0.00	0.00
2-3 m/s	0.00	0.00	0.00	0.00	0.00	0.00	0.00
3-4 m/s	0.07	0.07	0.07	0.07	0.07	0.07	0.07
4-5 m/s	0.31	0.33	0.32	0.33	0.33	0.33	0.33
5-6 m/s	0.80	0.83	0.81	0.84	0.84	0.84	0.84
6-7 m/s	1.60	1.65	1.60	1.65	1.66	1.68	1.68
7-8 m/s	2.72	2.80	2.72	2.80	2.83	2.87	2.88

Continued on next page

Table E.3 – continued from previous page

	Annual energy production [GWh]						
Wind speed	**WindCrete 135m**	**WindCrete 150m**	**ActiveFloat 135m**	**ActiveFloat 150m**	**Volturn-US-S**	**Reference TLP**	**Fixed turbine**
8-9 m/s	4.21	4.32	4.18	4.29	4.35	4.47	4.47
9-10 m/s	6.01	6.15	5.94	6.05	6.19	6.43	6.43
10-11 m/s	7.89	8.02	7.80	7.92	8.05	8.25	8.25
11-12 m/s	8.84	8.80	8.86	8.86	8.86	8.86	8.86
12-13 m/s	8.51	8.52	8.51	8.51	8.51	8.51	8.51
13-14 m/s	8.00	8.00	8.00	8.00	8.00	8.00	8.00
14-15 m/s	7.35	7.35	7.35	7.35	7.35	7.35	7.35
15-16 m/s	6.61	6.61	6.61	6.61	6.61	6.61	6.61
16-17 m/s	5.83	5.83	5.83	5.83	5.83	5.83	5.83
17-18 m/s	5.03	5.03	5.03	5.03	5.03	5.03	5.03
18-19 m/s	4.26	4.26	4.26	4.26	4.26	4.26	4.26
19-20 m/s	3.53	3.53	3.53	3.53	3.53	3.53	3.53
20-21 m/s	2.87	2.87	2.87	2.87	2.87	2.87	2.87
21-22 m/s	2.29	2.29	2.29	2.29	2.29	2.29	2.29
22-23 m/s	1.79	1.79	1.79	1.79	1.79	1.79	1.79
23-24 m/s	1.38	1.38	1.38	1.38	1.38	1.38	1.38
24-25 m/s	1.04	1.04	1.04	1.04	0.00	1.04	1.04
25-26 m/s	0.00	0.00	0.00	0.00	0.00	0.00	0.00
Totaal	90.94	91.48	90.79	91.31	90.63	92.31	92.31

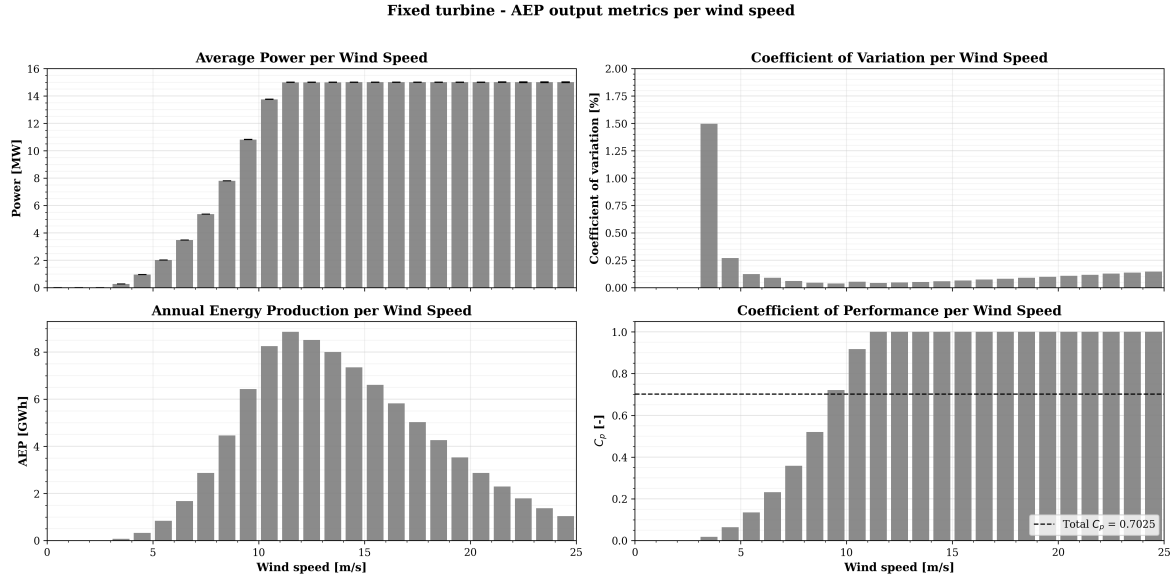

Figure E.1: Fixed turbine: from top left clockwise: power curve, CoV, C_p and AEP per wind speed.

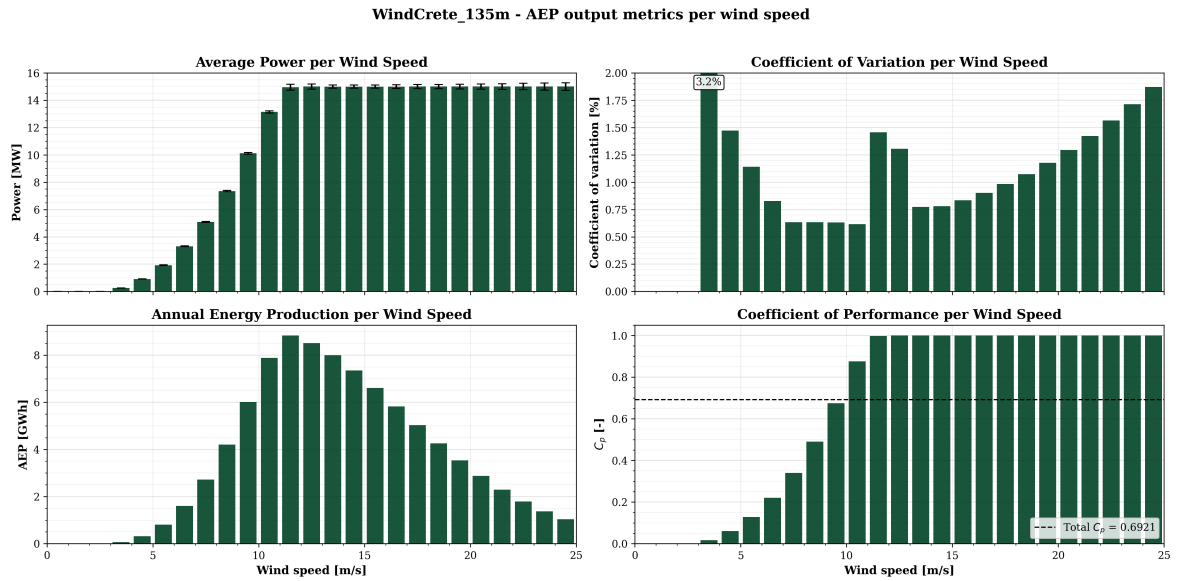

Figure E.2: WindCrete_135m: from top left clockwise: power curve, CoV, C_p and AEP per wind speed.

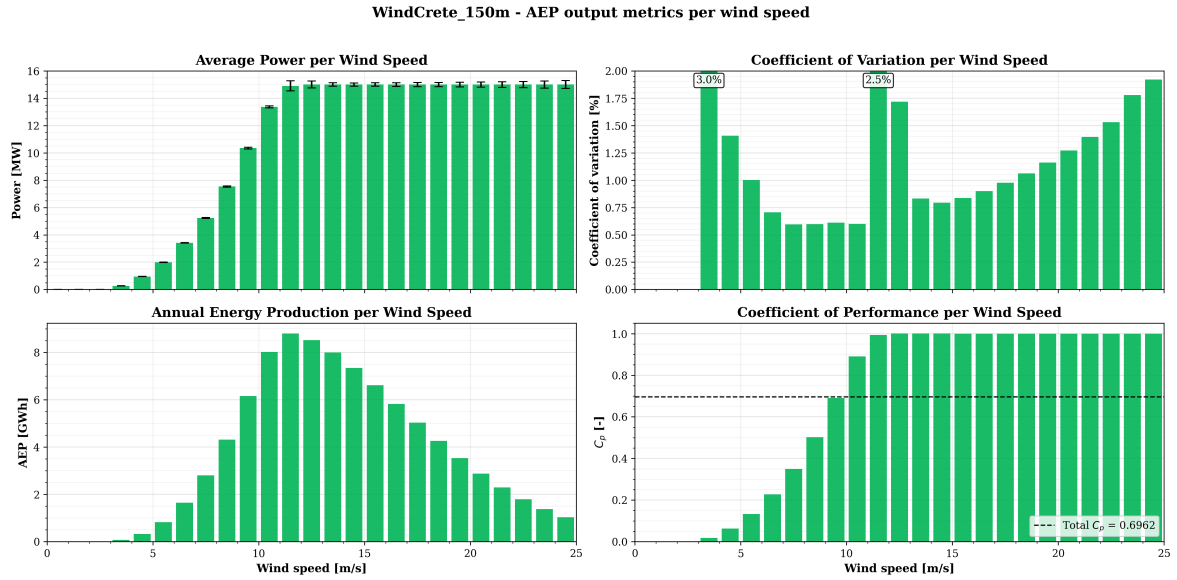

Figure E.3: WindCrete_150m: from top left clockwise: power curve, CoV, C_p and AEP per wind speed.

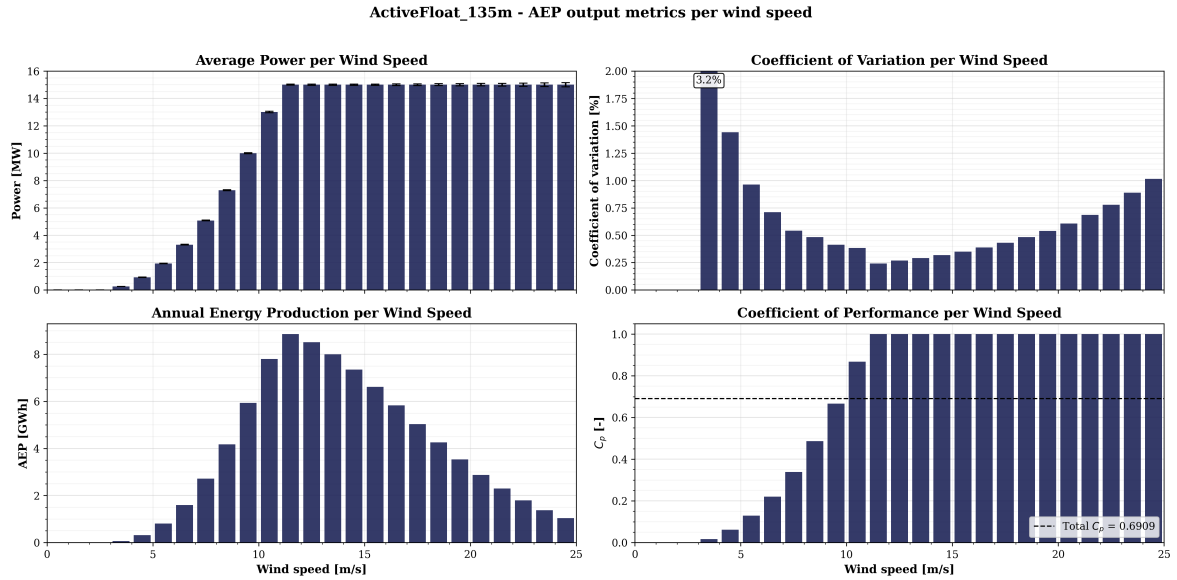

Figure E.4: ActiveFloat_135m: from top left clockwise: power curve, CoV, C_p and AEP per wind speed.

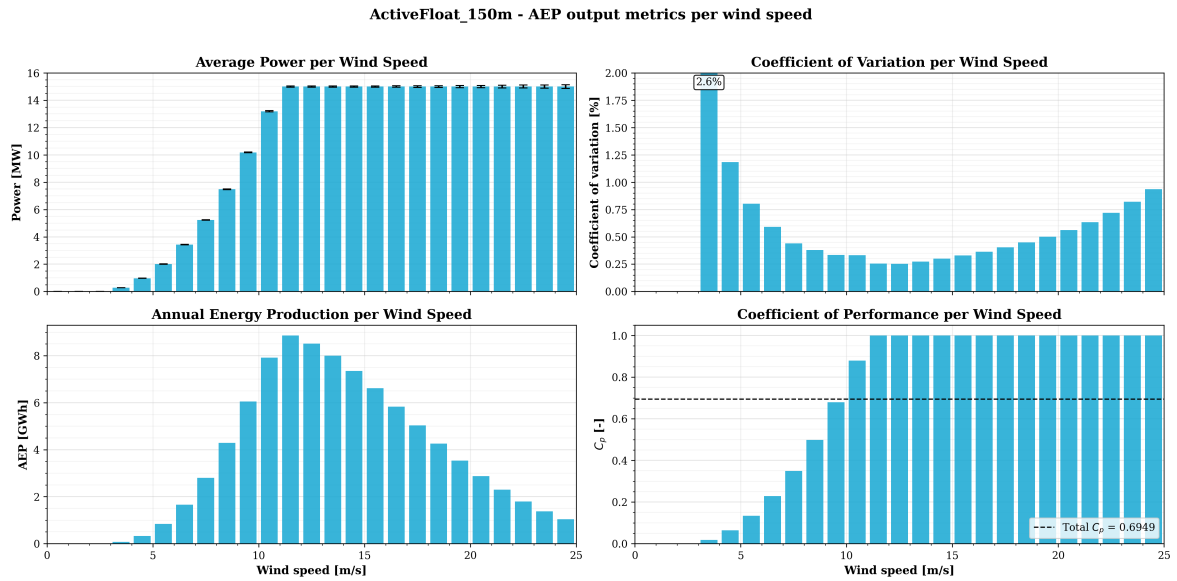

Figure E.5: ActiveFloat_150m: from top left clockwise: power curve, CoV, C_p and AEP per wind speed.

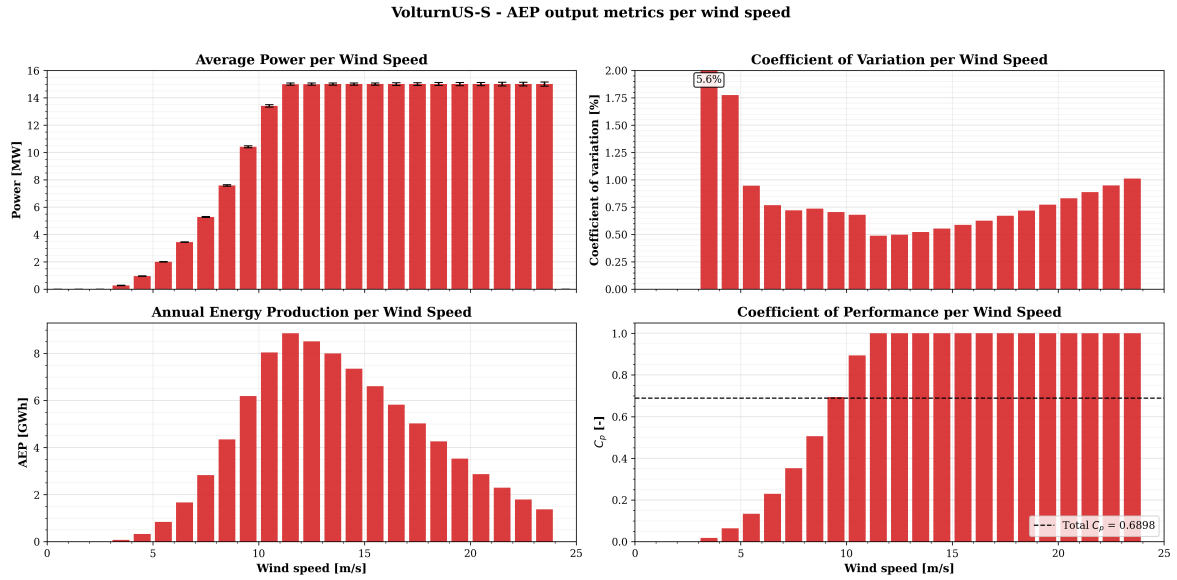

Figure E.6: VolturnUS-S: from top left clockwise: power curve, CoV, C_p and AEP per wind speed.

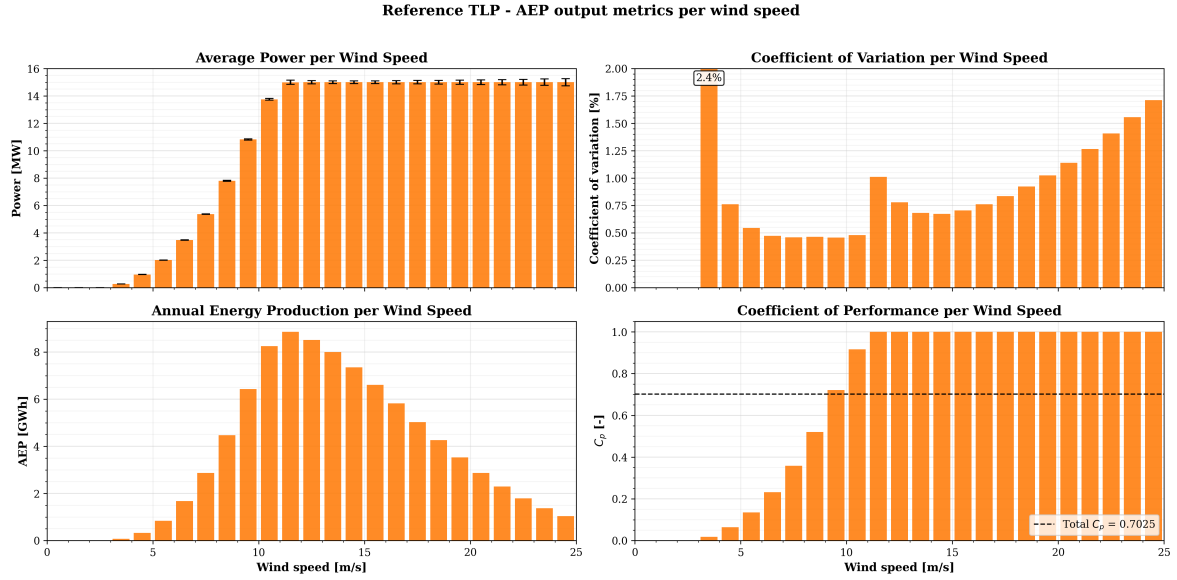

Figure E.7: Reference TLP: from top left clockwise: power curve, CoV, C_p and AEP per wind speed.

F

Verification of Simulation Duration

This appendix presents a comparison between the standard 15-minute simulation runs (with a 300 s transient exclusion and a 600 s averaging window) and extended 3-hour runs (10,800 s + 300 s transient, totalling 11,100 s) to verify the statistical convergence of the power output and variability metrics used in this study.

The comparison is performed for the VolturnUS-S for all wind speed bins in Table F.1 and for all platforms across selected wind speed bins in Table F.2 and Table F.3. The mean power output and coefficient of variation (CoV) are compared between the two simulation durations, with the relative difference Δ reported for each wind speed bin.

Table F.1: Comparison of mean power output, coefficient of variation (CoV) and annual energy production (AEP) per wind speed bin between the 10-minute and 3-hour simulation runs for the VolturnUS-S. Mean values are computed over the steady-state period, excluding the initial 300 s transient. The total AEP changes by -0.007%, confirming statistical convergence of the standard simulation duration.

VolturnUS-S									
Wind	**Power [kW]**			**CoV**			**AEP [MWh]**		
speed	**10-min**	**3-hr**	**Δ**	**10-min**	**3-hr**	**Δ**	**10-min**	**3-hr**	**Δ**
0-1 m/s	0	0	-	-	-	-	0.0	0.0	-
1-2 m/s	0	0	-	-	-	-	0.0	0.0	-
2-3 m/s	0	0	-	-	-	-	0.0	0.0	-
3-4 m/s	276	273	-1.220%	5.64%	2.29%	-59.39%	71.9	71.0	-1.220%
4-5 m/s	965	964	-0.148%	1.78%	0.91%	-48.69%	330.1	329.6	-0.148%
5-6 m/s	2010	2010	-0.009%	0.95%	0.62%	-34.80%	838.6	838.6	-0.009%
6-7 m/s	3446	3446	0.005%	0.77%	0.52%	-32.04%	1662.9	1663.0	0.005%
7-8 m/s	5281	5281	0.001%	0.72%	0.61%	-15.54%	2825.5	2825.5	0.001%
8-9 m/s	7595	7593	-0.022%	0.74%	0.62%	-16.09%	4349.0	4348.1	-0.022%
9-10 m/s	10410	10406	-0.036%	0.71%	0.63%	-10.20%	6187.2	6185.0	-0.036%
10-11 m/s	13409	13411	0.014%	0.68%	0.63%	-7.54%	8046.4	8047.6	0.014%
11-12 m/s	14999	15000	0.003%	0.49%	0.57%	16.11%	8859.0	8859.2	0.003%
12-13 m/s	15000	15000	-0.001%	0.50%	0.54%	8.87%	8513.6	8513.6	-0.001%
13-14 m/s	15000	15000	-0.003%	0.52%	0.57%	8.97%	7997.6	7997.3	-0.003%
14-15 m/s	15001	15000	-0.005%	0.55%	0.60%	8.39%	7350.1	7349.8	-0.005%
15-16 m/s	15001	15000	-0.005%	0.59%	0.64%	7.86%	6613.1	6612.7	-0.005%
16-17 m/s	15001	15000	-0.006%	0.63%	0.67%	7.19%	5827.8	5827.4	-0.006%
17-18 m/s	15001	15000	-0.006%	0.67%	0.71%	6.31%	5032.2	5031.9	-0.006%
18-19 m/s	15001	15000	-0.006%	0.72%	0.76%	5.22%	4258.9	4258.6	-0.006%
19-20 m/s	15001	15000	-0.007%	0.77%	0.81%	4.28%	3533.5	3533.2	-0.007%
20-21 m/s	15001	15000	-0.007%	0.83%	0.86%	3.03%	2874.4	2874.2	-0.007%
21-22 m/s	15001	15000	-0.008%	0.89%	0.90%	1.54%	2292.9	2292.7	-0.008%
22-23 m/s	15001	15000	-0.009%	0.95%	0.95%	-0.01%	1793.7	1793.6	-0.009%
23-24 m/s	15002	15000	-0.009%	1.01%	1.00%	-1.42%	1376.2	1376.0	-0.009%
24-25 m/s	0	0	-	-	-	-	0.0	0.0	-
25-26 m/s	0	0	-	0.00%	0.00%	-	0.0	0.0	-
Total	-	-	-	0.6537%	0.6534%	0.054%	90634.6	90628.6	-0.007%

Table F.2: Comparison of mean power output for several wind speed bins between the 10-minute and 3-hour simulation runs for all platforms. Δ denotes the relative difference between the simulations.

	Power [kW]																	
Wind	**WindCrete_135m**			**WindCrete_150m**			**ActiveFloat_135m**			**ActiveFloat_150m**			**VolturnUS-S**			**Reference TLP**		
speed	**10-min**	**3-hr**	**Δ**	**10-min**	**3-hr**	**Δ**	**10-min**	**3-hr**	**Δ**	**10-min**	**3-hr**	**Δ**	**10-min**	**3-hr**	**Δ**	**10-min**	**3-hr**	**Δ**
3-4 m/s	253	252	-0.477%	267	266	-0.339%	258	255	-1.196%	276	273	-0.942%	276	273	-1.220%	274	270	-1.356%
4-5 m/s	916	916	-0.080%	952	952	-0.048%	923	921	-0.207%	966	964	-0.160%	965	964	-0.148%	965	963	-0.192%
9-10 m/s	10120	10120	0.002%	10353	10353	-0.001%	9992	9992	0.001%	10184	10184	-0.005%	10410	10406	-0.036%	10824	10821	-0.023%
10-11 m/s	13144	13146	0.018%	13366	13369	0.019%	13006	13010	0.031%	13195	13198	0.029%	13409	13411	0.014%	13754	13760	0.043%
11-12 m/s	14959	14936	-0.153%	14906	14900	-0.044%	15000	15000	-0.001%	15000	15000	-0.003%	14999	15000	0.003%	14997	14991	-0.045%
23-24 m/s	15000	15000	0.002%	14999	15000	0.005%	15001	15000	-0.008%	15001	15000	-0.008%	15002	15000	-0.009%	15002	15000	-0.011%
24-25 m/s	15000	0	-100%	15000	0	-100%	15001	15000	-0.008%	15001	15000	-0.008%	0	0	-	15002	15000	-0.011%

Table F.3: Comparison of coefficient of variation for several wind speed bins between the 10-minute and 3-hour simulation runs for all platforms. Δ denotes the relative difference between the two simulations.

	Coefficient of variation																	
Wind	**WindCrete_135m**			**WindCrete_150m**			**ActiveFloat_135m**			**ActiveFloat_150m**			**VolturnUS-S**			**Reference TLP**		
speed	**10-min**	**3-hr**	**Δ**	**10-min**	**3-hr**	**Δ**	**10-min**	**3-hr**	**Δ**	**10-min**	**3-hr**	**Δ**	**10-min**	**3-hr**	**Δ**	**10-min**	**3-hr**	**Δ**
3-4 m/s	3.16%	2.19%	-30.57%	3.04%	2.12%	-30.29%	3.19%	1.31%	-59.06%	2.64%	1.15%	-56.50%	5.64%	2.29%	-59.39%	2.37%	1.67%	-29.48%
4-5 m/s	1.47%	0.94%	-35.89%	1.41%	0.91%	-35.65%	1.44%	0.56%	-61.25%	1.18%	0.50%	-57.68%	1.78%	0.91%	-48.69%	0.76%	0.73%	-4.21%
9-10 m/s	0.63%	0.65%	3.33%	0.61%	0.64%	3.92%	0.41%	0.30%	-27.10%	0.33%	0.29%	-13.61%	0.71%	0.63%	-10.20%	0.46%	0.49%	7.86%
10-11 m/s	0.62%	0.64%	4.30%	0.60%	0.63%	4.89%	0.38%	0.30%	-21.10%	0.33%	0.29%	-12.63%	0.68%	0.63%	-7.54%	0.48%	0.51%	6.82%
11-12 m/s	1.46%	1.69%	16.07%	2.50%	2.33%	-6.75%	0.24%	0.25%	1.29%	0.26%	0.23%	-9.01%	0.49%	0.57%	16.11%	1.01%	1.26%	24.80%
23-24 m/s	1.71%	1.79%	4.67%	1.78%	1.74%	-1.98%	0.89%	0.96%	7.85%	0.82%	0.89%	7.94%	1.01%	1.00%	-1.42%	1.56%	1.63%	4.93%
24-25 m/s	1.87%	0.00%	-100%	1.92%	0.00%	-100%	1.01%	1.11%	8.99%	0.94%	1.02%	9.05%	-	-	-	1.71%	1.80%	5.36%

G

Wave Influence

8-DOF motions, turbine power and coefficient of variation metrics for H_s = 0.5-5.0 m and corresponding T_p. The impact on the power and coefficient of variation is shown in Table G.1 and Table G.2. The Figures **??**- **??** show the influence on the motions, power and coefficient of variation per floater. All plots use consistent colour conventions from Figure 4.1 and Figure 4.2.

Table G.1: Turbine power for different significant wave heights H_s and periods T_p.

		Turbine power difference vs base ($\mathbf{H_s = 1.53}$ m & $\mathbf{T_p = 7.40}$ s)					
$\mathbf{H_s}$ **[m]**	$\mathbf{T_p}$ **[s]**	**WindCrete 135m**	**WindCrete 150m**	**ActiveFloat 135m**	**ActiveFloat 150m**	**Volturn-US-S**	**Reference TLP**
	3.55	-0.029%	-0.024%	0.019%	0.009%	-0.031%	-0.015%
0.5	**6.42**	-0.026%	-0.022%	0.014%	0.006%	-0.031%	-0.014%
	10.36	-0.026%	-0.022%	0.013%	0.005%	-0.029%	-0.015%
	4.12	-0.028%	-0.024%	0.009%	0.002%	-0.030%	-0.015%
1.0	**6.90**	-0.017%	-0.015%	0.004%	0.000%	-0.021%	-0.009%
	10.65	-0.014%	-0.012%	0.003%	-0.001%	-0.018%	-0.010%
	4.67	-0.025%	-0.020%	-0.003%	-0.006%	-0.050%	-0.013%
1.5	**7.37**	-0.001%	-0.001%	0.000%	0.000%	-0.002%	-0.001%
	10.93	0.007%	0.005%	-0.002%	-0.004%	-0.003%	0.000%
	5.22	-0.014%	-0.010%	-0.002%	-0.003%	-0.062%	-0.005%
2.0	**7.83**	0.026%	0.021%	0.001%	0.004%	0.028%	0.013%
	11.22	0.036%	0.031%	-0.002%	-0.002%	0.017%	0.018%
	5.75	0.015%	0.018%	0.011%	0.013%	0.070%	0.015%
2.5	**8.28**	0.065%	0.052%	0.007%	0.011%	0.066%	0.034%
	11.50	0.074%	0.066%	0.004%	0.003%	0.040%	0.041%
	6.26	0.056%	0.057%	0.024%	0.027%	0.083%	0.041%
3.0	**8.73**	0.115%	0.094%	0.014%	0.019%	0.110%	0.062%
	11.79	0.122%	0.111%	0.014%	0.012%	0.066%	0.069%
	7.26	0.196%	0.181%	0.068%	0.072%	0.270%	0.119%
4.0	**9.58**	0.255%	0.218%	0.033%	0.038%	0.199%	0.145%
	12.37	0.254%	0.236%	0.053%	0.047%	0.130%	0.147%
	8.21	0.325%	0.289%	0.064%	0.071%	0.445%	0.190%
5.0	**10.41**	0.450%	0.405%	0.062%	0.063%	0.281%	0.255%
	12.95	0.449%	0.420%	0.123%	0.111%	0.214%	0.259%
1.53	**7.40**	**10121 kW**	**10357 kW**	**9995 kW**	**10186 kW**	**10407 kW**	**10822 kW**

Table G.2: Coefficient of variation (CoV) for different significant wave heights H_s and periods T_p

		Coefficient of Variation					
$\mathbf{H_s}$ [m]	$\mathbf{T_p}$ [s]	WindCrete 135m	WindCrete 150m	ActiveFloat 135m	ActiveFloat 150m	Volturn-US-S	Reference TLP
	3.55	0.186%	0.690%	0.309%	0.221%	0.170%	0.030%
0.5	**6.42**	0.221%	0.704%	0.287%	0.206%	0.190%	0.108%
	10.36	0.426%	0.783%	0.335%	0.255%	0.253%	0.308%
	4.12	0.177%	0.690%	0.254%	0.181%	0.286%	0.043%
1.0	**6.90**	0.365%	0.765%	0.275%	0.222%	0.339%	0.255%
	10.65	0.811%	1.021%	0.426%	0.365%	0.463%	0.634%
	4.67	0.191%	0.695%	0.200%	0.149%	0.471%	0.094%
1.5	**7.37**	0.609%	0.902%	0.332%	0.302%	0.577%	0.458%
	10.93	1.227%	1.346%	0.591%	0.530%	0.691%	0.977%
	5.22	0.281%	0.730%	0.238%	0.215%	0.714%	0.204%
2.0	**7.83**	0.939%	1.137%	0.438%	0.414%	0.861%	0.721%
	11.22	1.664%	1.721%	0.797%	0.724%	0.921%	1.339%
	5.75	0.487%	0.834%	0.375%	0.359%	1.275%	0.385%
2.5	**8.28**	1.344%	1.467%	0.578%	0.549%	1.161%	1.041%
	11.50	2.119%	2.131%	1.034%	0.943%	1.149%	1.721%
	6.26	0.786%	1.035%	0.530%	0.515%	1.458%	0.625%
3.0	**8.73**	1.806%	1.870%	0.747%	0.706%	1.463%	1.408%
	11.79	2.595%	2.571%	1.298%	1.186%	1.379%	2.127%
	7.26	1.656%	1.749%	0.914%	0.898%	1.979%	1.296%
4.0	**9.58**	2.881%	2.857%	1.160%	1.081%	2.050%	2.265%
	12.37	3.621%	3.534%	1.901%	1.741%	1.860%	3.012%
	8.21	2.613%	2.616%	1.080%	1.051%	2.819%	2.023%
5.0	**10.41**	4.101%	4.007%	1.685%	1.555%	2.534%	3.252%
	12.95	4.758%	4.609%	2.603%	2.402%	2.404%	4.036%
1.53	**7.40**	**0.627%**	**0.914%**	**0.337%**	**0.309%**	**0.594%**	**0.472%**

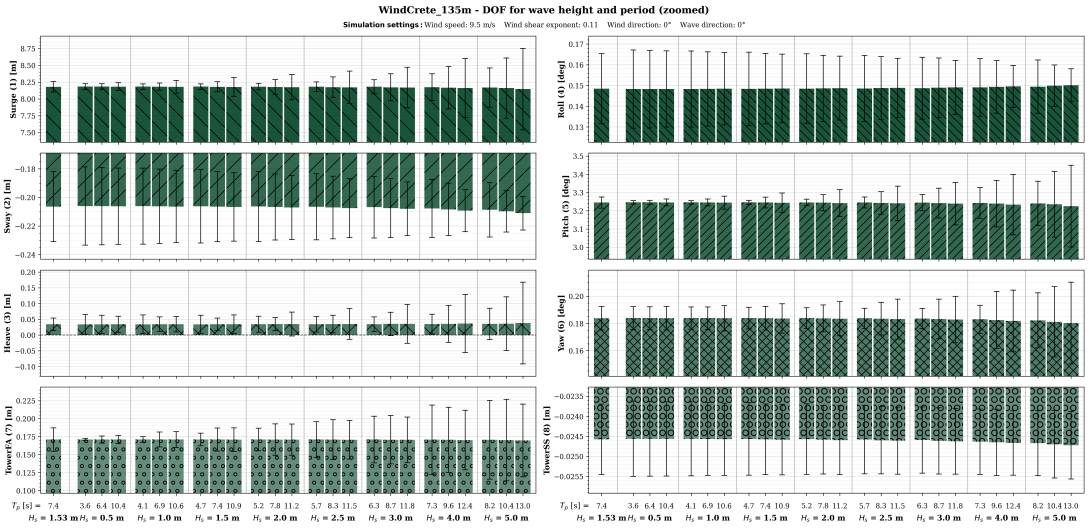

Figure G.1: WindCrete_135m: 8-DOF motions per H_s and T_p combination (vertical axis zoomed).

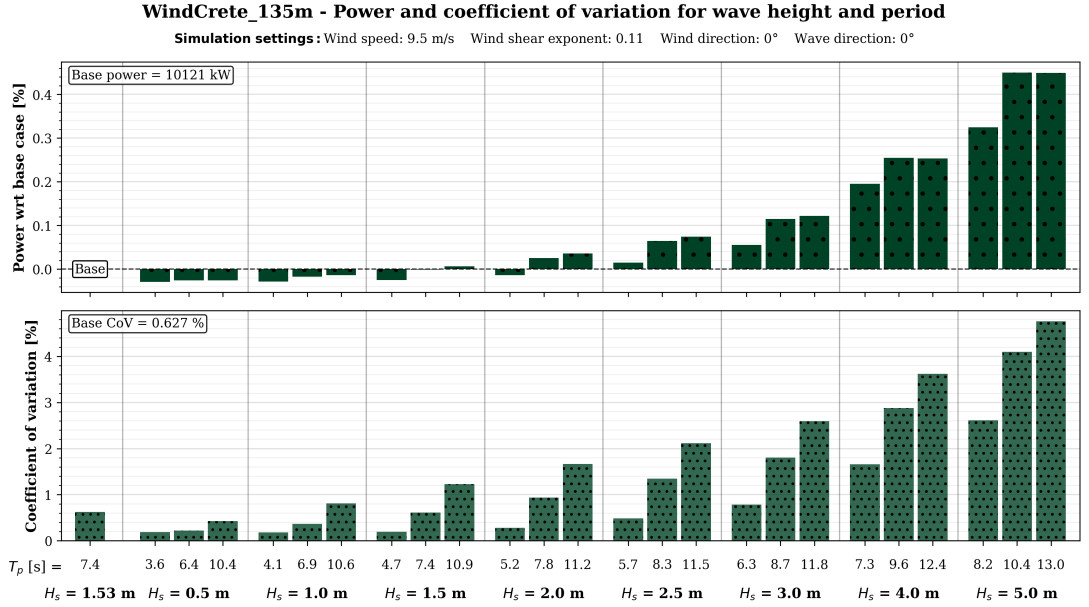

Figure G.2: WindCrete_135m: Power with respect to base and CoV per H_s and T_p combination.

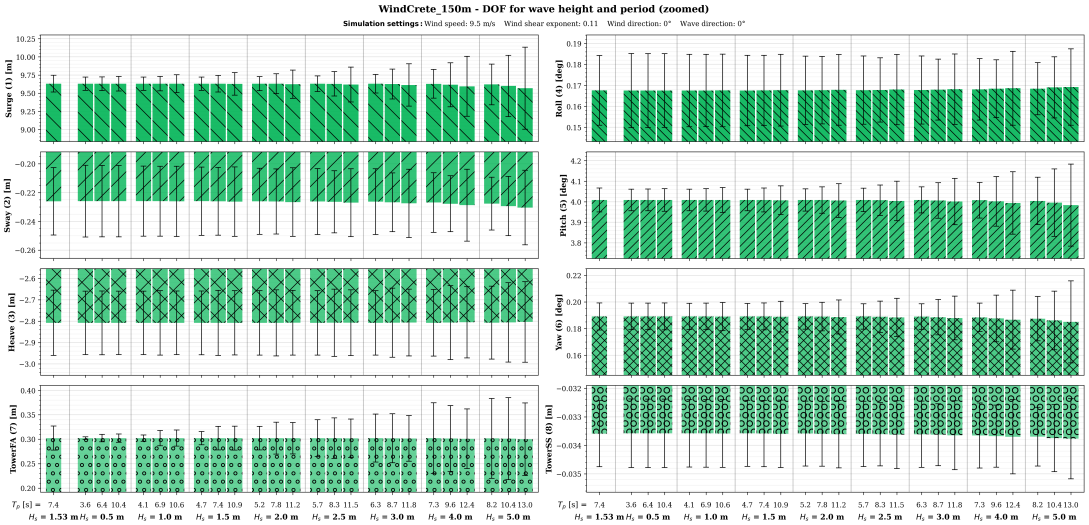

Figure G.3: WindCrete_150m: 8-DOF motions per H_s and T_p combination (vertical axis zoomed).

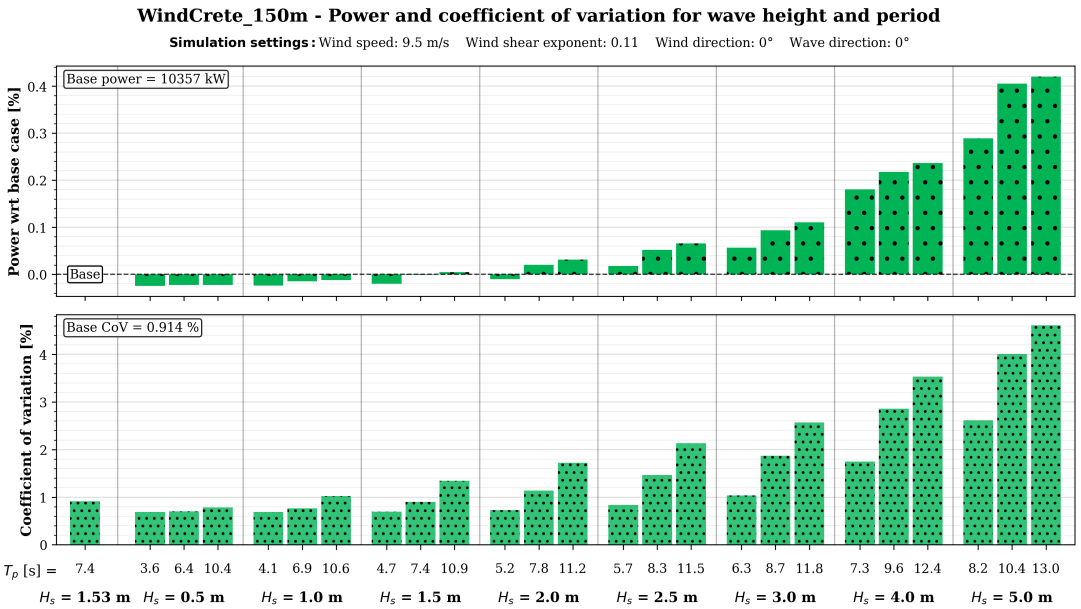

Figure G.4: WindCrete_150m: Power with respect to base and CoV per H_s and T_p combination.

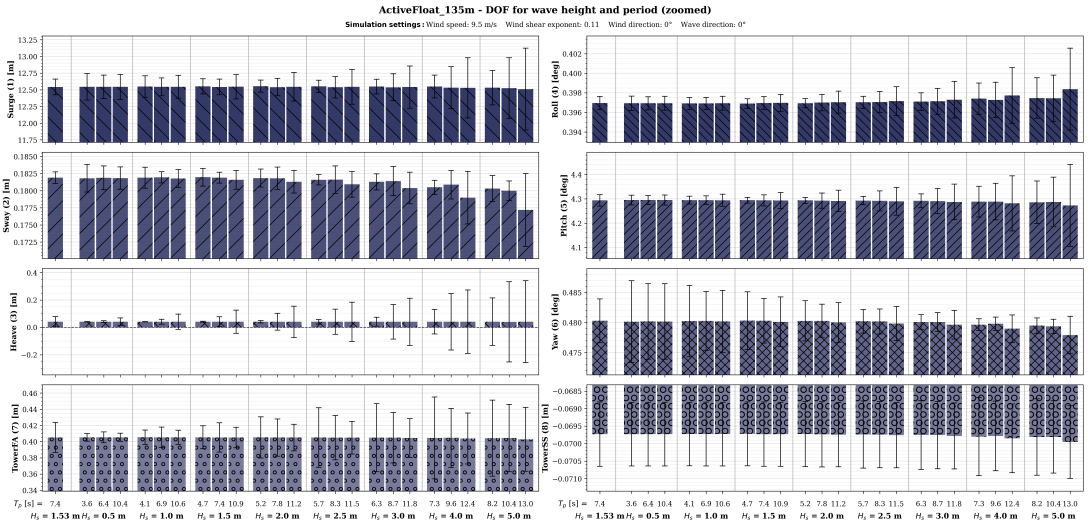

Figure G.5: ActiveFloat_135m: 8-DOF motions per H_s and T_p combination (vertical axis zoomed).

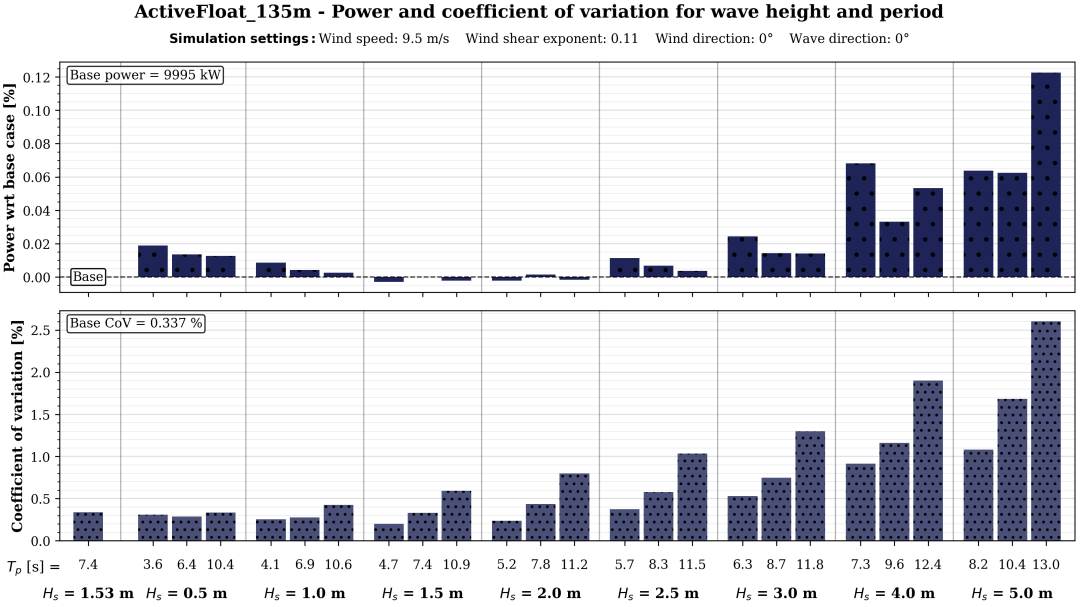

Figure G.6: ActiveFloat_135m: Power with respect to base and CoV per H_s and T_p combination.

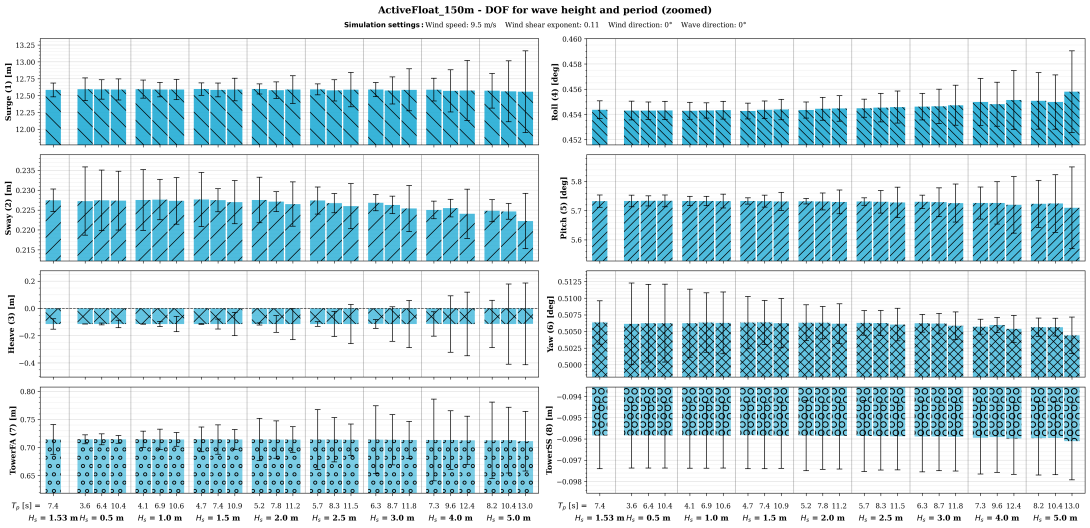

Figure G.7: ActiveFloat_150m: 8-DOF motions per H_s and T_p combination (vertical axis zoomed).

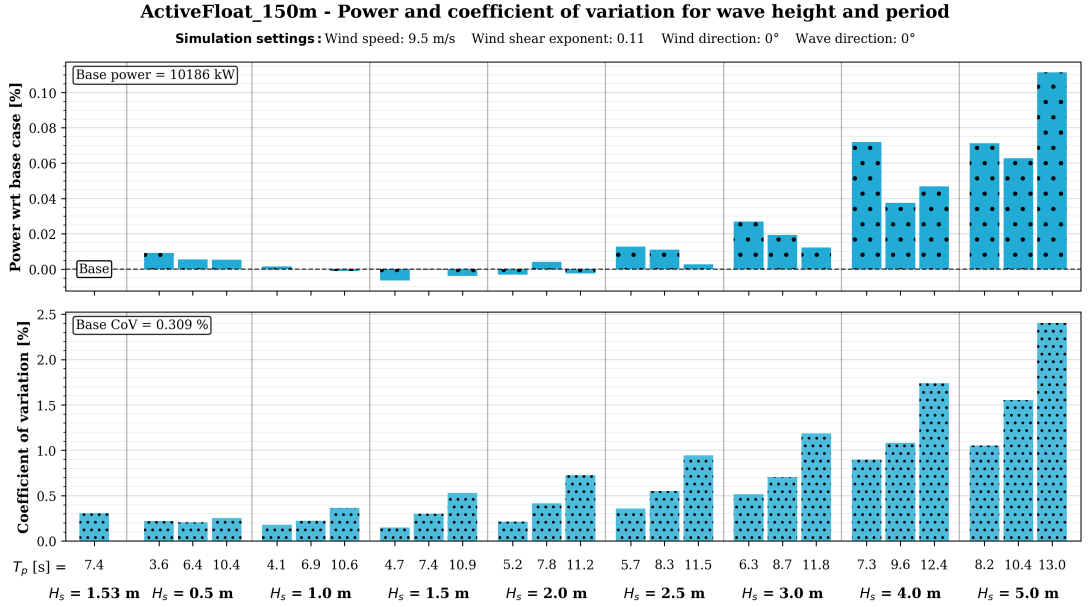

Figure G.8: ActiveFloat_150m: Power with respect to base and CoV per H_s and T_p combination.

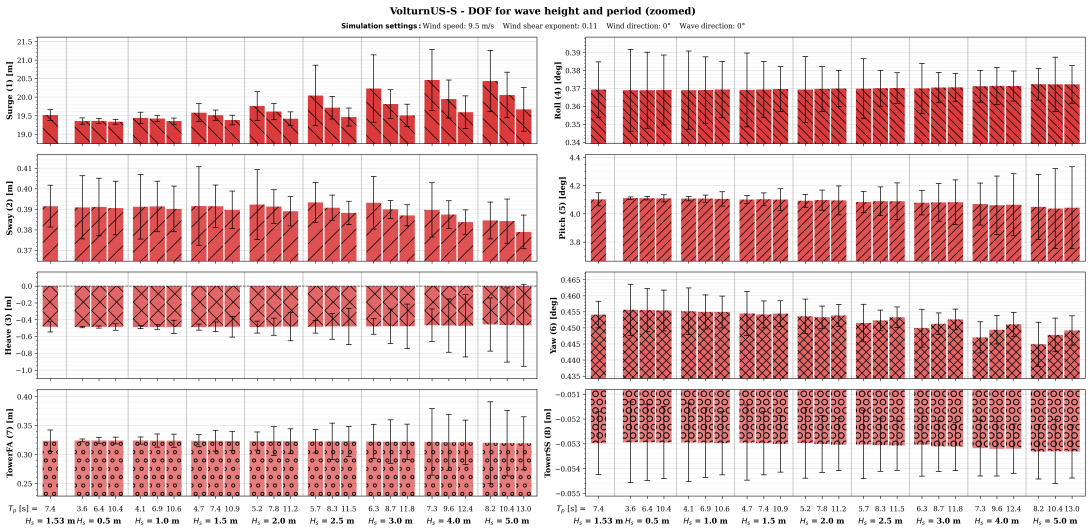

Figure G.9: VolturnUS-S: 8-DOF motions per H_s and T_p combination (vertical axis zoomed).

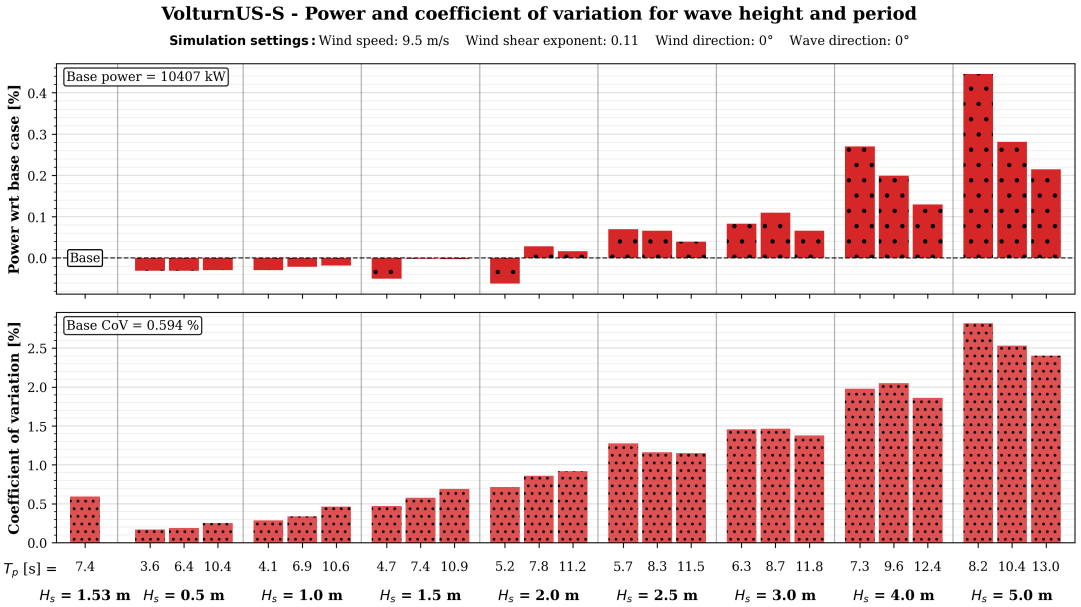

Figure G.10: VolturnUS-S: Power with respect to base and CoV per H_s and T_p combination.

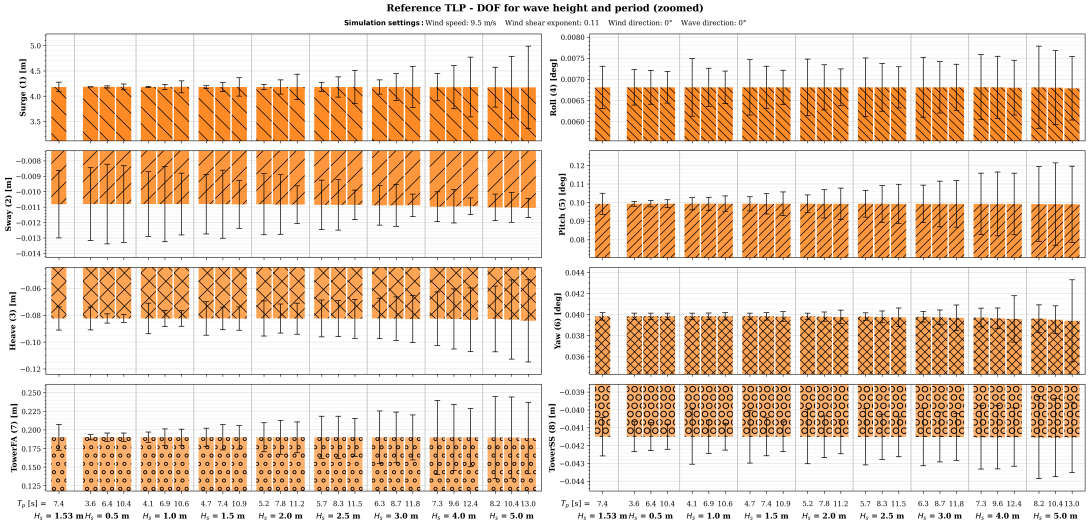

Figure G.11: Reference TLP: 8-DOF motions per H_s and T_p combination (vertical axis zoomed).

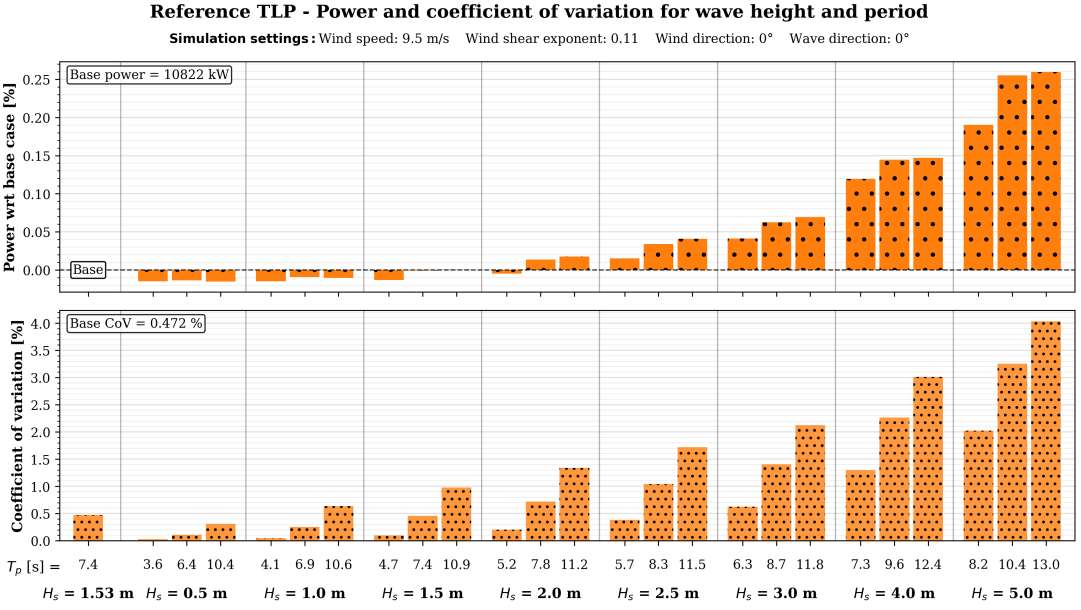

Figure G.12: Reference TLP: Power with respect to base and CoV per H_s and T_p combination.

H

Mooring Stiffness Influence: Natural Period and Damping

Natural periods and damping ratios per mooring stiffness (0.25-2.0 x original) from free-decay tests. The natural periods for surge, sway and yaw are given in Tables H.1 and H.2. The Figures H.1- H.6 show the influence on natural period and damping per degree of freedom. All plots use consistent colour conventions from Figure 4.1 and Figure 4.2.

Table H.1: Surge and sway natural periods for different mooring stiffnesses. Simulations for the TLP at *2.0 × EA* failed to converge and are excluded from the results.

	Surge / sway natural period [s]					
EA x	**WindCrete 135m**	**WindCrete 150m**	**ActiveFloat 135m**	**ActiveFloat 150m**	**Volturn-US-S**	**Reference TLP**
0.25	97.0 / 96.8	99.2 / 99.1	153.6 / 154.0	154.0 / 154.5	141.7 / 142.1	38.7 / 38.7
0.50	83.9 / 83.9	86.3 / 86.2	146.7 / 147.1	147.0 / 147.5	137.7 / 138.3	38.0 / 38.0
0.75	78.9 / 78.8	81.3 / 81.3	144.3 / 144.7	144.7 / 145.1	136.5 / 137.0	37.7 / 37.7
1.00	76.2 / 76.1	78.7 / 78.7	143.1 / 143.5	143.4 / 143.9	135.9 / 136.3	37.6 / 37.6
1.25	74.5 / 74.4	77.0 / 77.1	142.6 / 142.7	142.9 / 143.2	135.6 / 136.0	37.5 / 37.5
1.50	73.4 / 73.3	75.9 / 76.0	142.1 / 142.6	142.4 / 143.0	135.3 / 135.7	37.5 / 37.5
1.75	72.5 / 72.5	75.0 / 75.1	141.7 / 142.2	142.1 / 142.6	135.2 / 135.5	37.4 / 37.4
2.00	71.8 / 71.9	74.4 / 74.5	141.5 / 141.9	141.8 / 142.3	135.0 / 135.4	- / -

Table H.2: Yaw natural period for different mooring stiffnesses.

	Yaw natural period [s]					
EA x	**WindCrete 135m**	**WindCrete 150m**	**ActiveFloat 135m**	**ActiveFloat 150m**	**Volturn-US-S**	**Reference TLP**
0.25	14.0	14.6	85.3	85.5	92.0	23.0
0.50	12.5	13.1	83.5	83.6	90.7	22.6
0.75	11.9	12.5	82.8	82.9	90.3	22.5
1.00	11.7	12.3	82.5	82.6	90.1	22.4
1.25	11.5	12.1	82.3	82.4	90.0	22.4
1.50	11.4	12.0	82.1	82.3	89.9	22.3
1.75	11.4	11.9	82.0	82.2	89.8	22.3
2.00	11.3	11.8	82.0	82.1	89.8	22.4

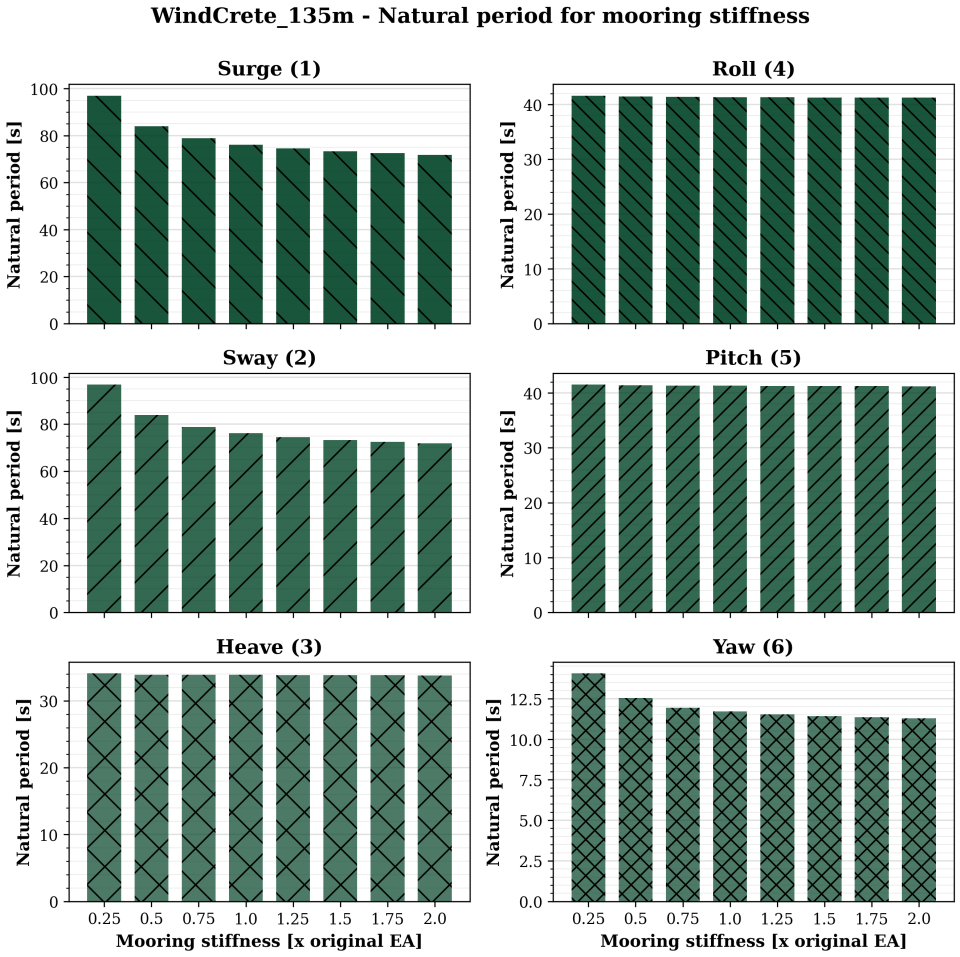

(a) Natural period vs mooring stiffness.

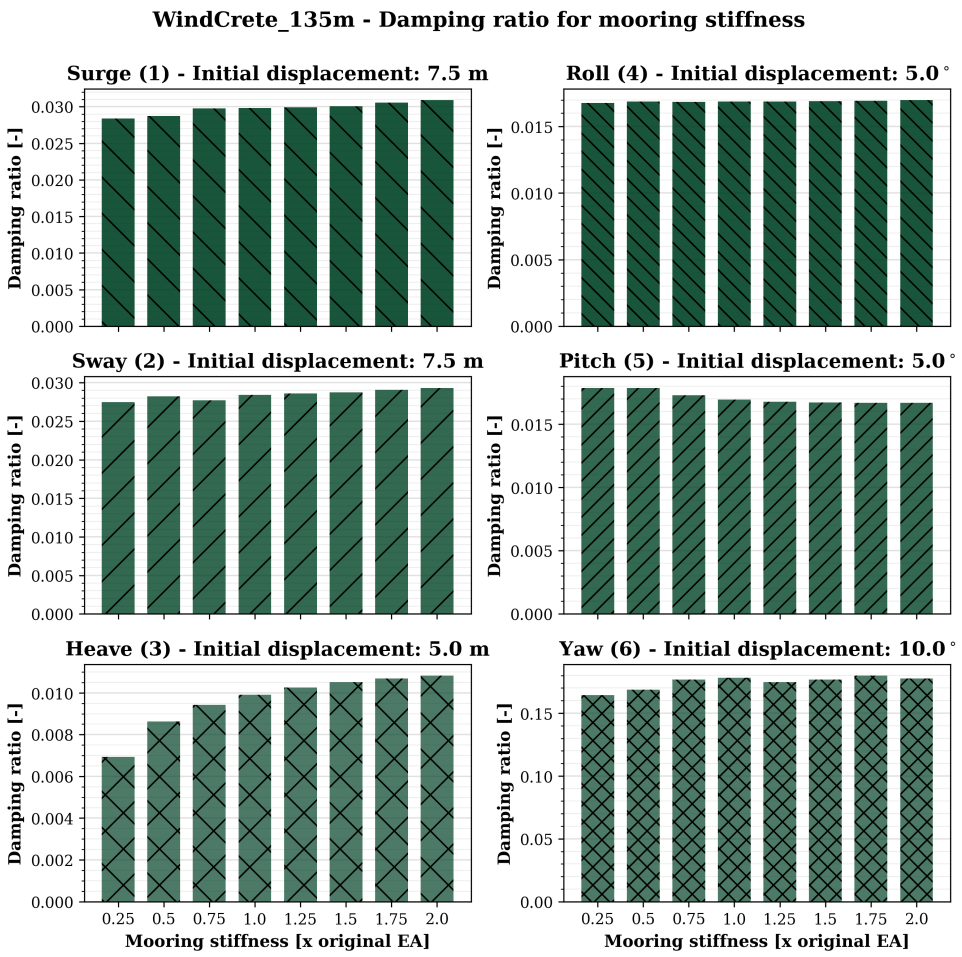

(b) Damping ratio vs mooring stiffness.

Figure H.1: WindCrete_135m: Natural period and damping ratio for degree of freedom vs mooring stiffness.

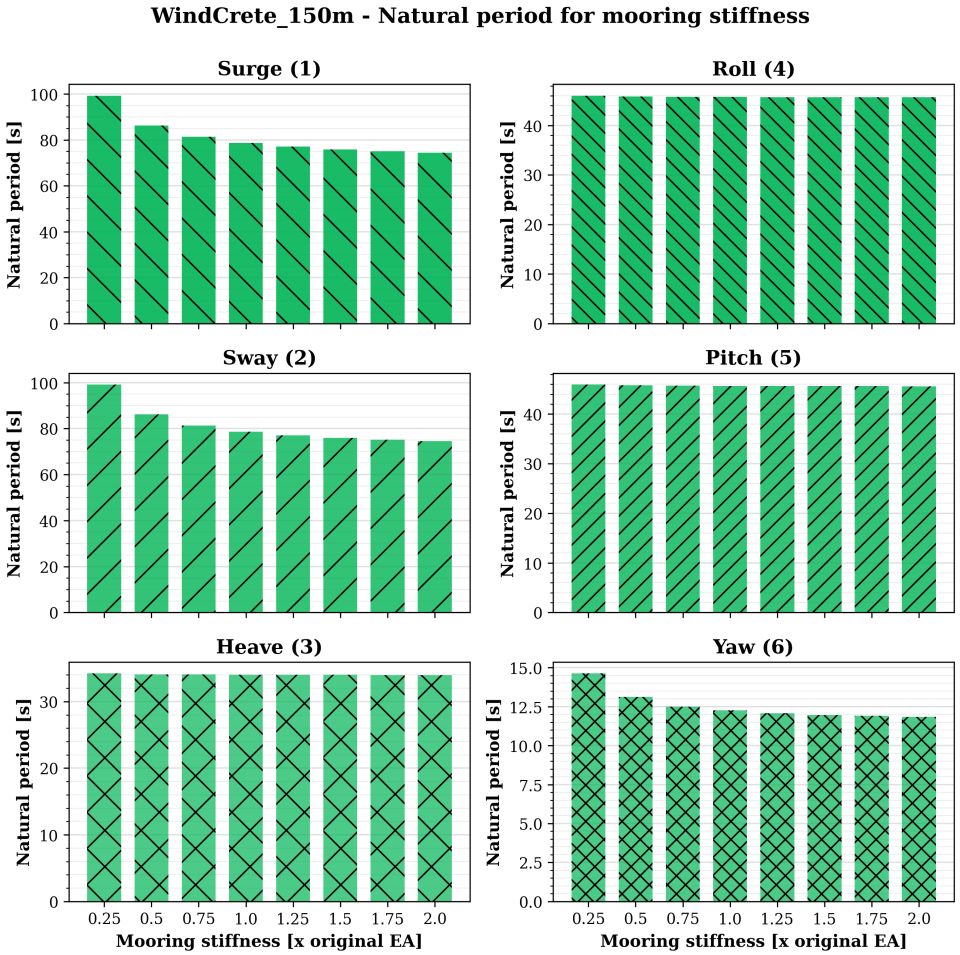

(a) Natural period vs mooring stiffness.

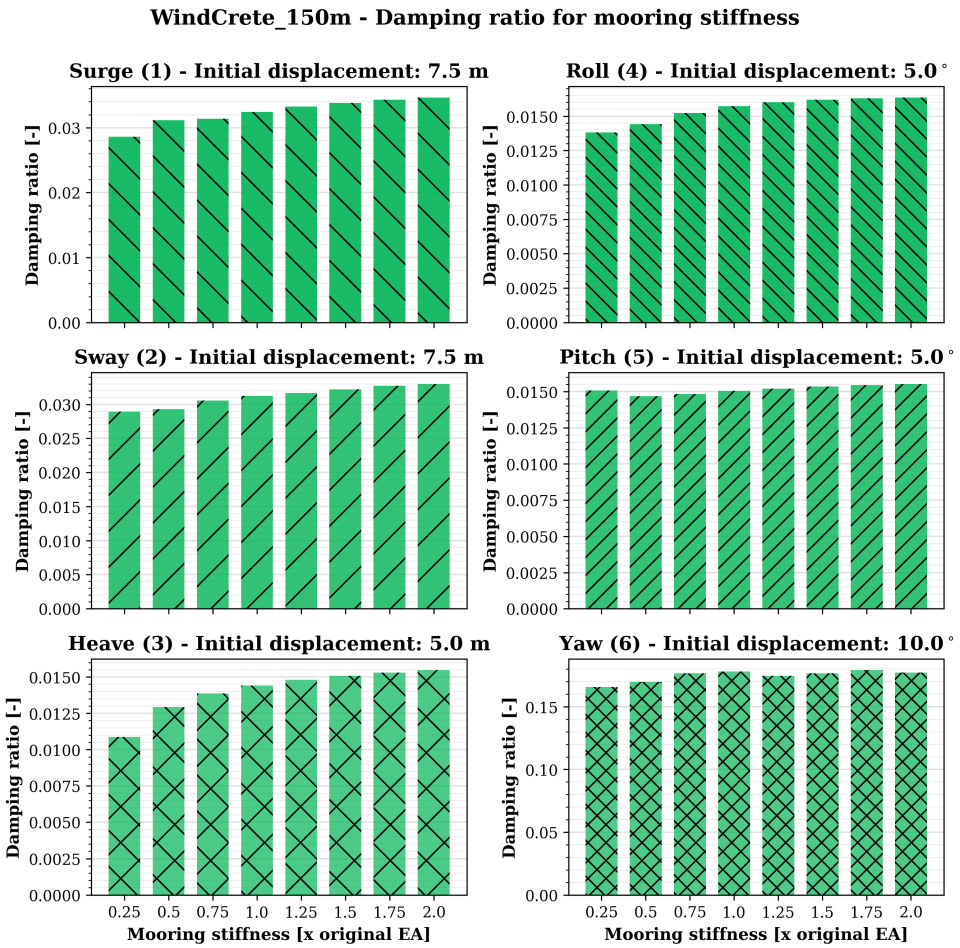

(b) Damping ratio vs mooring stiffness.

Figure H.2: WindCrete_150m: Natural period and damping ratio for degree of freedom vs mooring stiffness.

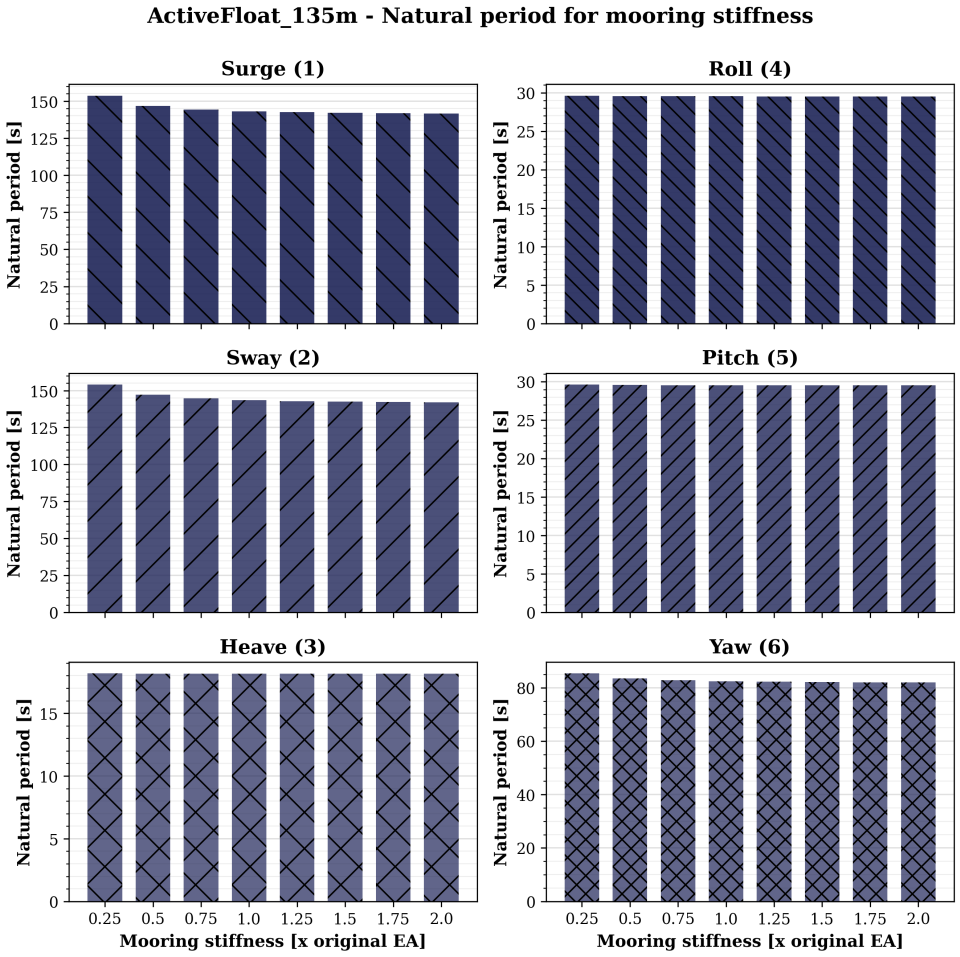

(a) Natural period vs mooring stiffness.

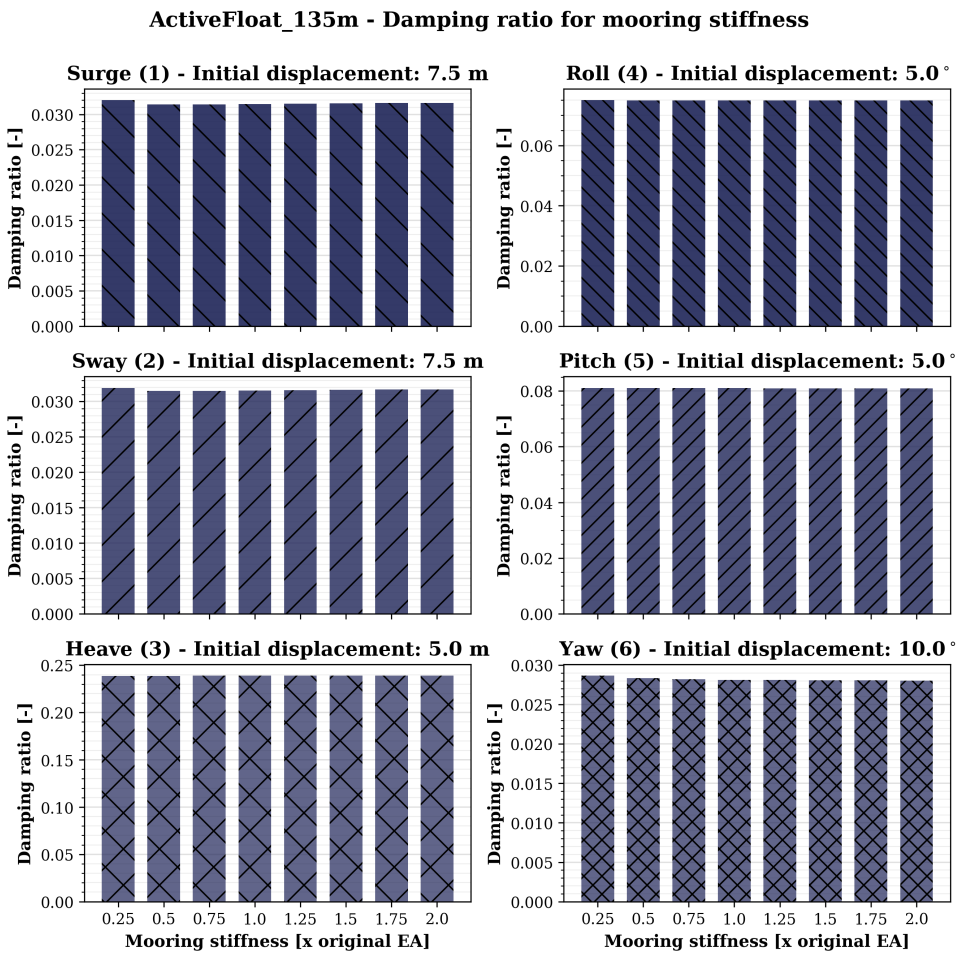

(b) Damping ratio vs mooring stiffness.

Figure H.3: ActiveFloat_135m: Natural period and damping ratio for degree of freedom vs mooring stiffness.

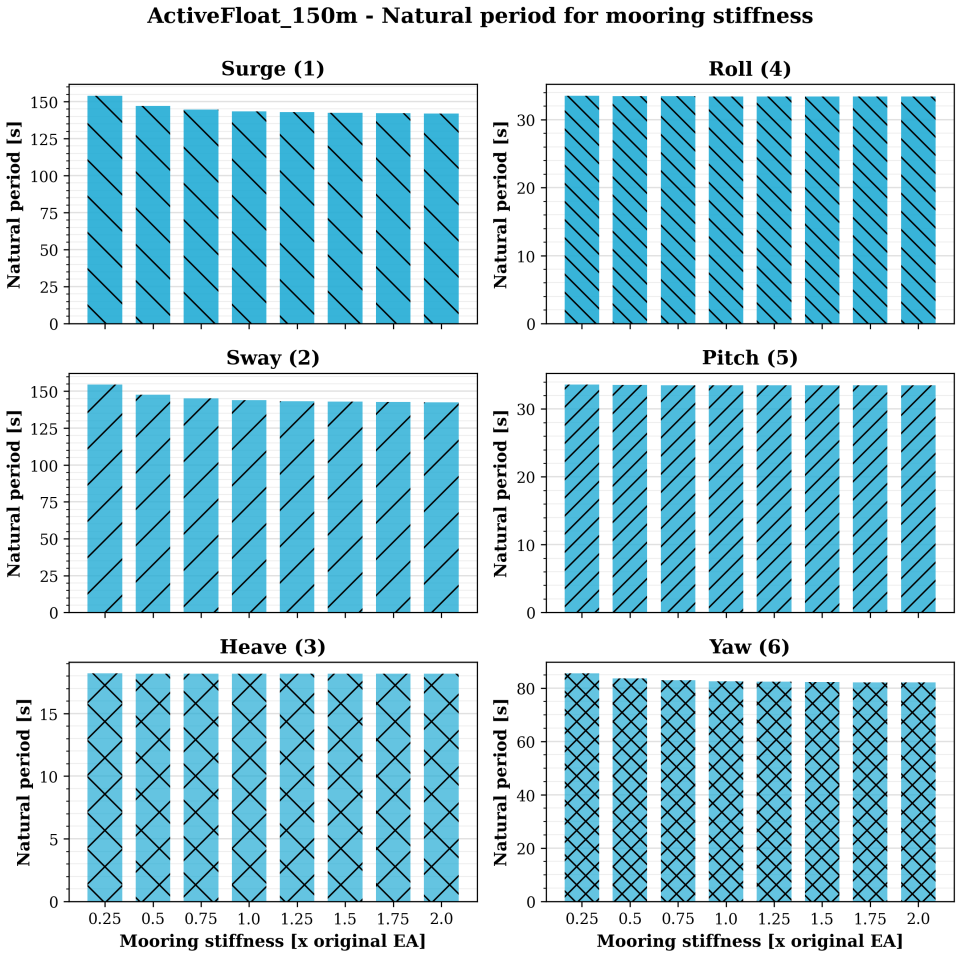

(a) Natural period vs mooring stiffness.

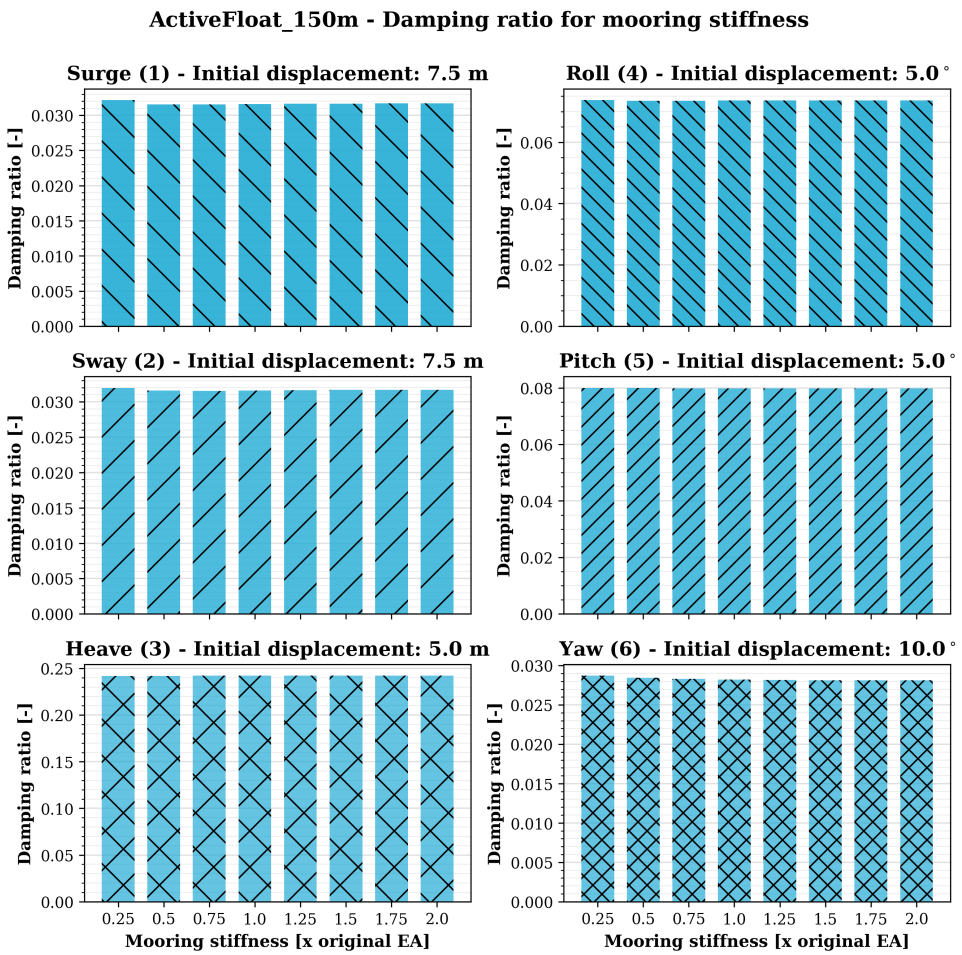

(b) Damping ratio vs mooring stiffness.

Figure H.4: ActiveFloat_150m: Natural period and damping ratio for degree of freedom vs mooring stiffness.

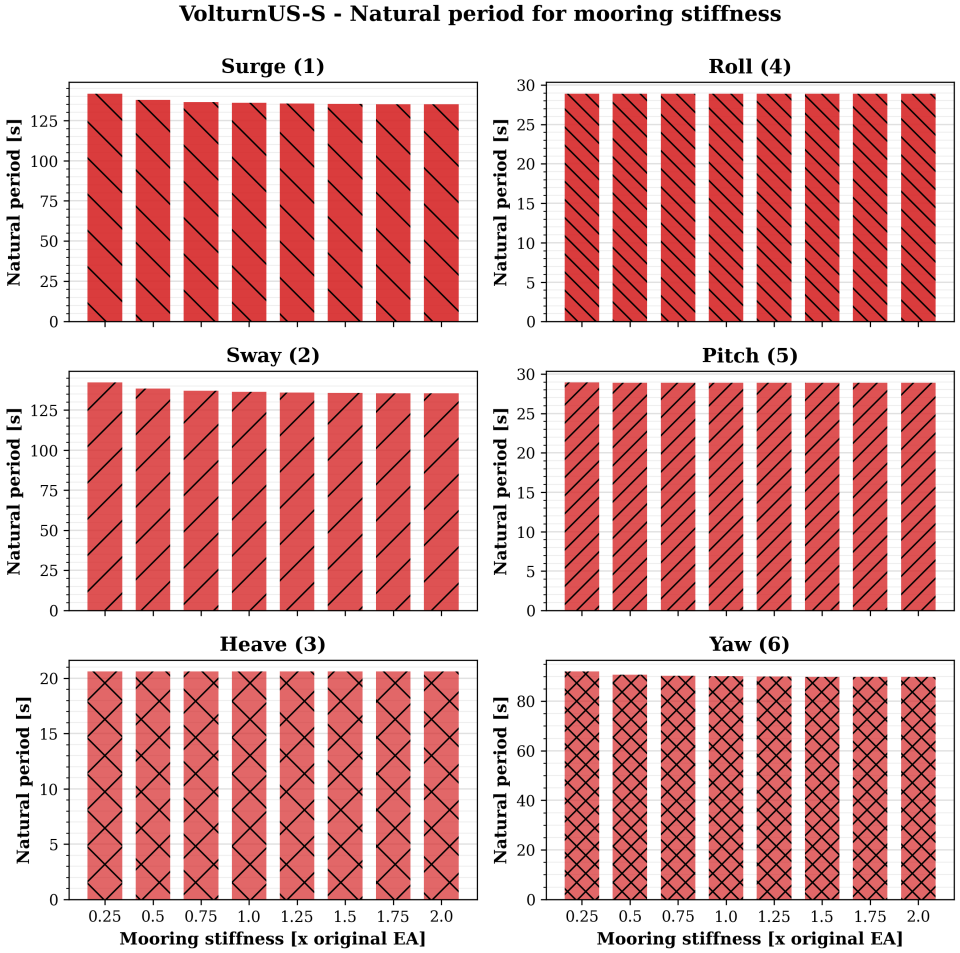

(a) Natural period vs mooring stiffness.

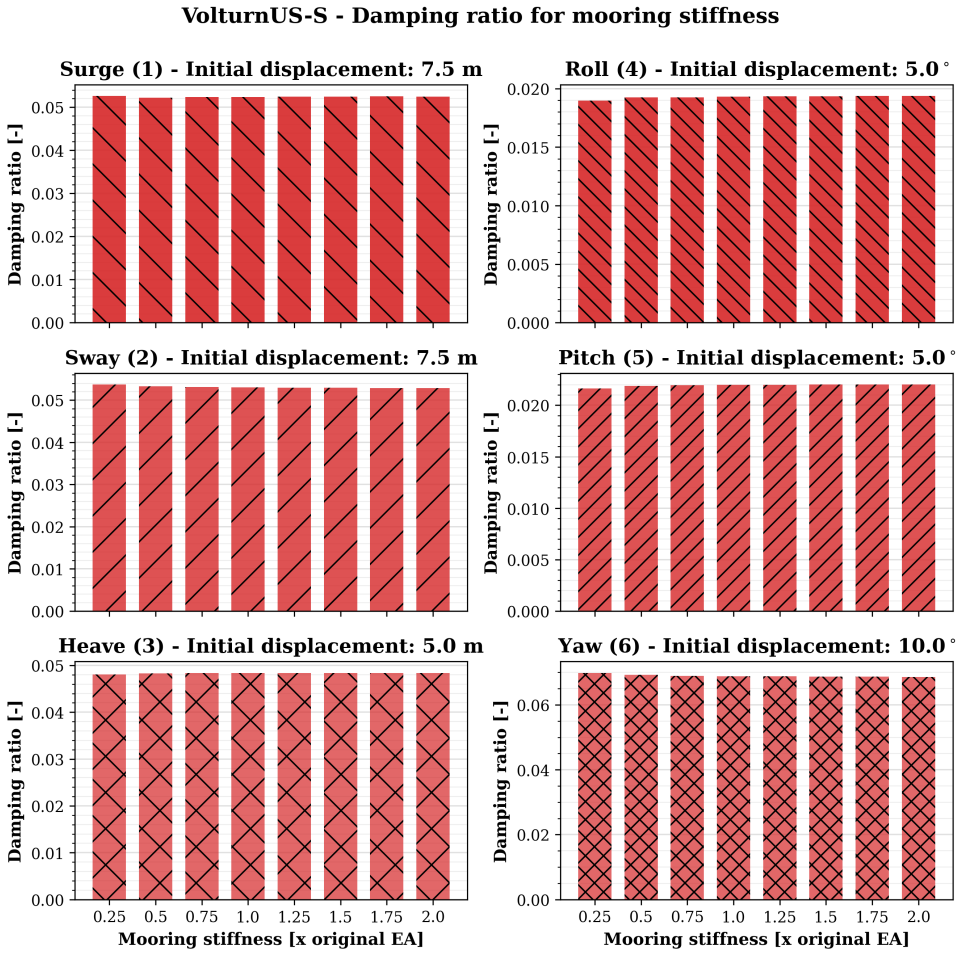

(b) Damping ratio vs mooring stiffness.

Figure H.5: VolturnUS-S: Natural period and damping ratio for degree of freedom vs mooring stiffness.

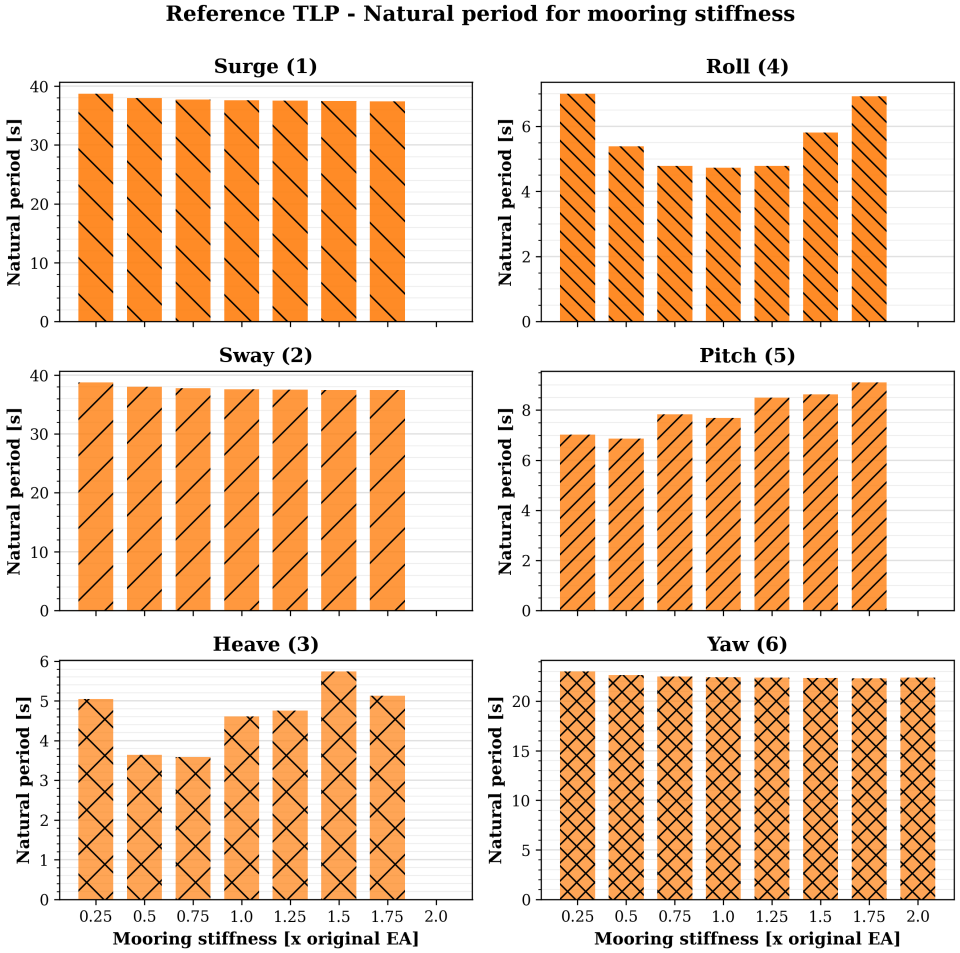

(a) Natural period vs mooring stiffness.

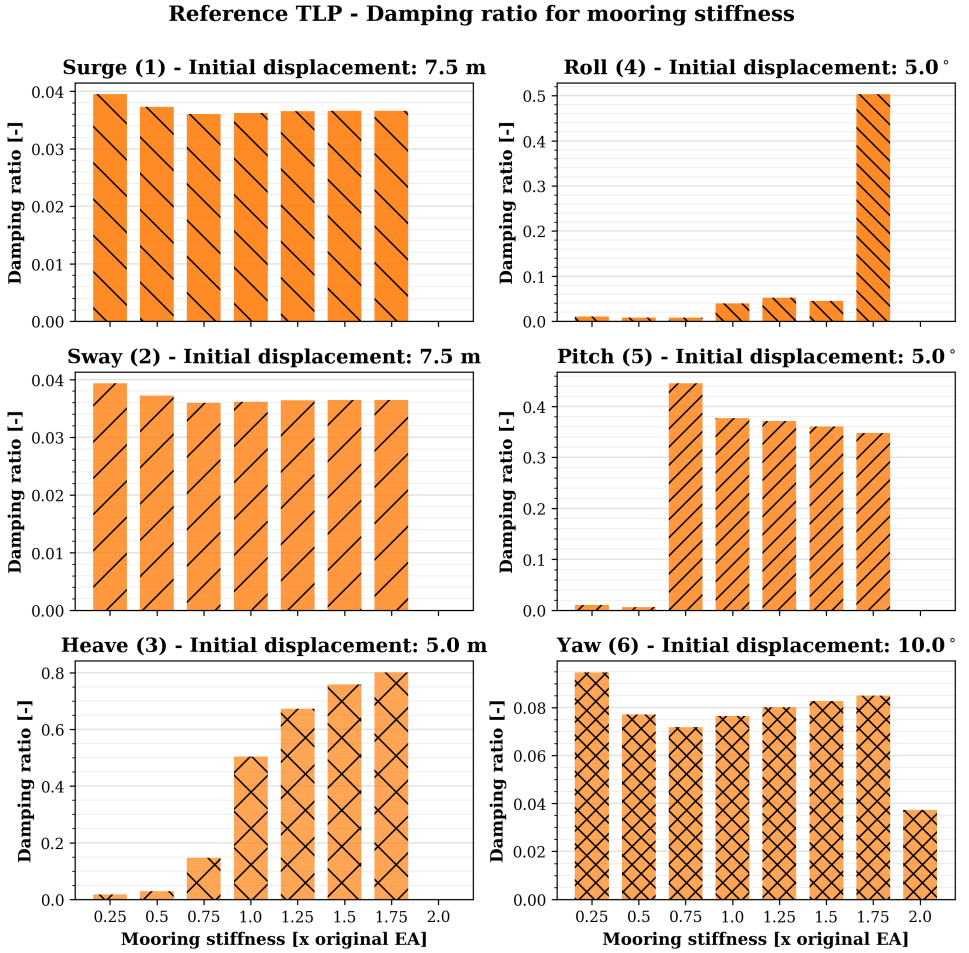

(b) Damping ratio vs mooring stiffness.

Figure H.6: Reference TLP: Natural period and damping ratio for degree of freedom vs mooring stiffness. Simulations at *2.0 × EA* failed to converge and are excluded from the results.

I

Mooring Stiffness Influence: Power Metrics

8-DOF motions, turbine power and coefficient of variation per mooring stiffness (0.25-2.0 x original). The Figures I.1- I.6 show the influence on the motions, power and coefficient of variation per floater. All plots use consistent colour conventions from Figure 4.1 and Figure 4.2.

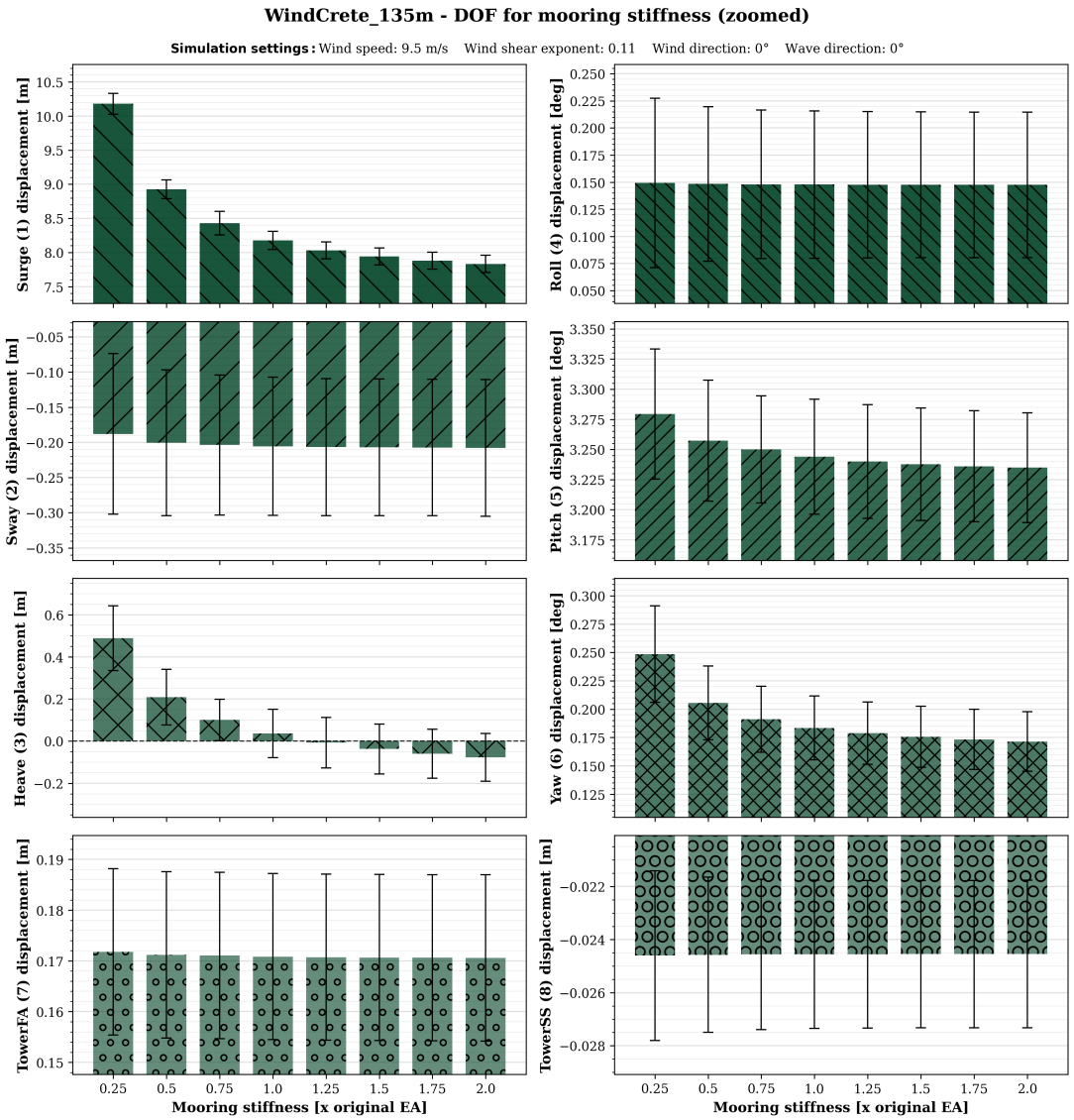

(a) 8-DOF per mooring stiffness.

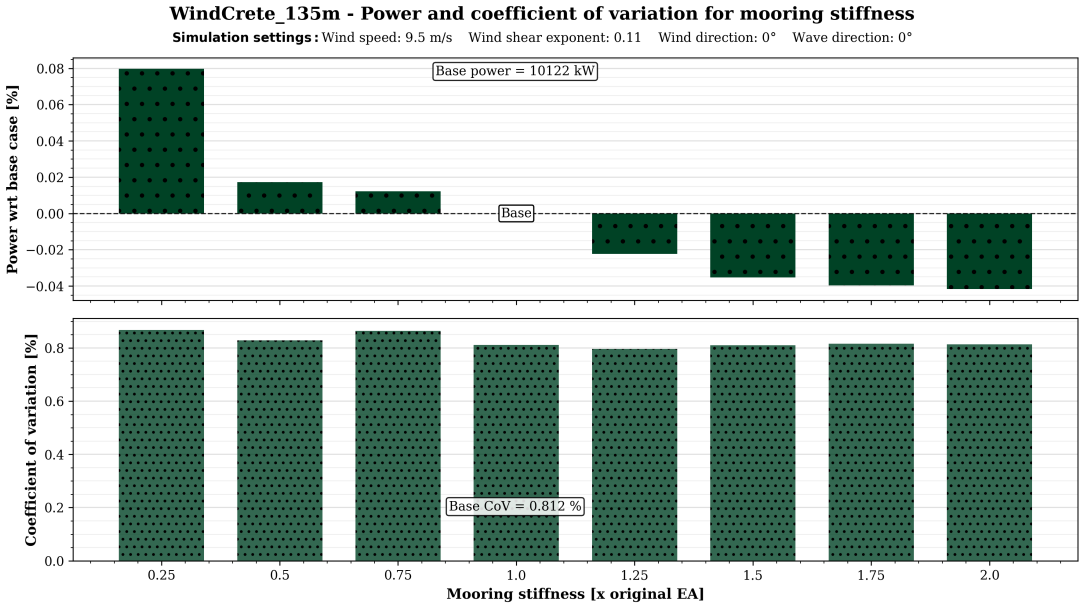

(b) Power and coefficient of variation (CoV) per mooring stiffness.

Figure I.1: WindCrete_135m:8-DOF, power and CoV per mooring stiffness.

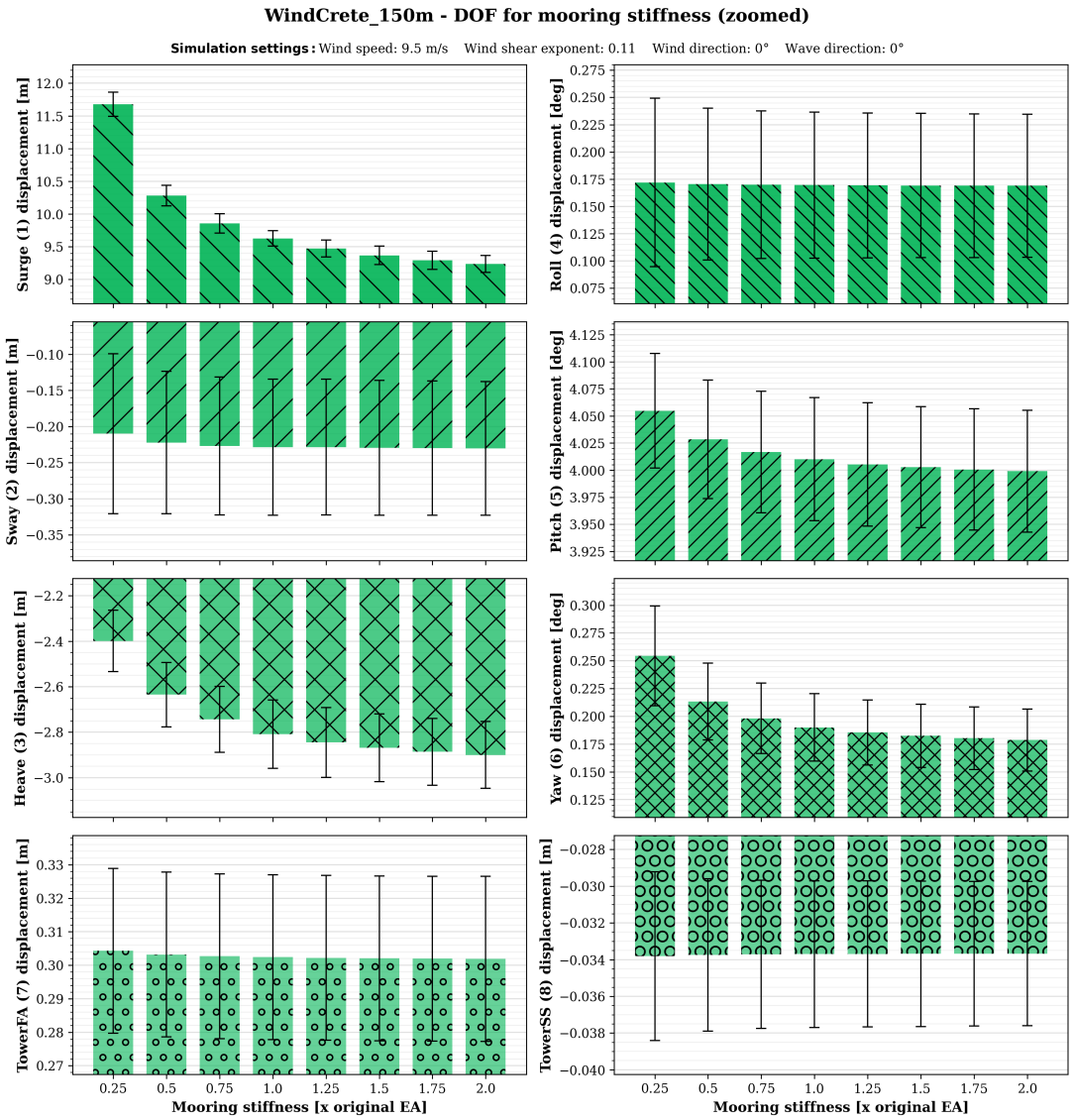

(a) 8-DOF per mooring stiffness.

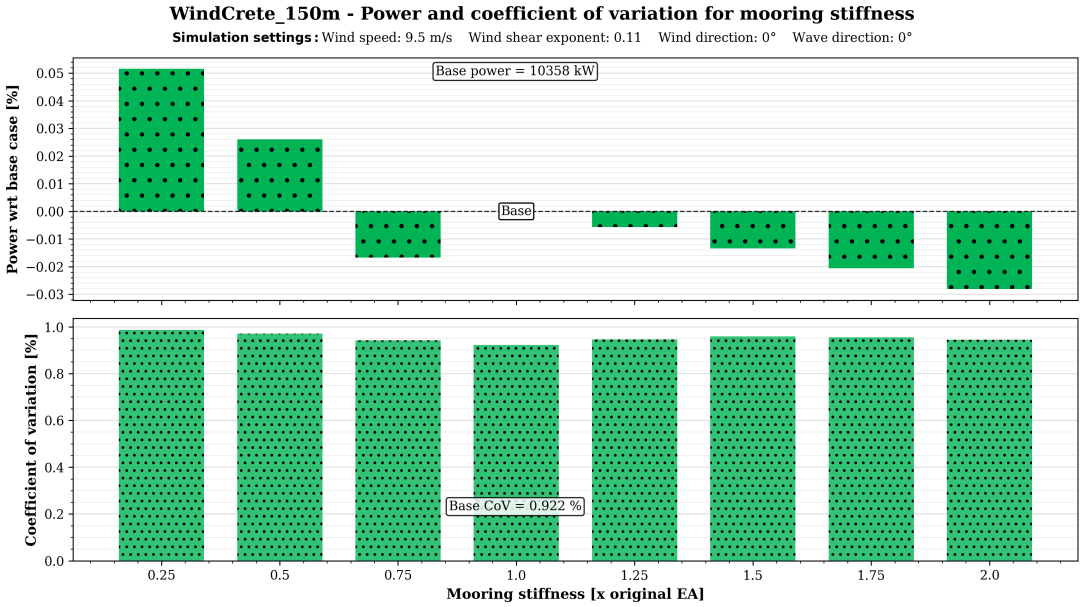

(b) Power and coefficient of variation (CoV) per mooring stiffness.

Figure I.2: WindCrete_150m:8-DOF, power and CoV per mooring stiffness.

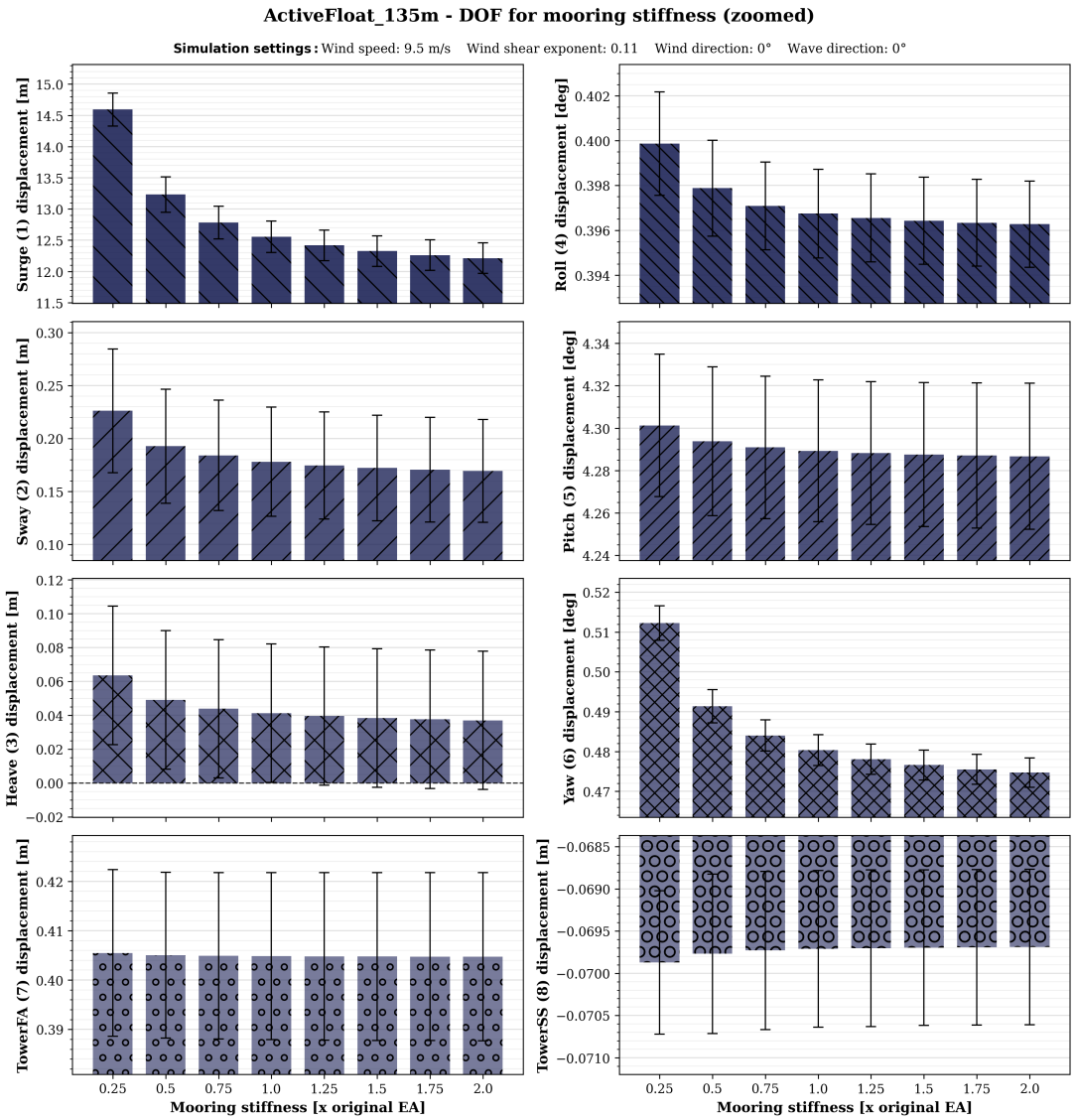

(a) 8-DOF per mooring stiffness.

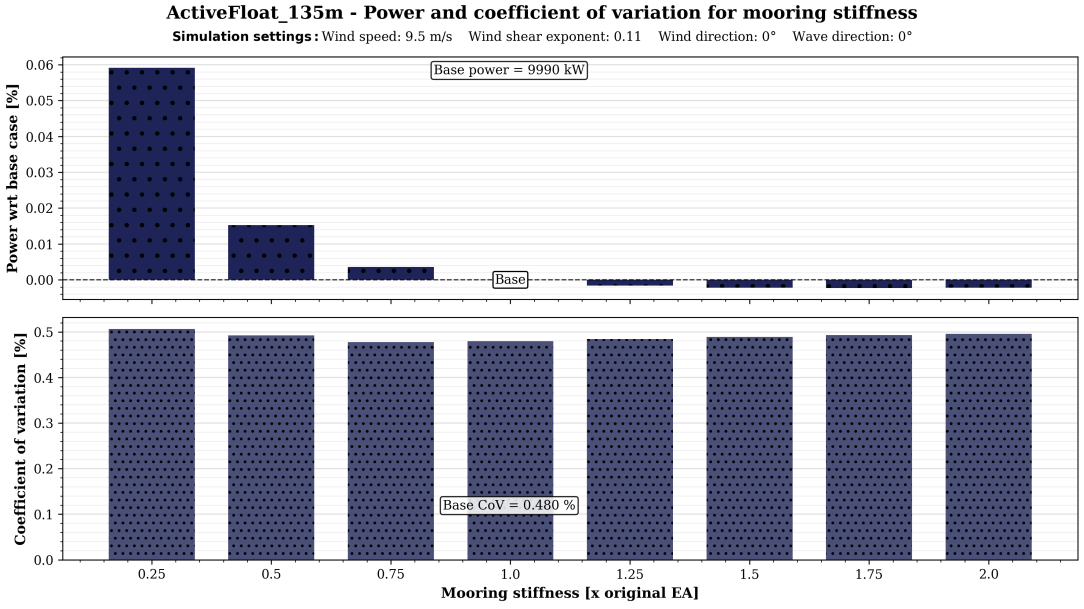

(b) Power and coefficient of variation (CoV) per mooring stiffness.

Figure I.3: ActiveFloat_135m:8-DOF, power and CoV per mooring stiffness.

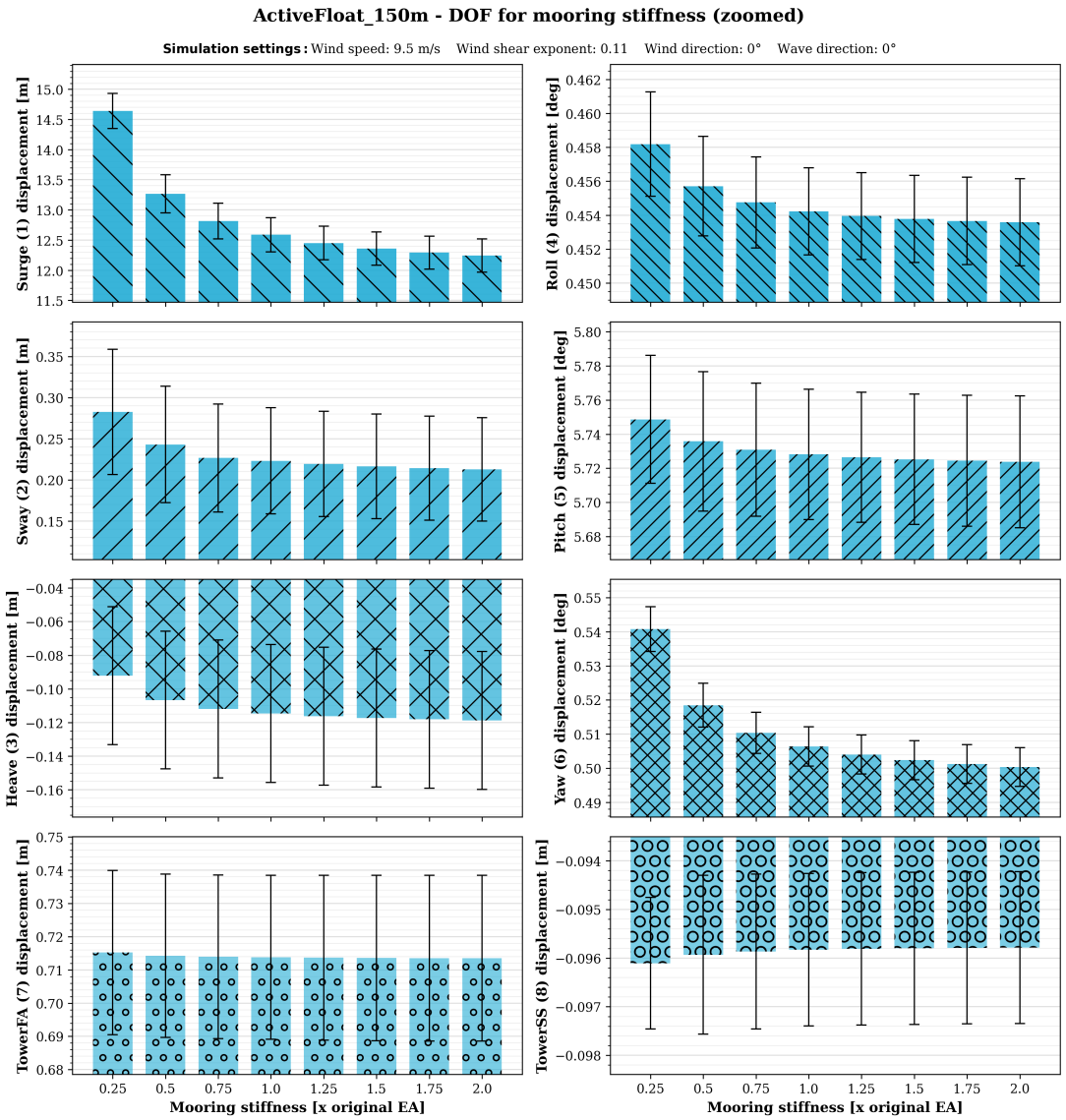

(a) 8-DOF per mooring stiffness.

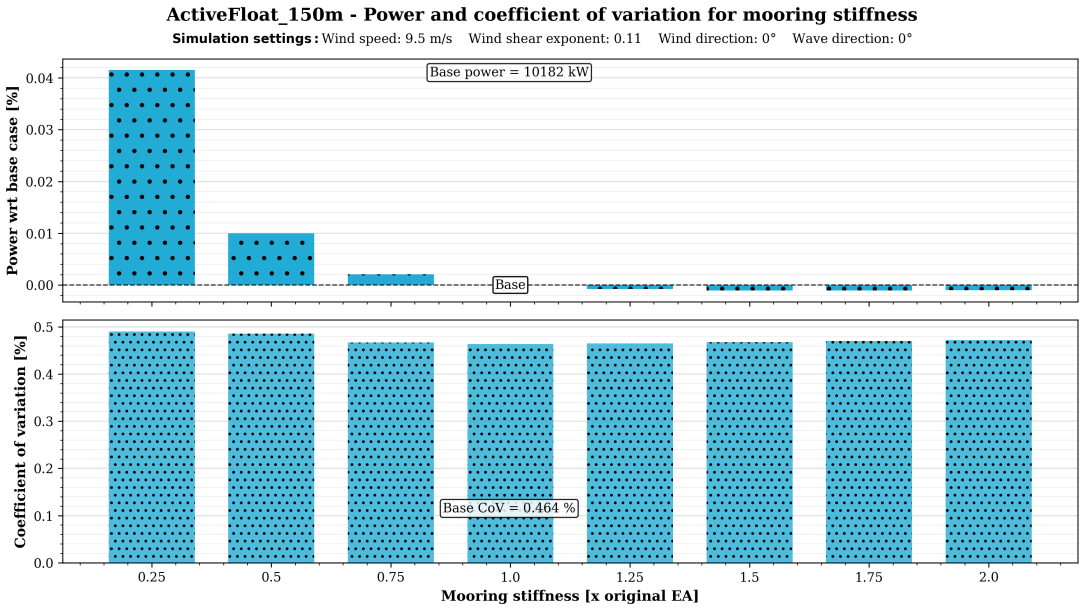

(b) Power and coefficient of variation (CoV) per mooring stiffness.

Figure I.4: ActiveFloat_150m:8-DOF, power and CoV per mooring stiffness.

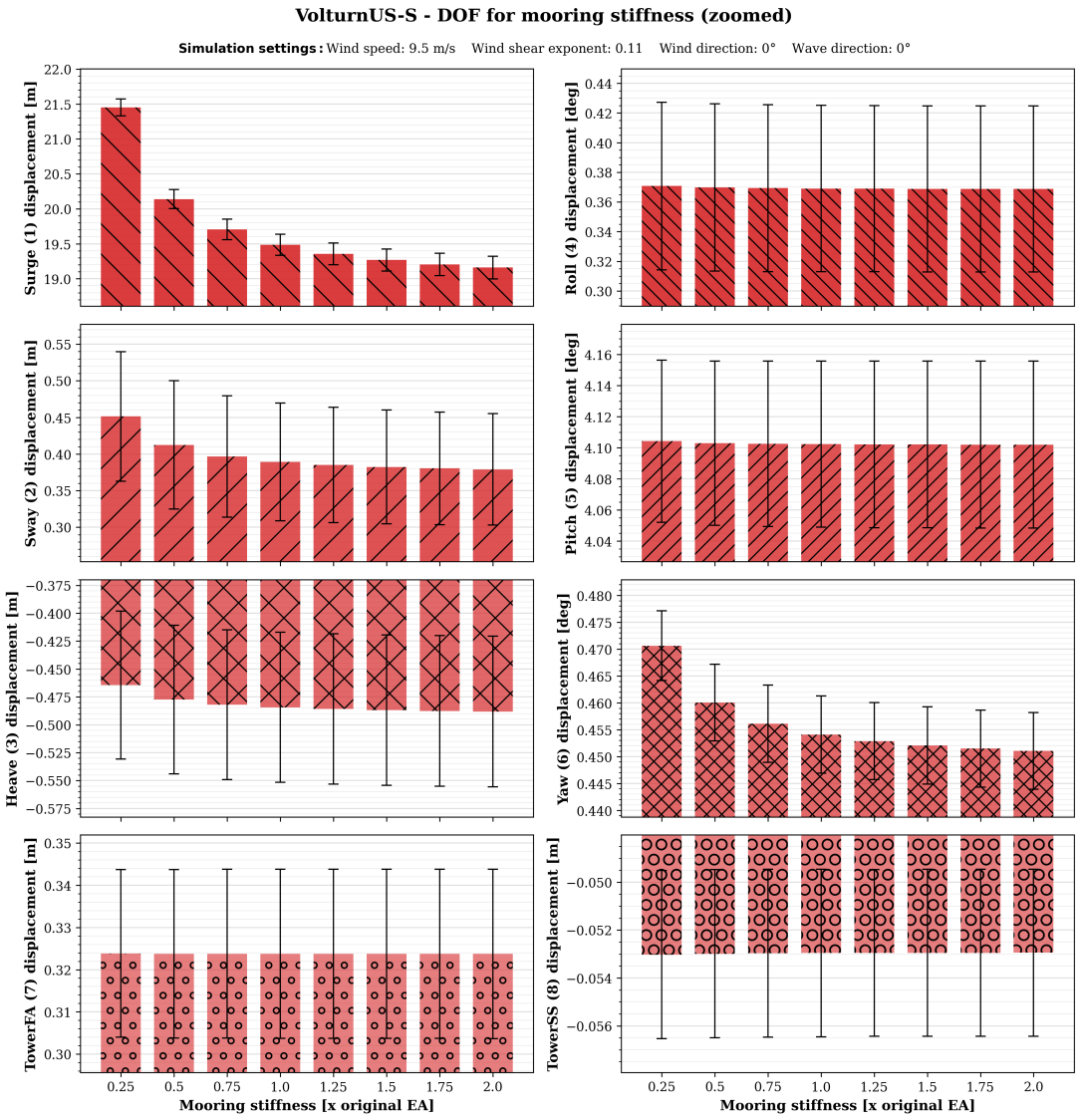

(a) 8-DOF per mooring stiffness.

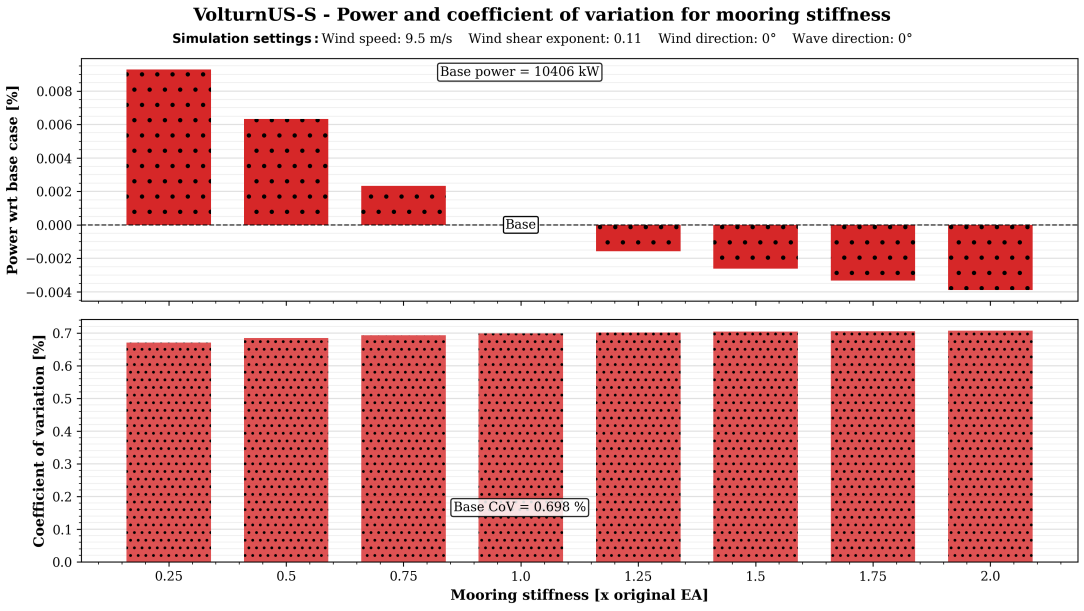

(b) Power and coefficient of variation (CoV) per mooring stiffness.

Figure I.5: VolturnUS-S:8-DOF, power and CoV per mooring stiffness.

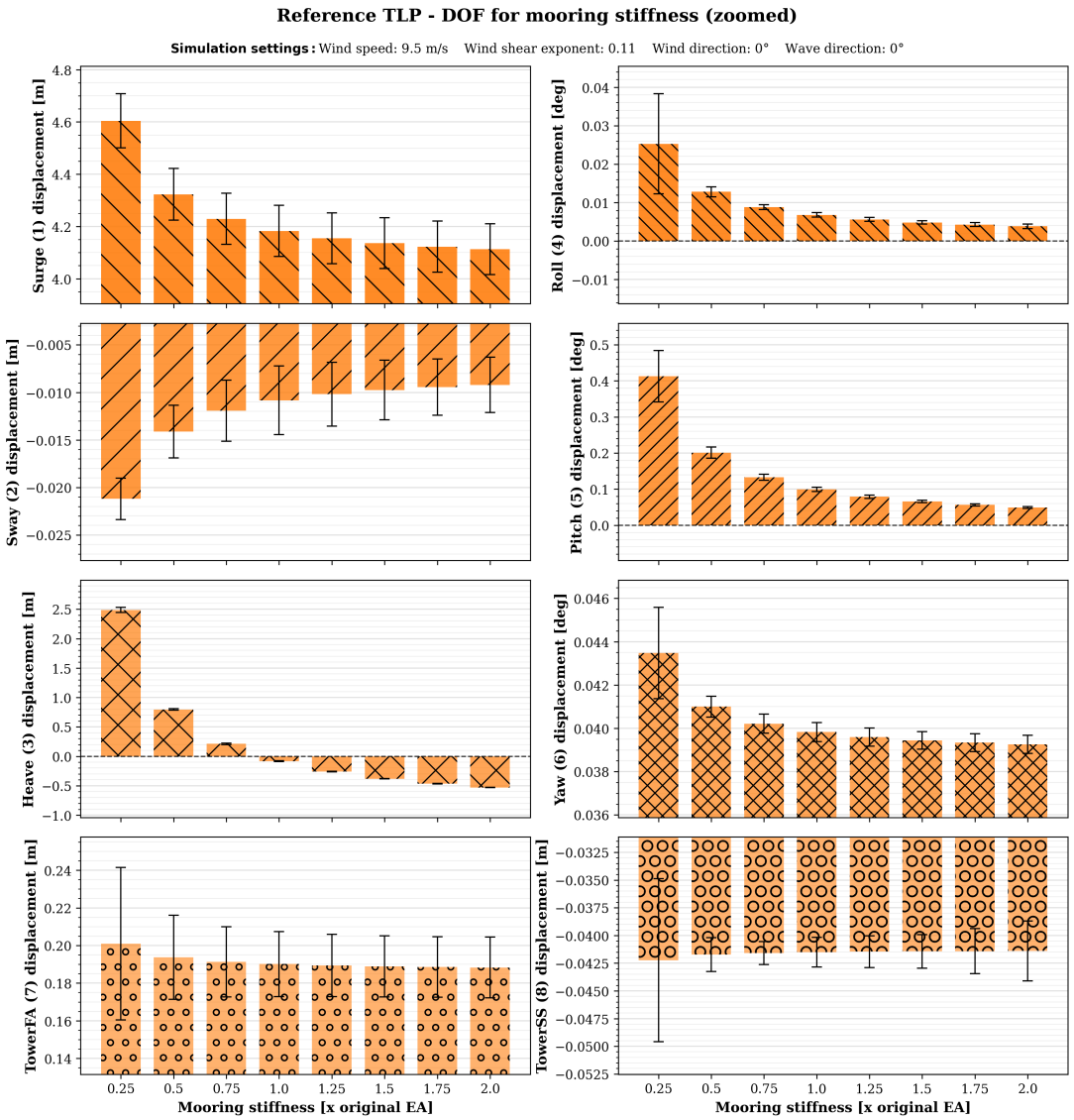

(a) 8-DOF per mooring stiffness.

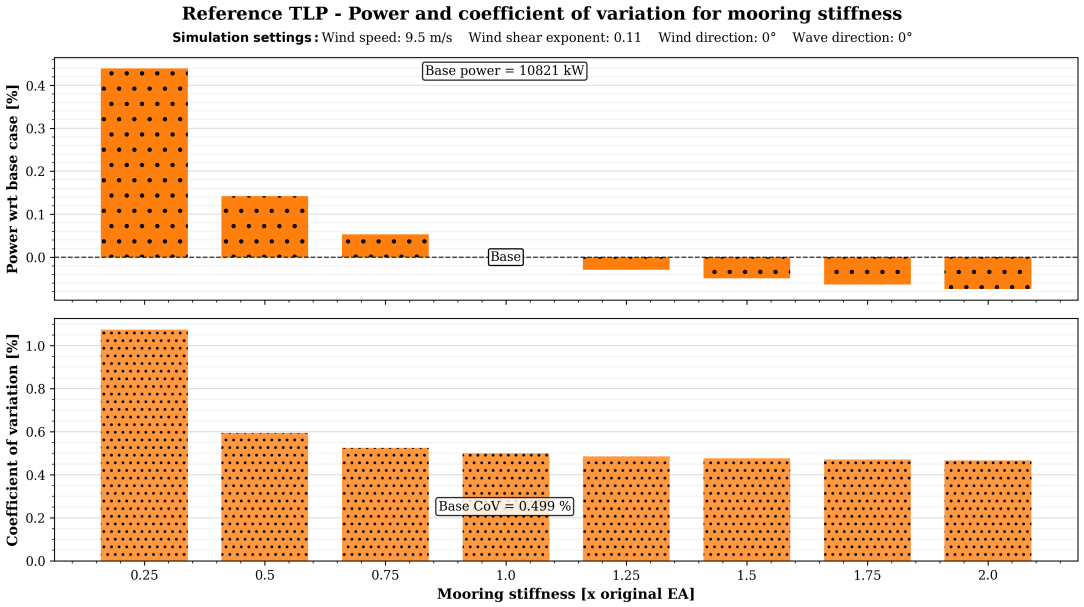

(b) Power and coefficient of variation (CoV) per mooring stiffness.

Figure I.6: Reference TLP:8-DOF, power and CoV per mooring stiffness.

J

Wind-Wave Misalignment Influence

8-DOF motions, turbine power and coefficient of variation metrics for different wind and wave directions. The impact on the power and coefficient of variation is shown in Table J.1 and Table J.2. The Figures J.1- J.6 show the influence on the motions, power and coefficient of variation per floater. All plots use consistent colour conventions from Figure 4.1 and Figure 4.2.

Table J.1: Power production for different wind and wave directions.

		Turbine power difference vs base (Wind = wave direction = 0 °)					
Wind direction	**Wave direction**	**WindCrete 135m**	**WindCrete 150m**	**ActiveFloat 135m**	**ActiveFloat 150m**	**Volturn-US-S**	**Reference TLP**
0°	**0°**	**10122 kW**	**10358 kW**	**9990 kW**	**10182 kW**	**10406 kW**	**10821 kW**
	15°	-0.004%	-0.004%	-0.009%	-0.009%	-0.016%	0.000%
	30°	-0.007%	-0.008%	-0.015%	-0.015%	-0.027%	-0.003%
	45°	-0.015%	-0.015%	-0.011%	-0.011%	-0.029%	-0.007%
	60°	-0.020%	-0.020%	-0.009%	-0.006%	-0.026%	-0.011%
15°	**0°**	-0.004%	-0.001%	0.005%	-0.009%	0.002%	-0.001%
	15°	-0.004%	-0.001%	-0.003%	-0.017%	-0.011%	0.000%
	30°	-0.005%	-0.002%	-0.009%	-0.023%	-0.020%	0.000%
	45°	-0.011%	-0.008%	-0.003%	-0.017%	-0.021%	-0.003%
	60°	-0.016%	-0.013%	0.000%	-0.012%	-0.016%	-0.007%
30°	**0°**	-0.034%	-0.013%	-0.035%	-0.076%	-0.054%	-0.004%
	15°	-0.031%	-0.011%	-0.040%	-0.081%	-0.065%	-0.001%
	30°	-0.028%	-0.008%	-0.043%	-0.085%	-0.070%	0.001%
	45°	-0.032%	-0.011%	-0.034%	-0.076%	-0.066%	-0.001%
	60°	-0.035%	-0.015%	-0.026%	-0.067%	-0.055%	-0.004%
45°	**0°**	-0.027%	-0.035%	-0.081%	-0.150%	-0.089%	-0.007%
	15°	-0.022%	-0.030%	-0.085%	-0.154%	-0.095%	-0.003%
	30°	-0.016%	-0.025%	-0.086%	-0.156%	-0.096%	0.000%
	45°	-0.016%	-0.025%	-0.075%	-0.146%	-0.088%	0.001%
	60°	-0.017%	-0.025%	-0.062%	-0.134%	-0.072%	-0.001%
60°	**0°**	-0.052%	-0.045%	-0.094%	-0.177%	-0.095%	-0.010%
	15°	-0.046%	-0.040%	-0.096%	-0.178%	-0.099%	-0.006%
	30°	-0.039%	-0.032%	-0.095%	-0.179%	-0.097%	-0.003%
	45°	-0.035%	-0.030%	-0.083%	-0.167%	-0.087%	0.000%

Table J.2: Coefficient of variation (CoV) for different wind and wave directions.

		Coefficient of Variation					
Wind direction	**Wave direction**	**WindCrete 135m**	**WindCrete 150m**	**ActiveFloat 135m**	**ActiveFloat 150m**	**Volturn-US-S**	**Reference TLP**
	0°	**0.812%**	**0.922%**	**0.480%**	**0.464%**	**0.667%**	**0.499%**
	15°	0.765%	0.884%	0.468%	0.450%	0.685%	0.469%
0°	**30°**	0.725%	0.850%	0.469%	0.454%	0.612%	0.410%
	45°	0.647%	0.786%	0.507%	0.492%	0.485%	0.328%
	60°	0.589%	0.738%	0.552%	0.534%	0.349%	0.232%
	0°	0.870%	0.948%	0.478%	0.458%	0.676%	0.494%
	15°	0.856%	0.936%	0.479%	0.458%	0.721%	0.496%
15°	**30°**	0.844%	0.925%	0.484%	0.468%	0.685%	0.466%
	45°	0.782%	0.869%	0.528%	0.512%	0.590%	0.409%
	60°	0.729%	0.822%	0.554%	0.537%	0.460%	0.328%
	0°	0.890%	0.997%	0.578%	0.550%	0.652%	0.458%
	15°	0.904%	1.011%	0.566%	0.541%	0.733%	0.491%
30°	**30°**	0.919%	1.025%	0.560%	0.539%	0.747%	0.493%
	45°	0.879%	0.990%	0.594%	0.572%	0.696%	0.464%
	60°	0.843%	0.959%	0.604%	0.579%	0.591%	0.408%
	0°	0.749%	0.916%	0.575%	0.551%	0.528%	0.392%
	15°	0.788%	0.948%	0.563%	0.543%	0.665%	0.454%
45°	**30°**	0.831%	0.985%	0.562%	0.548%	0.740%	0.487%
	45°	0.812%	0.972%	0.597%	0.579%	0.725%	0.491%
	60°	0.796%	0.960%	0.604%	0.581%	0.635%	0.464%
	0°	0.664%	0.848%	0.471%	0.452%	0.415%	0.303%
	15°	0.719%	0.893%	0.477%	0.462%	0.604%	0.388%
60°	**30°**	0.786%	0.947%	0.499%	0.488%	0.728%	0.451%
	45°	0.797%	0.958%	0.544%	0.531%	0.740%	0.487%
	60°	0.812%	0.971%	0.549%	0.530%	0.662%	0.491%

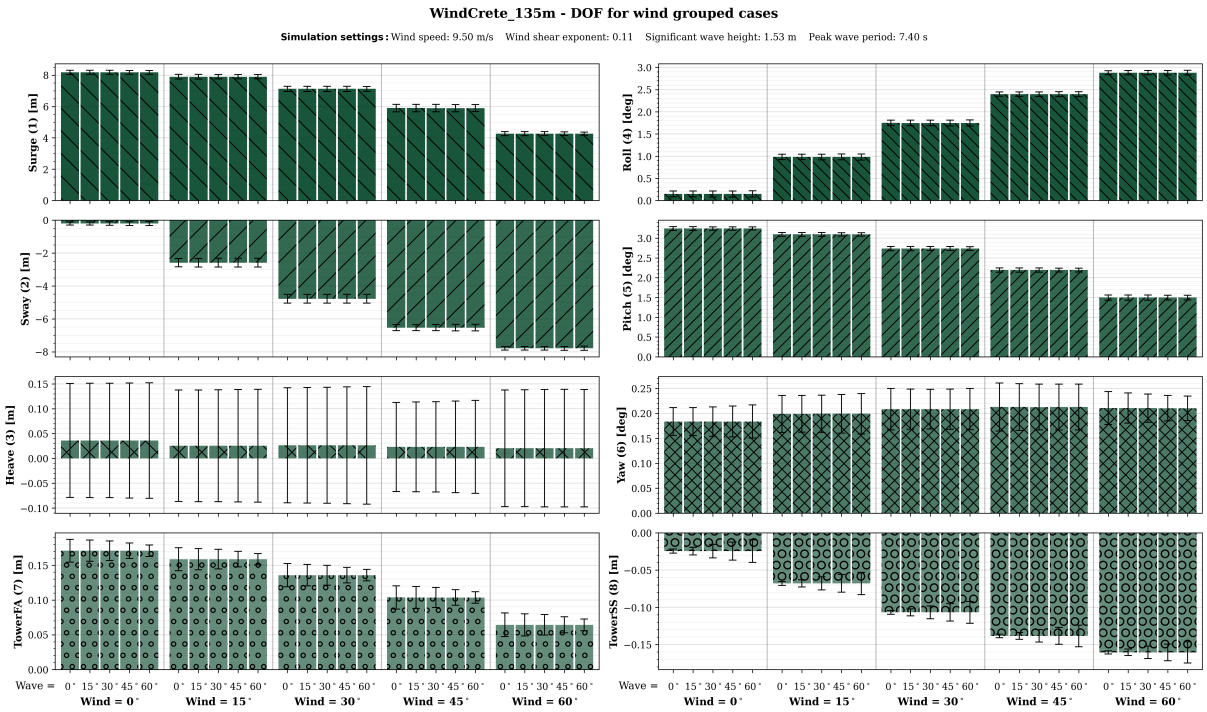

(a) 8-DOF motions (vertical axis zoomed).

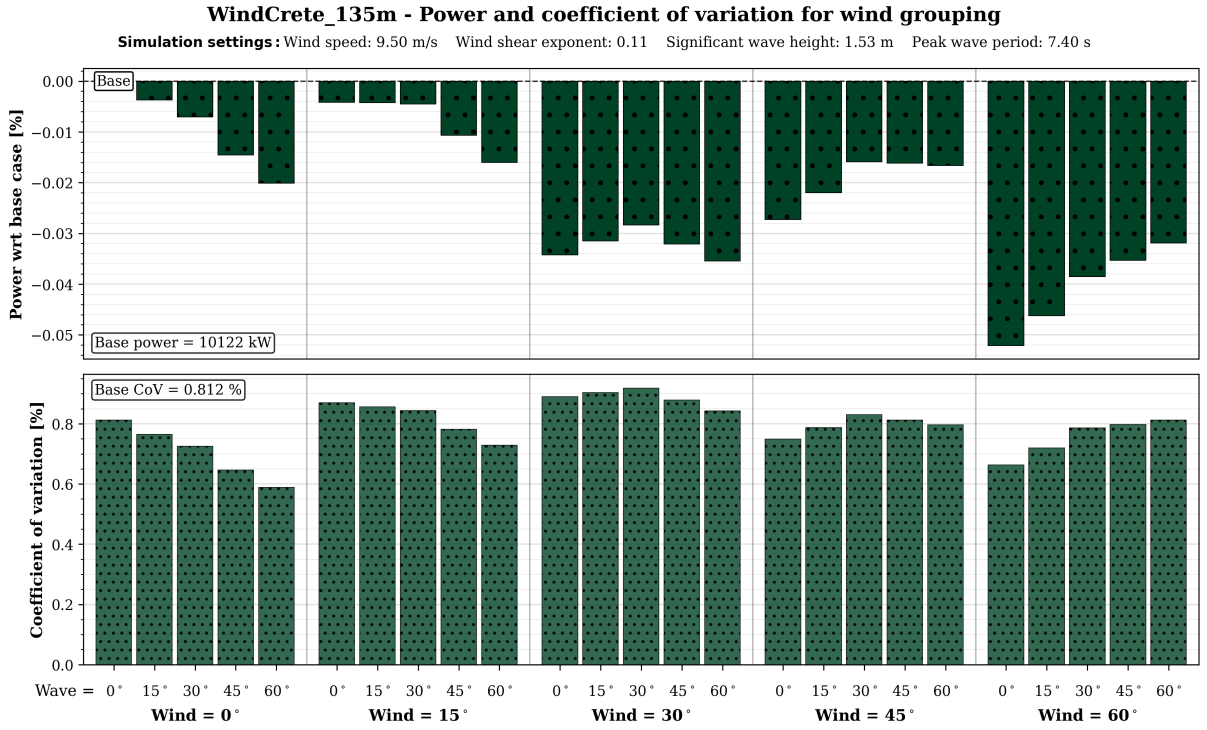

(b) Power with respect to base and CoV.

Figure J.1: WindCrete_135m: 8-DOF motions, power and CoV per wind and wave direction.

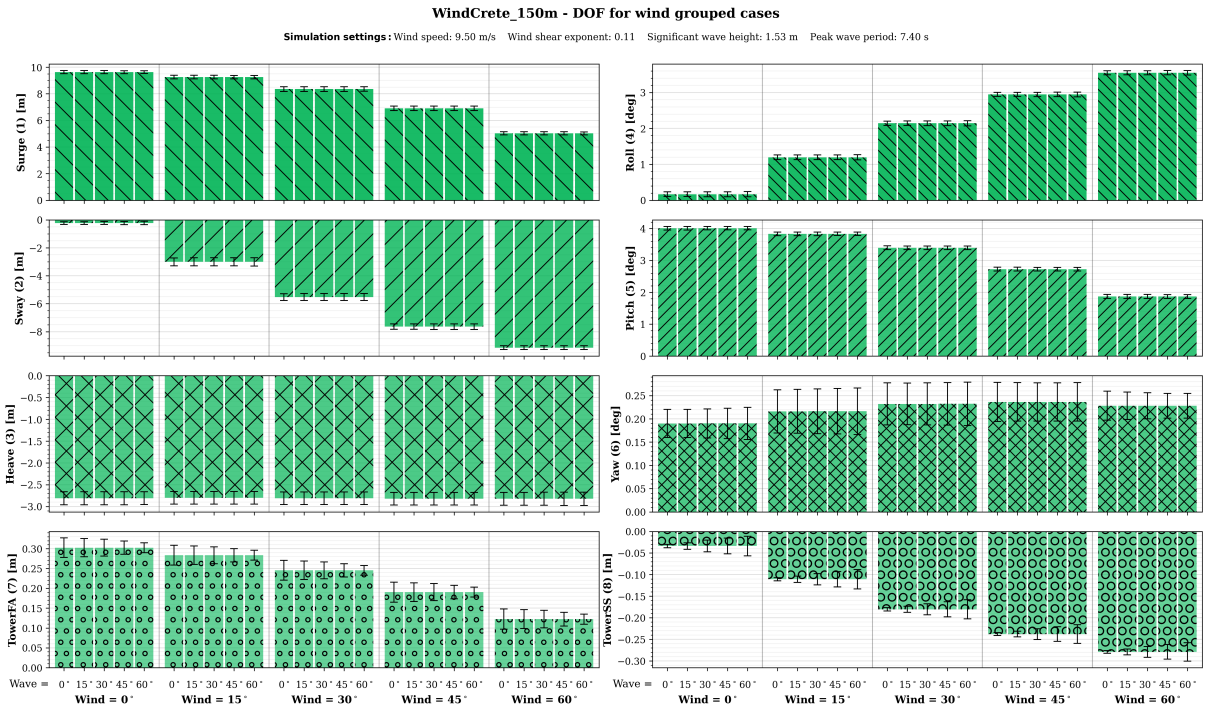

(a) 8-DOF motions (vertical axis zoomed).

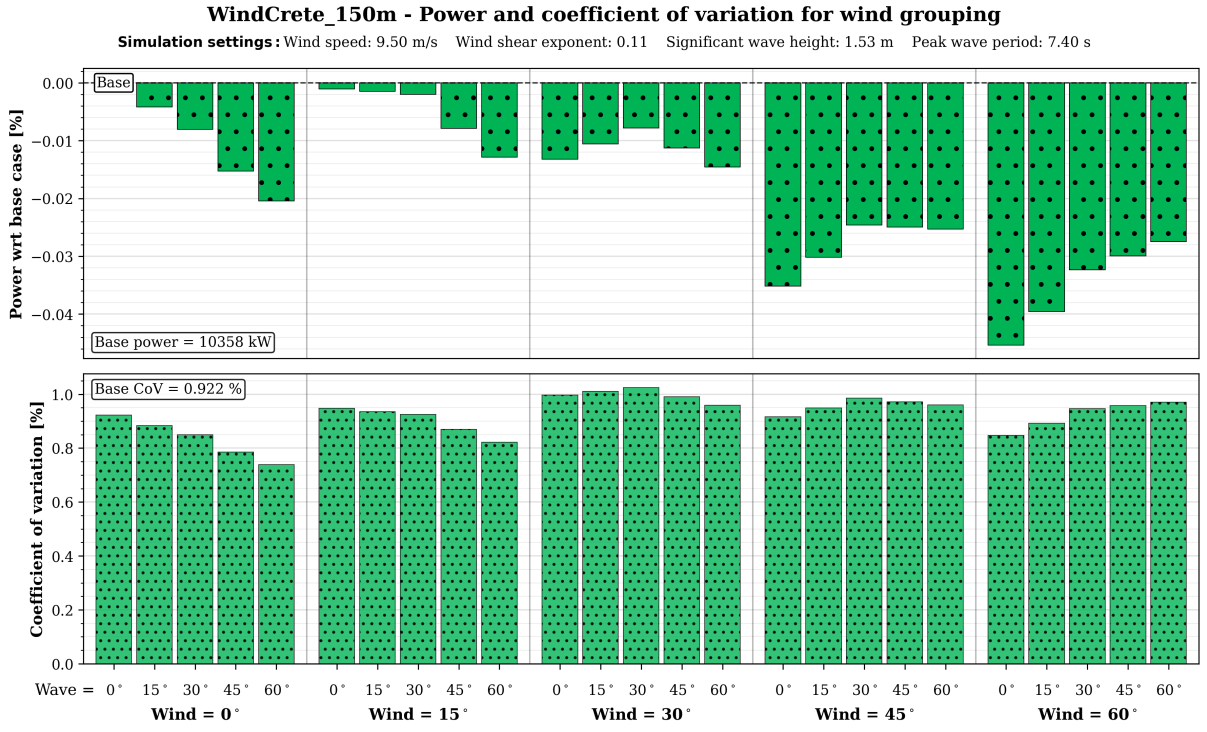

(b) Power with respect to base and CoV.

Figure J.2: WindCrete_150m: 8-DOF motions, power and CoV per wind and wave direction.

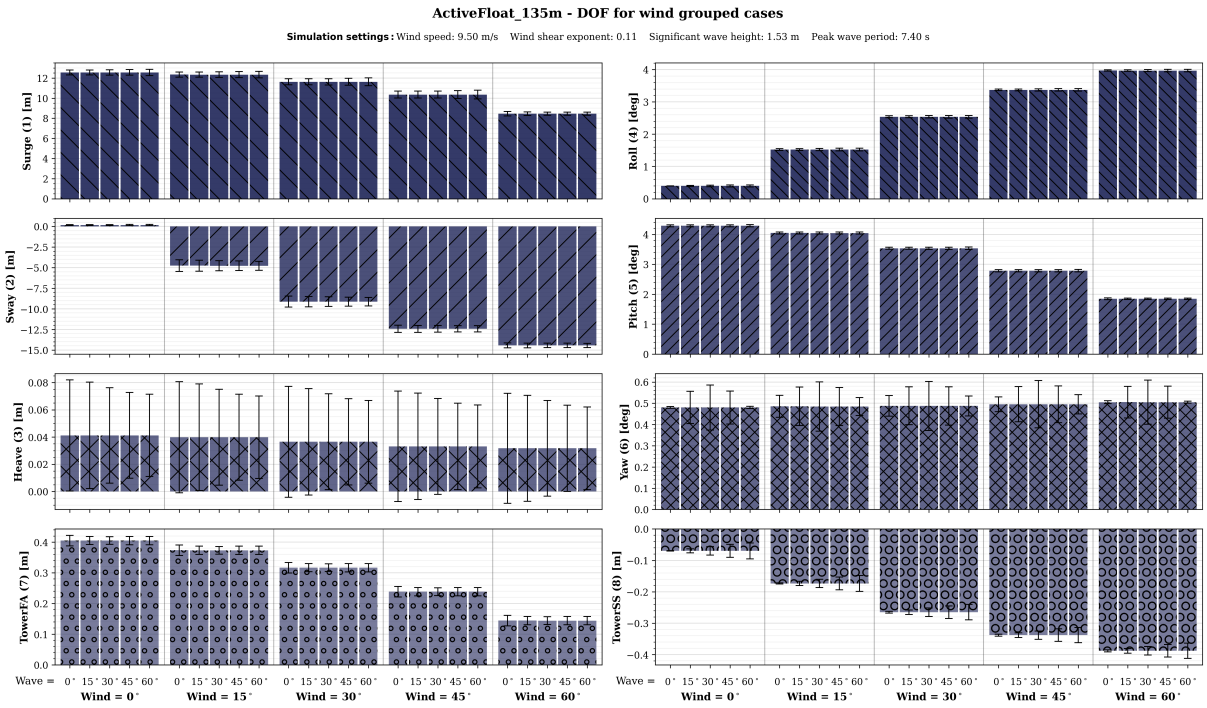

(a) 8-DOF motions (vertical axis zoomed).

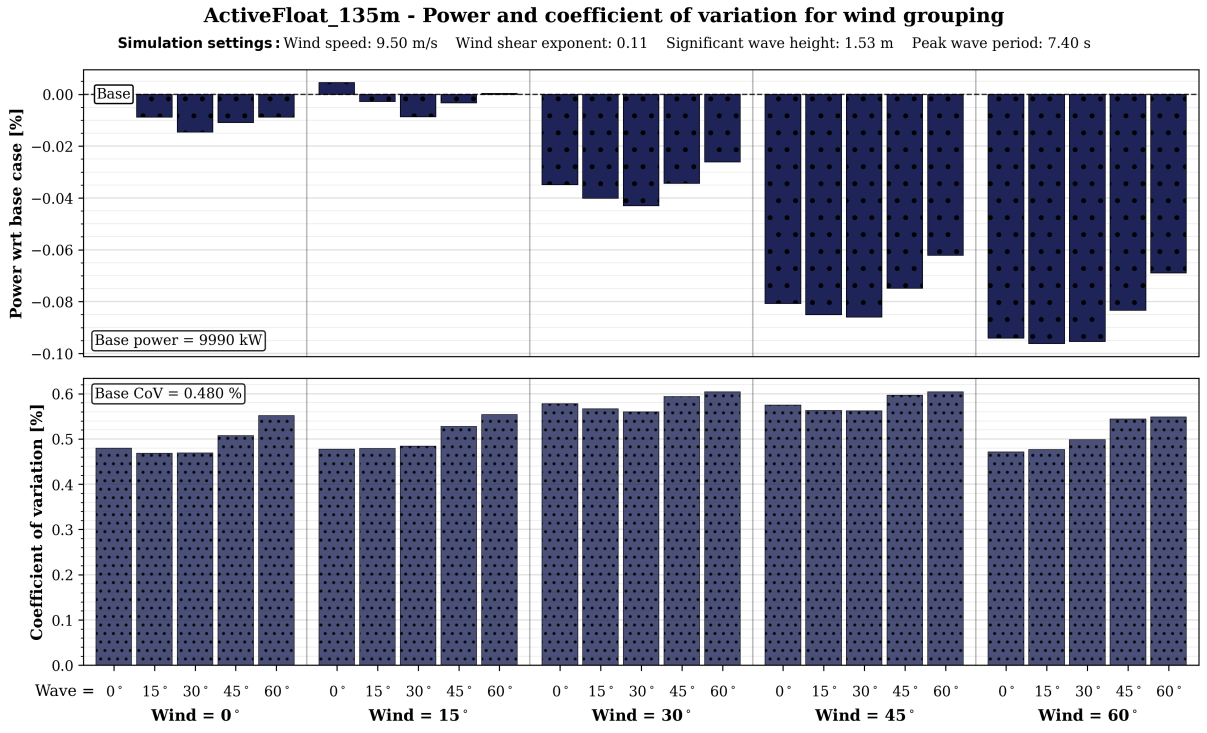

(b) Power with respect to base and CoV.

Figure J.3: ActiveFloat_135m: 8-DOF motions, power and CoV per wind and wave direction.

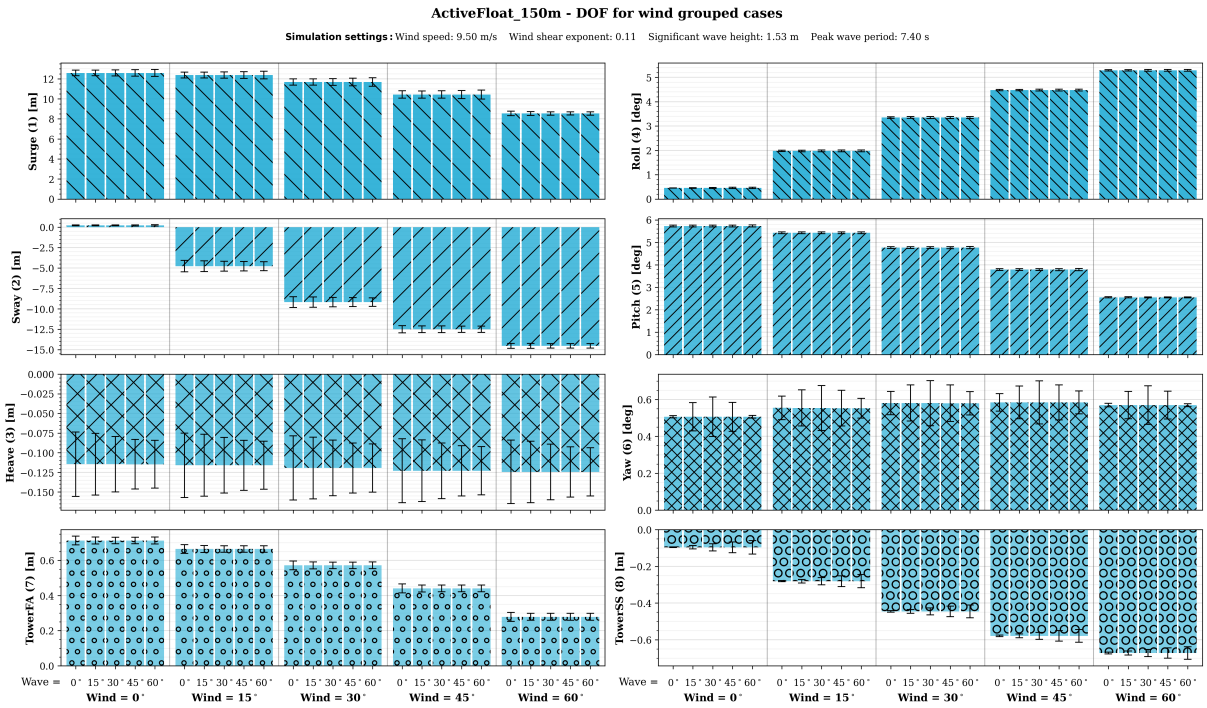

(a) 8-DOF motions (vertical axis zoomed).

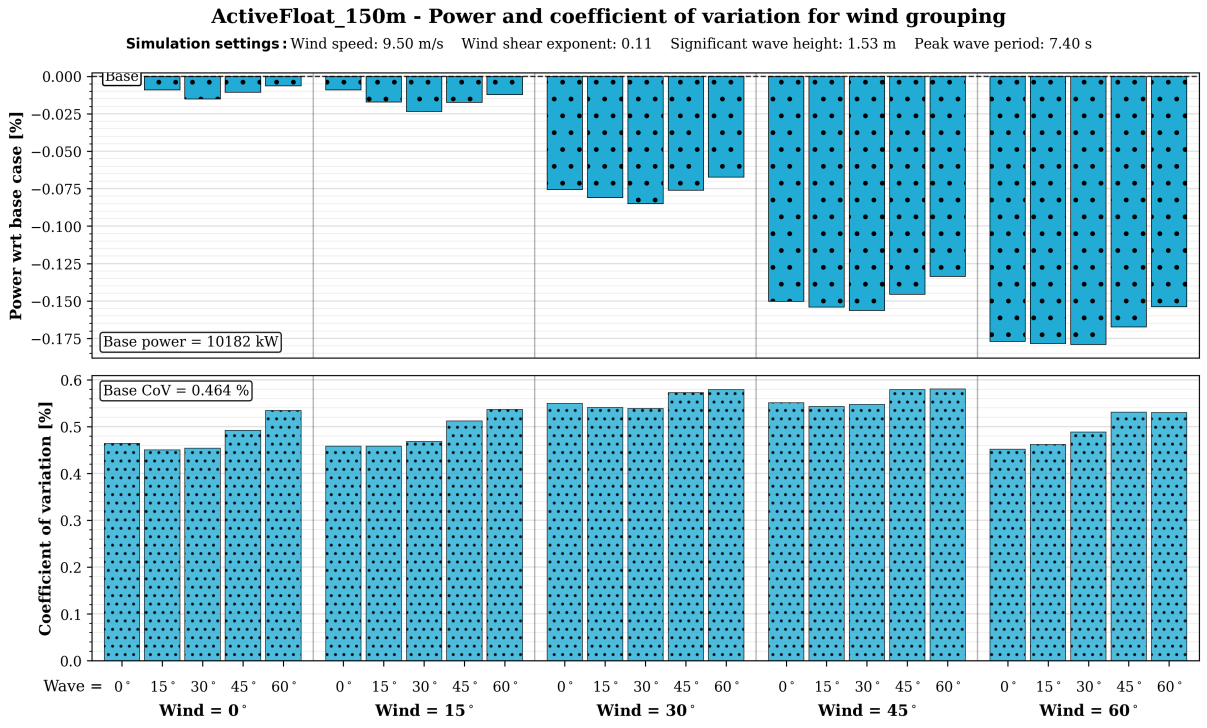

(b) Power with respect to base and CoV.

Figure J.4: ActiveFloat_150m: 8-DOF motions, power and CoV per wind and wave direction.

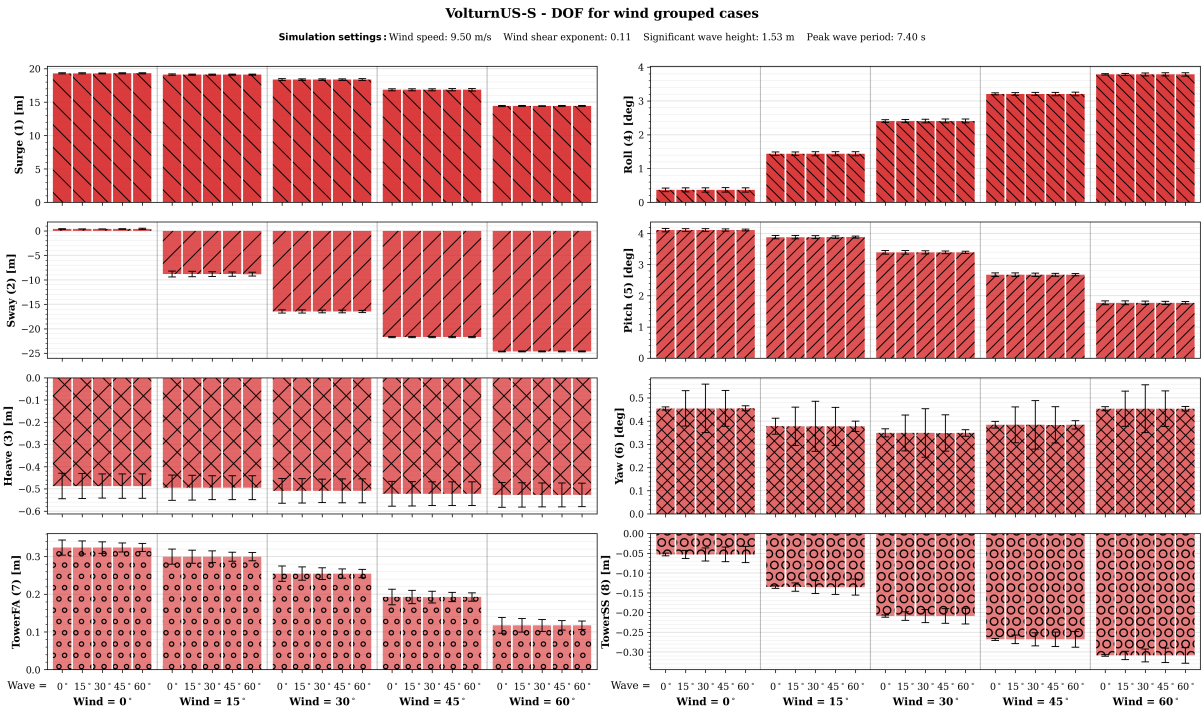

(a) 8-DOF motions (vertical axis zoomed).

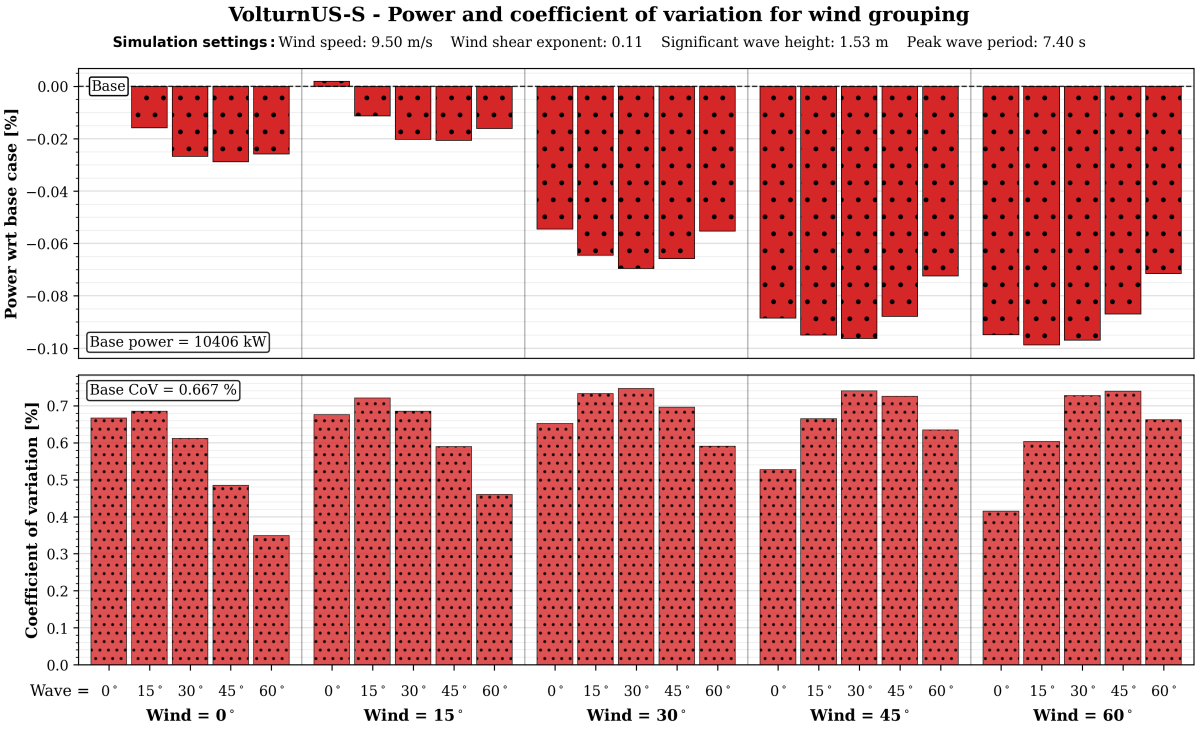

(b) Power with respect to base and CoV.

Figure J.5: VolturnUS-S: 8-DOF motions, power and CoV per wind and wave direction.

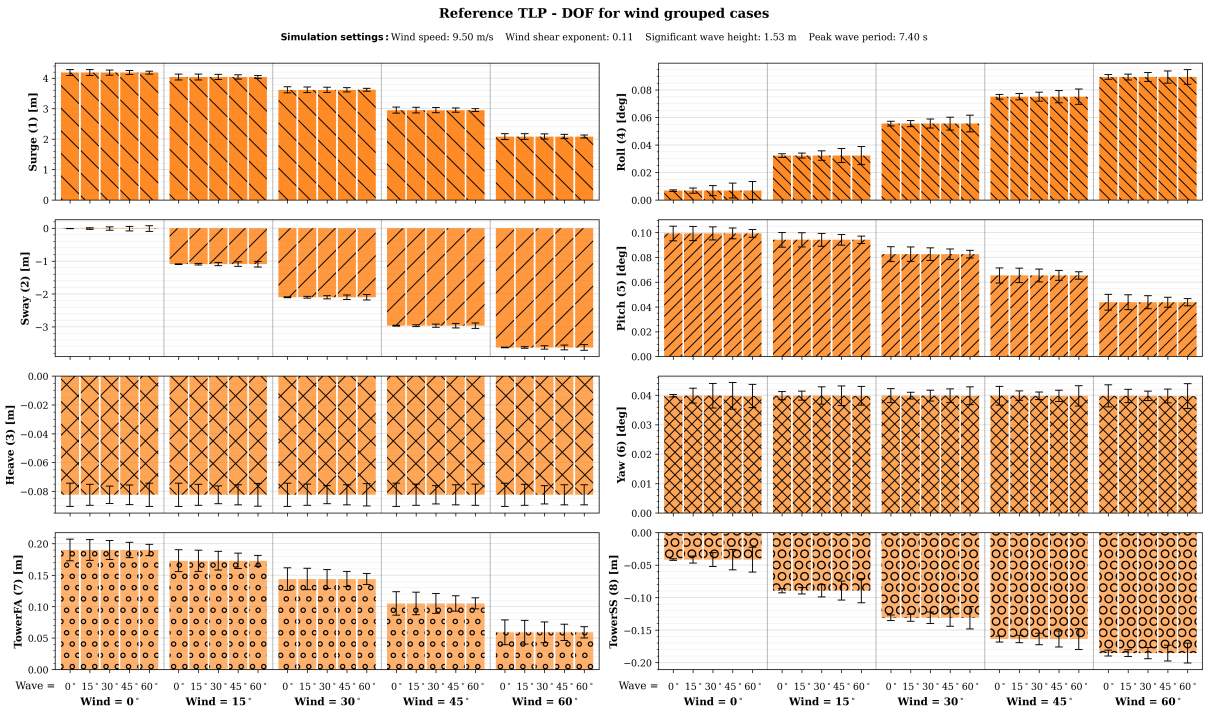

(a) 8-DOF motions (vertical axis zoomed).

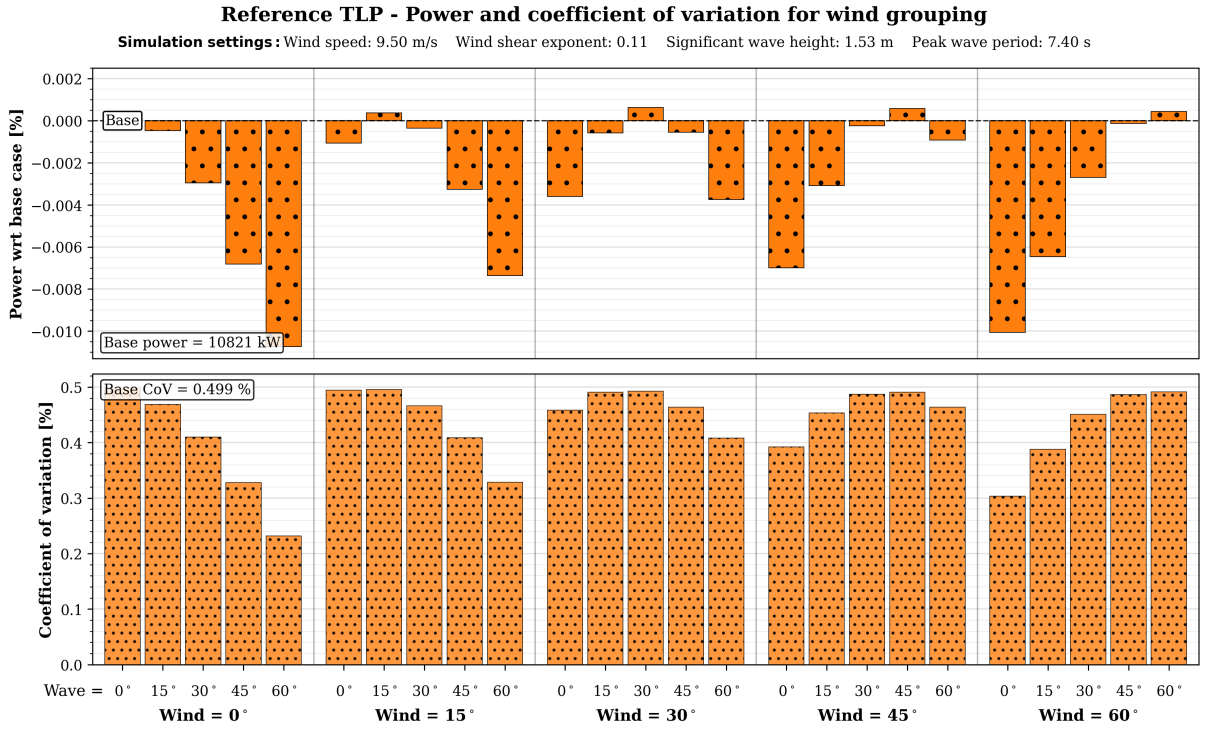

(b) Power with respect to base and CoV.

Figure J.6: Reference TLP: 8-DOF motions, power and CoV per wind and wave direction.